

Inaugural dissertation  
for  
obtaining the doctoral degree  
of the  
Combined Faculty of Mathematics, Engineering and Natural Sciences  
of the  
Ruprecht - Karls - University  
Heidelberg

Presented by

M.Sc. Andreas Hecker

born in: Bottrop, NRW, Germany

Oral examination: 04.11.2025

# **Deregulation of CYP1B1 leads to ocular phenotypes in a Srd5a3-KO medaka fish embryo model**

Referees: Prof. Dr. Britta Brügger

PD Dr. Christian Thiel



# Content

List of Abbreviation .....	VI
General .....	VI
Lipid classes .....	IX
Nucleobases .....	IX
Amino Acid Letter Code.....	X
Abbreviation and symbols of sugars .....	X
1. Zusammenfassung .....	1
2. Abstract.....	2
3. Introduction .....	3
3.1 Glycosylation .....	3
3.2 <i>N</i> -glycosylation .....	3
3.3 <i>De novo</i> biosynthesis and the role of Dolichol in Glycosylation .....	6
3.3 Congenital Disorders of Glycosylation .....	7
3.4 SRD5A3-CDG .....	9
3.4.1 SRD5A3-CDG Eye Pathologies: Coloboma, Retinitis pigmentosa and Optic nerve hypoplasia .....	10
3.5 The Eye .....	11
3.5.1 Early Eye Development .....	12
3.5.2 Retina and Optic Nerve .....	13
3.6 Cytochrome P450 family 1 subfamily B member 1 (CYP1B1) .....	13
3.7 AhR signalling and Nrf2 pathway axis .....	15
3.8 Cholesterol biosynthesis.....	16
3.9 Model organism: Medaka fish embryos.....	18
4. Aim of the Study .....	19
5. Material and Methods .....	20
5.1 Ethic and regulations .....	20
5.1.1 Patient's Material .....	20
5.1.2 Animal husbandry .....	20
5.2 Material .....	20
5.2.1 Consumables.....	20
5.2.2 Chemicals .....	22
5.2.3 Devices .....	23
5.2.4 Kits, standards and enzymes .....	25
5.2.5 Buffer .....	26
5.2.6 Oligonucleotides .....	28
5.2.7 Antibody .....	29
5.2.8 Lectin .....	30
5.2.9 Programs, online tools and data bases .....	30
5.3 Cell culture.....	31
5.3.1 Cell culture handling .....	31

5.3.2 Cell counting .....	32
5.3.3 Cryopreservation .....	32
5.4 Generation of Srd5a3- knock-out medaka fish embryo.....	32
5.4.1 Design of single guide RNAs (sgRNA).....	32
5.4.2 Microinjection: $\Delta$ Srd5a3 medaka fish embryos .....	33
5.4.3 Genetic validation of Srd5a3-KO medaka fish embryos .....	33
5.4.4 Mass spectrometry: Glycosylation profile of medaka fish embryos .....	34
5.5 CDG Diagnostic: Validation of SRD5A3-CDG deficiency in serum and patient-derived fibroblasts .....	34
5.5.1 Isoelectric focussing .....	34
5.5.2 LC-MS System: <i>N</i> -glycanprofile analysis .....	35
5.5.3 Lipid-linked oligosaccharide analysis .....	36
5.6 Molecular methods .....	36
5.6.1 RNA isolation .....	36
5.6.2 PCR Primer Design .....	37
5.6.3 Reverse Transcription .....	37
5.6.4 Polymerase Chain Reaction (PCR).....	37
5.6.5 Agarose Gel electrophoresis .....	39
5.6.6 Sanger Sequencing .....	39
5.6.7 Total lysate preparation .....	39
5.6.8 Total protein quantification .....	39
5.6.9 SDS-PAGE .....	40
5.6.10 Western and Lectin blot.....	41
5.6.11 Nuclei isolation .....	42
5.6.12 Quantification of cellular ROS .....	42
5.6.13 Glutathione assay .....	42
5.6.14 Immunofluorescence microscopy .....	43
5.6.15 Lipidomic analysis .....	43
5.6.16 “Shotgun-“proteomic analysis.....	43
5.6.17 <i>N</i> -Glycomic analysis .....	44
5.7 Transcriptomic analysis .....	46
5.7.1 Quantitative Real Time PCR analysis .....	46
5.7.2 nCounter analysis .....	47
5.7.3 Whole Transcriptomics .....	48
5.8 Statistic .....	48
5.9 Use of artificial intelligence .....	48
6. Results.....	49
6.1 Validation of SRD5A3-CDG in sera and patient-derived fibroblasts .....	49
6.1.1 Isoelectric focussing and genomic analysis .....	49
6.1.2 <i>N</i> -glycan analysis of whole sera by mass spectrometry and Lipid-linked oligosaccharide validation.....	50

6.1.2 Lipidomics .....	53
6.2 Elevated expression of <i>CYP1B1</i> in SRD5A3-CDG patient-derived fibroblasts on transcript level .....	56
6.3 Elevated expression of <i>CYP1B1</i> in SRD5A3-CDG patient-derived fibroblasts on protein level ..	60
6.4 Deregulation of <i>CYP1B1</i> in a variety of CDG-types on transcript and protein level .....	61
6.5 Downregulation of the AhR pathway in SRD5A3-CDG patient-derived fibroblasts .....	64
6.6 Decreased estrogen-receptor and increased TNF and IL6 gene expression in SRD5A3-CDG patient-derived fibroblasts .....	66
6.7 Alterations in the <i>Nrf2/NFE2L2</i> pathway and its regressor KEAP1 in SRD5A3-CDG patient-derived fibroblasts .....	67
6.8 Decreased antioxidative capacity in SRD5A3-CDG patient-derived fibroblasts .....	69
6.9 Elevated expression of coloboma-associated gene <i>PAX6</i> .....	74
6.10 Validation and characterisation of <i>Srd5a3</i> -knock out in medaka fish embryos.....	74
6.11 Increased expression of <i>Cyp1b1</i> <i>Srd5a3</i> -knock out medaka fish embryos correlating to phenotypical severity .....	80
6.12 Rescue approach: Double KO of <i>Srd5a3</i> and <i>Cyp1b1</i> results in lethal phenotype .....	82
7. Discussion .....	83
7.1 Validation confirms SRD5A3-CDG related hypoglycosylation phenotype in SRD5A3-CDG patient derived fibroblasts .....	83
7.2 Lipidomics.....	84
7.3 Elevated expression of <i>CYP1B1</i> is a molecular key characteristic among different subtypes of CDG.....	85
7.4 SRD5A3-KO medaka fish model: A suitable model to confirm organism wide elevated expression of <i>CYP1B1</i> 's ortholog, correlating to the development of coloboma.....	87
7.5 Deregulated AhR and <i>Nrf2/NFE2L2</i> signalling pathway are leading to increased oxidative stress in SRD5A3-CDG.....	89
7.6 Non-canonical or alternative pathways induce the elevated expression of <i>CYP1B1</i> in a hypoglycosylation context.....	92
7.7 Potential therapeutic approach regarding ophthalmological abnormalities in CDG.....	93
8. Outlook .....	96
9. References .....	97
10. Supplementary information.....	106
11. Danksagung .....	131

## List of figures

Figure 1: <i>N</i> -Glycosylation pathway.....	6
Figure 2: Schematic figure of the structures of the eye.....	12
Figure 3: Overview of human CYP1B1 .....	15
Figure 4: AhR and Nrf2 signalling pathway and their crosstalk.....	16
Figure 5: Biosynthesis pathway of cholesterol. ....	17
Figure 6: Isoelectric focussing of serum transferrin from SRD5A3-CDG patients and Sanger sequencing of exon 1 of the <i>SRD5A3</i> gene in fibroblasts .....	50
Figure 7: Whole serum <i>N</i> -glycan analysis by LC-MS (fluorescence) reveals no unique increase of the SRD5A3-CDG typical M3 and M4 in SRD5A3-CDG patient 3 serum.....	51
Figure 8: Increased relative M3 and M4 peaks in SRD5A3-CDG patient 3 according to whole serum <i>N</i> -glycan analysis by LC-MS (Mass). ....	52
Figure 9: Lipid-linked oligosaccharide analysis of SRD5A3-CDG patient-derived fibroblasts. ....	53
Figure 10: Mass spectrometric based lipidomic analysis of various lipid classes. ....	54
Figure 11: Physiological levels of cholesterol in SRD5A3-CDG patient-derived fibroblasts. ....	56
Figure 12: Deregulated gene expression in SRD5A3-CDG patient-derived fibroblasts. ....	57
Figure 14: Elevated expression of <i>CYP1B1</i> and physiological expression of <i>CYP1A1</i> in SRD5A3-CDG patient-derived fibroblasts. ....	60
Figure 15: Elevated CYPB1 protein levels in SRD5A3-CDG patient-derived fibroblasts.....	61
Figure 16: Elevated expression of <i>CYP1B1</i> transcripts in DHDDS- and MVK-CDG patient-derived fibroblasts .....	62
Figure 17: Elevated CYPB1 protein levels in a variety of early and late CDG-types. ....	63
Figure 18: Decreased expression of AhR and its interaction partners AhRR and ARNT2. ....	65
Figure 19: Downregulation of ESR1 and upregulation of cytokines TNF and IL-6 gene expression in SRD5A3-CDG patient-derived fibroblasts. ....	67
Figure 20: Reduced post-translational modification in <i>Nrf2</i> /NFE2L2 and decreased nuclear localisation of KEAP1 in SRD5A3-CDG patient-derived fibroblasts. ....	68
Figure 21: Decreased nuclear accumulation of KEAP1 in SRD5A3-CDG patient-derived fibroblasts. ....	69
Figure 22: Deregulated glutathione homeostasis and increased oxidative stress in SRD5A3-CDG patient-derived fibroblasts. ....	71
Figure 23: Decreased gene expression of genes involved in the antioxidative response in SRD5A3-CDG patient-derived fibroblasts. ....	73
Figure 24: Elevated transcript expression of coloboma-associated <i>PAX6</i> gene. ....	74
Figure 25: Knock-out of <i>Srd5a3</i> in medaka fish embryos validated by Sanger sequencing.....	75
Figure 26: Decreased gene expression of <i>Srd5a3</i> after performing a knock-out by microinjection in medaka fish embryos. ....	76
Figure 27: <i>Srd5a3</i> -KO medaka fish embryos mimic several clinical symptoms of SRD5A3-CDG patients. ....	77
Figure 28: Elevated expression of <i>Cyp1b1</i> in <i>Srd5a3</i> -KO medaka fish embryos with a severe phenotype. ....	81

## List of tables

Table 1: List of used consumables.....	20
Table 2: List of chemicals and respective companies.....	22
Table 3: List of used devices.....	23
Table 4: List of kits, standards and enzymes with respective companies.....	25
Table 5: List of buffers and their composition.....	26
Table 6: List of used oligonucleotides and gRNAs of corresponding method. (PAM in brackets).....	28
Table 7: List of used antibodies.....	29
Table 8: List of used lectins and HRP-coupled streptavidin.....	30
Table 9: List of used programs, online tools and data bases, including developer and corresponding online-links.....	30
Table 10: CRISPR/Cas9 mix.....	33
Table 11: Reaction mix for generation of cDNA from total RNA with Omniscript Reverse Transcription Kit.....	37
Table 12: PCR Mixes for <i>Taq</i> and <i>Phusion</i> <sup>TM</sup> polymerase and the corresponding PCR protocol.....	38
Table 13: Composition of 8, 10 and 12.5 % separation gel and stacking gel.....	40
Table 14: qRT-PCR mix and qRT-PCR protocol.....	47
Table 15: Values of Mass spectrometric based lipidomic analysis of various lipid classes.....	55
Table 16: Significantly deregulated expression of genes in SRD5A3-CDG patient-derived fibroblasts.....	58
Table 17: CYPB1 protein levels in early and late CDG-types.....	64
Table 18: Distribution of severity of the Srd5a3- and Oca2-KO (injection-control) medaka fish embryos.....	78
Table 19: Altered accumulations of N-glycan structures in Srd5a3-KO medaka fish hatchlings compared to wild type.....	79
Table 20: Lethality of Srd5a3-, Srd5a3- + Cyp1b1-KO, and uninjected medaka fish embryos.....	82
Table S1: Targeted genes in nCounter analysis and corresponding differential expression.....	106
Table S2: Significantly deregulated transcripts in SRD5A3 patient-derived fibroblasts.....	109
Table S3: N-Glycomic analysis of Srd5a3-KO medaka fish hatchlings compared to wild type.....	124



## List of Abbreviation

### General

ABBREVIATION	CONTENT
%	Percent
~	Approximately
±	Plus/minus
°C	Degree Celsius
ALG 1/3	Asparagine linked glycosylation 1/3
AMP	Ampicillin
APO-CIII	Apolipoprotein CIII
APS	Ammonium peroxide disulfate
ATP	Adenosine triphosphate
B3GALNT2	β 1 3 N-acetylgalactosaminyltransferase 2
B4GALT1/2	Beta-1,4-galactosyltransferase 1/2
BP	Base pairs
BSA	Bovine serum albumin
CAS	CRISPR-associated protein
C14ORF1	Ergosterol biosynthetic protein 28
CDG	Congenital disorders of glycosylation
CDNA	Complementary desoxyribonucleic acid
CMP	Cytidine monophosphate
CONA	Concavalin A
CRISPR	clustered regularly interspaced short palindromic repeat
CRRNA	Cas9-CRISPR RNA
CT	Cycle threshold
CTP	Cytidine diphosphate
CTRL	Control
CYP1B1	Cytochrome P450 1B1
DHDDS	Dehydrolipichyl diphosphate synthase
DHCR7	7-Dehydrocholesterol reductase
DHCR24	24-Dehydrocholesterol reductase
DMEM	Dulbecco's Modified Eagle's Medium
DMSO	Dimethyl sulfoxide
DNA	Desoxyribonucleic acid
DNTP	Desoxy nucleotide triphosphate
DOL-P	Dolichol-phosphate
DOLPP1	Dolichyldiphosphatase 1
DOL-P-MAN	Dolichol-phosphate mannose
DPAGT1	UDP-N-acetylglucosamine--dolichyl-phosphate acetylglucosaminophosphotransferase
DPBS	Dulbecco's phosphate-buffered saline
DPF	Days post fertilisation
DPM	Dolichol-phosphate mannosyltransferase subunit 1
DSDNA	Double-stranded DNA
DTT	Dithiothreitol
ECL	Enhanced chemiluminescence

<b>ECM</b>	Extracellular matrix
<b>EET</b>	Epoxyeicosatrienoic acids
<b>ER</b>	Endoplasmic reticulum
<b>ERM</b>	embryo-rearing medium
<b>ERG28</b>	Ergosterol biosynthetic protein 28
<b>ESI</b>	Electrospray ionisation
<b>EX</b>	Exon
<b>FCS</b>	Fetal calf serum
<b>FDFT1</b>	farnesyl-diphosphate farnesyltransferase 1
<b>FGFR1</b>	fibroblast growth factor receptor 1
<b>G</b>	Gram
<b>G418</b>	Genitacin
<b>GA</b>	Golgi-apparatus
<b>GALNACT</b>	GalNAc transferase
<b>GAPDH</b>	Glyceraldehyde 3-phosphate dehydrogenase
<b>GDNA</b>	Genomic desoxyribonucleic acid
<b>GDP</b>	Guanosine diphosphate
<b>GFUS</b>	GDP-L-Fucose Synthase
<b>GLCNACT</b>	N-acetylglucosamine transferase
<b>GLUTMRM</b>	Glutamine multiple reaction monitoring
<b>GM130</b>	Golgi-matrix Protein 130
<b>GPI</b>	Glucose-6-phosphate-isomerase
<b>H</b>	Hours
<b>HEICAS9</b>	high efficiency-tag Cas9
<b>HETE</b>	Hydroxyeicosatetraenoic acid
<b>HPLC</b>	High performance liquid chromatography
<b>HRP</b>	Horseradish peroxidase
<b>IEF</b>	Isoelectric focusing
<b>KDA</b>	Kilo Dalton
<b>KO</b>	Knockout
<b>L</b>	Liter
<b>LLO</b>	Lipid-linked-oligosaccharide
<b>M</b>	Molar (mol/litre)
<b>MA</b>	Milliampere
<b>MAN2A1</b>	Mannosidase Alpha Class 2A Member 1
<b>MG</b>	Milligram
<b>MGAT1</b>	alpha-1,3-mannosyl-glycoprotein 2-beta-N-acetylglucosaminyltransferase
<b>MGAT5</b>	alpha-1,6-mannosylglycoprotein 6-beta-N-acetylglucosaminyltransferase
<b>MIN</b>	Minutes
<b>ML</b>	Millilitre
<b>MM</b>	Millimetre
<b>MM</b>	Millimolar
<b>MPDU1</b>	mannose-P-dolichol utilization defect 1
<b>MRNA</b>	Messenger RNA
<b>MS</b>	Mass spectrometry
<b>NAAC</b>	Sodium acetate

<b>NM</b>	Nanometer
<b>NG</b>	Nanogram
<b>NM</b>	Nanomolar
<b>OCA2</b>	oculocutaneous albinism II
<b>OST</b>	Oligosaccharyl transferase-complex
<b>P</b>	<i>P</i> -value
<b>PAM</b>	protospacer adjacent motif
<b>PBS</b>	Phosphate buffered saline
<b>PBS-T</b>	Phosphate buffered saline tween
<b>PCR</b>	Polymerase chain reaction
<b>PEP</b>	Phosphoenolpyruvate
<b>PIM</b>	Protease inhibitor mix
<b>PMM2</b>	Phosphomannomutase 2
<b>POI</b>	Protein of interest
<b>PTM</b>	Posttranslational modification
<b>QRT-PCR</b>	Quantitative real time polymerase chain reaction
<b>RIPA</b>	Radioimmunoprecipitation assay buffer
<b>RNA</b>	Ribonucleic acid
<b>RNASE</b>	Ribonuclease
<b>RCF</b>	Relative centrifugal force
<b>RT</b>	Room temperature
<b>SDS-PAGE</b>	Sodium dodecyl sulfate polyacrylamide gel electrophoresis
<b>SEC</b>	Second
<b>SGRNA</b>	Single guide RNA
<b>SIRNA</b>	Small interfering RNA
<b>SLC35A1/2/5</b>	Solute carrier family 35 member A1/2/5
<b>SLC35C1</b>	Solute carrier family 35 member C1
<b>SLC35D2</b>	Solute carrier family 35 member D2
<b>SRD5A3</b>	steroid 5 alpha-reductase 3
<b>ST3GAL3</b>	CMP-N-acetylneuraminate-beta-1,4-galactoside alpha-2,3-sialyltransferase
<b>STT3B</b>	STT3 oligosaccharyltransferase complex catalytic subunit B
<b>TBS</b>	Tris buffered saline
<b>TBST</b>	Tris buffered saline tween
<b>TEMED</b>	Tetramethylethylenediamine
<b>TF</b>	Transferrin
<b>TUNEL</b>	TdT-mediated dUTP-biotin nick end labeling
<b>TRRNA</b>	trans-activating CRISPR RNA
<b>U</b>	Unit
<b>UDP</b>	Uridine diphosphate
<b>UV</b>	Ultraviolet
<b>V</b>	Volt
<b>WB</b>	Washing Buffer
<b>WES</b>	Whole-Exom-Sequencing
<b>WGA</b>	Wheat germ agglutinin
<b>WT</b>	Wildtype

## Lipid classes

ABBREVIATION	LIPID
CE	Cholesteryl ester
CER	Ceramide
CHOL	Cholesterol
DAG	Diacylglycerol
HEX2CER	Dihexosylceramide
HEXCER	Hexosylceramide
LPC	Lysophosphatidylcholine
PA	Phosphatidic acid
PA O-	Alkylphosphatidic acid
PC	Phosphatidylcholine
PC O-	Alkylphosphatidylcholine
PE	Phosphatidylethanolamine
PE O-	Alkylphosphatidylethanolamine
PE P-	Phosphatidylethanolamine plasmalogen
PG	Phosphatidylglycerol
PG O-	Alkylphosphatidylglycerol
PI	Phosphatidylinositol
PI O-	Alkylphosphatidylinositol
PS	Phosphatidylserine
PS O-	Alkylphosphatidylserine
SM	Sphingomyelin
TAG	Triacylglycerol








## Nucleobases

LETTER	NUCLEOBASE
A	Adenine
C	Cytosine
G	Guanine
N	Any base
T	Thymine
U	Uracil

## Amino Acid Letter Code

ONE-LETTER CODE	THREE-LETTER CODE	AMINO ACID
<b>A</b>	<b>Ala</b>	Alanine
<b>C</b>	<b>Cys</b>	Cysteine
<b>D</b>	<b>Asp</b>	Aspartic acid
<b>E</b>	<b>Glu</b>	Glutamic acid
<b>F</b>	<b>Phe</b>	Phenylalanine
<b>G</b>	<b>Gly</b>	Glycine
<b>H</b>	<b>His</b>	Histidine
<b>I</b>	<b>Ile</b>	Isoleucine
<b>K</b>	<b>Lys</b>	Lysine
<b>L</b>	<b>Leu</b>	Leucine
<b>M</b>	<b>Met</b>	Methionine
<b>N</b>	<b>Asn</b>	Asparagine
<b>P</b>	<b>Pro</b>	Proline
<b>Q</b>	<b>Gln</b>	Glutamine
<b>R</b>	<b>Arg</b>	Arginine
<b>S</b>	<b>Ser</b>	Serine
<b>T</b>	<b>Thr</b>	Threonine
<b>V</b>	<b>Val</b>	Valine
<b>W</b>	<b>Trp</b>	Tryptophan
<b>Y</b>	<b>Tyr</b>	Tyrosine

## Abbreviation and symbols of sugars

ABBREVIATION	SYMBOL	CONTENT
FUC		Fucose
GAL		Galactose
GALNAC		N-Acetylgalactosamine
GLC		Glucose
GLCNAC		N-Acetylglucosamine
MAN		Mannose
SIA		Sialic acid

# 1. Zusammenfassung

*Congenital disorders of glycosylation* (CDG) sind eine schnell wachsende Gruppe mit bisher über 190 identifizierten erblich bedingten Stoffwechselerkrankungen. SRD5A3-CDG ist ein seltener Subtyp, der u.a. durch neurologische Auffälligkeiten kombiniert mit Entwicklungs- und Wachstumsstörung gekennzeichnet ist. Charakteristisch für SRD5A3-CDG sind schwere okuläre Abnormalitäten, einschließlich Retinitis pigmentosa und Kolobom, die klinischen, diagnostischen Merkmale darstellen. Bis heute sind die molekularen Mechanismen, die den okulären Manifestationen zugrunde liegen ungeklärt.

CYP1B1, ein Cytochrom P450-Enzym, ist primär an Entgiftungsprozessen und der Regulation von Steroidhormonen beteiligt. Jedoch spielt es auch in der physiologischen Entwicklung des Auges eine wesentliche Rolle. Ein Mangel an CYP1B1 ist mit *Congenital primary glaucoma* assoziiert. Überexpression hingegen führt in Zebrafischen zur Entwicklung von Kolobomen. Meine Arbeit untersucht die potenzielle Verbindung zwischen SRD5A3-CDG und CYP1B1. Hierzu habe ich ein SRD5A3-CDG-Fibroblasten und ein CRISPR-Cas9-basiertes SRD5A3-Knockout-Modell in Medaka-Fischembryonen (*Oryzias latipes*) verwendet – der Phänotyp des Modells spiegelte klinische Symptome von SRD5A3-CDG Patienten. Meine Ergebnisse zeigen eine erhöhte CYP1B1-Expression basierend auf transkriptomischen (nCounter, Transkriptom-Analyse und qRT-PCR) sowie proteomischen Methoden (Western Blotting und Massenspektrometrie). Die erhöhte *Cyp1b1*-Expression in Medaka-Embryonen korrelierte stark mit der Entwicklung von Kolobomen. Darüber hinaus ergaben Massenspektrometrie- und Transkriptom-Analysen erhöhte CYP1B1-Level auch in einer Vielzahl von CDG-Typen, einschließlich früher und später CDG-Subtypen.

Meine FACS-Analysen von SRD5A3-CDG-Fibroblasten zeigen zudem einen erhöhten oxidativen Stress. Dies weist auf eine Störung des AhR-Nrf2-Signalwegs hin, die zu einer erhöhten Expression von CYP1B1 führen könnte, da AhR dessen Expression reguliert und Nrf2 eine Schlüsselrolle in der oxidativen Stressantwort spielt. Eine Runterregulation von AhR und seinem Repressor, AhRR, sowie eine potenziell reduzierte Aktivität von Nrf2 deuteten zudem darauf hin, dass noch nicht identifizierte, glykosylierungsabhängige Signalwege an der Hochregulation von CYP1B1 in SRD5A3-CDG-Patienten und Srd5a3-Knock-Fischembryonen beteiligt sind und vermutlich auch zur erhöhten Expression von CYP1B1 in anderen CDG-Defekten führt, was dann auch bei diesen ophthalmologischen Anomalien begünstigt.

Meine Ergebnisse liefern Einblicke in die molekularen Mechanismen mit erhöhter CYP1B1-Expression, die dem okulären Phänotyp bei SRD5A3-CDG zugrunde liegen. Diese betont die kritische Rolle von CYP1B1 bei einer Vielzahl von CDG-Typen und eröffnet die Möglichkeit für neue therapeutische Strategien zur Behandlung ophthalmologischer Abnormalitäten.

## 2. Abstract

Congenital Disorders of Glycosylation (CDG) compromise a rapidly expanding group of inherited metabolic disorders, with to date over 190 identified defects. SRD5A3-CDG is an ultra-rare subtype clinically presenting common CDG manifestations such as neurological, developmental impairments and failure to thrive. Characteristic for SRD5A3-CDG are severe ocular abnormalities, including retinitis pigmentosa and coloboma – which represent the clinical key features in the diagnostic. To date, the molecular mechanisms underlying the ocular manifestations remain poorly understood.

CYP1B1, a cytochrome P450 enzyme, is primarily involved in detoxification processes and the regulation of steroid hormones, but it is also essential for physiological eye development. CYP1B1 deficiency is linked to congenital primary glaucoma, while overexpression in zebrafish has been shown to induce coloboma. My study aims to explore the potential connection between SRD5A3-CDG and CYP1B1. For this, I used fibroblasts from SRD5A3-CDG patients and generated and established a CRISPR-Cas9-based *Srd5a3* knockout model in medaka (*Oryzias latipes*) embryos, representing clinical features of SRD5A3-CDG patients. My results reveal an upregulation of CYP1B1 expression in patient-derived fibroblasts and in *Srd5a3* knockout medaka fish embryos – assessed by multiple experimental approaches, including qRT-PCR, nCounter targeted analysis, transcriptome analysis, and proteomic investigations (Western blotting and mass spectrometry). Elevated *Cyp1b1* expression in *Srd5a3*-KO medaka fish embryos correlate strongly with the development of coloboma. Additionally, mass spectrometry and transcriptome analysis revealed elevated levels of CYP1B1 also in a broad variety of CDG types, including late and early CDG subtypes.

My FACS analysis of SRD5A3-CDG fibroblasts indicate increased oxidative stress. This points to a disruption in the AhR-Nrf2 signaling pathway leading to elevated expression of CYP1B1 since AhR regulates its expression and Nrf2 plays a key role in the oxidative stress response. Downregulation of AhR and its repressor AhRR as well as potential decreased activity of Nrf2 propose instead that rather unconventional and yet unidentified pathway which are associated with general glycosylation defects are activated or prone to induce an elevated expression of CYP1B1, resulting in ophthalmological abnormalities – independent of the type of CDG.

My findings provide valuable insights into the molecular mechanisms driving the ocular phenotype in SRD5A3-CDG, highlighting the elevated expression of CYP1B1 as a potential key factor. These results emphasize the critical role CYP1B1 among a variety of CDG types and opens opportunities for novel therapeutic strategies to treat ophthalmological abnormalities.

### 3. Introduction

#### 3.1 Glycosylation

Glycosylation, the enzymatic process of covalently attaching glycans (mono- or oligosaccharides) to proteins or other biomolecules, is a ubiquitous post-translational modification (PTM) that plays a crucial role in a huge variety of biological processes [2, 3]. This sugar attachment occurs across all domains of life, from archaea and bacteria to eukaryotes, underscoring its evolutionary conservation and significance [4]. The glycosylation machinery, primarily localized in the endoplasmic reticulum (ER) and Golgi apparatus, involves a complex interplay of glycosidases, glycosyltransferases, and other enzymes that orchestrate the synthesis, transfer, and processing of glycans [5]. These glycan structures are assembled from nucleotide-activated sugar donors or dolichol-linked oligosaccharide precursors, which are subsequently transferred to specific acceptor sites on target biomolecules [5, 6].

The diversity of glycosylation is remarkable, with various types including the most prevalent *N*-glycosylation (attachment to asparagine residues) and *O*-glycosylation (attachment to serine or threonine residues), as well as the rare *C*-mannosylation (attachment to tryptophan residues), and glycosylphosphatidylinositol (GPI) anchoring [2, 5, 7, 8]. This structural heterogeneity, coupled with the vast combinatorial possibilities of glycan composition and branching, contributes to the immense complexity of the glycoproteome [9]. Glycosylation profoundly influences biological properties and function of biomolecules: physicochemical properties, folding, stability, and more. Additionally, glycans serve as molecular codes, mediating crucial cellular processes such as protein trafficking, cell-cell interactions, immune recognition, and signal transduction [5, 10-13]. For instance, the glycosylation of immunoglobulins modulates their effector functions, while aberrant glycosylation patterns are implicated in various pathological conditions, including cancer and congenital disorders of glycosylation (CDG) [12, 14, 15].

#### 3.2 *N*-glycosylation

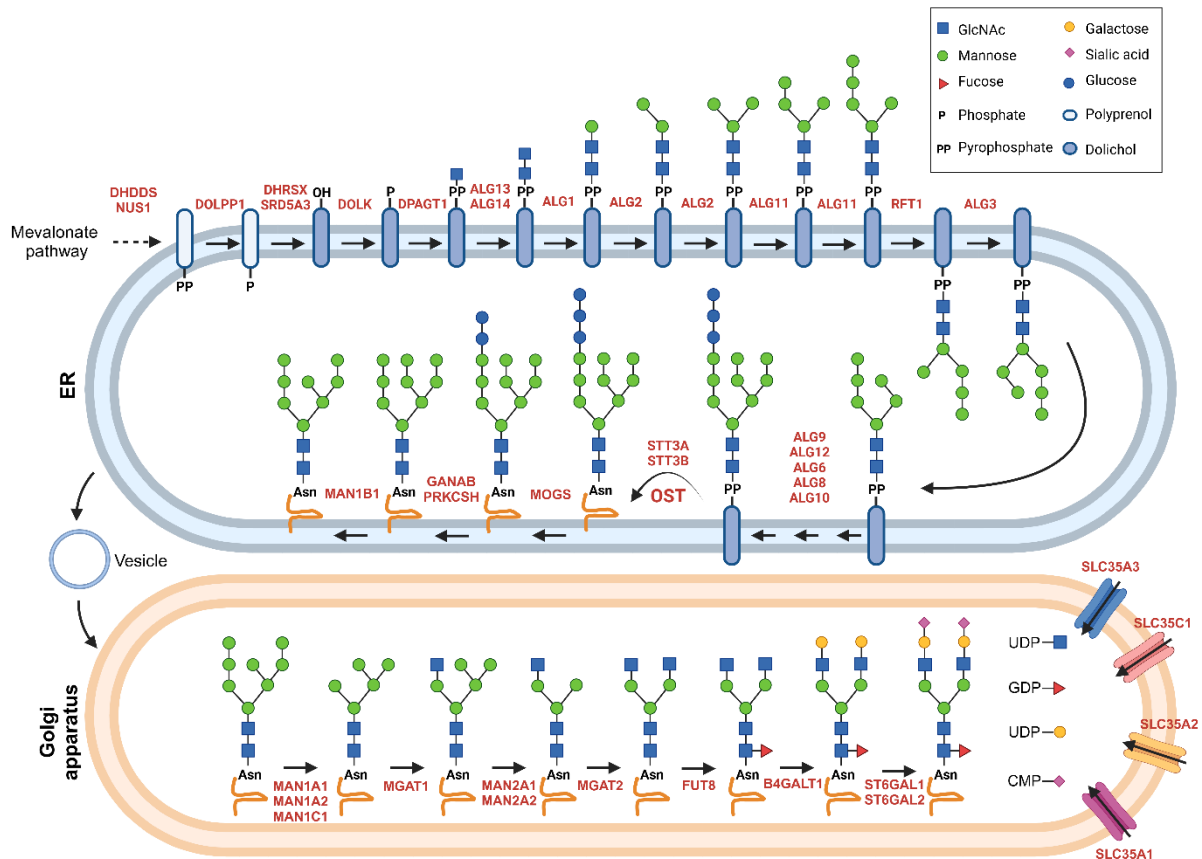
*N*-glycosylation is a crucial co- and PTM that occurs in the endoplasmic reticulum (ER) and Golgi apparatus of eukaryotic cells (Fig. 1) [1, 14-16]. The process begins with the biosynthesis of Dolichol-phosphate (DoIP), an isoprene derivative, which derives from the mevalonate pathway — a pathway which is also used for the biosynthesis of cholesterol and ubiquinone [6, 17]. ER bound DoIP serves as a lipid anchor for the attachment of oligosaccharides, therefore called lipid-linked oligosaccharides (LLO) [5, 6, 16]. For the transfer and linkage of sugars, sugars need to be nucleotide-activated. This process primarily occurs in the cytosol through the activity of various kinases. The most common nucleotide-activated sugar substrates are UDP-glucose (Glc), UDP-galactose (Gal), UDP-*N*-acetylglucosamine (GlcNAc),



GDP-mannose (Man), GDP-fucose (Fuc), and CMP-N-acetylneuraminic acid (Neu5Ac/"sialic acid", Sia) [5, 18]. For glycosylation reactions occurring within the ER, mannosyl- and glucosyltransferases depend on Dol-P-Man and Dol-P-Glc as sugar donors. These are allocated by transferring mannose and glucose residues from GDP-Man and UDP-Glc to dolichol-phosphate, catalysed by DPM1-3 together with MPDU1 and ALG5, respectively [18]. In contrast, UDP-Gal, UDP-GlcNAc, GDP-Fuc, and CMP-Sia are transported into the Golgi lumen by various transporter proteins of the SLC35 protein family [1].

The initial stages of *N*-glycosylation are proceeded on the cytosolic site of the ER membrane. Here, N-acetylglucosamine-1-phosphate (GlcNAc-1-P) is transferred onto DolP, catalysed by DPAGT1 (ALG7 in *Saccharomyces cerevisiae*) followed by the addition of another N-acetylglucosamine residue by ALG13/ALG14 [19, 20]. In the following, five mannose residues are transferred onto the growing LLO, catalysed by ALG1, ALG2 and ALG11 [5, 19]. The Dol-P<sub>2</sub>-GlcNAc<sub>2</sub>Man<sub>5</sub> intermediate gets translocated into the ER lumen by help of RFT1 [5, 19, 21]. Here, the mannosyltransferases ALG3, ALG9, ALG12 add four more mannose residues. Finally, the glucosyltransferases ALG6, ALG8 and ALG10 attach glucose (Glc) residues leading to the final LLO, called Dol-P<sub>2</sub>-GlcNAc<sub>2</sub>Man<sub>9</sub>Glc<sub>3</sub> [19]. The transfer of this oligosaccharide onto nascent polypeptides is catalysed by the oligosaccharyltransferase (OST) complex. This complex recognizes and binds the LLO precursor, as well as a specific Asn-X-Ser/Thr sequon (where X can be any amino acid except proline) on the polypeptide [5, 19]. It then catalyzes an *en bloc* transfer of the entire Glc<sub>3</sub>Man<sub>9</sub>GlcNAc<sub>2</sub> oligosaccharide from the DolPP carrier to the asparagine residue of the sequon – the first GlcNAc residue is always attached to the nitrogen atom (N) of the asparagine's amid group in a  $\beta$ -conformation [5, 19, 22, 23]. In metazoans, OST is composed of eight subunits arranged in three subcomplexes. OST1 and OST5 belong to the subcomplex I, OST3 (or OST6), STT3, and OST4 belong to the subcomplex II while OST2, WBP1, and SWP1 belong to the subcomplex III. Subcomplex II contains the main catalytic subunits (STT3A and STT3B) [24]. STT3A catalyses a co-translational transfer, whereas STT3B operates post-translationally [5, 22]. The polypeptide-attached glycan is then trimmed and modified by various glycosidases and glycosyltransferases as it is mediated through the ER and Golgi. The first steps of the trimming and modification is catalysed by the glucosidases MOGS and GANAB, which remove the three Glc residues [25, 26]. The mannosidase MAN1B1 removes one Man residue, leading to the formation of a GlcNAc<sub>2</sub>Man<sub>8</sub> glycan. This processing is crucial for proper protein folding and quality control, as the glycan acts as a signal for ER chaperones and lectins and initiates its transport into the Golgi apparatus [27, 28]. In the cis-Golgi, specific mannosidases (MAN1A1, MAN1A2 and MAN1C1) remove additional Man residues, forming GlcNAc<sub>2</sub>Man<sub>5</sub> [29]. This process is a crucial step in the *N*-glycosylation pathway since further modifications discriminate the type of *N*-glycosylation – every *N*-glycan inherits this glycan as

the core structure. In the medial- and trans-Golgi, various glycosyltransferases add diverse monosaccharides, such as N-acetylglucosamine (GlcNAc), galactose (Gal), fucose (Fuc), and sialic acid (Sia), resulting in the formation of three types of *N*-glycans: complex, oligomannose and hybrid *N*-glycan. Complex *N*-glycans are described by the addition of at least two GlcNAc and other glycan residues at their “antennae”. The oligomannose-type consists only of Man residues and the hybrid *N*-glycans consist of antennae similar to the complex type as well as mannose-rich antennae. Complex glycans rely on the catalytic activity of the GlcNAc transferase MGAT1, the mannosidase MAN2A1 and MAN2A2 as well as MGAT2, resulting in the biantennary glycan  $\text{GlcNAc}_2\text{Man}_3\text{GlcNAc}_2$ . In addition, up to two more antennae can be formed by the activity of MGAT4 and MGAT5. In case of hybrid glycans, the removing of the two mannose residues are missing in the medial-Golgi. Complex and hybrid type glycans can be further modified by the attachment of a GlcNAc residue between the antennae (“bisecting”) to the core structure by MGAT3, but this is usually not extended by further sugars [23, 30, 31]. Commonly, Gal residues are attached to the antennae of the complex types by B4GALT1 [23, 32]. Moreover, the sialyltransferases ST3GAL and ST6GAL can each add one terminal Sia in an  $\alpha$ -2,3 and  $\alpha$ -2,6 conformation, respectively [33].



**Figure 1: N-Glycosylation pathway**

Overview of the N-glycosylation pathway. This figure illustrates the simplified pathway for the biosynthesis of a N-glycans. Highlighted in red are the key enzymes required for the formation of N-glycans. Additionally, it includes the provision of nucleotide-activated sugar substrates in the Golgi through various SLC35 transporters. The figure was created in BioRender.com, based on the work of Ng and Freeze [1]. Asn, asparagine; CMP, Cytidine monophosphate; GDP, Guanosine diphosphate; UDP, Uridine diphosphate.

### 3.3 *De novo* biosynthesis and the role of Dolichol in Glycosylation

Dolichol, a long-chain polyisoprenoid alcohol, plays a crucial role in various glycosylation processes, particularly in N-linked protein glycosylation. In human, dolichol consists of 18-21 isoprene units [6]. Its *de novo* biosynthesis originates from the mevalonate pathway (=polyisoprenoid pathway) [5, 6, 19].

The mevalonate pathway is a crucial metabolic pathway conserved across eukaryotes and some prokaryotes. The initial step consists of the condensation of acetyl-CoA molecules to 3-hydroxy-3-methylglutaryl-CoA (HMG-CoA), catalyzed by the HMG-CoA synthase. HMG-CoA reductase is the rate-limiting enzyme and converts HMG-CoA to mevalonate. Subsequent steps involve phosphorylation and decarboxylation and end up in the synthesis of isopentenyl pyrophosphate (IPP). IPP then undergoes isomerization to dimethylallyl

pyrophosphate (DMAPP) by IPP isomerase. Farnesyl pyrophosphate (FPP) synthase then catalyzes the sequential condensation of DMAPP with two IPP units to produce FPP [17, 34]. FPP is the common precursor molecule which is the building block for dolichol but ubiquinone and cholesterol, too. That indicates that not only the *de novo* biosynthesis of dolichol but also ubiquinone and cholesterol are relying on the mevalonate pathway [17, 34-36]. For dolichol synthesis, the cis-prenyltransferase complex elongates FPP by addition of isoprene units from IPP, generating polyprenol. Polyprenol needs to be converted to dolichol by polyprenol reductases. Here, dehydrogenase/reductase X-linked (DHRSX) and steroid 5 alpha-reductase 3 (SRD5A3), facilitating a three-step process converting polyprenol to dolichol via intermediate stages of polyprenal and dolichal [6].

Research has highlighted the importance of dolichol biosynthesis in maintaining glycosylation efficiency, with inhibition of squalene biosynthesis shown to increase dolichol availability and improve N-linked glycosylation [37].

### 3.3 Congenital Disorders of Glycosylation

Congenital disorders of glycosylation (CDG) constitute a rapidly expanding group of rare inherited metabolic disorders characterized by defective glycosylation [14-16, 38, 39]. As previously described, glycosylation displays crucial post- and co-translational modifications by which glycans are attached to proteins and lipids. These attachments ensure the functionality and biochemical properties of these biomolecules. Impairments in this process, such as malfunctioning of involved proteins, lead to CDG. These malfunctions are mostly caused by monogenetic variants [40, 41], inherited in an autosomal-recessive manner and impair the proteins involved in various glycosylation processes [41, 42].

CDG can be broadly classified into four categories based on the type of glycosidic linkage affected: N-glycosylation, O-glycosylation, combined N- and O-glycosylation, and lipid and glycosylphosphatidylinositol (GPI) anchor biosynthesis defects [41]. Based on the glycosylation status of serum transferrin as marker for N-glycosylation disorders, these disorders are further subdivided into Type I (CDG-I), presenting early glycosylation defects affecting LLO synthesis and the transfer of the oligosaccharide to the protein, and Type II (CDG-II), involving late defects in the processing of N-glycans in the ER and Golgi apparatus [40]. Following the nomenclature for CDG defects, a deficiency is named by the affected protein and the postfix “-CDG”, e.g. PMM2-CDG. PMM2-CDG is caused by a defect in phosphomannomutase 2 (PMM2) and is the most common type of CDG in Europe, accounting for about 60-70 % of all CDG patients [43]. Since its clinical discovery in 1981 by Jaeken *et al.*, the number of identified glycosylation defects has significantly increased, currently counting up to approximately 190 different types [44, 45].

The clinical spectrum of CDG is remarkably heterogeneous, reflecting the crucial nature of glycosylation in various biological processes. Since glycosylation is required for physiological development beginning at embryonic stages, such as cell growth, differentiation, and organ development, patients typically exhibit a multisystemic phenotype [39, 46]. Common symptoms include neurological deficits, delayed development, microcephaly, epilepsy, hypotonia, hepatosplenomegaly, strabismus, dysmorphisms, failure to thrive, coagulation disorders, gastrointestinal issues, inverted nipples, and displaced fat pads [39]. In addition, ophthalmological signs, e.g. retinitis pigmentosa/retinal dystrophy, optic nerve hypoplasia and coloboma, are common symptoms, e.g. representing the key diagnostic feature in SRD5A3-CDG [47, 48]. The severity range is broad from mild to severe forms with about 20% lethality in the first years of life [49].

The huge heterogeneity of the clinical presentation and the amount of different types of CDG complicate the diagnosis – leading to long stressful and burdensome patient journeys in some cases. Molecular biological methods are widely used to identify abnormalities in protein glycosylation, including isoelectric focusing (IEF) of serum proteins like transferrin, high-performance liquid chromatography (HPLC), capillary zone electrophoresis (CE) and mass spectrometry (MS) [50]. For years IEF has been the gold standard. Here, the different glycoforms of serum transferrin are electrophoretically separated in a gel with a pH gradient based on their isoelectric point. The isoelectric point is the point at which the charge of the glycoprotein is 0, depending on the pH. At this stage the glycoprotein does not move anymore in the electrophoretic field and represents a solid band in the gel [51]. Sialic acid residues are negatively charged, so their number determines the isoelectric point of a protein's glycoform. Transferrin carries two biantennary *N*-glycans of the complex type with terminal sialic acid residues – therefore, five glycoforms of the protein can be distinguished in IEF: The physiologically glycosylated form with four sialic acid residues, called 'tetrasialo', the glycoforms with reduced numbers of terminal sialic acids, 'tri-, di-, and monosialo', and the glycoform without sialic acid residues, 'asialo' [52]. Depending on the type of CDG, different transferrin patterns can be detected in IEF, HPLC or CE. Type I CDG displays in a pattern of decreased amount of tetrasialo forms with a simultaneous increase in di- and asialo glycoforms. This is due to early defects impairing the transfer of oligosaccharides to the protein leading to the lack of whole glycan structures. In contrast, type II CDG displays a pattern of monosialo and trisialo bands, since late defects affect glycan processing in the ER and golgi [40]. In CDG type II most glycan structures are attached but not fully processed and tend to be shorter and missing sialic acids. Other proteins that also can indicate glycosylation defects through their abnormal banding patterns include  $\alpha$ 1-antitrypsin (*N*-glycosylation) and apolipoprotein C-III (ApoCIII, O-mucin-type glycosylation) [40, 53].

Nowadays newer diagnostic approaches focus on comprehensive "glycoprofile" analysis, examining all glycans in serum or cell lysates to reveal anomalies in glycan structure, distribution, or changes in ratios of different glycan types. Here, mass spectrometric techniques are widely used. These analysis techniques enable a deeper understanding of the patients glycoprofile and help to detect patients whose impaired glycoprofile could not be detected by IEF [50, 54-56].

In the era of genetic screens, patients often are diagnosed first through a whole exome sequencing and later their glycoprofile by IEF or mass spectrometric techniques validated to verify the genetic finding [57].

Therapeutic options for CDG are currently limited and mostly focus on symptomatic treatment [42, 56, 58]. A known medication to reduce the number of stroke-like episodes in PMM2-CDG is Acetazolamide [56, 58]. Acetazolamide is a carbonic anhydrase inhibitor and is currently evaluated in the AZATAX trial for safety and efficiency in patients [59]. It is hypothesized that hypoglycosylated calcium ion channels are leading to ataxia and stroke-like episodes in PMM2-CDG patients since increased levels of calcium are known to be an inhibitor of PMM2. Therefore, acetazolamide, as a non-competitive inhibitor of carbonic anhydrase, has the potential to act on the transmembrane potential by interfering with pH [56, 58]. For a very few numbers of CDG types causal therapeutic options are available by supplementation of corresponding sugars. These supplementations elevate the substrate level of an affected enzyme or transporter or can even bypass the molecular defect and improve physiological glycosylation. Examples are supplementation of Man in MPI-CDG, Fuc in GFUS-CDG and SLC35C1, Gal in PGM1-, TMEM165- and SLC35A2-, and manganese in SLC39A8-CDG [60, 61]. Still, research is required to develop and discover new therapeutic approaches to increase the quality of life for patients and their families. Strategies for this are repurposing existing drugs, development of chaperons to increase the stability and folding of impaired enzymes or gene therapy approaches.

### **3.4 SRD5A3-CDG**

SRD5A3-CDG is an ultra-rare CDG caused by autosomal recessive variants in the SRD5A3 gene. With a prevalence estimated below 1 in 1,000,000 live births, this multisystemic condition is characterized by defective protein *N*-glycosylation due to impaired synthesis of dolichol [47, 62, 63]. For years it was thought that steroid 5 alpha-reductase 3 (SRD5A3) is responsible for the conversion of polyprenol to dolichol. Instead, recently published results suggest, that this conversion is performed in a three-step reaction – depending on the enzymatic activity of dehydrogenase/reductase X-linked (DHRX) and SRD5A3. DHRX is working uniquely in a dual substrate and cofactor specificity, enabling it to function as a

NAD<sup>+</sup>-dependent dehydrogenase and a NADPH-dependent reductase in two separate steps. First, it reduces polyprenol to polyprenal. Then, SRD5A3 produces dolichal out of polyprenal. Finally, DHRSX metabolizes dolichal in dolichol [6]. Pathogenic variants in SRD5A3 therefore lead to a disruption in the biosynthesis of dolichol which is used as the lipid anchor in *N*-glycosylation and as lipid component for Dol-P-Glc and Dol-P-Man, needed in *N*-glycosylation, *O*-mannosylation, *C*-mannosylation and GPI-anchor biosynthesis. Besides SRD5A3-CDG, a broad range of CDG types are caused by defects in the dolichol biosynthesis (e.g. DHDDS-, NUS1-, DOLK-CDG) or its metabolism (e.g. MPDU1-, DPM1-3-CDG, POMT1-2, ALG5-CDG) [47, 64, 65].

The clinical presentation of SRD5A3-CDG is highly variable. Patients typically show neurological manifestations such as intellectual disability, hypotonia, ataxia, and cerebellar abnormalities [47]. The clinical key feature in the diagnosis of SRD5A3-CDG are ophthalmological abnormalities: Especially early-onset retinal dystrophy and optic nerve hypoplasia but also iris and optic nerve colobomas, and retinitis pigmentosa [47]. Other reported findings include dystonia, anxiety disorders, gastrointestinal symptoms, cardiac defects, and hypertrichosis [47]. Currently, no causal and definitive treatment options are available – patient management remains supportive and individually. This highlights the urgent need for patients and families.

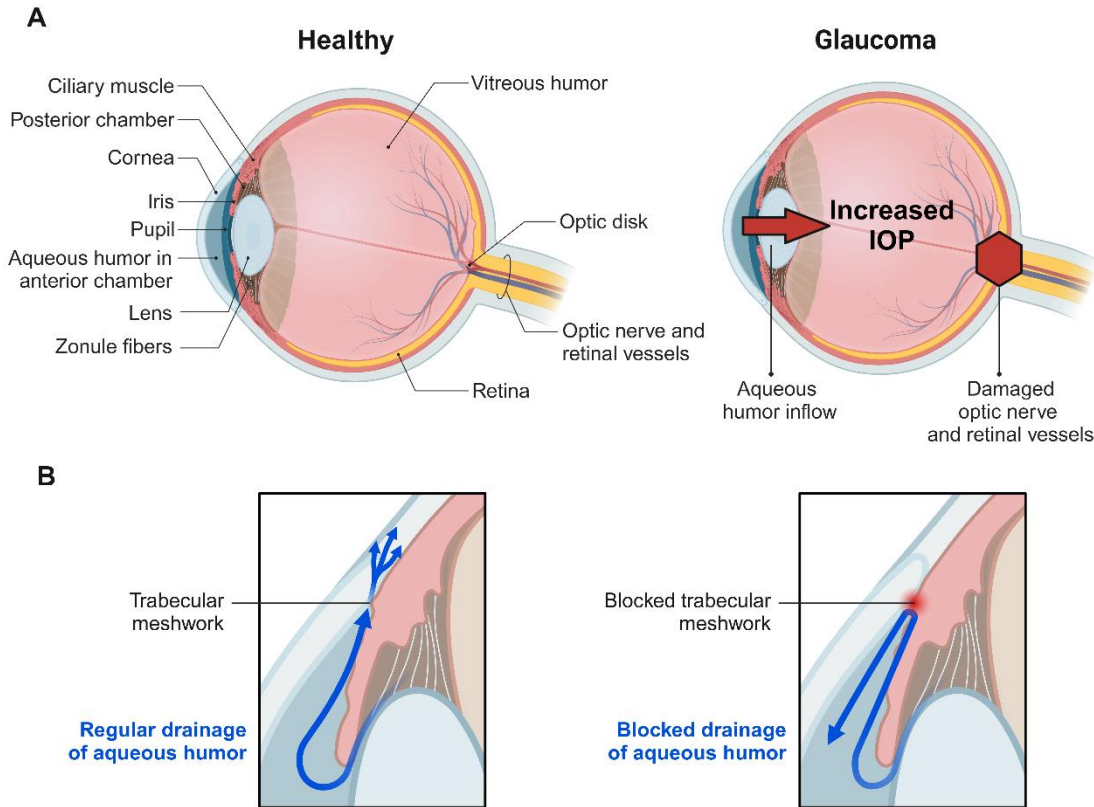
### **3.4.1 SRD5A3-CDG Eye Pathologies: Coloboma, Retinitis pigmentosa and Optic nerve hypoplasia**

Congenital disorders of glycosylation, such as SRD5A3-CDG, often affect eye development and function [39, 47, 62]. SRD5A3-CDG is clinically characterized by retinitis pigmentosa/dystrophy, optic nerve hypoplasia, nystagmus, and ocular colobomas [47, 62]. A complete coloboma is a malformation of the optic disc, retina, ciliary body, zonules, lens (notching) and iris due to an incomplete closure of the embryonic fissure during eye development – resulting in a gap and missing structural tissue in the eye. Depending on the involved structures, the vision can be strongly affected [66]. Expression of *visual system homeobox 2* (*vsx2*), *pax6* and *shh* are clinically associated with the development of coloboma [67]. Retinal dystrophy describes the condition of inherited disorders characterized by progressive degeneration of photoreceptor cells which can lead to vision loss. One of the most common types is retinitis pigmentosa, characterized by a variable clinical presentation. Typically, patients suffer from vision problems, such as night blindness, loss of mid-peripheral visual field, tunnel vision due to the progressive death of rod photoreceptors [68]. Optic nerve hypoplasia is a non-progressive underdevelopment of the optic nerve which results in moderate to severe vision loss [69].

### 3.5 The Eye

The eye is a complex sensory organ composed of several structures – each with unique functions. In total, the human eye can be divided into three parts: Surface, anterior and dorsal part. The surface consists of the conjunctiva which is a clear membrane covering the surface of the eye and the inner surface of the eyelids. The tear film coats the ocular surface for protection from environmental factors, lubrication, smoothing the surface for light refraction and maintaining the health of the conjunctiva and the avascular cornea [70]. The tear film composed of an aqueous-mucin layer, which includes fluid and soluble components secreted by the lacrimal glands as well as mucin produced by the goblet cells. This layer is covered by an additional lipid layer, derived from the Meibomian glands [70]. The anterior part of the eye consists of the transparent, dome-shaped cornea, iris, pupil and the lens. All together these structures aim to focus the light and ensure the focusing power. The cornea together with the lens are responsible for conducting external light into the eye, focus it onto the retina [71]. Muscles in the iris adjust the pupil size to control the amount of light entering the eye. The focused light passes then through the viscous fluid onto the retina – a light-sensitive tissue. This sensory feature is based on photoreceptors in the retina, the so-called rods and cones. In these structures sensor light and transmit the information to the brain. Rods are responsible to transmit information about black and white, whereas cones are sensitive to specific wavelength of light and therefore contribute to colour vision [72]. Ultimately, the electric impulses generated in the rods and cones are send through the optic nerve to the brain into the visual cortex [73]. The intraocular pressure (IOP) is generated by a balance of aqueous humor inflow and outflow rate. This balance is regulated by the trabecular meshwork (TM) and the Schlemm's canal inner wall endothelium (SCE). Elevated IOPs are the major risk factor for the development of glaucoma. Glaucoma are eye diseases which can result in blindness due to optic nerve damage (Fig. 2) [74].





**Figure 2: Schematic figure of the structures of the eye.**

(A) Schematic figure of the human eye, highlighting certain ophthalmological structures. Indicated by the red arrow is the glaucoma-specific increased intraocular pressure (IOP) by an aqueous humor inflow due to blocked trabecular meshwork. (B) Schematic zoom in into the anterior segment of the human eye, focussing on the drainage of aqueous humor through the trabecular meshwork. The figure was created in BioRender.com. Red arrow, aqueous humor inflow; red hexagon, damage at the optic nerve and retinal vessels due to increased IOP; blue arrow, aqueous humor flow.

### 3.5.1 Early Eye Development

The eye development relies on certain cell groups which play major roles. These include neuroectoderm (forming the neural tube and neural crest cells), the surface ectoderm and, to lesser extent, the mesoderm. In human, eye development begins at gestational day 17. Since the eye field is determined very early, abnormal development at this early stage can be responsible for eye malformations, e.g. microphthalmia and coloboma iridis – even before the formation of the ocular primordia, the precursor cell structures of the eye. This stage of development is mainly controlled by three transcription factors: Paired box protein Pax-2 (PAX2), PAX6 and sonic hedgehog (SHH). SHH is expressed in the prechordal plate and is responsible for the separation of the eye field into two parts. Its expression leads to an upregulation of PAX2 and a downregulation of PAX6 in the centre of the eye field. This regulatory pattern will continue as PAX2 is expressed in the optic stalk and PAX6 in the optic

cup and surface ectoderm – leading to the formation of the lens. In later development stages, PAX6 will no longer be needed, and other transcription factors start suppressing SHH in the midline of the forebrain. Defects at the stage can interfere with the separation of the eye field and result in cyclopia. Developing eyes will appear as a pair in the shallow grooves at gestational day 22. Three days later the so-called optic vesicles will have formed, influenced by signals from the surface ectoderm. At gestational day 28 the optic cups are formed by invagination. This process also includes the optic stalk, which contributes to the formation of the optic or choroid fissure. Mesenchyme, neural crest cells, then moves into the optic cup and fissure, leading to further development of the lens and retina [75]. Closing the ocular fissure is a complex process which takes place at gestational day 28 and requires the correct evagination of the optic vesicle from the forebrain and further strictly regulation, e.g. precise spatial arrangement of the optic cup along the dorsal-ventral and proximal-distal axes [67].

### 3.5.2 Retina and Optic Nerve

The retina develops from the invagination of the optic vesicle to form the optic cup. The invagination creates an inner and an outer layer, which create an intraretinal space – this space gets obliterated as both layers come together. The outer layer develops into the pigmented layer of the retina whereas the inner layer differentiates into the neural retina, containing the light sensitive rod and cone cells. At last, the optic nerves develop after axons from the neural retina extend into the optic stalk and proliferate [75, 76].

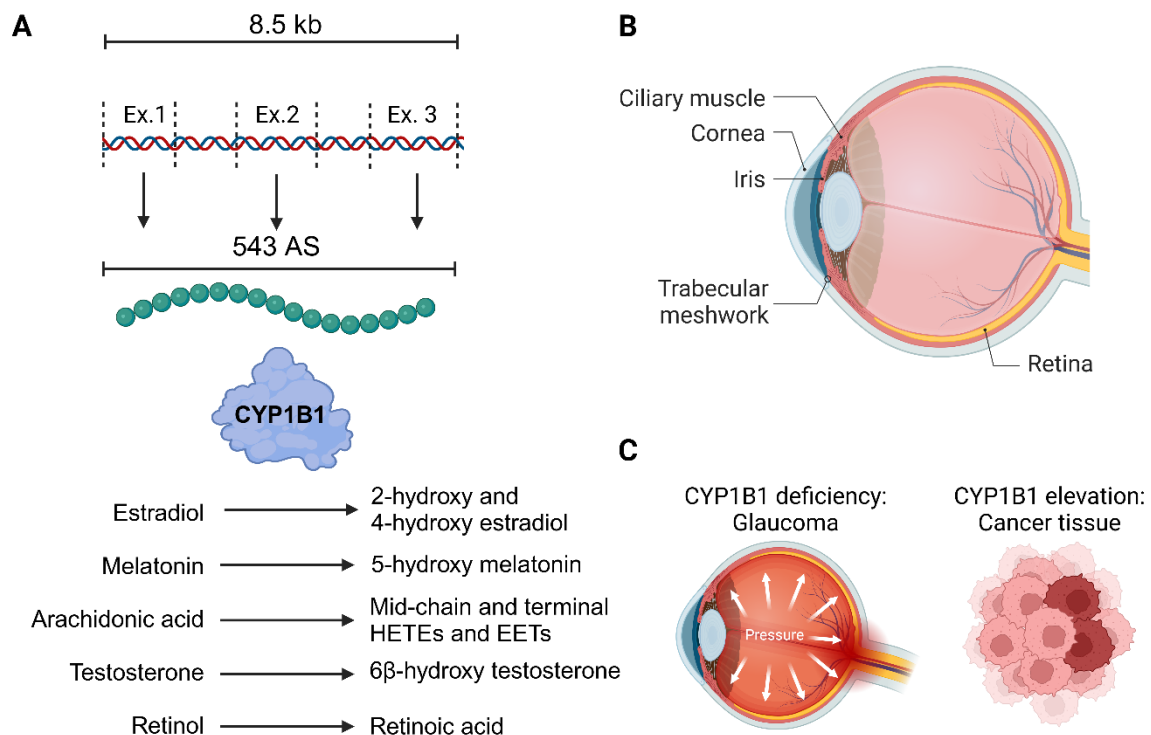
### 3.6 Cytochrome P450 family 1 subfamily B member 1 (CYP1B1)

A crucial player for the eye development, particularly in the anterior segment, is Cytochrome P450 1B1 (CYP1B1) [77-80]. *CYP1B1* has a length of 8.5 kilobase pairs and consists of three exons and two introns with an open reading frame and its start codon at the 5' end of the second exon. The corresponding protein is predicted to have 543 amino acids (Fig. 3A) [81]. *CYP1B1* is expressed extrahepatically in adult and fetal healthy tissue, including brain, kidney, adrenal glands, prostate, breast cervix, uterus, ovary, lymph nodes, heart, placenta, lung, skeletal muscle as well as ocular tissue [77, 80]. Ocular expression of CYP1B1 includes ciliary body, iris, cornea, trabecular meshwork, and retina (Fig. 3B,C) [82].

It is a membrane protein, located in the ER, cell surface and in mitochondria and works as a heme-binding mono-oxygenase [77, 83]. The CYP1 family is mainly responsible for the metabolism of endogenous (e.g. bile acids, steroid hormones, lipids) and exogenous compounds (e.g. polycyclic aromatic hydrocarbons and ~ 80 % of currently used drugs) [81, 83].

CYP1B1 mediates its role in the eye development through the metabolism of retinoic acid (RA), a derivative of vitamin A – ensuring the correct differentiation and development of ocular

structures [67, 79, 84]. RA is a vital signalling molecule involved in the regulation of gene expression during embryogenesis. However, studies in zebrafish showed that although Cyp1b1 regulates local RA levels, the effect on fissure closure was independent of RA. As previously mentioned, incomplete fissure closure is a characteristic of coloboma – a common symptom in SRD5A3-CDG patients. Instead, it was shown that Cyp1b1 regulates the coloboma-clinically relevant expressions of *vsx2*, *pax6*, and *shh*. In zebrafish model it could be shown that induced overexpression of Cyp1b1 resulted in incomplete fissure closure and ultimately in the development of coloboma – thus, Cyp1b1 indirectly interferes with the development of coloboma [67]. Clinically well studied are variants in *CYP1B1* which disrupt normal eye development leading to primary congenital glaucoma (PCG). Variants in *CYP1B1* are linked to elevated intraocular pressure (IOP), optic nerve damage and anterior segment dysgenesis which result in impaired vision and blindness (Fig. 3C) [84-86]. These variants often occur in highly conserved regions of the gene, affecting the enzyme's stability and function. CYP1B1 is highly conserved across species [67]. Besides its role in development, CYP1B1 is supposed to play a role in cellular redox homeostasis. Studies in mice revealed that deficiency of Cyp1b1 resulted in increased levels of oxidative stress, especially in retinal and trabecular meshwork cells [82, 86]. Its expression is mainly mediated through the aryl hydrocarbon receptor (AhR).



### Figure 3: Overview of human CYP1B1

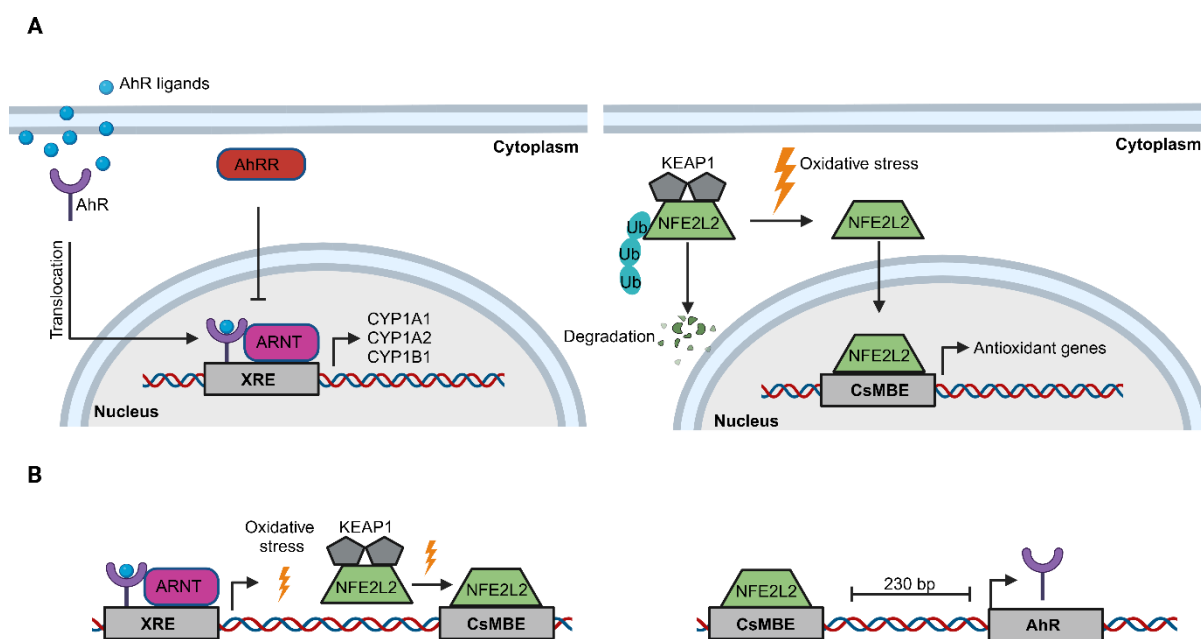
(A) Schematic figure illustrating the genomic, proteomic and endogen functional characteristics of the human CYP1B1. The blue-red helix loop represents DNA, the green chain the amino acids sequence. Kb, kilobases; Ex, exon; AS, amino acid; HETE, Hydroxyecosatetraenoic acid; EET, epoxyecosatrienoic acid. Based on Alsubait, et al and Carrera, et al. [81, 87]. (B) Schematic figure of the human eye, highlighting ophthalmological tissues known to express CYP1B1. (C) Clinical associations of deregulated CYP1B1 in human. White arrows, representing IOP. The figure was created in BioRender.com.

### 3.7 AhR signalling and Nrf2 pathway axis

The AhR signalling pathway relies on its eponym, the aryl hydrocarbon receptor (AhR) – a ligand-dependent transcription factor. The AhR pathway responds to environmental and endogenous signals (e.g. 3-Methylcholanthrene (3MC), 2,3,7,8-tetrachlorodibenzo-p-dioxin (TCDD), kynurenine metabolites) to maintain cellular homeostasis and works as a sensor for environmental changes [88-92]. There is evidence that the AhR signalling pathway is a key player in various biological process, such as development (including development of ocular tissue), immunity, haematopoiesis, drug, detoxification, and more [89-92]. Dysregulations of the AhR pathway are associated with eye-related diseases, such age-related macular degeneration, autoimmune uveitis, retinitis pigmentosa, and other ocular pathologies as well as cancer [90, 92-94].

AhR itself is strictly regulated through multiple mechanisms: After ligand binding, AhR undergoes a conformational change and becomes activated, translocates into the nucleus and heterodimerizes with Aryl hydrocarbon receptor nuclear translocator (ARNT). This complex binds to the xenobiotic response elements (XRE) on the DNA and initiates the transcription of AhR-responsive genes, including cytochrome P450 enzymes such as CYP1A1, CYP1A2, and CYP1B1. The activity of AhR is regulated through its repressor (AhRR) which competes for ARNT binding and therefore suppressing AhR-mediated gene expression (Fig. 4A) [95, 96]. AhR signaling exhibits an extensive crosstalk with the nuclear factor erythroid 2-related factor 2 (*Nrf2*/NFE2L2) pathway [96]. *Nrf2*/NFE2L2 is a member of the small family of basic leucine zipper (bZIP) proteins and is considered to be the key regulator in the cellular antioxidant response and cytoprotective genes (Fig. 4A) [97, 98]. Downstream target effectors of *Nrf2*/NFE2L2 include antioxidant genes, such as *SOD3*, *GSTM3-5*, *GSTK1*, *GPX3/7*, *PRDX2*, and *NQO1* [97-100]. Regulation of *Nrf2*/NFE2L2 is primarily mediated through the kelch-like ECH-associated protein 1 (KEAP1). Under homeostatic conditions, KEAP1 binds to NFE2L2 in the cytoplasm and prohibits its nuclear translocation by inducing a constant proteasomal degradation, mediated by ubiquitination. Under oxidative stress, NFE2L2 and KEAP1 dissociate from each another. This enables NFE2L2's translocation into the nucleus where it

binds to small Maf proteins and forms a transcriptionally active complex, binding to the CNC-sMAF binding element (CsMBE) – which is also known as the antioxidant response elements (ARE) (Fig. 4A) [96-98]. AhR and Nrf2 have a reciprocal relationship [90, 96]. On the one hand, NFE2L2 binds to the CsMBE at – 230 of the AhR promoter to increase its expression [90]. It could be shown that the expression of *Ahr*, *Cyp1a1* and *Cyp1b1* was demolished by a *Nrf2*-knockout in mouse embryonic fibroblasts [96]. On the other hand, it is assumed that an AhR-mediated upregulation of cytochrome P450 enzymes are associated with higher production of free radicals and ROS which lead to activation of *Nrf2* (Fig. 4B) [90].



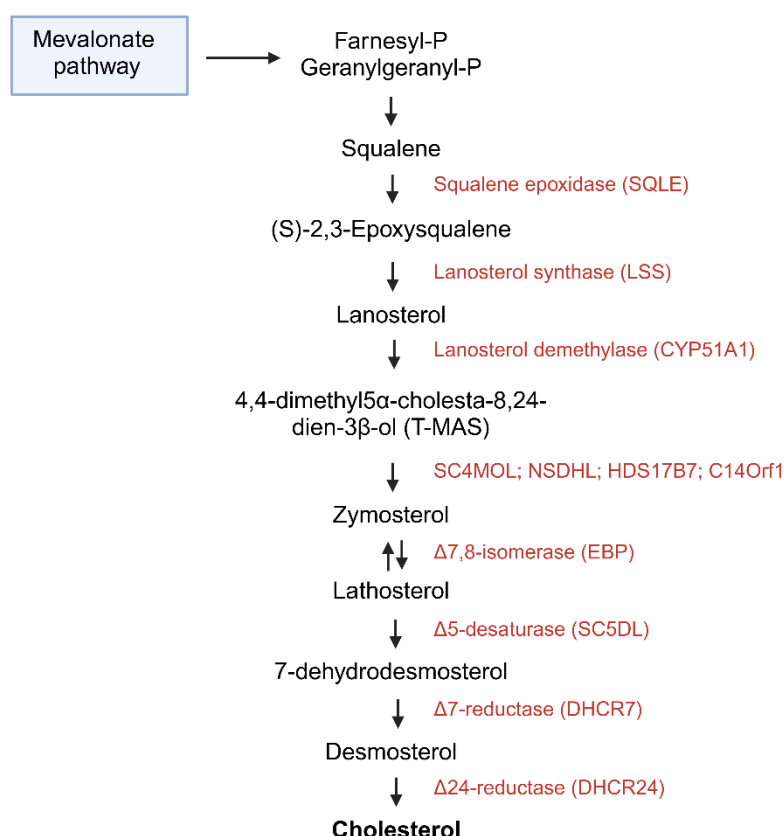
**Figure 4: AhR and Nrf2 signalling pathway and their crosstalk.**

(A) Simplified illustration of the AhR and Nrf2/NFE2L2 pathway. (B) Simplified illustration of the cross talk between AhR and Nrf/NFE2L2. The figure was created in BioRender.com, based on Edamitsu, et al [96]. Bp, base pair, Ub, ubiquitin.

### 3.8 Cholesterol biosynthesis

Cholesterol is a vital, major sterol molecule, present in all animal tissue. It is an essential component of the cell membrane and the crucial precursor molecule for several steroid hormones. The biosynthesis of cholesterol depends on the mevalonate pathway – therefore, sharing the same precursor molecules as dolichol [17, 101, 102]. Since the biosynthesis of cholesterol depends on the mevalonate pathway, it takes place primarily in the cytosol and ER and depends on HMG-CoA reductase as the key regulatory step. The HMG-CoA reductase converts HMG-CoA into mevalonate, which is subsequently phosphorylated and decarboxylated to form isoprenoid intermediates, leading to the formation of farnesyl-PP. At this step, farnesyl-diphosphate farnesyltransferase 1 (FDFT1) marks the first cholesterol-

specific reaction by catalysing the dimerization of two farnesyl-PP in a two-step reaction to form squalene - a large isoprenoid molecule. Based on squalene, squalene epoxidase (SQLE) and lanosterol synthase (LSS) catalyse reactions to form lanosterol, which subsequently is converted into zymosterol depending on ergosterol biosynthesis 28 homolog (C14orf1/ERG28) - among other enzymes. The enzymes 7-dehydrocholesterol reductase (DHCR7) and Delta(24)-sterol reductase (DHCR24) play critical roles in the final steps: DHCR7 catalyses the reduction of 7-dehydrodesmosterol to desmosterol, while DHCR24 is involved in the reduction of the delta-24 double bond, which ultimately results in the production of cholesterol (Fig. 5) [103].



**Figure 5: Biosynthesis pathway of cholesterol.**

Illustration of the biosynthesis of cholesterol, highlighting key steps and corresponding enzymes. The figure was created in BioRender.com, based on Gorin, et al [103]. SC4MOL, Methylsterol monooxygenase 1; NSDHL, Sterol-4- $\alpha$ -carboxylate 3-dehydrogenase, decarboxylating; HSD17B7, 3-keto-steroid reductase/17- $\beta$ -hydroxysteroid dehydrogenase 7; C14Orf1, Ergosterol biosynthetic protein 28 homolog.

### 3.9 Model organism: Medaka fish embryos

Medaka fish embryos (*Oryzias latipes*) present several significant advantages as a model organism for investigating genetic disorders. Genetic manipulations can easily be carried out by microinjection in a CRISPR/Cas9 approach. In addition, medaka fish are considered to be a vertebrate model suitable for large scale variants since their genome is 20 to 40 % the size of mammalian genome [104]. This enables precise gene editing to generate reliable and reproducible medaka fish CDG models. CDG has already been studied in this animal model, e.g. alpha-1,3/1,6-mannosyltransferase (ALG2)-CDG. Here, it could be shown that disruption of ALG2 leads to reduced levels of *N*-glycosylation and a multisystemic phenotype comparable to the patient's syndrome [105]. The transparency of medaka embryos permits real-time, non-invasive observation of developmental processes and phenotypic manifestations [104]. Additionally, medaka exhibit rapid developmental cycles, with embryos hatching within 8 days at 28°C and reaching maturity in 2-3 months, facilitating high-throughput genetic studies and mutant screening due to their high fecundity, producing 30-50 eggs per fertilization event. Medaka fish embryos can be used to investigate the eye development and structures in SRD5A3-CDG since key aspects of the development are conserved between human and medaka fish [106].

## 4. Aim of the Study

SRD5A3-CDG is an ultra-rare metabolic disease which is based on deficient biosynthesis of dolichol. SRD5A3-CDG patients suffer from common CDG symptoms, such as failure to thrive, neurological deficits, delayed development, ophthalmological abnormalities, and many more. Ophthalmological abnormalities, such as retinitis pigmentosa and coloboma, have an outstanding clinical importance in SRD5A3-CDG – they are considered to be the clinical key feature in its diagnosis. The molecular mechanisms underlying ocular manifestations remain unclear.

The AhR signaling pathway and especially its downstream gene *CYP1B1*, are primarily involved in detoxification and the regulation of steroid hormones. Additionally, Ahr and CYP1B1 play a critical role in the normal development of the eye. A deficiency in Ahr and CYP1B1 result in ophthalmological abnormalities, such as retinitis pigmentosa and Congenital Primary Glaucoma, respectively. While overexpression of Cyp1b1 in zebrafish leads to development of coloboma – a SRD5A3-CDG common symptom. In addition, it could be shown that many CDG-types exhibit oxidative stress, e.g. PMM2-, ATP6AP1-, ALG8-, RFT1-, and SLC10A7-CDG [107]. The key transcription factor for the antioxidative response is *Nrf2*. *Nrf2* and *AhR* exhibit a reciprocal relationship. The clinical presentation of AhR deficiency and SRD5A3-CDG show similarities. Therefore, I was investigating the crosstalk between *Nrf2* and *AhR* in the context of glycosylation disorders which could be crucial for a better understanding of CDG-related clinical features.

In this study I aim to explore the potential relationship between Ahr, CYP1B1 as well as *Nrf2* in a SRD5A3-CDG setting by utilizing fibroblasts derived from SRD5A3-CDG patients and a CRISPR-Cas9-generated SRD5A3-knockout model in Japanese rice fish (*Oryzias latipes*, medaka) embryos.



## 5. Material and Methods

### 5.1 Ethic and regulations

#### 5.1.1 Patient's Material

The parents consented in writing to the use of the patient's material for biochemical, genetic and cell biological analyses. Investigation on patient material was conducted in accordance with the Declaration of Helsinki and performed as part of the diagnosis. SRD5A3-CDG primary skin fibroblasts of two male and one female patient were characterized. The female Patient 1 (Pat. 1) inherited a premature stop codon (*SRD5A3c.57G>A*). The two male Patient 2 (Pat. 2) and 3 (Pat. 3) inherited a frameshift mutation due to an insertion (*SRD5A3c.79\_80insGGAA*).

#### 5.1.2 Animal husbandry

The Medaka fish (*Oryzias latipes*) Cab strain was kept in closed stocks in compliance with §11, Abs. 1, Nr. 1 of the German Animal Protection Act and the European Union's animal welfare guidelines. The fish were housed in a stable recirculating system at 28 °C with a 14-hour light and 10-hour dark cycle (Zucht- und Haltungserlaubnis AZ35-9185.64/BH). After collection from female adults, embryos were maintained in 1× ERM with 2 mg/l Methylene Blue at 26-28°C. Access to the fish facility at the Centre for Organismal Studies (COS), Heidelberg University, as well as medaka-related consumables, were provided by Prof. Dr. Jochen Wittbrodt and Dr. Thomas Thumberger (Wittbrodt Lab).

#### 5.1.3 Declaration of independence

The work presented in this dissertation was carried out by me, Andreas Hecker, unless otherwise stated in the text, figures, or tables.

## 5.2 Material

### 5.2.1 Consumables

**Table 1: List of used consumables.**

Consumable	Company
4-, 6-, 24-well Cell culture plates	Sarstedt, Nümbrecht
Blotting Paper 330 g/cm <sup>2</sup>	neoLab, Heidelberg
Cannulas Sterican (sterile) 22 G x 1 1/2"	Braun, Melsungen
Cell culture flasks; T25, T75, T125	Sarstedt, Nümbrecht
Cell culture plates; 60 mm, 100 mm, 150 mm (Partially provided by Wittbrodt Lab)	Sarstedt, Nümbrecht
Cell scraper	Sarstedt, Nümbrecht

Cover slips Nr. 1, round, 12 mm	Paul Marienfeld, Lauda-Königshofen
Cryovials	Nunc, Wiesbaden
Disposable syringes 1 ml, 5 ml, 25 ml	Braun, Melsungen
Erlenmeyer flask 100 ml, 500 ml	Schott, Mainz
Falcon Tubes 15 ml, 50 ml (Partially provided by Wittbrodt Lab)	Sarstedt, Nümbrecht
Glas bottles 100 ml, 250 ml, 1000 ml	Schott, Mainz
Hyperfilm ECL	GE Healthcare, München
IEF Electrode Strip	Amersham Biosciences, Freiburg
IEF/SDS Strip	Amersham Biosciences, Freiburg
Immersion oil 518C	Zeiss, Oberkochen
Leukotape classic	BSN medical, Hamburg
Microplate, 96-Well, flat floor	Greiner Bio-One, Kremsmünster
Microscope slide with frosted edge	Laborservice Brenzinger, Walldorf
Nitrocellulose membrane Hybond ECL	GE Healthcare, München
Parafilm	American National, Neenah, USA
PCR plates Star Seal	Star Lab, Hamburg
PCR-Tubes Multiply-Pro 0,2 ml	Sarstedt, Nümbrecht
Phast Gel Casette	GE Healthcare, München
Phast Gel Dry Gel	GE Healthcare, München
Phast Gel Sample Applicator	GE Healthcare, München
Pipette tips (Partially provided by Wittbrodt Lab)	Sarstedt, Nümbrecht
Plastic pipettes, sterile 5 ml, 10 ml, 25 ml	Sarstedt, Nümbrecht
Reaction tubes ("E-Cup") 1,5 ml, 2,0 ml	Sarstedt, Nümbrecht
Scalpel, sterile	Braun, Melsungen
Sterile filter 0,2 µm, 0,45 µm	Sartorius AG, Göttingen
Thermo Fast 96-well PCR Plates	Applied Biosystems
Two-chamber cell counter slide	Bio-Rad, München

### 5.2.2 Chemicals

**Table 2: List of chemicals and respective companies.**

Chemicals	Company
Agarose (Provided by Wittbrodt Lab)	Sigma-Aldrich, St. Louis, USA
2-mercaptoethanol	Merck, Darmstadt
Acetic acid, 100 %, p.a.	Roth, Karlsruhe
Ammonium ferric citrate	Sigma-Aldrich, St. Louis, USA
Bromophenol blue, ACS, Reag. Ph Eur	Merck, Darmstadt
Calcium chloride, dehydrated, powdered, pure 95 %	Merck, Darmstadt
Dimethyl sulfoxide, dried	Merck, Darmstadt
Di-sodium hydrogen phosphate dodecahydrate	Merck, Darmstadt
Dodecylsulfat, Na-salt in pellets	Serva, Heidelberg
EDTA, ≥ 99 %, p.a., ACS	Roth, Karlsruhe
Ethidium bromide - solution 1 %	Applichem, Darmstadt
Formaldehyde 4 %	Merck Darmstadt
Glycerine, anhydrous	neoLab, Heidelberg
Glycine, ≥ 99 %	Roth, Karlsruhe
H <sub>2</sub> O, HPLC-grade	Roth, Karlsruhe
Isopropanol	Roth, Karlsruhe
Potassium chloride	Merck, Darmstadt
Potassium dihydrogen phosphate, p.a.	Merck, Darmstadt
Magnesium chloride hexahydrate	Merck, Darmstadt
Milkpowder, blotting grade	Roth, Karlsruhe
Sodium acetate, crystalline, p.a.	Merck, Darmstadt
Sodium azide	Merck, Darmstadt
Sodium carbonate	Merck, Darmstadt
Dimethyl sulfoxide	Merck, Darmstadt
Di-sodium hydrogen phosphate	Roth, Karlsruhe
Paraformaldehyde, pure, DAC	Roth, Karlsruhe
Phosphoric acid, ACS reagent, ≥85 wt. % in H <sub>2</sub> O	Sigma-Aldrich, St. Louis, USA
Hydrochloric acid, smoking 37 %, p.a.	Roth, Karlsruhe
Sucrose	Roth, Karlsruhe
TEMED, 99 %, p.a.	Roth, Karlsruhe
TMS ((E)-2,3',4,5'-tetramethoxystilbene)	Santa Cruz Biotechnology, Heidelberg

Tris-(hydroxymethyl)-aminomethane ≥ 99.9 %, p.a.	Roth, Karlsruhe
Triton X-100	Serva, Heidelberg
Trypan Blue Solution	Fluka, Buchs, Switzerland
Tween 20, Ph.Eur.	Roth, Karlsruhe
UltraPure Agarose	ThermoFisher, Waltham, USA
NucBlue™	ThermoFisher, Waltham, USA
Sodium azide	Merck, Darmstadt
Sodium chloride ≥ 99.5 %, p.a.	Roth, Karlsruhe
Ethanol ≥ 99.8 %, p.a.	Roth, Karlsruhe
Methanol ≥ 99.9 %, p.a., ACS	Roth, Karlsruhe
Albumin bovine Fraction V, pH 7.0	Serva, Heidelberg
30 % acrylamide /0.8 % bisacrylamide	Roth, Karlsruhe
Rotiphorese Gel 30 (37, 5:1)	Roth, Karlsruhe

### 5.2.3 Devices

**Table 3: List of used devices.**

Device	Company
Accu-Jet Pro	Eppendorf, Hamburg
Autoklav VX-95	Systec, Linden
Bench centrifuge Biofuge Pico	ThermoFisher, Waltham, USA
Block heater Thermomixer	Eppendorf, Hamburg
Blotting-Chamber PerfectBlue Semi-Dry SEDEC M	Peqlab, Erlangen
Cell counter TC20™	Biorad, München
Centrifuge 5415D	Eppendorf, Hamburg
Centrifuge 5804 R	Eppendorf, Hamburg
Centrifuge Rotina 48 R	Hettich, Tuttlingen
CFX Connect™ Real-Time PCR Cycler	Biorad, München
CO <sub>2</sub> Incubator MCO-20A/C	Sanyo, Loughborough, UK
Cooling centrifuge Biofuge fresco	Heraeus, Hanau
Electrophoresis Power Supply EPS601	Bioscience, Amersham, UK
FemtoJet 4i (Provided by Wittbrodt Lab)	Eppendorf, Hamburg
Fine balance XP56	Mettler Toledo, Greifensee, CH

Fish incubator (Provided by Wittbrodt Lab)	Heraeus instruments, Hanau/ RuMed, Laatzen
Fluoreszenzmikroskop DMI4000B	Leica Wetzlar
Forceps 5, 55 Inox stainless steel	Dumont
Freezer -20 °C	Liebherr Bulle, CH
Freezer -80 °C	Ewald Innovationstechnik, Rodenberg
Freezer -80 °C (Provided by Wittbrodt Lab)	Thermo Scientific Waltham, USA
Fridge 4 °C (Partially provided by Wittbrodt Lab)	Liebherr Bulle, Schweiz
Gel documentation Jet Imager	Intas Science Imaging, Göttingen
Gelelektrophorese-Kammer (SDS) Mini-PROTEAN 3 Cell	Biorad, München
GeneAmp® PCR-System 2700	Applied Biosystems, Waltham, USA
FACS verse cytometer	BD Biosciences, Heidelberg
Ice machine	Ziegra, Isernhagen
Incubator HTMR-133 HLC	Haep Labor Consult, Bovenden
InjectMan NI2 (Provided by Wittbrodt Lab)	Eppendorf, Hamburg
Magnetic stirrer MR 3001	Heidolph, Schwabach
Microscope AE2000	Motic, Carlsbad, USA
Microwave R-233 (W)	Sharp, Osaka, Japan
Microwave R-939 (Provided by Wittbrodt Lab)	Sharp, Osaka, Japan
Millipore GenPure Pro UV-TOC/UF	ThermoFisher, Waltham, USA
NanoDrop™ Lite Spectrophotometer	ThermoFisher, Waltham, USA
nCounter® SPRINT profiler	Nanostring, Seattle, USA
Needle puller P-30 (Provided by Wittbrodt Lab)	Sutter Instrument Company, USA
Nikon SMZ18 stereomikroskop (Provided by Wittbrodt Lab)	Nikon, Minato, Japan
Nitril gloves (Provided by Wittbrodt Lab)	STARLAB, Hamburg
Olympus SZX7 (Provided by Wittbrodt Lab)	Olympus, Tokio, Japan
pH-Meter inoLab pH Level 1	WTW, Weilheim

Photometer SpectraMax Plus 384	Molecular Devices, Sunnyvale, USA
Pipettes Research Plus (Partially provided by Wittbrodt Lab)	Eppendorf, Hamburg
Power unit E835	Consort, Turnhout, BEL
Scale PH204L Mettler	Mettler Toledo, Greifensee, CH
Shaker Rocky 1100	Labortechnik Fröbe, Lindau
Spark® Multimode microplate reader	Tecan Trading, Männedorf, Switzerland
Stereo microscope SZX7 (Provided by Wittbrodt Lab)	Olympus, Tokio, Japan
Sterile bank Class 2 SterilGard III Advance	The Baker Company, Sanford, USA
T100 Thermal Cycler	Biorad, München
Ultrasound Sonifier 450 Converter 102C; Beaker resonator 101-147-047	Branson, Dietzenbach
Vortexer Vortex-Genie 2	Scientific Industries, Bohemia, USA
Washer G7883CD	Miele, Gütersloh
Water bath 1092	GFL, Burgwedel
Westernblot Imaging Fusion SL4	Peqlab, Erlangen

### 5.2.4 Kits, standards and enzymes

**Table 4: List of kits, standards and enzymes with respective companies.**

Component	Company
Bicinchoninic acid (BCA) assay	ThermoFisher, Waltham, USA
Bovine Serum Albumin (BSA)	Serva, Heidelberg
CellROX™ deep red	ThermoFisher, Waltham, USA
cOmplete™ EDTA-free Protease Inhibitor Cocktail	Roche, Heidelberg
DC™ Protein Assay Kit	Bio-Rad, München
Dimethyl sulfoxide (DMSO)	Merck, Darmstadt
DNA-Loading Dye	Fermentas, St. Leon Rot
dNTP Mix, 10 mM	ThermoFisher, Waltham, USA
DTT	ThermoFisher, Waltham, USA
ECL Plus Western Blotting Substrate	Pierce Biotechnology, Rockford
Fluoromount-G™ Mounting Medium	ThermoFisher, Waltham, USA
GeneRuler 1 kb/100 bp DNA Ladder	ThermoFisher, Waltham, USA

GFP mRNA (Provided by Wittbrodt Lab)	Lab Stock
GSH-Glo™ Glutathione Assay	Promega Corporation, Madison, USA
HeiCas9 (Provided by Wittbrodt Lab) [109]	Lab stock, based on a pCS2+ plasmid
HF-Puffer for Phusion Polymerase (10x)	ThermoFisher, Waltham, USA
MgCl <sub>2</sub> , 25 mM	ThermoFisher, Waltham, USA
Omniscript RT Kit (50)	Qiagen, Hilden
PageRuler Prestained Protein Ladder	ThermoFisher, Waltham, USA
peqGOLD Gel Extraction Kit	Peqlab, Erlangen
PerfeCTa® SYBR® Green FastMix®	Quantbio, Beverly, USA
Phusion Polymerase (2 U/μl)	ThermoFisher, Waltham, USA
Protease Inhibitor Mix (PIM) complete	Roche, Heidelberg
Proteinase K (Provided by Wittbrodt Lab)	Roth, Karlsruhe
QIAshredder	Qiagen, Hilden
Revert Aid First Strand cDNA Synthesis Kit	ThermoFisher, Waltham, USA
RiboLock RNase Inhibitor	Fermentas, St. Leon Rot
RIPA-buffer Pierce™	ThermoFisher, Waltham, USA
RNase-Free DNase Set	Qiagen, Hilden
Rneasy® Mini Kit	Qiagen, Hilden
Taq DNA-Polymerase (5 U/μl)	ThermoFisher, Waltham, USA
Taq Puffer (10x) with potassium chloride	ThermoFisher, Waltham, USA
UPX Protein Extraction buffer	Abcam, Cambridge, UK

## 5.2.5 Buffer

**Table 5: List of buffers and their composition.**

Buffer	Compostion
ABC buffer	50 nM Ammonium bicarbonate In H <sub>2</sub> O
Anode buffer (Semi-Dry Blot)	20 % Methanol (v/v) 9 g/l Tris/HCl pH 7,4 In H <sub>2</sub> O
Cathode buffer (Semi-Dry Blot)	5,2 g/l 6-Aminocaproic acid 20 % Methanol (v/v) 3 g/l Tris/HCl pH 9,0 In H <sub>2</sub> O

ERM (10x) (Provided by Wittbrodt Lab)	170 mM NaCl 4 mM KCl 2.7 mM CaCl <sub>2</sub> ·2H <sub>2</sub> O 6.6 mM MgSO <sub>4</sub> ·7H <sub>2</sub> O 170 mM HEPES
Extraction buffer	0.4 M Tris-HCl pH 8.0 5 mM EDTA pH 8.0 0.15 M NaCl 0.1% SDS in H <sub>2</sub> O
Extraction buffer (fish) (Provided by Wittbrodt Lab)	2 M Tris-HCL pH 8.0 5 M NaCl 20% SDS 0,5 M EDTA pH8 In H <sub>2</sub> O
FACS buffer	2 % FBS 2mM EDTA 0.1 % sodium azide In PBS
Fixation buffer	40 % Ethanol (v/v) 7,5 % Acetic acid (v/v) In H <sub>2</sub> O
Loading buffer; DNA- gelectrophoresis (4x)	40 % Saccharose (w/v) 0.25 % Bromphenol blue (w/v) In H <sub>2</sub> O
Loading buffer; SDS-PAGE (6x)	12 % SDS (w/v) 45 % Glycerin (v/v) 12 % β-Mercaptoethanol (v/v) 0.06 % Bromphenol blue (w/v) 480 mM Tris/HCl pH 6,8 In H <sub>2</sub> O
Nucleus isolation buffer	1 % Triton X-100 1x protease inhibitor 1x TBS (pH:7.4)
PBS (10x)	80 g/l NaCl 14.4 g/l Na <sub>2</sub> HPO <sub>4</sub> ·2H <sub>2</sub> O 2 g/l KCl 2 g/l KH <sub>2</sub> PO <sub>4</sub> In H <sub>2</sub> O
PBS-T 0.1 %	0.1 % Tween 20 (v/v) In 1x PBS
PFA	4 % Paraformaldehyde (w/v) 8 g/l NaCl 11,5 g/l Na <sub>2</sub> HPO <sub>4</sub> 0.2 g/l KCl 0.2 g/l KH <sub>2</sub> PO <sub>4</sub> Tris/HCl pH 8.0 In H <sub>2</sub> O
Pierce™ RIPA-Puffer	25 mM Tris HCl pH 7,6 150 mM NaCl 1 % NP-40 (v/v) 1 % Sodium deoxycholic acid (w/v) 0.1 % Sodium dodecyl sulfate (w/v) In H <sub>2</sub> O



Running buffer für SDS-PAGE (10x)	30.2 g/l Tris 10 g/l SDS 144 g/l Glycine In H <sub>2</sub> O
Separation buffer; SDS-PAGE	0.1 % SDS (w/v) 1.5 M Tris/HCl pH 8.8 In H <sub>2</sub> O
Stacking buffer; SDS-PAGE	0.1 % SDS (w/v) 0.5 M Tris/HCl pH 6.8 In H <sub>2</sub> O
TAE-Buffer (50x)	EDTA 100 mM 2 M Tris/Acetate pH 8.0 In H <sub>2</sub> O
TBS (10x)	80 g/l NaCl 2 g/l KCl 30 g/l Tris/HCl pH 8.0 In H <sub>2</sub> O
TBS-T 0.1 %/ 0.5 %	0.1/0.5 % Tween 20 (v/v) Tris/HCl pH 7.4 In 1x TBS
Washing buffer	50 % Methanol (v/v) 5 % Acetic acid (v/v) In H <sub>2</sub> O

## 5.2.6 Oligonucleotides

**Table 6: List of used oligonucleotides and gRNAs of corresponding method. (PAM in brackets).**

Oligonucleotide	Application	Sequence
Human <i>CYP1B1</i> forward	qRT-PCR	5'-AGCTCAACCGCAACTTCAG
Human <i>CYP1B1</i> reverse	qRT-PCR	5'-CTCCTCCTCTTCACCAGGTATC
Fish <i>CYP1B1</i> forward	qRT-PCR	5'-GCTGACCTCCGTGACTCTC
Fish <i>CYP1B1</i> reverse	qRT-PCR	5'-GTGCTGAACGGAGACTCCA
Human $\beta$ <i>ACTIN</i> forward	qRT-PCR	5'-AGAGCTACGAGCTGCCTGAC
Human $\beta$ <i>ACTIN</i> reverse	qRT-PCR	5'-AGCACTGTGTTGGCGTACAG
Fish <i>Srd5a3</i> forward	qRT-PCR	5'-AACTGGAGCCTGGTAGATG
Fish <i>Srd5a3</i> reverse	qRT-PCR	5'-ACCTGACAACACATCTAATATAGC AATC
Fish <i>Srd5a3_PCR Screening forward</i>	Sequencing	5'-CGCGGAGATGTCGTGGAG

Fish <i>Srd5a3_PCR</i> <i>Screening reverse</i>	Sequencing	5'-CTGTCCACGGCTCTGGTG
Fish <i>Cyp1b1</i> (Provided by Wittbrodt Lab)	CRISPR	5'-CCCCGGCCCGTTTGCC[TGG]CCGC
Fish <i>Srd5a3</i> (Ex.1) (Provided by Wittbrodt Lab)	CRISPR	5'-TTCCAGGATCTTATTCGCTA[CGG]
Fish <i>Srd5a3</i> (Ex.2) (Provided by Wittbrodt Lab)	CRISPR	5'- ATCGGCAATCTTACCCATCA[TGG]
Fish <i>Oca2</i> (Provided by Wittbrodt Lab) [111]	CRISPR	5'- TTGCAGGAATCATTCTGTGT[GGG]-3'

### 5.2.7 Antibody

Primary antibodies were used for Western blotting and immunofluorescence microscopy. For Western blotting they were diluted 1:1,000 in PBS-T 0.1 %, and 1:400 in PBS supplemented with 1 % BSA for immunofluorescence microscopy. HRP- and fluorophore-coupled secondary antibodies were diluted 1:10,000 and 1:700 in the corresponding buffer, respectively.

**Table 7: List of used antibodies.**

<b>Antibody</b>	<b>Primary/ secondary antibody</b>	<b>Company</b>
Rabbit anti-human CYP1B1	Primary	Proteintech, Manchester, USA
Mouse anti-human βACTIN	Primary	Sigma-Aldrich, St. Louis, USA
Rabbit anti-human PMM2	Primary	Proteintech, Manchester, USA
Rabbit anti-human KI67	Primary	Proteintech, Manchester, USA
Rabbit anti-human <i>Nrf2</i> /NFE2L2	Primary	Proteintech, Manchester, USA
Rabbit anti-human GPX4	Primary	Abcam, Cambridge, UK
Rabbit anti-human Transferrin	Primary	BIOZOL Diagnostica, Eching

Goat anti-rabbit Alexa Fluor 488	Secondary	ThermoFisher, Waltham, USA
Goat anti-rabbit HRP	Secondary	Dianova, Hamburg
Goat anti-mouse HRP	Secondary	Santa Cruz Biotechnology, Heidelberg

### 5.2.8 Lectin

Biotinylated lectins were used to stain specific glycan structures in total lysate. Lectins were diluted 1:400 and HRP-coupled streptavidin 1:10,000 in TBS-T 0.1 %.

**Table 8: List of used lectins and HRP-coupled streptavidin.**

Lectin	Abbreviation	Company
Concanavalin A	ConA	Vector Laboratories (Burlingham, USA)
Wheat germ agglutinin	WGA	
HRP-coupled streptavidin	-	

### 5.2.9 Programs, online tools and data bases

**Table 9: List of used programs, online tools and data bases, including developer and corresponding online-links.**

Name	Type	Developer	Online-Link
ApE	Programm	M. Wayne Davis	
BioRender	Online- Tool	-	<a href="https://www.biorender.com/">https://www.biorender.com/</a>
CCTop	Online- Tool	Stemmer M. et al [108].	<a href="https://cctop.cos.uni-heidelberg.de/">https://cctop.cos.uni-heidelberg.de/</a>
ChatGPT	Online- Tool	OpenAI	<a href="https://openai.com/index/chatgpt/">https://openai.com/index/chatgpt/</a>
ClinVar	Online- Tool	NCBI	<a href="https://www.ncbi.nlm.nih.gov/clinvar/">https://www.ncbi.nlm.nih.gov/clinvar/</a>
Dr. Tom	Online- Tool	BGI	<a href="https://biosys.bgi.com/#/report/login">https://biosys.bgi.com/#/report/login</a>
DTU Health Tech	Online- Tool	Department of Health Technology	<a href="https://services.healthtech.dtu.dk/">https://services.healthtech.dtu.dk/</a>

Ensembl	Database	-	<a href="https://www.ensembl.org/index.html">https://www.ensembl.org/index.html</a>
FlowJo	Program	-	<a href="https://www.flowjo.com/">https://www.flowjo.com/</a>
GraphPad PRISM 8	Program	GraphPad Software, Inc.	<a href="https://www.graphpad.com/features">https://www.graphpad.com/features</a>
ImageJ	Program	Wayne Rasband (NIH)	<a href="https://imagej.net/ij/">https://imagej.net/ij/</a>
Microsoft Office	Program	Microsoft	-
NCBI	Database	-	<a href="https://www.ncbi.nlm.nih.gov/">https://www.ncbi.nlm.nih.gov/</a>
NCBI BLAST	Online- Tool		<a href="https://blast.ncbi.nlm.nih.gov/Blast.cgi">https://blast.ncbi.nlm.nih.gov/Blast.cgi</a>
NEB Tm Calculator	Online- Tool	-	<a href="http://www.tmcalculator.neb.com">www.tmcalculator.neb.com</a>
Tecan Sparkcontrol	Program	Tecan	-
UniProt	Database	-	<a href="https://www.uniprot.org/">https://www.uniprot.org/</a>

## 5.3 Cell culture

### 5.3.1 Cell culture handling

I conducted cell cultured experiments with three SRD5A3-CDG patient-derived fibroblasts lines (Pat. 1 – 3) which were obtained after skin biopsy. Five independent commercially available dermal fibroblast cell lines were used as healthy controls (NHDF, PromoCell; SSC, Millipore; PCS, ATCC; NHDF and HDF, both from Sigma-Aldrich). Growth media was DMEM (Gibco Life Sciences, ThermoFisher) supplemented with 10% heat-inactivated FCS (incubated at 56 °C for 1 hour), 1% penicillin/streptomycin (10,000 U/ml), and 1% amphotericin B (250 µg/ml), referred to as complete DMEM media. Cells were kept at 5 % CO<sub>2</sub> and 37 °C in cell culture flasks T25, T75, T175, cell plates and plastic Petri dishes. Until cells reached 80 – 100 % confluency, media was changed once a week. Once they reached full confluency, cells were splitted by washing in warm PBS and addition of 0.25 % trypsin-EDTA solution (PANBiotech). After 3 min incubation at 37 °C, 5 times the volume complete DMEM media were added, and cells were diluted as required in a fresh cell culture container.

Cell harvesting was achieved by rinsing cells twice with ice-cold PBS and scraping. Scraped cells were diluted in ice-cold PBS and centrifuged for 5 min at 400 rcf and 4 °C. Cell pellets were snap-frozen in liquid nitrogen and stored at -80 °C until use.

### 5.3.2 Cell counting

Determination of the cell count was achieved using the TC20 Automated Cell Counter (Bio-Rad). Trypsinized cells (5.3.1) were resuspended with 8 ml of complete DMEM medium. From this suspension, 10 µl were mixed with 10 µl of trypan blue. Then, 10 µl of this mixture was pipetted onto a cell counting slide and analyzed using the TC20 Automated Cell Counter.

### 5.3.3 Cryopreservation

For preservation of cell lines, cells were stored at -80 °C. Once cells were grown to a confluency of 80 – 100 % in a T75 flask, they were rinsed with PBS and trypsinized with 2 ml 0.25 % Trypsin-EDTA for 3 min. Detached cells were then resuspended in 8 ml complete DMEM medium, transferred into a 15 ml flask and pelleted by centrifugation at 400 rcf at 4°C for 5 min. Supernatant was removed and cells were resuspended in 2 ml ice-cold complete DMEM medium supplemented with 8.5 % DMSO. 1 ml of this suspension was then transferred into a cryo-vial and incubated for at least 3 hours at -20 °C before being stored in liquid nitrogen. Taking cryo-cultures back into live-cell culture was achieved by defreezing of cryo-culture at room temperature, slow addition of 1 ml warm complete DMEM medium and transfer into a T75 flask. Medium was refreshed one day later.

## 5.4 Generation of *Srd5a3*- knock-out medaka fish embryo

### 5.4.1 Design of RNAs for CRISPR/Cas9

I genetically manipulated Medaka fish embryos (*Oryzias latipes*) by a CRISPR/Cas9 approach to mimic SRD5A3-CDG and investigate its pathological phenotype. In this approach the published *heiCas9* was used for higher efficiency and provided by the Wittbrodt Lab [109]. For the *Srd5a3* knock-out (KO) and the *Cyp1b1*-KO, three CRISPR RNAs (crRNAs) were designed with CCTop and ordered from Integrated DNA Technologies (IDT) [108]. The two crRNAs targeting the *Srd5a3* gene were designed by Kaisa Pakari, the crRNA targeting the *Cyp1b1* gene was designed by Dr. Thomas Thumberger. Prior to the microinjection in medaka fish embryos, the crRNA was combined with trans-activating CRISPR RNA (trRNA) to form a complex [110]. Since the region in which the genetic variations of Pat. 1 – 3 are not conserved in medaka fish, the design was carried out to delete a ~297 base pair DNA fragment between exon 1 and exon 2 in *Srd5a3*. This region is close to the genetic variations in Pat 1 – 3. The following conserved target sites between human and medaka were used (PAM in brackets):

*Srd5a3* Ex.1, 5'-TTCCAGGATCTTATTCGCTA[CGG]-3'

(Designed by Kaisa Pakari and provided by Wittbrodt Lab)

*Srd5a3* Ex.2, 5'-ATCGGCAATCTTACCCATCA[TGG]-3'

(Designed by Kaisa Pakari and provided by Wittbrodt Lab)

*Cyp1b1*, 5'-CCCCGGCCCGTTTGCC[TGG]CCGC-3'

(Designed by Dr. Thomas Thumberger and provided by Wittbrodt Lab)

In addition, one single guide RNA (sgRNA) was used which worked as an injection control by targeting the *Oca2* gene. The sgRNA was already published in Lischik CQ, et al. 2019 and was provided by the Wittbrodt Lab [111]:

*Oca2*, 5'- TTGCAGGAATCATTCTGTGT[GGG]-3'

#### 5.4.2 Microinjection: Δ*Srd5a3* medaka fish embryos

Fertilised medaka fish eggs were used for genetic manipulation using CRISPR/Cas9 by microinjection. Regarding its handling, I harvested fertilised eggs in a one-cell stage from female adults. Developmental progression was delayed by storing eggs in ice-cold 1x ERM.

Fertilised one-cell stage eggs from healthy wt medaka Cab strain were detangled and isolated and placed in 1.5 % agarose (H<sub>2</sub>O) molds in a 10 cm plastic petri dish. The CRISPR/Cas9 mix (Tab. 10) supplemented with GFP mRNA as tracer was then carefully microinjected into the single cell. At least 6 hours after microinjection, I separated GFP positive crispants from noninjected embryos and raised them.

**Table 10: CRISPR/Cas9 mix.**

Compound	Volume (10 µl)	End concentration
(hei)Cas9 mRNA	According to stock concentration	150 ng/µl
sgRNA ( <i>Srd5a3</i> exon1 and exon 2) Stock: 150 ng/µl	Each 1 µl	Each 15 ng/µl
GFP mRNA Stock: 100 ng/µl	1 µl	10 ng/µl
RNAse-free H <sub>2</sub> O	Fill up to 10 µl total volume	-

Embryos were maintained at 28 °C in 1× ERM media with 2 mg/l methylene blue, until the desired developmental stage.

#### 5.4.3 Genetic validation of *Srd5a3*-KO medaka fish embryos

To evaluate the knockout efficiency, genotyping was performed using gDNA isolated from hatched and not-hatched embryos. I treated embryos with an extraction buffer (fish) containing

Proteinase K (1 mg/ml; 20 mg/ml stock) and incubated them overnight at 60 °C. The Proteinase K was inactivated by heating at 95°C for 20 – 25 min, and the samples were diluted in two volumes of DNase-free water. Genotyping PCR was carried out using Phusion™ High-Fidelity DNA Polymerase with the protocol as described in 5.6.4.

### The primers used:

*Srd5a3*\_Forward: 5'-CGCGGAGATGTCGTGGAG-3'

*Srd5a3*\_Reverse: 5'-CTGTCCACGGCTCTGGTG-3'

*Cyp1b1*\_Forward: 5'-TGCCAGGTTACAGTTAATGGTTC-3'

*Cyp1b1*\_Reverse: 5'-CTTGGCAACGCTCCTCAC-3'

I separated PCR products by gel electrophoresis as described in 5.6.5, *Srd5a3* bands (1,000 bp) were cut out from the gel. Gel extraction was carried out with the peqGold Gel Extraction Kit, according to the manufacturer's instructions. Elution was performed with 50 µl DNase-free H<sub>2</sub>O and samples were sent to Sanger sequencing as described in 5.6.6 (Seqlab Microsynth GmbH, Göttingen).

### 5.4.4 Mass spectrometry: Glycosylation profile of medaka fish embryos

Mass spectrometric analysis to validate the glycosylation profile in *Srd5a3*-KO medaka fish embryos was carried out by Ivan Andújar Martínez from the Bio/ Process Analytics group of Dr. Erdmann Rapp in Magdeburg [105]. I performed the *Srd5a3*-KO in medaka fish embryos by microinjection and use of CRISPR/Cas9 as described in 5.4.2. Since the yolk contains maternal proteins which eventually interfere with the mass spectrometric analysis, I raised embryos until almost all the yolk was metabolized (~5 days post hatching). At this stage, *Srd5a3*-KO and uninjected medaka fish embryos were snap-frozen in liquid nitrogen and stored at -80 °C until shipping. Detailed protocol can be found in 5.6.17.

## 5.5 CDG Diagnostic: Validation of SRD5A3-CDG deficiency in serum and patient-derived fibroblasts

### 5.5.1 Isoelectric focussing

Isoelectric focusing (IEF) separates different glycoforms of a protein within a gel based on their isoelectric points. In CDG diagnostic, serum protein transferrin displays the gold standard and is used to identify *N*-glycosylation defects and their differentiation between CDG type-I and type-II. Its two biantennary *N*-glycans of the complex type carry four terminal sialic acid residues at all and give the protein a negative charge. If a glycosylation defect causes the glycans on the proteins to be incomplete or absent, the lack of sialic acid alters the isoelectric point. This change affects how the protein migrates during IEF.

IEF analysis of transferrin of the patients was performed according to Himmelreich *et al.* and Niehues *et al* [112, 113]. Patient's serum sample (10 µl, ~600 µg) was diluted 1:5 in H<sub>2</sub>O and incubated for 20 minutes in a 2.25 mM ferric citrate solution to saturate all iron-binding sites of the protein. Separation was performed using a PhastGel™ with a pH gradient of 4 to 6.5. The gel was pre-focused for 10 minutes at 2000 V and 15 °C in the PhastSystem™. Then, 1 µl of the iron-saturated patient serum and controls were loaded. The IEF of the samples was carried out for 15 minutes at 2000 V, 2.5 mA, and 15 °C. Fixation of the transferrin bands was performed by incubation of the gel for 40 minutes in a rabbit anti-human transferrin antibody solution prepared in 0.9% NaCl. To remove nonspecifically bound antibodies, the gel was washed in H<sub>2</sub>O and further incubated overnight in 0.9% NaCl. Finally, the protein bands were visualized using silver staining.

### 5.5.2 LC-MS System: *N*-glycanprofile analysis

The *N*-glycan analysis using the BioAccord LC-MS System (Waters) was conducted with the help of Simone Hengst (AG Thiel, Heidelberg). 2 mg/ml of total protein was used to perform the *N*-glycan analysis of serum samples – the serum sample (approximately 60 mg/ml) was diluted 1:30 with H<sub>2</sub>O. 7.5 µl of the diluted samples were denatured at 95 °C for 5 minutes by adding 3 µl of 5% Rapi Gest SF and 3.3 µl of LC-MS water. After cooling the sample on ice, *N*-glycans were released from its glycoprotein by addition of 1.2 µl of GlycoWorks PNGase F (Waters) and incubating the mixture at 50 °C for 30 minutes. The sample was then cooled on ice, and released glycans were fluorescently labeled with 6 µl of GlycoWorks Rapi-Fluor-MS Reagent (Waters) for 5 minutes at RT. To remove protein residues, 179 µl of acetonitrile was added to the sample. Labeled glycans were purified using a HILIC SPE plate (Waters) and finally eluted in 90 µl of GlycoWorks SPE Elution Buffer. The eluate was mixed with 310 µl of GlycoWorks Sample Diluent (Waters) and analysed by using the BioAccord LC-MS System (Waters). The sample was first separated by liquid chromatography (LC), followed by analysis using UPLC and fluorescence (FLR) detection.

For extraction of *N*-glycans from fibroblasts, I initially started with total cell lysates preparation (5.6.8) and protein quantification (5.6.7). I loaded 100 µg of total protein from each sample into three wells of a 10% SDS-PAGE and the gel was run at 100 V for approximately 10 min until the marker began to separate. At that point the run was stopped and the protein bands were cut out of the gel with a sterile scalpel and incubated in a fixation solution (52.5% H<sub>2</sub>O, 40% ethanol, 7.5% acetic acid) for one hour. The gel slices were then rinsed twice for 10 min in H<sub>2</sub>O, cut into approximately 2x2 mm pieces and transferred into 1.5 ml tubes. The gel pieces were incubated for 60 minutes at 900 rpm in a Thermomixer with 500 µl of washing buffer (50% methanol, 45% H<sub>2</sub>O, 5% acetic acid). Afterward, the liquid was discarded and 500 µl of acetonitrile (80% acetonitrile, 20% H<sub>2</sub>O) was added for 5 minutes at 900 rpm. The acetonitrile



was discarded and the pieces were then dried using a lyophilizer for approximately 45 min. Once the gel pieces were dry, they were incubated for 30 minutes at 56 °C and 900 rpm in 500 µl of DTT (45 mM in H<sub>2</sub>O). The DTT solution was discarded, and the gel pieces were incubated again in 500 µl of acetonitrile for 5 minutes at 900 rpm. The acetonitrile was then replaced by ABC buffer (50 mM in H<sub>2</sub>O) and incubated for 10 min at 900 rpm. The gel pieces were then incubated in 500 µl of acetonitrile for 5 minutes at 900 rpm and dried completely in the lyophilizer – which could take couple of hours. Dried gel pieces were treated with 50 µl of PNGase F solution (0.1 U/µl; consisting of 2 µl PNGase F (1:100 in H<sub>2</sub>O) and 98 µl ABC buffer). After 5 minutes, the solution was filled up with 200 µl of ABC buffer and incubated overnight at 37°C. The next day, I transferred the entire liquid to a fresh 1.5 ml tube. The gel pieces were incubated for 10 minutes at 1000 rpm with 200 µl of H<sub>2</sub>O and the supernatant was added to the previously collected liquid. This step was repeated three times. The collected sample liquid was dried in the lyophilizer to concentrate the *N*-glycans.

### 5.5.3 Lipid-linked oligosaccharide analysis

LLO analysis was performed by Virginia Geiger (AG Thiel, Heidelberg), according to Körner et al., 1998, with modifications [114]. Specifically,  $1 \times 10^6$  fibroblasts from a control and a SRD5A3-CDG patient 1 were used, and labelling with [2-<sup>3</sup>H]mannose was conducted for a duration of 30 minutes. Lipid-linked oligosaccharides (LLOs) were extracted and analysed by high-pressure liquid chromatography (HPLC), employing 90 fractions collected over a 1.5-hour period with 1ml final volume per sample.

## 5.6 Molecular methods

### 5.6.1 RNA isolation

I isolated total RNA from cell pellets and medaka fish embryos using Qiashredder (Qiagen) and the RNeasy Mini Kit (Qiagen). 350 µl RLT buffer supplemented with 1 % β-Mercaptoethanol, were used to lyse cells/tissue prior to loading on the Qiashredder with maximum centrifugation speed for 2 min. The homogenized solutions were then purified according to the manufacturer's instructions of the RNeasy Mini Kit. In case of the medaka fish embryos, the tissue was disrupted by sonification (3x 10 sec) prior to the loading on the Qiashredder. The concentration and quality of total RNA (260 /280 nm) was then measured photometrically by using the NanoDrop™ Lite (ThermoFisher). In case of RNA, a 260 /280 nm ratio of 2.0 is considered to be pure. RNA samples were stored at -80 °C.

### 5.6.2 PCR Primer Design

The primers used for PCR, sequencing, and gene-specific reverse transcription were selected to be 15–25 bases in length with a G/C of 40 - 60% and a melting temperature ( $T_m$ ) of 55 - 60 °C. For finding appropriate primers and calculating the  $T_m$ , I used ApE and the NEB  $T_m$  Calculator, respectively.

For qRT-PCR, primers were required to span exon-exon junctions, and the amplified product size was set between 150 - 350 base pairs. For these primers, the  $T_m$  range was set at 50 - 65 °C, with a length of approximately 20 bases.

### 5.6.3 Reverse Transcription

Generation of cDNA from total RNA (1 µl input; 300 ng) for PCRs was accomplished with the Omniscript Reverse Transcription Kit (Qiagen) according to the manufacturer's instructions. After setting up the reaction mix, I incubated the mix for 1 h at 37 °C. Generated cDNA was stored at -20 °C.

**Table 11: Reaction mix for generation of cDNA from total RNA with Omniscript Reverse Transcription Kit.**

Compound	Volume
Total RNA (200 ng/µl)	3 µl
Reaction buffer (10x)	2 µl
dNTPs (5 mM)	2 µl
Specific reverse primer (10 µM)	2 µl
<i>Omniscript Reverse Transcriptase</i> (4 U/µl)	1 µl
RiboLock (20 U/µl)	1 µl
H <sub>2</sub> O	9 µl

### 5.6.4 Polymerase Chain Reaction (PCR)

The Polymerase Chain Reaction (PCR) was used to amplify specific DNA fragments. I performed nested PCRs to improve amplification accuracy, if needed. In those cases, two independent primer pairs were used. The first pair binds upstream and downstream the 5' and 3' end of the required DNA fragment, whereas the second pair binds within the first PCR product. 1 µl of the first PCR reaction serves as template for the second PCR.

I used two different polymerases for amplification of DNA sequences: *Taq* polymerase and *Phusion<sup>TM</sup>* polymerase. *Taq* polymerase was used for validation of the genetic variants in SRD5A3-CDG patient-derived fibroblasts by Sanger sequencing. *Phusion* polymerase was

used to validate genetic manipulations in the Srd5a3-KO medaka fish embryos – also by Sanger sequencing.

**Table 12: PCR Mixes for *Taq* and *Phusion*<sup>TM</sup> polymerase and the corresponding PCR protocol.**

Compound	Volume
DNA (50 ng)	1 µl
Taq Puffer + (NH <sub>4</sub> ) <sub>2</sub> SO <sub>4</sub> (10x)	5 µl
MgCl <sub>2</sub> (25 mM)	4 µl
DMSO (100 %)	1 µl
dNTPs (10 mM)	0.5 µl
Primer forward/ reverse (10 µM)	Each 1.25 µl
<i>Taq</i> Polymerase (5 U/µl)	0.2 µl
H <sub>2</sub> O	Fil to 50 µl

Step	Temperature [°C]	Duration	Cycle
Initial denaturation	95 °C	10 sec	-
Denaturation	95 °C	30 sec	x35
Annealing	55 °C	30 sec	
Extension	72 °C	1 min/kb	
Final Extension	72 °C	2 min	-

Compound	Volume
DNA (50 ng)	1 µl
HF buffer (10x)	10 µl
DMSO (100 %)	1 µl
dNTPs (10 mM)	0.5 µl
Primer forward/ reverse (10 µM)	Each 1.25 µl
<i>Phusion</i> Polymerase (2 U/µl)	0.2 µl
H <sub>2</sub> O	Fil to 50 µl

Step	Temperature [°C]	Duration	Cycle
Initial denaturation	98 °C	30 sec	-
Denaturation	98 °C	10 sec	x25
Annealing	65 °C	30 sec	
Extension	72 °C	30 sec	
Final Extension	72 °C	5 min	-

### 5.6.5 Agarose Gel electrophoresis

Agarose Gel electrophoresis can be used to visualize PCR products and to purify them for sequencing. I supplemented PCR products with 10 % (v/v) loading buffer and loaded them on an ethidium bromide supplemented agarose gel (1 %; 1x TAE buffer) together with 1kb Ladder as marker. Electrophoretic separation was performed by applying 120 V for 1 h to the gel. Ethidium bromide is a fluorescent tag for nucleic acid stains which can be visualized under UV-light. For sequencing, desired DNA bands were cut out with a clean scalpel and transferred into a 2 ml E-cup. Gel extraction was carried out with the peqGold Gel Extraction Kit and was performed according to the supplier's manual. Elution was performed with 50 µl DNase-free H<sub>2</sub>O and samples were sent to Sanger sequencing as described in 5.6.6 (Seqlab Microsynth GmbH, Göttingen) or stored at -20 °C.

### 5.6.6 Sanger Sequencing

I used Sanger sequencing to verify sequences of PCR products derived from cDNA and genomic DNA. Sanger sequencing of PCR products was carried out by SeqLab Microsynth GmbH (Göttingen). For optimal quality a concentration of 1.5 ng/ µl per 100 bp was required. For this reason, 3 µl gene specific primer (10µM) was mixed with the desired amount of PCR product and filled to 12 µl total volume with H<sub>2</sub>O. Results were provided and analyzed as FASTA data and electropherograms by using ApE.

### 5.6.7 Total lysate preparation

Protein isolation required additional steps for medaka fish embryos compared to fibroblasts. I homogenized embryos by using a pestle in 100 µl RIPA buffer (ThermoFisher) supplemented with 1x protease inhibitor mix (PIM, Roche Diagnostics). The homogenized embryos were lysed through sonication and then incubated on ice for 30 minutes. Fibroblasts, harvested either from a confluent T75 flask or frozen pellets as described in 5.3.1, were lysed by adding 125 µl of RIPA buffer with 1x PIM, followed by a 30 minutes incubation on ice. After this initial different preparation, lysates from both medaka fish embryos and fibroblasts were processed identically. I disrupted samples by passing them 20 times through a 22G x 1 ½" safety needle. The lysates were then centrifuged for 30 minutes at 18,000 rcf and 4 °C. I collected supernatant containing the proteins and measured the total protein content photometrically using the Lowry assay (DC Protein Assay, BioRad).

### 5.6.8 Total protein quantification

For SDS-PAGE and Western blot analysis, samples need to be loaded equally for comparison. Therefore, I quantified total protein concentration after lysis using the protein quantification assay according to Lowry [115]. The assay was performed with DC Protein Assay Kits (BioRad) according to manufacturer's protocol. Preparation for the photometrical quantification

was carried out by pipetting 5 µl total protein sample into a 96-well plate – dilution of the samples might have been required. 25 µl and 200 µl of solution A and B (Bio-Rad) were added to the sample, respectively. After 15 min shaking at RT, I measured the absorbance at 750 nm of the samples photometrically. As references, I measured a BSA calibration, ranging from a concentration of 0 - 2 mg/ml in eight fractions solved in RIPA-buffer.

### 5.6.9 SDS-PAGE

SDS-PAGE is used to separate proteins according to their molecular size in an acrylamide gel. I self-casted gels, consisting of a stacking and a separation gel. The stacking gel is supposed to align the protein samples before entering the separation gel. In the separation gel, proteins transfer at different speed through the gel, according to their molecular size. The separation gel varied between 8 - 12.5 % acrylamide, depending on the protein size to be addressed. After pouring the separation gel into the cast, I added isopropanol on top of the gel to create an even line. After successful polymerisation of the separation gel, isopropanol I removed it by using Whatman paper and the stacking gel was poured onto it. A comb with 10 or 15 slots were used to generate pockets to load the samples in.

**Table 13: Composition of 8, 10 and 12.5 % separation gel and stacking gel.**

Compound	Separation gel (8 %)	Separation gel (10 %)	Separation gel (12.5 %)	Stacking gel
Rotiphorese 30	1600 µl	2000 µl	2500 µl	338 µl
Separation gel buffer	1500 µl	1500 µl	1500 µl	-
Stacking gel buffer	-	-	-	338 µl
APS (10 %)	60 µl	60 µl	60 µl	30 µl
TEMED	6 µl	6 µl	6 µl	3 µl
H <sub>2</sub> O	2900 µl	2500 µl	2000 µl	1500 µl

Since this method is based on the electric charge of the proteins, which varies between proteins, all proteins are receiving a negative charge by addition of SDS. For loading, 10 µg total protein, adjusted with H<sub>2</sub>O, were mixed with 1x SDS-loading buffer (6x) and boiled at 95 °C for 5 min for denaturation. As a marker the PageRuler Prestained (ThermoFisher) was added, too. Initially, the SDS-PAGE starts with applying 100 V until the running front enters the separation gel. At this point, after roughly 10 minutes, the voltage was increased to 140 V. I stopped the electrophoretic separation when the running front ran out of the gel, or the desired separation was achieved.

### 5.6.10 Western and Lectin blot

The transfer of proteins from the SDS-PAGE gel onto a nitrocellulose membrane (GE Healthcare) was conducted by semi-dry Western blot. Due to the negative charge of the proteins in gel, the proteins move towards the anode onto the membrane, once voltage is applied. Preparation of the semi-dry Western blot required the stacking of:

#### *Anode*

- Three Whatman paper (soaked in anode buffer)
- One nitrocellulose membrane (soaked in cathode buffer)
  - One SDS-PAGE gel (soaked in cathode buffer)
- Three Whatmann paper (soaked in anode buffer)

#### *Cathode*

After closing the lid of the chamber, I performed the electrophoretic transfer at 47 mV per blot ( $1 \text{ mA/cm}^2$ ) for 50 minutes. To reduce and prevent unspecific binding of antibodies and lectins, the membrane was “blocked” with 5% milk powder (0.1 % PBS-T) and 0.5% TBS-T for 20 minutes, respectively. After rinsing the membrane with 0.1 % PBS-T and 0.1% TBS-T, primary antibodies (1:1,000 in 0.1 % PBS-T) and lectins (1:400 in 0.1% TBS-T) were applied and incubated over night at 4 °C. After incubation, I rinsed membranes 3x for 5 min in the corresponding buffer. The secondary HRP-couples antibody (1:10,000 in 0.1 % PBS-T) and HRP-coupled streptavidin (Vector Laboratories, SA5004) were applied to the membrane and incubated for 45 min at RT. Horseradish peroxidase (HRP) is used to visualize bound antibodies by a chemiluminescence reaction. The enhanced chemiluminescence reagent (ECL) plus Western blot substrate (ThermoFisher) serves as the substrate for the HRP. After applying the substrate, the membrane was incubated for 5 min at RT in the dark and then captured by using a chemiluminescence imaging system Fusion SL4 (PeqLab). Secondary antibodies can be detached from the membrane by applying 10 % acetic acid for 15 min. This procedure is called “stripping” and allows to use a second primary antibody as long as its Fc domain derives from another host compared to the first primary antibody. After incubation, I rinsed the membrane 3x with 0.1 % PBS-T for 5 min and the second primary antibody was applied to the membrane and incubated over night at 4 °C. From here, the procedure was identical to the prior handling.

As loading control  $\beta$ -ACTIN-HRP antibody (Proteintech, HRP-60008) was used. Regarding the nucleus isolation blots (see 5.6.11), KI67 (Proteintech, 27309-1-AP) and PMM2 (Proteintech, 10666-1-AP) were used as loading controls for the nucleus and cytosol, respectively.

### 5.6.11 Nuclei isolation

To investigate the nuclei abundance in regard of its cytoplasmic abundance, I isolated nuclei of fibroblasts by centrifugation steps. Cell pellets, obtained as described in 5.3.1, were resuspended in nucleus isolation buffer and lysed by sonification. Cell nuclei were separated from the remaining cell organelles and cytoplasm by centrifugation at 800 rcf for 10 min at 4 °C. Due to the high molecular mass of the nucleus, the nuclei formed a pellet, whereas other cell organelles as well as the cytoplasm remained in the supernatant. 75 µl PIM-supplemented RIPA buffer were added to the isolated cell nuclei and 200 µl to the cell organelle and cytoplasm containing supernatant. The structures were disrupted after 20 min incubation at 4 °C by pipetting through a 22G x 1 ½" safety needle. Purification from cell debris was performed by an additional centrifugation step at 18,000 rcf for 30 min at 4 °C. Quantification of total protein of isolated and lysed cell nuclei and the cytoplasm, including remaining cell organelles, were conducted as described in 5.6.8 and were loaded on SDS-PAGE for Western blot analysis as described in 5.6.9 and 5.6.10.

### 5.6.12 Quantification of cellular ROS

CellROX™ Deep Red is a fluorogenic probe to quantify cellular oxidative stress in cell cultures. In a non-oxidative environment, CellROX™ Deep Red is a non-fluorescent dye. In an oxidative environment, the probe binds to DNA, becomes fluorescent active and has an emission maximum at ~665 nm. The level on fluorescence intensity corresponds with the level of reactive oxygen species (ROS) – the higher the CellROX™ signal, the higher the amount of ROS in the cell. I seeded fibroblasts in T25-Flasks and let them grow to a confluency of 80 - 100 %. At this confluency, I discarded the media and washed cells with PBS before incubation with 5 µM CellROX™ Deep Red diluted in complete DMEM medium for 30 min at 37 °C. Cells were washed with PBS, trypsinized as described in 5.3.1, pelleted by centrifugation at 400 rcf for 5 min, and resuspended in 100 µl FACS buffer. I quantified the CellROX™ Deep Red signal using the FACS verse cytometer (BD Biosciences) for flow cytometry with the assistance of Dr. Josephine Bock from the AG Leuschner (Klinikum Heidelberg). Analysis of obtained results and gating was achieved by using FlowJo\_v10.6.1. Gating focused on single cells and excluded all cell debris and cell accumulations.

### 5.6.13 Glutathione assay

Total glutathione was quantified to investigate the downstream effects of the *Nrf2* pathway, the major player for antioxidative responds. Glutathione is a major antioxidant by scavenging ROS and its regulation is therefore crucial for cell survival [116]. Quantification was achieved by using the GSH/GSSG-Glo™ Assay Kit (Promega). I plated fibroblasts were plated in triplicate into a black 96-well cell culture microplate (Greiner) and cultured until they reached 80 - 100% confluency. Cells were lysed and prepared in each well according to the manufacturer's

protocol. For normalization, I stained cell nuclei with NucBlue™ Live ReadyProbes™ reagent. For this reason, I seeded technical replica alongside with the samples for the glutathione assay as described previously. Luminescence and NucBlue™ fluorescence signals were measured using the Spark® Microplate Reader (Tecan). The luminescence signal correlates with the amount of total glutathione present in cells and NucBlue™ fluorescence to cell number.

#### 5.6.14 Immunofluorescence microscopy

Immunofluorescence staining was conducted to visualize specific proteins within cells, allowing the determination of their intracellular localization and abundance by semi-quantification. I seeded fibroblasts (30,000 cells per well) onto coverslips in a 24-well plate and incubated overnight to adhere. The next day, I rinsed cells with ice-cold PBS. All following steps were performed at RT, stated otherwise. Fixation was performed with 4% paraformaldehyde (PFA) in PBS for 20 minutes at RT, followed by permeabilization with 0.5% Triton X-100 in PBS for 10 minutes at RT to facilitate antibody penetration. To minimize nonspecific antibody binding, cells were blocked for 1 hour with 5% bovine serum albumin (BSA) in PBS. Primary antibodies, diluted 1:400 in 1% BSA, were applied to the cells and incubated for 1 hour at 37°C, followed by three washes with PBS. Secondary antibodies conjugated to fluorescent markers were diluted 1:700 in 1% BSA and incubated with the cells for 30 minutes at 37°C. The cells were rinsed three times. During the second washing step, I supplemented PBS with NucBlue™ Live ReadyProbes™ reagent (Invitrogen, ThermoFisher) for nuclear staining. The cells were mounted using Fluoromount™ (Sigma-Aldrich) on microscope slides and stored overnight before imaging with a fluorescence microscope. Prepared slides were stored protected from light at 4°C to preserve fluorescence.

The abundance of KEAP1 in the nucleus was semi-quantified using ImageJ. Here, the nucleus was first isolated by masking the NucBlue™. In this mask, the maxima which correlate to accumulations of KEAP1, were counted by using “Find maxima” and use of a prominence >10.

#### 5.6.15 Lipidomic analysis

Quantification of cholesterol in lysates of SRD5A3-CDG patient-derived fibroblasts and controls was performed in the laboratory of Prof. Dr. Britta Brügger (Biochemistry Center of Heidelberg University). The quantification was performed according to Liebsch *et al* [117], and Özbacı *et al* [118] and is based on the Nanoelectrospray Ionization Tandem Mass Spectrometry (ESI-MS/MS).

#### 5.6.16 “Shotgun-“proteomic analysis

Potential deregulated protein levels in patient cells were validated by performing an untargeted 'shotgun' proteomics analysis`. The analysis was conducted by Dr. Andreas Harst from the AG



of Dr. Thomas Ruppert from the Core Facility for Mass Spectrometry and Proteomics at the Centre for Molecular Biology, University of Heidelberg. I seeded three confluent T75 flasks of both patient and control cells were harvested and pelleted, from which proteins were isolated using a chloroform-methanol precipitation method. The analysis was carried out using liquid chromatography coupled with an Orbitrap QE HF (Thermo Fisher) mass spectrometer (LC-MS/MS). For the duplicates, mean values were calculated. The peptide values detected in the patient cells were compared to those of the control cells.

### 5.6.17 N-Glycomic analysis

N-Glycomic analysis was performed in the laboratory of Dr. Erdmann Rapp at the Bio/Process Analytics Team, (BPE), Max Planck Institute for Dynamics of Complex Technical Systems in Magdeburg by Ivan Andújar Martínez and Robert Burock. The following protocol was adapted from Ivan Andújar Martínez's provided protocol.

Hatchlings (5 days post hatch) of *Oryzias latipes* (medaka) were used as biological samples. Four groups were analyzed: 2x wildtype-precipitated and 2x SRD5A3-KO1-precipitated proteomes. Each group of 10 hatchlings was processed individually. Lysis was carried out by adding 500 µL of lysis buffer, consisting of 10.5 mL UPX Protein Extraction buffer (abcam, ab270054) supplemented with one tablet of cComplete™ EDTA-free Protease Inhibitor Cocktail (Roche, 1183617001). Tissue homogenization was performed using a Branson Sonifier in pulse mode at 30% amplitude for 1 minute on ice. Samples were heat denaturated at 100°C for 10 minutes, followed by centrifugation at 15,000 × g for 10 minutes. The supernatants were transferred to fresh 1.5 mL tubes.

Protein concentrations were estimated using the bicinchoninic acid (BCA) assay (Thermo Fisher Scientific) in triplicates. The protein quantification assay was performed by preparing triplicate dilutions, starting with a 1/4 dilution of the samples to ensure a final tris(2-carboxyethyl)phosphine hydrochloride (TCEP) concentration of 6.25 mM, as BCA quantification allows up to 10 mM TCEP hydrochloride (UPX buffer contains 25 mM) and following the manufacturer's protocol (ThermoFisher Scientific). The incubator was preheated to 37 °C. Subsequently, 25 µL of each dilution was pipetted into the corresponding wells of a microplate. The BCA working reagent was prepared by mixing Reagent A and Reagent B in a 49:1 ratio. Each well of a 96-well microplate was loaded with 25 µL of sample dilution and 200 µL of working reagent. Plates were incubated at 37°C for 30 minutes with agitation at 300 rpm, cooled to room temperature, and absorbance was measured at 562 nm.

Proteins were purified using the methanol/chloroform precipitation method described by Wessel and Flügge (1984) [119]. 100 µg of protein per sample was used. Four volumes of methanol, leading to a final concentration of 80%, were added and centrifuged at 9,000 rpm

for 1 minute. Then, 100  $\mu$ L chloroform was added, followed by further centrifugation. After adding 300  $\mu$ L MilliQ water, centrifugation was repeated and the upper phase was removed. Subsequently, 300  $\mu$ L of methanol was added and the mixture was centrifuged for 2 min. The supernatant was removed, and the protein pellet was dried and stored until further use. Protein pellets (~50 - 60  $\mu$ g) were resuspended in 200  $\mu$ L 8 M urea (0.1 M Tris-HCl, pH 8.5). The Nanosep centrifugal filter unit (10K Omega membrane, Pall Corporation) was then rinsed by adding 50  $\mu$ L of urea buffer and centrifuging at  $14,000 \times g$  for 5 minutes at RT. Then, 200  $\mu$ L of the reconstituted protein pellet was added, followed by vortexing and incubation for 5 minutes in a thermomixer. The protein solution was centrifuged at  $14,000 \times g$  for 5 minutes at RT and the flow-through was discarded.

By adding 100  $\mu$ L 40 mM dithiothreitol (DDT) to the filter unit disulfide bonds were reduced. Here, the filter unit was mixed for 1 min at 600 rpm using a thermomixer at RT and incubated at 56 °C for 20 min with gentle agitation (300 rpm). Filters were centrifuged ( $14,000 \times g$ , 10 minutes, RT) and 100  $\mu$ L 55 mM iodoacetamide (IAA) was added, mixed for 1 min at 600 rpm using a thermomixer at RT, and 20 minutes incubated in the dark. The filter unit was centrifuged at  $14,000 \times g$  for 10 minutes at RT and the flow-through was discarded. Next, the filter unit was rinsed three times with 100  $\mu$ L of urea buffer. For each step, the buffer incubated for 1 min at RT at 600 rpm, centrifuged for 10 min and the flow-through was discarded. This rinsing process was repeated three times with 100  $\mu$ L of 1x ammonium bicarbonate (ABC) buffer (50 mM). Enzyme solution leakage during digestion was prevented by cutting the filter tube cap and retaining to seal the filter unit. The filter was then transferred to a new 2 ml tube.

For digestion, trypsin (Promega) was prepared in ABC buffer with 5% acetonitrile and 1 mM  $\text{CaCl}_2$ , at a 1:100 enzyme-to-substrate ratio. The solution was then added to the filter unit, mixed for 1 min at 600 rpm using a thermomixer, and incubated at 37 °C overnight with gentle agitation (350 rpm). The next day, the filter unit was centrifuged at  $8,000 \times g$  for 7 min at RT. Additional rinsing was performed by adding 50  $\mu$ L digestion buffer (50 mM ABC buffer with 5 % ACN) and 50  $\mu$ L of MilliQ water. Each step, the filter unit was centrifuged at  $8,000 \times g$  for 7 minutes, retaining the flow-through. Digest was dried in a SpeedVac and stored at -20 °C until use. For glycan analysis, digests were reconstituted in 5%  $\text{ACN}_{\text{aq}}$  to a final concentration of 1  $\mu$ g/ $\mu$ L. 25  $\mu$ g of each sample was used for *N*-glycan release.

*N*-glycans were prepared and analyzed as described by Hennig et al. (2015, 2016), [120, 121] with modifications. Dried digests were resuspended in 2  $\mu$ L 1X PBS and 4  $\mu$ L 2% SDS in PBS, followed by mixing, centrifugation, and incubation at 60°C for 10 minutes. After incubation, 4  $\mu$ L 8% IGEPAL (Sigma-Aldrich) in PBS was added to each sample, mixed, and centrifuged. *N*-glycans were enzymatically released via PNGase F (Sigma-Aldrich) digestion at 37°C for 12 hours. Released glycans were fluorescently labeled with 8-aminopyrene-1,3,6-trisulfonic acid

(APTS, Synchem) using reduX (glyXera) as a reducing agent. Excess label and contaminants were removed by hydrophilic interaction liquid chromatography-solid phase extraction (HILIC-SPE).

Labeled *N*-glycans were analyzed using multiplexed capillary gel electrophoresis with laser-induced fluorescence detection (xCGE-LIF), using the glycoanalysis system glyXboxCE [glyXera; incl. 4-capillary xCGE-LIF instrument, software (glyXtoolCE v6.1.0) and database (glyXbaseCE)]. Electropherogram data were aligned to an orthogonal internal standard (GeneScan™ 500 LIZ Size Standard, Thermo Fisher Scientific & glyXalign GA2; glyXera) using glyXalign GA2 software to generate reproducible *N*-glycan fingerprints. Subsequently, glyXtoolCE was utilized for automated peak picking, integration, and relative quantification, as well as for the structural assignment of the *N*-glycan peaks by migration time matching to the *N*-glycan database glyXbaseCE.

Symbolic representation of *N*-glycans was created using GlycoWorkbench in accordance with the guidelines of the Consortium for Functional Glycomics [122, 123].

## 5.7 Transcriptomic analysis

### 5.7.1 Quantitative Real Time PCR analysis

Quantitative Real Time PCR (qRT-PCR) analysis can be used to investigate and semi-quantify the expression of genes on mRNA level. Generation of cDNA, suitable for qRT-PCR, was achieved by using 1 µg total RNA and the RevertAid First Strand cDNA Synthesis Kit (ThermoFisher), using random primers. cDNA conversion was accomplished according to the manufacture's protocol. After cDNA generation, I diluted all samples to 25 ng/µl with RNase free H<sub>2</sub>O, assuming all RNA is converted into cDNA and stored at -80 °C.

The fluorescent dye SYBR Green (PerfeCTa® SYBR® Green FastMix®, Quantabio) was used to semi-quantify the amount of a specific transcript in qRT-PCR. This dye binds to the double-stranded DNA fragments formed during the PCR reaction. The fluorescence of the sample was measured after each PCR cycle, resulting in a corresponding fluorescence signal with each cycle. The point at which a predefined threshold is reached is recorded as the "Ct value". The more initial transcripts present in the sample, the faster the threshold is reached, leading to a lower Ct value.

I performed qRT-PCR measurements in technical triplicates. To normalize the data, the expression of the reference gene *β-actin* was also measured in triplicate for each sample. As a control, the qRT-PCR master mix was tested three times with water (H<sub>2</sub>O) instead of cDNA to rule out contamination with DNA.

**Table 14: qRT-PCR mix and qRT-PCR protocol.**

Compound	Volume
PerfeCTa SYBR Green FastMix (2x)	5 µl
Primer forward/ reverse (10 µM)	Each 0.2 µl
cDNA (25 ng/µl)	1 µl
RNAse free H <sub>2</sub> O	3.6 µl

Step	Temperature [°C]	Duration	Cycle
Initial denaturation	95 °C	30 sec	-
Denaturation	95 °C	4 sec	x40
Annealing	55 °C	15 sec	
Extension	70 °C	10 sec	

Semi-quantification was carried out, based on the  $\Delta\Delta C_t$  value. This value describes the expression of a specific gene relative to the expression of the reference gene (here: *β-actin*), normalized to the expression in the control sample. This allows to determine the fold-change in the expression of the gene of interest (GOI) in the sample compared to the control according to the formula, which was established by Dr. Kristina Falkenstein:

$$\text{Fold change} = 2^{-\Delta\Delta C_t} = 2^{-((C_{tGOI}-C_{t\beta ACTIN})_{\text{Sample}} - (C_{tGOI}-C_{t\beta ACTIN})_{\text{Control}})}$$

### 5.7.2 nCounter analysis

nCounter analysis is a technique which can be used to quantify the native amount of mRNA. This is achieved by using a capture probe which is designed to a specific mRNA. This complex is then binding to a specific probe with a unique fluorescence tag. The whole complex, once formed, is immobilized and the fluorescence tags are automatically read out. One specific fluorescence tag is therefore corresponding to one specific mRNA – without any enzymatic reactions, making this method very precise.

I obtained 50 ng total RNA from fibroblast cell pellets as described in 5.6.1 and shipped to Ralph Röth (nCounter Core Facility at the Institute for Human Genetics of the University Heidelberg) who conducted the nCounter analysis. In total, the expression of 190 targeted genes were quantified, 6 genes (*ACTB*, *C1ord43*, *GAPDH*, *RAB7A*, *SNRPD3*, *ACADL*) were used as housekeeping genes as controls and for normalization. Among the 190 genes, genes were selected which play key roles in the following pathways: Glycosylation, mevalonate pathway, cholesterol/ steroid metabolism, oxidative/ cellular stress related pathways,

GPI-anchor biosynthesis. Values were normalized by using housekeeping gene's expression and a multiple Mann-Whitney test was used.

### 5.7.3 Transcriptome analyses

I obtained biological triplets of total RNA from fibroblast cell pellets as described in 5.6.1. The concentration of total RNA was minimum > 4 ng/μl. cDNA library preparation and sequencing were conducted by the Beijing Genomics Institute (BGI) using the DNBSEQ-G400 platform. Initial bioinformatics processing, including data analysis and statistical evaluations, followed BGI's established protocols. The sequencing data achieved an average mapping rate of 93.35% to the reference genome (GRCh38.p13), identifying 17,475 genes, with an average gene-specific mapping rate of 82.07%. Results were provided on Dr. Tom by BGI (<https://biosys.bgi.com/#/report/login>).

### 5.8 Statistic

I usually conducted experiments in triplicates to increase its informative value and show reproducibility. The statistical test is stated for each experiment individually, due to the experimental design. Significance is assumed to be a *P*-values < 0.05. Different levels of significance are indicated by stars:  $p \leq 0,05$  \*,  $p \leq 0,01$  \*\*,  $p \leq 0,001$  \*\*\*,  $p \leq 0,0001$  \*\*\*\*.

### 5.9 Use of artificial intelligence

I partially used ChatGPT (OpenAI) for writing purposes only. This ensured a more sophisticated language and better structure to improve the scientific writing quality. No data analysis or hypothetical ideas were done or generated with the help of ChatGPT.

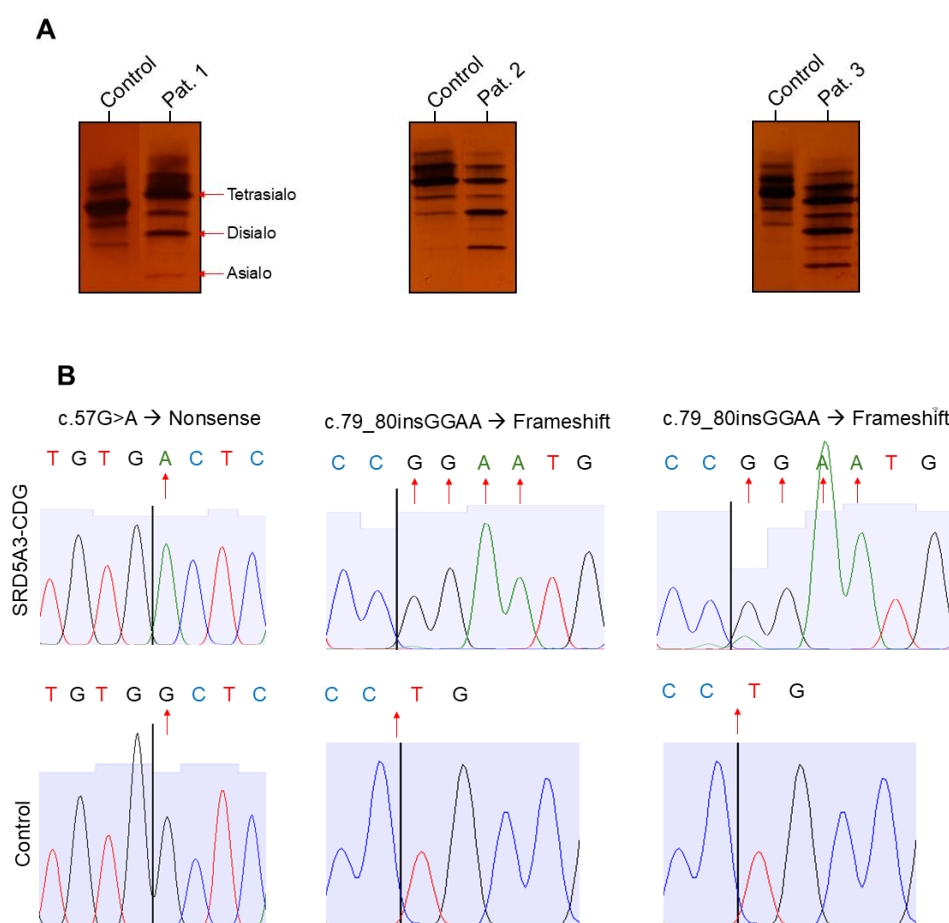
## 6. Results

### 6.1 Validation of SRD5A3-CDG in sera and patient-derived fibroblasts

#### 6.1.1 Isoelectric focussing and genomic analysis

Isoelectric focussing (IEF) of serum transferrin still displays the worldwide gold standard in CDG diagnostics for identifying *N*-glycosylation defects and differentiate between early (CDG type-I) and late (type-II) glycosylation deficiencies. IEF of sera of the three SRD5A3-CDG patients revealed a CDG-I pattern, characterized by elevated di- and asialotransferrin bands in comparison to the controls which showed physiologically primarily strong tetrasialo band (Fig. 6A).

I used fibroblasts from these three SRD5A3-CDG patients for diagnosis. Sanger sequencing revealed biallelic variants in the *SRD5A3* gene. Pat. 1 inherited a homozygotic c.57G>A nonsense variation, Pat. 2 and 3 inherited homozygotic c.79\_80insGGAA frameshift variation (Fig. 6B).



### **Figure 6: Isoelectric focussing of serum transferrin from SRD5A3-CDG patients and Sanger sequencing of exon 1 of the *SRD5A3* gene in fibroblasts**

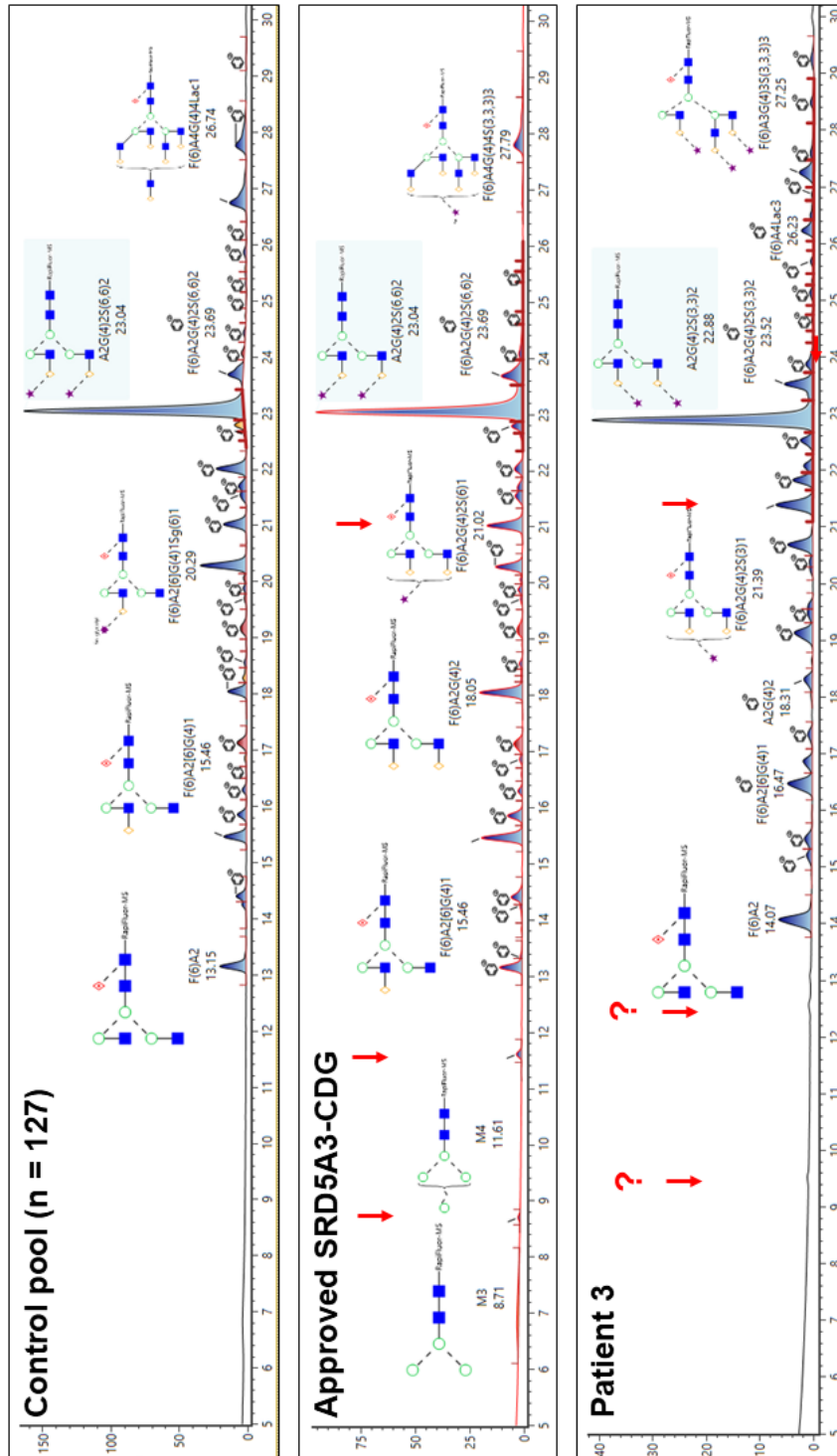
(A) Isoelectric focussing of transferrin from SRD5A3-CDG patients and controls showing elevated di- and asialo transferrin with reduced amounts of tetrasialo transferrin bands in parallel in case of the patients. Red arrow, Tetra-, Di, and Asialo band. (B) Genetic variants in the SRD5A3-CDG patient-derived fibroblasts were verified by Sanger sequencing of exon 1. Red arrows indicate the genetic variant. A, adenine; T, thymine; C, cytosine; G, guanine.

In addition, maintaining and growth of cell cultured fibroblasts derived from the three SRD5A3-CDG patients revealed dysfunctions. All three cell lines had lower proliferation, were more easily stressed by trypsination and stopped growing at an earlier passage compared to healthy control cell lines.

#### **6.1.2 *N*-glycan analysis of whole sera by mass spectrometry and Lipid-linked oligosaccharide validation**

The *N*-glycan analysis of whole sera was performed on a LC-MS system (UPLC mit FLR-Detektor) and showed elevated Man3 (M3) and Man4 (M4) peaks in case of patients 1 and 2. Both elevations could clearly be seen in the positive but not in the healthy control, as expected. However, analysis of *N*-glycans of SRD5A3-CDG patient 3 did not represent clear elevations of the M3 and M4 peaks as indicated by question marks in figure 7. Instead, only very slight peaks could be detected at the expected retention time around 9 and 12 minutes, respectively. Furthermore, an elevation of the F(6)A2G(4)2S(3)1 peak could be detected in SRD5A3-CDG patient 3 as well as in the positive control in comparison to the healthy control pool. (Fig. 7).

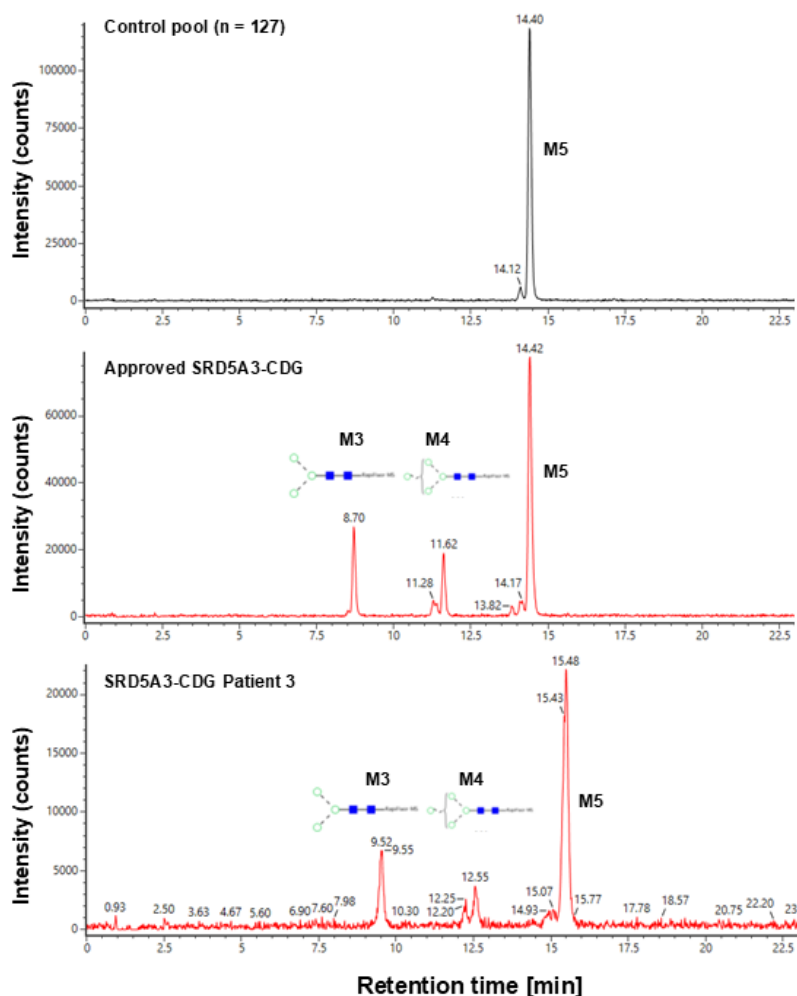
To further clarify and validate the SRD5A3-CDG associated hypoglycosylation phenotype *N*-glycans were separated by their mass in the BioAccord LC-MS system. In this analysis elevated M3 and M4 peaks were clearly detectable in the positive control as well as in SRD5A3-CDG patient 3. In the healthy control only a strong M5 peak used as internal standard could be detected (Fig. 8).



**Figure 7: Whole serum N-glycan analysis by LC-MS (fluorescence) reveals no unique increase of the SRD5A3-CDG typical M3 and M4 in SRD5A3-CDG patient 3 serum.**

Mass spectrometric analysis of whole serum N-glycans by BioAccord LC-MS Systems (Waters) after fluorescence labelling. The control pool consists of whole serum samples from 127 healthy controls. Red arrow, M3, M5 and F(6)A2G(4)2S(3)1 peak, respectively according to increased retention time; question mark, missing or small peak of M3 and M5 in SRD5A3-CDG patient 3 samples.

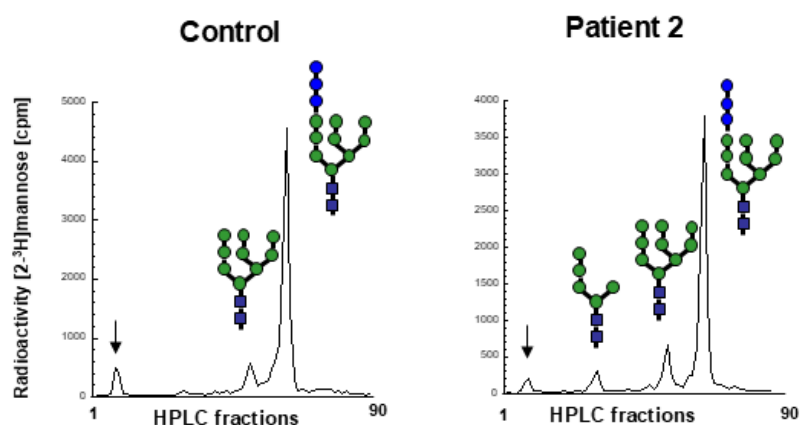




**Figure 8: Increased relative M3 and M4 peaks in SRD5A3-CDG patient 3 according to whole serum *N*-glycan analysis by LC-MS (Mass).**

Mass spectrometric analysis of whole serum *N*-glycans by BioAccord LC-MS Systems (Waters) showed elevated M3 (C<sub>51</sub>H<sub>85</sub>N<sub>7</sub>O<sub>27</sub>, *m/z* 611.7585) and M4 (C<sub>57</sub>H<sub>89</sub>N<sub>7</sub>O<sub>32</sub>, *m/z* 692.78488) in case of the approved SRD5A3 patient and patient 3. M5 (C<sub>63</sub>H<sub>89</sub>N<sub>7</sub>O<sub>37</sub>, *m/z* 773.8113) was used as internal control. The control pool consists of serum samples from 127 healthy controls.

Furthermore, LLO analysis after metabolic labelling with [2-<sup>3</sup>H]mannose of control and patient-derived fibroblasts was carried out. Pat. 2 showed a borderline abnormal LLO pattern, marked by an accumulation of intermediate oligosaccharide structures: Man5GlcNAc2-PP- and Man9GlcNAc2-PP-dolichol presumably due to shortage of dolichol as lipid component in Dol-P-Man and Dol-P-Glc synthesis. Incorporation of total [2-<sup>3</sup>H]mannose into dolichol-bound sugar structures was found to be at levels similar to the control (Fig. 9).

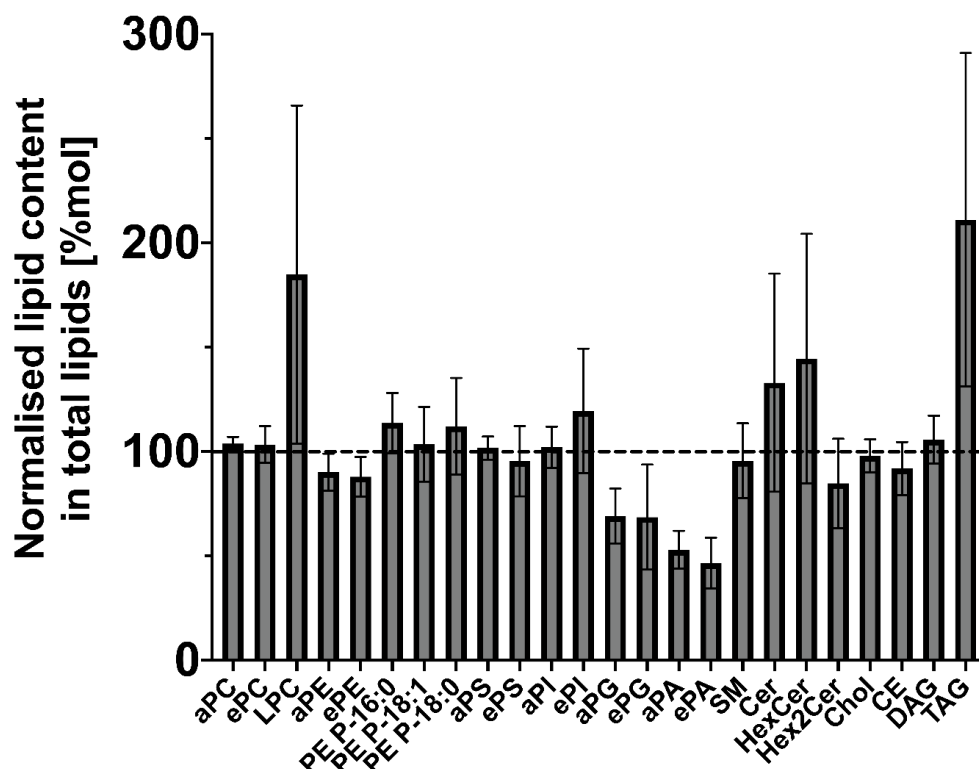


**Figure 9: Lipid-linked oligosaccharide analysis of SRD5A3-CDG patient-derived fibroblasts.**

Fibroblasts from a healthy control and SRD5A3-CDG patient 2 were labelled metabolically with [2-<sup>3</sup>H]mannose for 30 min. [<sup>3</sup>H]oligosaccharides were released from dolichol through mild acid hydrolysis and then separated by size using HPLC (fractionated). Shown sugar trees represent the positions of Glc<sub>3</sub>Man<sub>9</sub>GlcNAc<sub>2</sub>, Man<sub>5</sub>GlcNAc<sub>2</sub>, and Man<sub>9</sub>GlcNAc<sub>2</sub> standards, respectively. The initial peaks in both samples (grey arrow) reflect a small amount of free [2-<sup>3</sup>H]mannose, which was used for labelling but escaped the purification procedure.

### 6.1.2 Lipidomics

Characterisation of the SRD5A3-CDG patient derived fibroblasts included analysis and quantification of lipids by mass spectrometry in total lysates. The amount of most lipids was similar compared to controls. However, some lipid classes showed alterations: Lysophosphatidylcholine (LPC) and triacylglycerol (TAG) did reveal increased amounts with 184.85 % (SD: ±80.97) and 211.11 % (SD: ±79.85), respectively. In contrast, the relative amount of phosphatidylglycerol (a/ePG) and alkylphosphatidic acid (a/ePA) were strongly decreased with 69.1 % (SD: ±13.08), 68.61 % (SD: ±25.14), 52.99 % (SD: ± 9.09) and 46.61 % (SD: ±12.12), respectively (Fig. 10, Tab. 15).



**Figure 10: Mass spectrometric based lipidomic analysis of various lipid classes.**

Mass spectrometry analysis of a various lipid classes in SRD5A3-CDG patient derived fibroblasts (n = 3) compared to healthy controls (n = 2). The amount of phosphatidic acid (PA), phosphatidylcholine (PC), some glycerophospholipids (lysophosphatidylcholine (LPC)), phosphatidylethanolamine (PE), phosphatidylethanolamine plasmalogen (PE P-), phosphatidylserine (PS), phosphatidylinositol (PI), phosphatidylglycerol (PG), alkylphosphatidic acid (PA), sphingomyelin (SM), ceramides (Cer), hexosylceramide (HexCer, Hex2Cer), cholesterol (Chol), cholesteryl ester (CE), glycerolipids diacylglycerol (DAG), as well as triacylglycerol (TAG) were quantified. The measured amount of each lipid in the patient cells was normalized to the control value. aX, alkyl ether form of the lipid; eX, ether form of the lipid. Data produced jointly with the laboratory of Prof. Dr. Britta Brügger from the Heidelberg University Biochemistry Center.

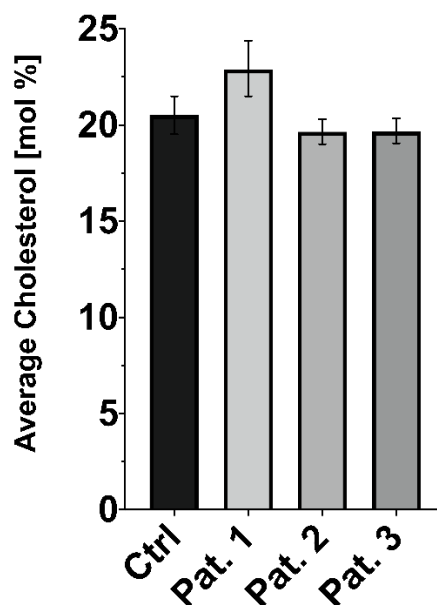
**Table 15: Values of Mass spectrometric based lipidomic analysis of various lipid classes.**

Corresponding values of Mass spectrometry analysis of a various lipid classes in SRD5A3-CDG patient derived fibroblasts (n = 3) compared to healthy controls (n = 2). Amounts of lipids were quantified. The measured amount of each lipid in the patient cells was normalized to the control value. aX, alkyl ether form of the lipid; eX, ether form of the lipid. Data produced jointly with the laboratory of Prof. Dr. Britta Brügger from the Heidelberg University Biochemistry Center.

Lipid class	Normalised amount [%]
aPC	103.8391558
ePC	103.429957
LPC	184.852231
aPE	90.1985891
ePE	87.9693468
PE P-16:0	113.698068
PE P-18:1	103.56847
PE P-18:0	112.106843
aPS	101.732167
ePS	95.423845
aPI	102.111601
ePI	119.483584
aPG	69.0955407
ePG	68.6083086
aPA	52.9876295
ePA	46.6082472
SM	95.6028644
Cer	133.013671
HexCer	144.559706
Hex2Cer	84.7668622
Chol	97.9277827
CE	91.9166785
DAG	105.682697
TAG	211.110363

Transcript analysis by nCounter revealed decreased gene expression of genes involved in the cholesterol biosynthesis: *C14Orf1* or *ERG28*, *DHCR24*, *DHCR7*, *FDFT1*, and *FGFR1* (Fig. 12, Tab. 15). Due to the genetic downregulation a decrease of cholesterol amount was expected. Still, lipidomic analysis revealed physiological levels of cholesterol compared to healthy control cell lines. The average mole was 22.9 % (SD:  $\pm 1.45$ ), 19.65 % (SD:  $\pm 0.63$ ), and 19.68 % (SD:  $\pm 0.58$ ) in Pat. 1 - 3, respectively, compared to 20.525 % (SD:  $\pm 1.01$ ) in control (Fig. 11).

In conclusion, although transcriptomic analysis revealed downregulation of cholesterol biosynthesis related genes (*C14Orf1* or *ERG28*, *DHCR24*, *DHCR7*, *FDFT1*, and *FGFR1*), mass spectrometric analysis showed no significant alteration and decrease of cholesterol levels. In contrast, the lipid classes LPC and TAG did reveal increased amounts while the relative amount of a/ePG and a/ePA were strongly decreased.

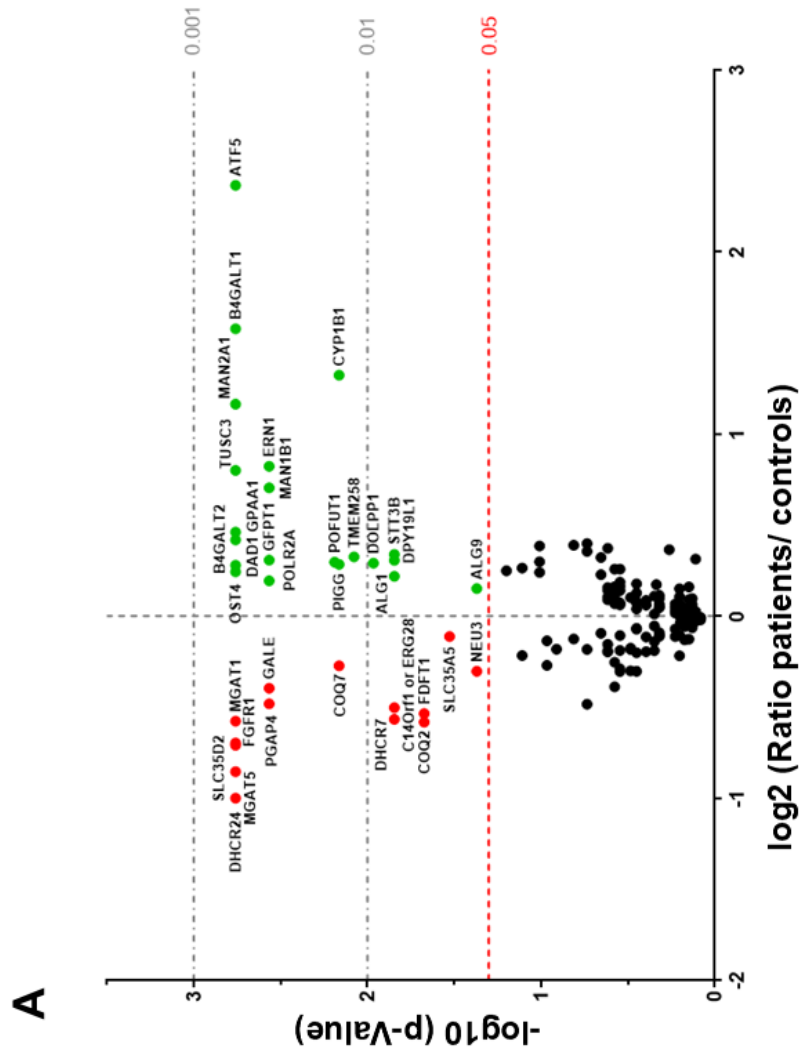


**Figure 11: Physiological levels of cholesterol in SRD5A3-CDG patient-derived fibroblasts.**

Mass spectrometric analysis for the quantification of cholesterol in SRD5A3-CDG patient-derived fibroblast (n = 3) and control (n = 2) lysates. The values are given as average mole in percentage, indicating the percentage of cholesterol of the total lipid composition. Data produced jointly with the laboratory of Prof. Dr. Britta Brügger from the Heidelberg University Biochemistry Center.

## **6.2 Elevated expression of *CYP1B1* in SRD5A3-CDG patient-derived fibroblasts on transcript level**

Gene regulation of 190 genes, including genes involved in glycosylation (N- and O-glycosylation, O-GlcNAcylation and O- and C-mannosylation), mevalonate pathway, cholesterol/ steroid metabolism, oxidative/ cellular stress related pathways, GPI-anchor biosynthesis, were investigated to gain a precise overview of possible deregulated pathways in SRD5A3-CDG fibroblasts. Transcripts of 156 of the total 190 targeted genes could be found across all samples, including the 6 house-keeping genes. The remaining 34 gene transcripts were not consistently detectable across all samples and were therefore excluded from the analysis. From these 156 gene transcripts, 34 genes showed a significant differential expression compared to controls (see Fig. 12 and Tab. 16). Non-significant deregulated gene expressions can be found in the supplementary information (Fig. S1).



**Figure 12: Deregulated gene expression in SRD5A3-CDG patient-derived fibroblasts.**

(A) The expression of 190 genes was quantified using nCounter analysis based on transcript quantity in SRD5A3-CDG patient-derived fibroblasts ( $n = 3$ ) and controls ( $n = 5$ ). The  $-\log_{10}(P\text{-value})$  is plotted against the ratio of transcript quantity in patient versus control samples on a  $\log_2$  scale. The line at  $x = 0$  represents the expression in control samples. The red line corresponds to the significance threshold of  $p = 0.05$ . Black points represent genes with insignificant expression in patient cells, while red points indicate genes with significantly decreased transcript levels in patient cells. Green points represent genes with significantly increased transcript levels. Data produced jointly with the nCounter Core Facility of the Heidelberg University Hospital.

## Results

**Table 16: Significantly deregulated expression of genes in SRD5A3-CDG patient-derived fibroblasts.**

Blue, related to glycosylation; red, related to (oxidative) stress response; green, related to cholesterol, steroid hormones and lipid metabolism; brown, related to GPI-anchor biosynthesis. Data produced jointly with the nCounter Core Facility of the Heidelberg University Hospital.

Gene	P-value	Q-value	Log2 ratio (Patients/ Ctrl)
ALG1	0.003322	0.0143	1.27906339
ATF5	0.000175	0.001737	1.5849625
B4GALT1	0.000175	0.001737	1.5849625
B4GALT2	0.000175	0.001737	1.5849625
C14Orf1 or ERG28	0.003322	0.0143	-1.14536641
COQ2	0.005245	0.021168	-1.09911131
COQ7	0.001224	0.006872	-1.23696542
CYP1B1	0.001224	0.006872	1.39775166
DAD1	0.000175	0.001737	1.5849625
DHCR24	0.000175	0.001737	-1.37851162
DHCR7	0.003322	0.0143	-1.14536641
DOLPP1	0.002098	0.010838	1.33855967
DPY19L1	0.003322	0.0143	1.27906339
ERN1	0.0004	0.002716	1.6520767
FDFT1	0.005245	0.021168	-1.09911131
FGFR1	0.000175	0.001737	-1.37851162
GALE	0.0004	0.002716	-1.32192809
GFPT1	0.00035	0.002716	1.52100099
GPAA1	0.000175	0.001737	1.5849625
MAN1B1	0.0004	0.002716	1.6520767
MAN2A1	0.000175	0.001737	1.5849625
MGAT1	0.000175	0.001737	-1.37851162
MGAT5	0.000175	0.001737	-1.37851162
NEU3	0.011538	0.042577	-1.01000943
OST4	0.000175	0.001737	1.5849625
PGAP4	0.00035	0.002716	-1.33121315
PIGG	0.001224	0.006872	1.39775166
POFUT1	0.000999	0.006451	1.73696559
POLR2A	0.00035	0.002716	1.52100099
SLC35A5	0.007592	0.029714	-1.07068606
SLC35D2	0.000175	0.001737	-1.37851162
STT3B	0.003322	0.0143	1.27906339
TMEM258	0.001554	0.008362	1.66296501
TUSC3	0.000175	0.001737	1.5849625

Among the significantly deregulated genes, several genes involved in all targeted pathways (Tab. 15; blue marked) were found, e.g. 21 genes involved in the different glycosylation pathways. Interestingly, although SRD5A3-CDG displays an early defect in *N*-glycosylation,

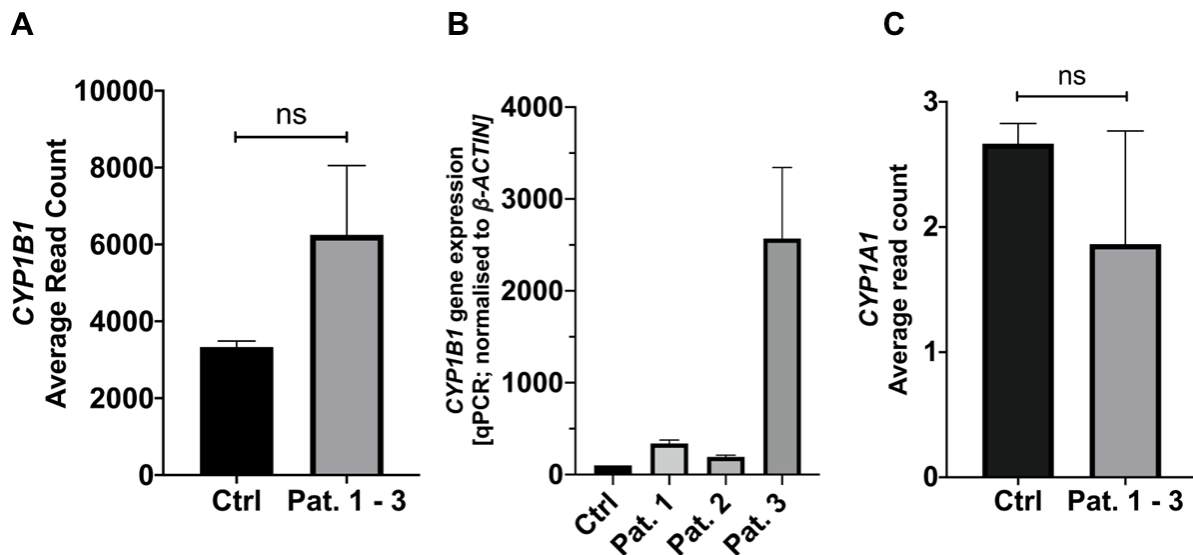
also genes involved in late glycosylation processes were dysregulated, such as *B4GALT1/2*, *MAN2A1*, *MGAT1*, *MGAT5*, *SLC35A5*, *SLC35D2* and *STT3B*. In contrast, genes directly associated with the mevalonate pathway in the context of dolichol biosynthesis, including *SRD5A3*, showed no significant deregulation – except of *DOLPP1* which exhibited an elevated expression.

Since dolichol and cholesterol rely on the same precursor molecule, farnesyl-PP, cholesterol/sterol-related genes were targeted and *C14Orf1* or *ERG28*, *DHCR24*, *DHCR7*, *FDFT1*, *FGFR1* and *CYP1B1* were found being significantly deregulated in SRD5A3-CDG fibroblasts. Except *CYP1B1*, those genes exhibited a decreased expression. In contrast, the expression of *CYP1B1* was highly elevated by a 2.5-fold increase (Ratio (Log2): +1.39775166; *P*-value: 0.001224, *Q*-value: 0.006872) and therefore inhibited a special status among those genes. In its function it also plays an interdisciplinary role: It does not only play a role in the metabolism of cholesterol and steroid hormones but is also associated with oxidative stress. *ATF5*, known to be a sensor for cellular stress, exhibited an elevated expression, just as *CYP1B1*.

Since ophthalmological abnormalities are a key diagnostic feature in SRD5A3-CDG and the development of the eye also depend on *CYP1B1* among others, the results of the nCounter analysis regarding the *CYP1B1* expression were further validated by transcriptome analysis and qRT-PCR. Transcriptome analysis identified in total 17,475 genes, with an average gene-specific mapping rate of 82.07%. 2,193 transcripts were found to be significantly upregulated and 2,437 were significantly downregulated in SRD5A3-patient derived fibroblasts compared to control. Elevated expression of *CYP1B1* could be verified by both techniques. Regarding *CYP1B1*, transcriptome analysis revealed an increased average read counts (ARC) of 7137.02 to 3772.61 (*P*-value = 0.064048756, *Q*-value = 0.21150187) compared to controls. In addition, the qRT-PCR analysis showed an elevated expression in Pat. 1 - 3 of +239 % (SD: ±37;), +93 % (SD: ±18), and +2470 % (SD: ±773), respectively (Fig. 14A,B). Gene expression of *CYP1B1* and *CYP1A1* are both mainly controlled through the AhR signalling pathway. Surprisingly, although *CYP1B1* was highly expressed, *CYP1A1* was expressed comparable to control at a low basal level of only 2.35 vs. 1.66 ARC (*P*-value: 0.69711087; *Q*-value: 0.90244298) (Fig. 14C).

To sum up, different transcript analysis revealed an elevated *CYP1B1* expression in SRD5A3-CDG patient-derived fibroblasts. In addition, also gene transcripts regarding glycosylation, (oxidative) stress response, steroid hormones, lipid metabolism, and GPI-anchor biosynthesis were deregulated.



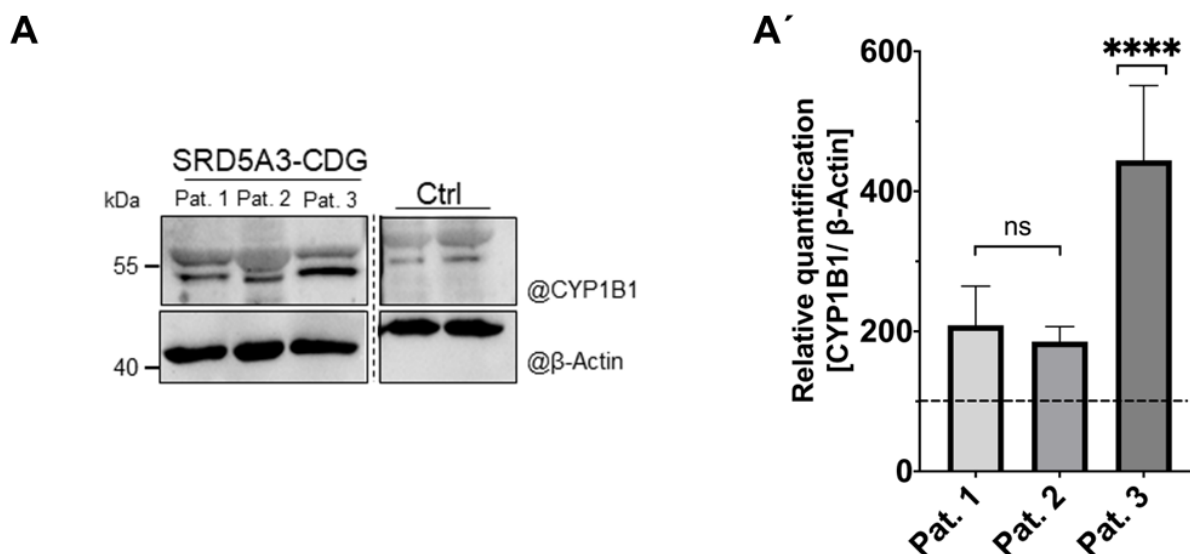


**Figure 14: Elevated expression of *CYP1B1* and physiological expression of *CYP1A1* in SRD5A3-CDG patient-derived fibroblasts.**

(A,C) *CYP1B1* and *CYP1A1* expression quantified by transcriptome analysis, measured by average read counts in SRD5A3-CDG patient-derived fibroblasts ( $n = 3$ ) and control ( $n = 5$ ). The differential expression genes based on an absolute  $\log_2$ -Ratio of  $\log_2$ -Ratio  $\geq 1$  and FDR  $\leq 0.001$ . Data produced jointly with BGI. ns, not significant (B) *CYP1B1* expression in SRD5A3-CDG patient-derived fibroblasts ( $n = 3$ ) and pooled controls ( $n = 2$ ) quantified by qRT-PCR. Expression of  $\beta$ -ACTIN was used to normalise the Ct values of *CYP1B1*.

### 6.3 Elevated expression of *CYP1B1* in SRD5A3-CDG patient-derived fibroblasts on protein level

Gene expression does not always completely correspond to the protein level due to mRNA processing and translational regulations. Therefore, quantifying the protein level of *CYP1B1* was crucial to consider the elevated gene expression biologically relevant to the cells. To this aim, I performed Western blots using  $\beta$ -ACTIN as a loading and normalisation control. *CYP1B1* exhibits a molecular weight of 60.8 kDa. Around the running height of  $\sim 55$  kDa, two bands could be detected. One of higher molecular weight which was present as a rather cloudy, hazy band and one sharp band of lower molecular weight. According to the antibody manufacturer, the running height of 52 kDa. Therefore, I considered the lower band to be the specific and corresponding *CYP1B1* band. Relative quantification revealed an overall elevated expression through all the SRD5A3-CDG patient cell lines with +108.61 % (SD:  $\pm 55.98$ ;  $P$ -value: 0.0691), +85.37 % (SD:  $\pm 21.3$ ;  $P$ -value: 0.1807), and +344.25 % (SD:  $\pm 106.92$ ;  $P$ -value:  $< 0.0001$ ), respectively (Fig. 15A,A').

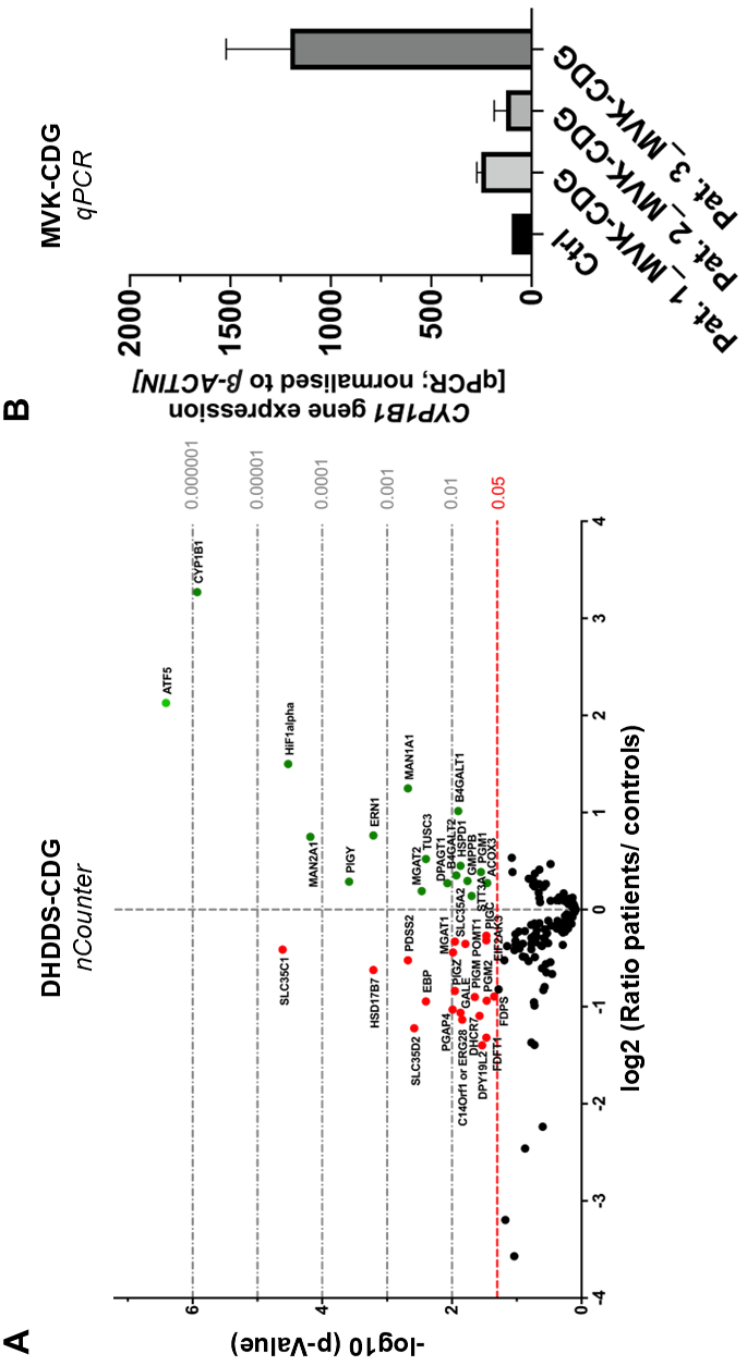


**Figure 15: Elevated CYP1B1 protein levels in SRD5A3-CDG patient-derived fibroblasts.**

(A,A') Western blot against CYP1B1 of SRD5A3-CDG patient-derived fibroblasts and pooled controls (n = 5) and its corresponding relative quantification. CYP1B1 signals were normalised to  $\beta$ -ACTIN loading control. One-way ANOVA test. Ns, not significant; \*\*\*\*,  $P$ -value < 0.0001.

## 6.4 Deregulation of CYP1B1/CYP1B1 in a variety of CDG-types on transcript and protein level

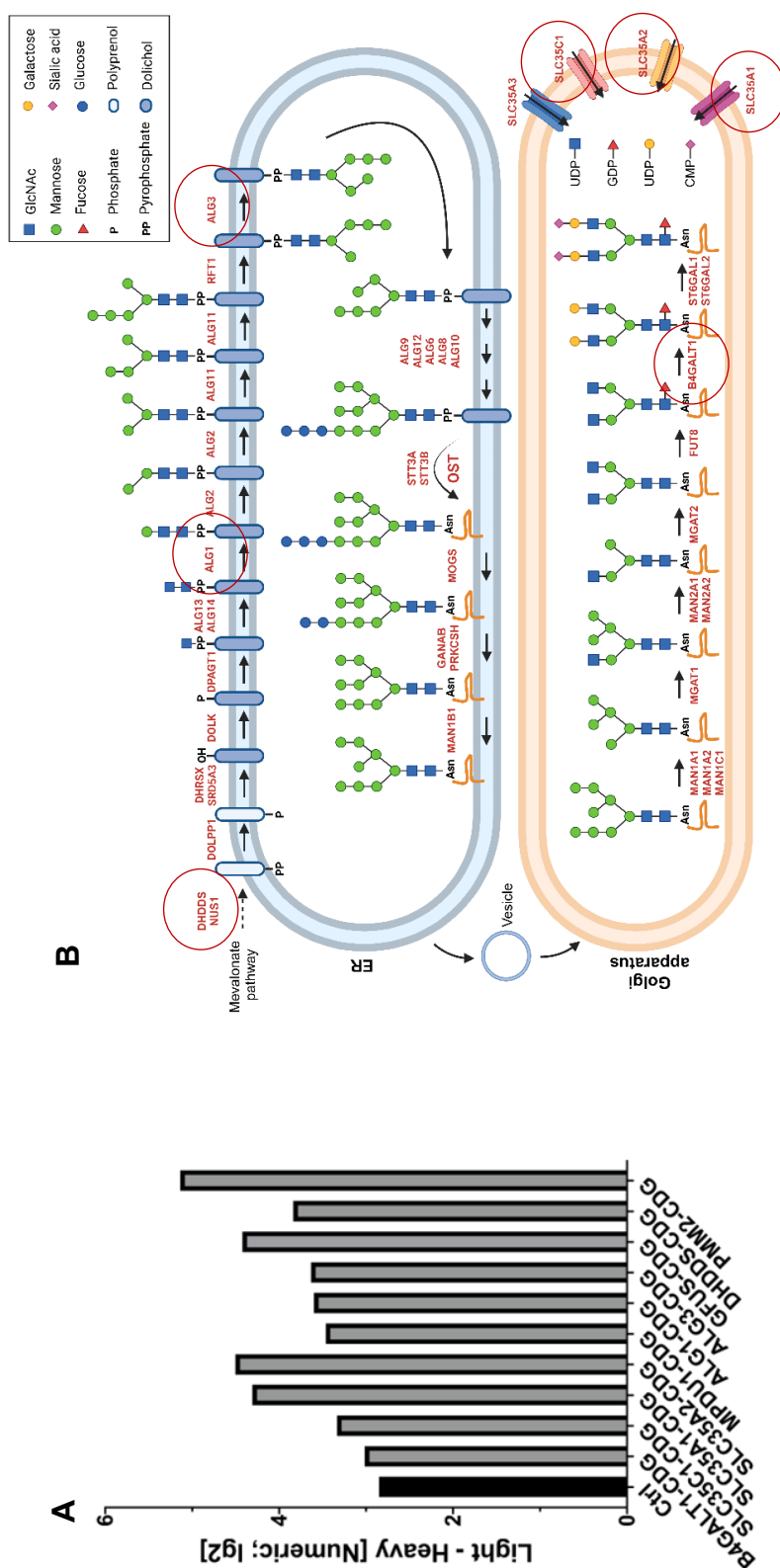
To investigate whether the elevated expression was unique to SRD5A3-CDG, I performed qRT-PCR and nCounter analysis on MVK- and DHDDS-CDG, respectively. MVK-CDG is caused by a deficiency of the mevalonate kinase (MVK) which exhibits the phosphorylation of mevalonate to mevalonate-5-phosphate – marking a crucial step in the biosynthesis of dolichol and cholesterol [17]. According to qRT-PCR analysis, the expression of *CYP1B1* in MVK-CDG patient-derived fibroblasts was elevated by +151 % (SD:  $\pm$ 23), +28 (SD:  $\pm$ 59) and +1103 % (SD:  $\pm$ 319) in Pat. 1 - 3\_MVK-CDG, respectively (Fig. 16B). DHDDS-CDG is caused by deficiency of Dehydrodolichyl diphosphate synthase (DHDDS) which is a crucial enzyme for extending the chain length of farnesyl diphosphate, resulting in the synthesis of polyprenol. Polyprenol is later being used as a substrate of DHRSX and SRD5A3 to produce dolichol [124]. Since SRD5A3 and DHDDS work side by side, an elevated expression of *CYP1B1* was assumed and could be verified by nCounter analysis: Its expression in DHDDS-CDG patient-derived fibroblasts revealed an almost 10-fold higher expression ( $P$ -value: <0.000001;  $Q$ -value: <0.000001) (Fig. 16A). This indicated that the elevation expression of *CYP1B1* is common in different types of CDG.



**Figure 16: Elevated expression of CYP1B1 transcripts in DHDDS- and MVK-CDG patient-derived fibroblasts.**

(A) The expression of 190 genes was quantified using nCounter analysis based on transcript quantity in DHDDS-CDG patient-derived fibroblasts ( $n = 3$ ) and controls ( $n = 4$ ). The  $-\log_{10}(P\text{-value})$  is plotted against the ratio of transcript quantity in patient versus control samples on a log2 scale. The line at  $x = 0$  represents the expression in control samples. The red line corresponds to the significance threshold of  $p = 0.05$ . Black points represent genes with insignificant expression in patient cells, while red points indicate genes with significantly decreased transcript levels in patient cells. Green points represent genes with significantly increased transcript levels. Data produced jointly with the nCounter Core Facility of the Heidelberg University Hospital. (B) CYP1B1 expression in MVK-CDG patient-derived fibroblasts quantified by qRT-PCR. Expression of  $\beta\text{-ACTIN}$  was used to normalise the Ct values of CYP1B1.

Notably, a shotgun mass spectrometric analysis of proteins isolated from fibroblasts of patients suffering from early glycosylation defects (PMM2-, DHDDS-, ALG1-, ALG3-, and MPDU1-CDG) and late glycosylation defects (SLC35A1-, SLC35A2-, SLC35C1-, and B4GALT1-CDG) as well as fucosylation defects (GFUS-CDG), revealed an elevated protein level of CYP1B1 in all patient cells. The highest expression could be found in PMM2-CDG fibroblasts with  $\Delta\log_2$  of 2.28652 relative protein amount – representing a  $\sim +4.8$ -fold expression. The lowest relative protein amount of CYP1B1 could be found in B4GALT1-CDG fibroblasts with  $\Delta\log_2$  of 0.16268 (Fig. 17, Tab. 17).



**Figure 17: Elevated CYPB1 protein levels in a variety of early and late CDG-types.**

(A) CYP1B1 amounts were quantified by 'shotgun'-proteomic analysis in fibroblasts derived from PMM2-, DHDDS-, GFUS-, ALG3-, ALG1-, MPDU1-, SLC35A1-, SLC35A2-, SLC35C1-, and B4GALT1-CDG patients and compared to control (n = 2). Protein levels were presented as log2 light/heavy ratios. Data produced jointly with Dr. Andreas Harst from the Centre for Molecular Biology (ZMBH) Heidelberg. (B) Overview of the N-glycosylation pathway. This figure illustrates the simplified pathway for the biosynthesis of a N-glycans. Highlighted in red are the key enzymes required for the formation of N-glycans. Additionally, it includes the provision of nucleotide-activated sugar substrates in the Golgi through various SLC35 transporters. Highlighted in red circles are a selection of corresponding enzymes from the figure 17A. The figure was created in BioRender.com, based on the work of Ng and Freeze [1]. Asn, asparagine; CMP, Cytidine monophosphate; GDP, Guanosine diphosphate; UDP, Uridine diphosphate.

**Table 17: CYP1B1 protein levels in early and late CDG-types.**

CYP1B1 amounts were quantified by ‘shotgun-’proteomic analysis in fibroblasts derived from PMM2-, DHDDS-, GFUS-, ALG3-, ALG1-, MPDU1-, SLC35A2-, SLC35A1-, SLC35C1-, and B4GALT1-CDG patients and compared to control (n = 2). Protein levels were presented as log2 light/heavy ratios. Data produced jointly with Dr. Andreas Harst from the Centre for Molecular Biology (ZMBH) Heidelberg.

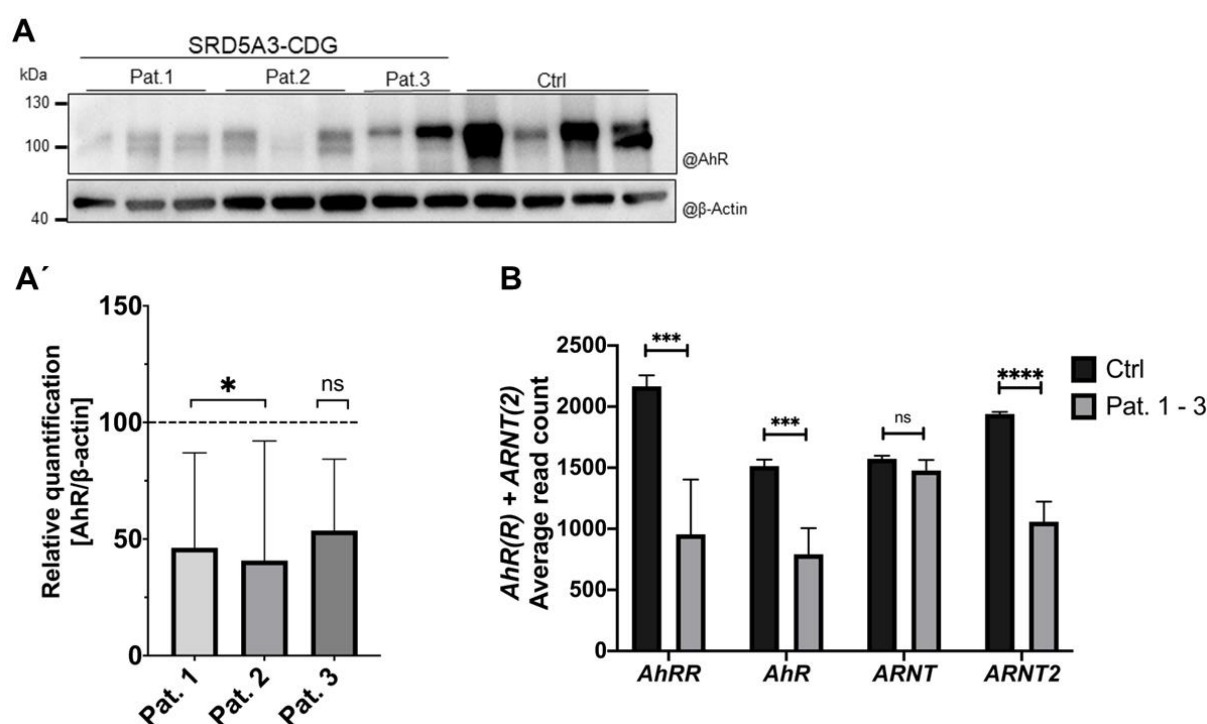
<b>CDG-Type/ Control</b>	<b>CYP1B1 expression Light – heavy [Numeric; lg2]</b>
Ctrl	2.85182
B4GALT1-CDG	3.0145
SLC35C1-CDG	3.33434
SLC35A1-CDG	4.30777
SLC35A2-CDG	4.50244
MPDU1-CDG	3.46489
ALG1-CDG	3.60034
ALG3-CDG	3.63441
GFUS-CDG	4.42182
DHDDS-CDG	3.83826
PMM2-CDG	5.13834

Western blot and mass spectrometric analysis indeed confirmed the transcriptome analysis results of an elevated expression of CYP1B1 in SRD5A3- as well as a variety of CDG-types – highlighting elevated CYP1B1 levels potentially being connected to general glycosylation defects.

## **6.5 Downregulation of the AhR pathway in SRD5A3-CDG patient-derived fibroblasts**

Since *CYP1B1*'s gene expression is elevated in SRD5A3-CDG patient-derived fibroblasts, it could be a downstream effect of a deregulation of the AhR pathway. AhR is a ligand-dependent transcription factor which translocates to the nucleus, forming a complex with ARNT, and initiates the expression of its downstream genes by binding to the XRE region of the DNA. AhR's activity is strictly controlled by its repressor, called AhRR, which competes with AhR for heterodimerisation with ARNT. I validated the AhR expression by Western blot and transcriptome analysis on protein and mRNA level, respectively. The Western blot analysis revealed significantly reduced AhR levels with 46.29 % (SD:  $\pm 40.71$ ; adjusted *P*-value: 0.0293) and 40.8 % (SD: 51.26; adjusted *P*-value: 0.0146) remaining relative signal intensity compared to control, respectively. Pat. 3 exhibited a milder decreased AhR expression of 53.68 % (SD: 30.56; adjusted *P*-value: 0.2315). Notably, the expression of AhR seemed to be dynamic since signal intensities within each sample group could vary strongly, e.g. Pat. 3's biological replica or within the different control fibroblasts cell lines (Fig. 18A,A'). Still, the tendency of decreased protein level of AhR in the patient fibroblasts is clearly visible.

Transcriptome analysis corresponds to the Western blots results – the gene expression of *AhR* in Pat. 1 - 3 was significantly reduced by 47.5 % (1233.45 vs. 647.07 ARC; *P*-value: 0.000872, *Q*-value: 0.009562069). Furthermore, I quantified the gene expression of *AhR*'s regressor, *AhRR*, and its heterodimerisation partner ARNT. Gene expression of *AhRR* was significantly decreased by 55.5% (1693,5 vs. 753,34 ARC; *P*-value: 0.000576, *Q*-value: 0.006984278) whereas the expression of ARNT remained similar to controls (1494,74 vs. 1398,42 ARC; *P*-value: 0.37929826, *Q*-value: 0.6504432). In contrast, ARNT's homolog ARNT2 gene expression was also significantly decreased by 45.6 % (1597.63 vs. 868.83 ARC; *P*-value: 0.000054, *Q*-value: 0.00104329) (Fig. 18B). Although ARNT2 is associated with other pathways than the *AhR* pathway as well, it also exhibits an affinity for binding to *AhR*. Taken together, the *AhR* signalling pathway appeared to be affected in SRD5A3-CDG patient-derived fibroblasts.



**Figure 18: Decreased expression of AhR and its interaction partners AhRR and ARNT2.**

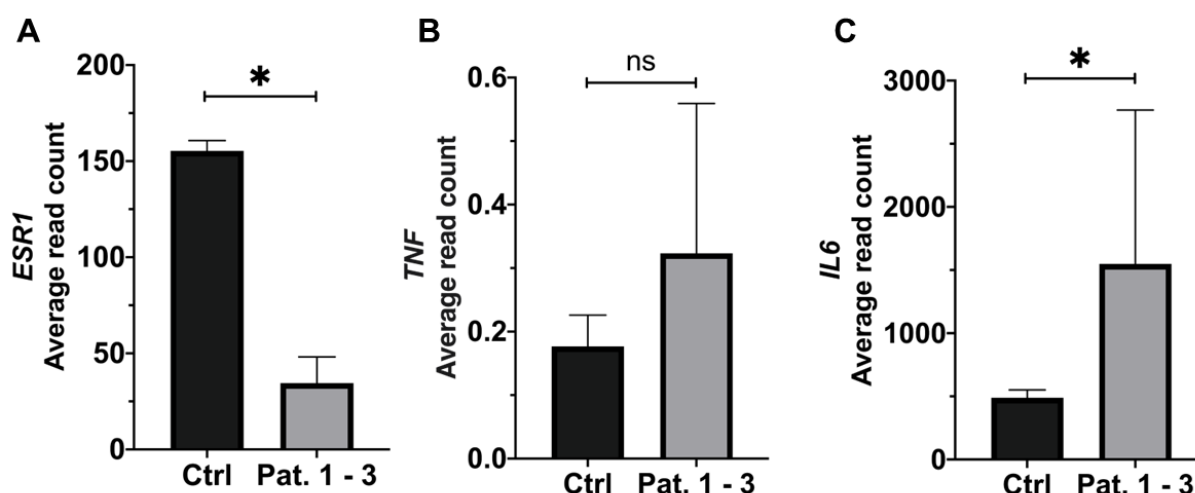
(A) Western blot against AhR of SRD5A3-CDG patient-derived fibroblasts and pooled controls (*n* = 5) and its corresponding relative quantification. AhR signals were normalised to β-ACTIN loading control. One-way anova test. Ns, not significant; \*, *P*-value < 0.05. (B) Gene expression quantified by transcriptome analysis of *AhR*, *AhRR*, *ARNT* and *ARNT2*, measured by average read counts. The differential expression genes based on an absolute log2-Ratio of log2-Ratio ≥ 1 and FDR ≤ 0.001. Data produced jointly with BGI. ns, not significant. ns, not significant; \*\*\*, *P*-value < 0.001; \*\*\*\*, *P*-value < 0.0001.

## 6.6 Decreased estrogen-receptor and increased TNF and IL6 gene expression in SRD5A3-CDG patient-derived fibroblasts

Next, potential alternative mechanisms that also could lead to the elevated expression of *CYP1B1* in the context of glycosylation defects were addressed as the hormonal regulation via estrogen receptors, or the action of inflammatory cytokines such as tumor necrosis factor (TNF) and interleukin-6 (IL-6). *CYP1B1* plays a crucial role in the metabolism of 17 $\beta$ -estradiol, generating several metabolites and it could be shown that 17 $\beta$ -estradiol induces *CYP1B1* expression in estrogen receptor (ER)-positive MCF-7 breast cancer cells through the direct interaction of ER- $\alpha$  with the estrogen response element (ERE) in the *CYP1B1* promoter region [125]. Furthermore, it has been reported that TNF- $\alpha$  and IL-6 are able to induce its expression [126].

Transcriptome analysis revealed a significant downregulation of the estrogen-receptor corresponding gene *ESR1* with 106.25 vs 23.76 ARC (*P*-value: 0.01337472; *Q*-value: 0.07097479) compared to control (Fig. 19A). In contrast, both pro-inflammatory cytokines *TNF* and *IL6* are upregulated according to their transcript level. However, *TNF*'s gene expression is only insignificantly increased and in total its expression is on a very low level with 0.23 vs. 0.35 ARC (*P*-value: 0.86096654; *Q*-value: 0.96211613) which does not imply a biological relevance (Fig. 19B). Instead, the gene expression of *IL6* is significantly increased with 601.84 vs. 2039 ARC (*P*-value: 0.02633115; *Q*-value: 0.1149708) which represents an elevation of ~ 3-fold (Fig. 19C).





**Figure 19: Downregulation of *ESR1* and upregulation of cytokines *TNF* and *IL-6* gene expression in SRD5A3-CDG patient-derived fibroblasts.**

Gene expression quantified by transcriptome analysis of *ESR1*, *TNF*, and *IL6*, measured by average read counts in SRD5A3-CDG patient-derived fibroblasts ( $n = 3$ ) and controls ( $n = 5$ ). The differential expression genes based on an absolute  $\log_2$ -Ratio of  $\log_2$ -Ratio  $\geq 1$  and  $FDR \leq 0.001$ . Data produced jointly with BGI. ns, not significant; \*,  $P$ -value  $< 0.05$ .

## 6.7 Alterations in the *Nrf2/NFE2L2* pathway and its regressor KEAP1 in SRD5A3-CDG patient-derived fibroblasts

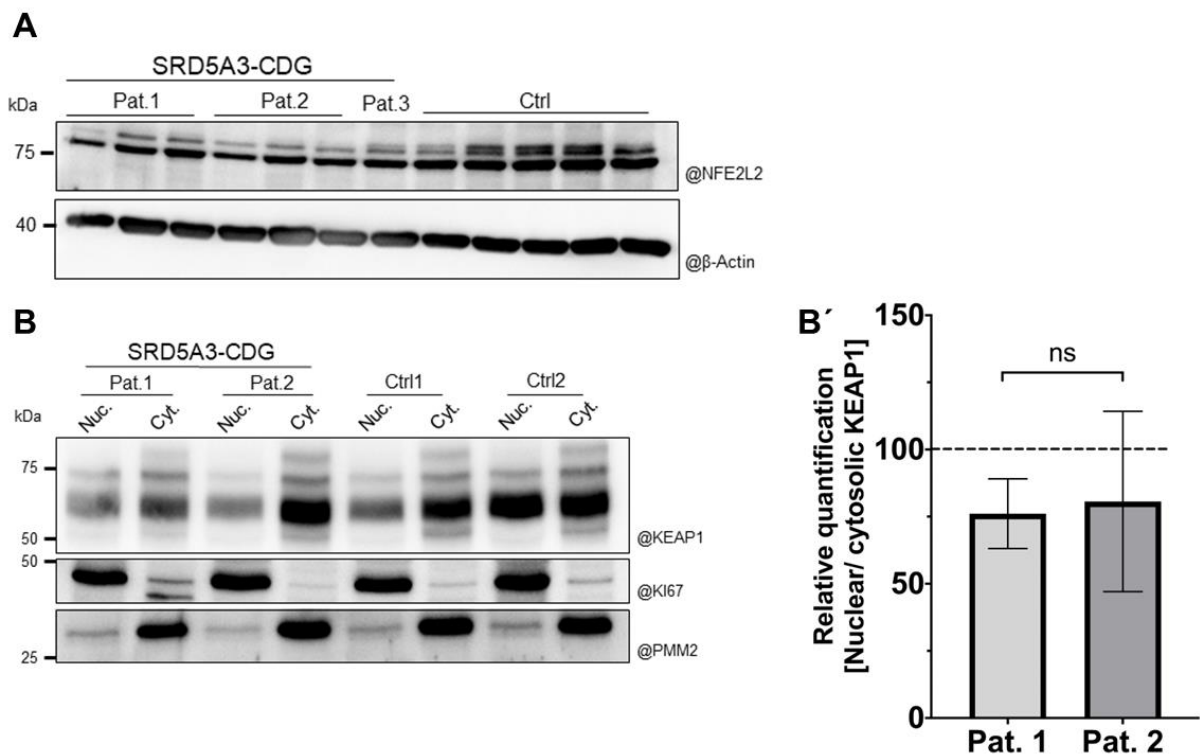
It could be shown in different types of CDG that cells suffer from oxidative stress (PMM2-, ATP6AP1-, ALG8-, RFT1-, and SLC10A7-CDG) [107]. Under physiological conditions, cells can tolerate and scavenge reactive oxygen species (ROS) by activation of the antioxidant response through the transcription factor *Nrf2/NFE2L2*. A reciprocal relationship between *Nrf2/NFE2L2* and AhR is known. Considering common oxidative stress in CDG and the reciprocal relationship, I investigated the expression of *Nrf2/NFE2L2* and its regressor KEAP1 by Western blot. The Western blot revealed a specific and prominent band close the molecular weight of 75 kDa which corresponded to NFE2L2's calculated molecular weight of 67.8 kDa. The signal intensity of this band did not differ significantly between the patient's fibroblasts and controls. But interestingly, the Western blot also revealed a fainter double band of a little higher molecular band in the control. In patient's fibroblasts, this double band was fainter or only one band was visible (Fig. 20A).

This double band might correspond to post-translational modifications of NFE2L2 which were missing in SRD5A3-CDG. Digestion with PNGaseF was carried out to rule out the possibility that the double bands are due to glycosylation. The double bands were still visible, which is why glycosylation could be ruled out. Instead, post-translational modification in form of



## Results

ubiquitination is known to regulate NFE2L2's activity. KEAP1 is a ubiquitin transferase which controls its activity and leads to degradation of NFE2L2 through ubiquitination. KEAP1 is localised in the cytosol and nucleus. I evaluated KEAP1's cellular localisation by Western blot after nuclear isolation and immunofluorescence microscopy. Nuclear isolation was successful which could be seen by nuclear and cytosolic specific loading controls of KI67 and PMM2, respectively. The band pattern of KEAP1 remained the same throughout the different fractions and conditions. Nevertheless, the signal intensities varied between the patient's fibroblasts Pat 1. and 2. Relative quantification revealed a slight decrease of nuclear KEAP1 in ratio to its cytosolic fraction. Signal intensities were decreased by 23.9 % (adjusted *P*-value: 0.4390) and 19.36 % (adjusted *P*-value: 0.5727) in Pat. 1 and 2, respectively (Fig. 20B,B').

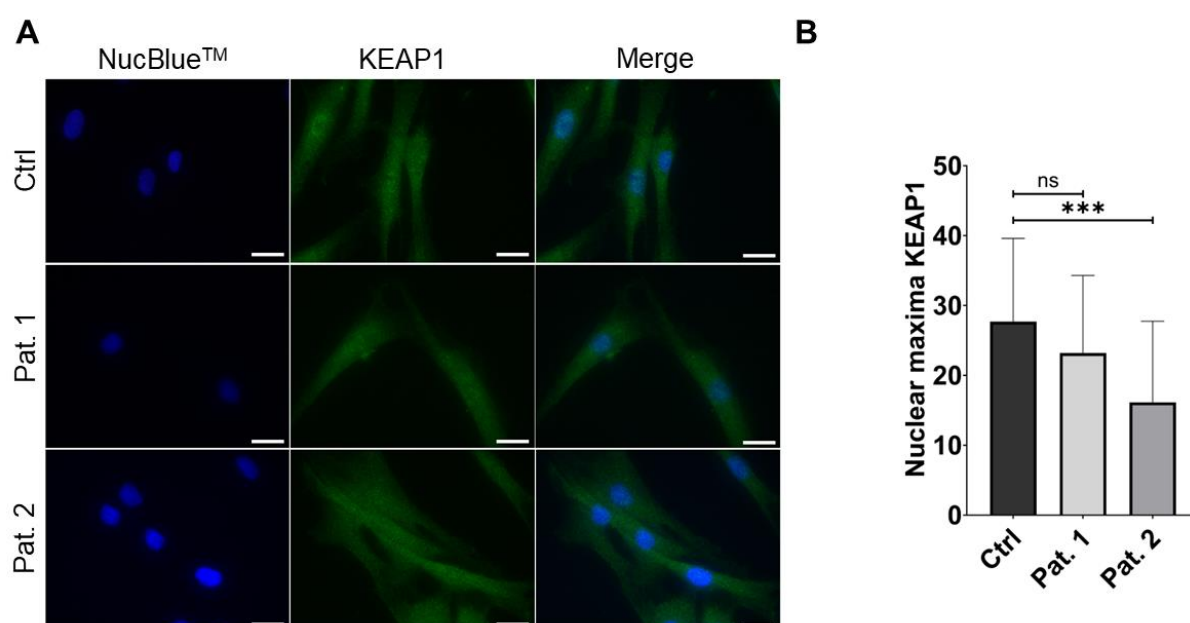


**Figure 20: Reduced post-translational modification in *Nrf2*/NFE2L2 and decreased nuclear localisation of KEAP1 in SRD5A3-CDG patient-derived fibroblasts.**

(A) Western blot against *Nrf2*/NFE2L2 of SRD5A3-CDG patient-derived fibroblasts and controls (*n* = 5). β-ACTIN was used as a loading control. (B/B') Western blot against KEAP1 of SRD5A3-CDG patient-derived fibroblasts of patient 1 and 2 and controls (*n* = 2) and its corresponding relative quantification after nuclear isolation. Nuclear and cytosolic KEAP1 signals were normalised to KI67 and PMM2 as loading controls, respectively. SRD5A3-CDG patient 3 was not included in the analysis due to bad cell proliferation in cell culture. One-way anova test. Ns, not significant.

Similar results were obtained through immunofluorescence microscopy. KEAP1 could be detected throughout the cell with nuclear accumulation in Pat 1 and 2 as well as in the control cell line. After isolation of the nucleus through NucBlue™ staining by masking, nuclear accumulations of KEAP1 were identified and counted by ImageJ. Nuclear accumulations were defined as signal maxima of KEAP1 with a prominence >10. Patient fibroblasts showed decreased number of accumulations with an in average of 23.19 counts (SD: 11.11; adjusted *P*-value: 0.2005) in Pat. 1 and 16.14 counts (SD: 11.60; adjusted *P*-value: 0.0002) in Pat. 2 compared to 27.69 in controls (Fig. 21A,B).

In total, my findings suggest decreased post-translational modifications of NFE2L2, possibly due to lack of ubiquitination, and lower localisation of nuclear KEAP1.



**Figure 21: Decreased nuclear accumulation of KEAP1 in SRD5A3-CDG patient-derived fibroblasts.**

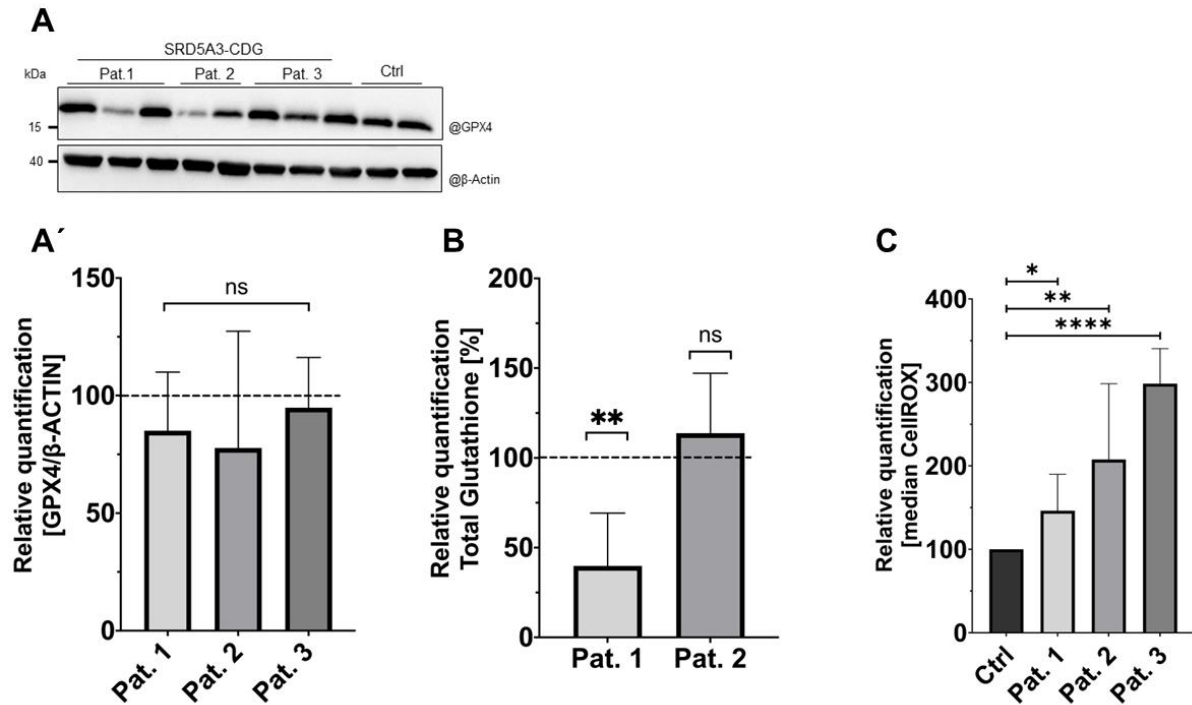
(A) Immunofluorescence microscopy images of patient fibroblasts patient 1 ( $n = 55$ ) and 2 ( $n = 77$ ) and control fibroblast ( $n = 69$ ) were obtained by staining KEAP1. The nucleus was stained with NucBlue™ to localize nuclei. Scale bar: 25  $\mu\text{m}$ . (B) Quantification of nuclear accumulation of KEAP1 by measuring the nuclear signal maxima. Nuclear maxima were identified by using ImageJ with a prominence > 30.00. SRD5A3-CDG patient 3 was not included in the analysis due to bad cell proliferation in cell culture. One-way anova test. Ns, not significant; \*\*\*, *P*-value < 0.001.

## 6.8 Decreased antioxidative capacity in SRD5A3-CDG patient-derived fibroblasts

Due to the alterations in the *Nrf2*/NFE2L2 pathway, I investigated the antioxidative capacity and oxidative status by Western blot of GPX4, the amount of total glutathione and

## Results

quantification of CellROX™ deep red by FACS. GPX4 is one of the cassettes of glutathione associated genes which are crucial to maintain a sufficient oxidative tolerance. Western blot analysis revealed a specific band close above the molecular weight of 15 kDa. The signal intensity varied between the biological replica of SRD5A3-CDG patient-derived fibroblasts, resulting in high standard deviations in its relative quantifications with 24.93, 49.67 and 21.35 % in Pat. 1 - 3, respectively. Overall, the GPX4 protein levels were slightly decreased in patient's fibroblasts by 85.05 - 94.85 % remaining signal intensity (Fig. 22A,A'). Although alterations in GPX4 protein levels were discreet, relative quantification after normalisation to cell number revealed significant decrease of total glutathione in Pat. 1 with only 39.78 % remaining total glutathione (SD: 29.47; *P*-value: 0.0059). In contrast, Pat. 2 fibroblasts showed increased total glutathione levels with 113.74% (SD: 33.42; *P*-value: 0.5974) (Fig. 22B). Since it is known that oxidative stress is common in different types of CDG and SRD5A3-CDG patient-derived fibroblast exhibit reduced levels of GPX4 (Pat. 1 - 2) and total glutathione (Pat. 1), oxidative stress was quantified by using CellROX™ deep red using FACS. The median fluorescence signal was increased in all three patient's fibroblasts: +46.27 % (SD: 43.68; *P*-value: 0.0332), +107.65 % (SD: 90.85; *P*-value: 0.0027), and +198.57^% (SD: 42.04; *P*-value: <0.0001) in Pat. 1 - 3, respectively (Fig. 22C).



**Figure 22: Deregulated glutathione homeostasis and increased oxidative stress in SRD5A3-CDG patient-derived fibroblasts.**

(A,A') Western blot against GPX4 of SRD5A3-CDG patient-derived fibroblasts and pooled controls ( $n = 5$ ) and its corresponding relative quantification. GPX4 signals were normalised to  $\beta$ -ACTIN loading control. One-way anova test. ns, not significant. (B) Relative quantification of total glutathione in Pat. 1 and 2 SRD5A3-CDG patient-derived fibroblasts and two independent controls by chemiluminescence assay according to the GSH/GSSG-GloTM Assay Kit. NucBlue™ was used to quantify the cell number and use for normalisation. SRD5A3-CDG patient 3 was not included in the analysis due to bad cell proliferation in cell culture. Unpaired t-test. ns, not significant; \*\*,  $P$ -value  $< 0.01$ . (C) Relative quantification of reactive oxygen species (ROS) levels indicated by CellROX™ deep red median intensities in SRD5A3-CDG patient fibroblasts and controls ( $n = 5$ ). CellROX™ signals were quantified using FACS verse cytometer (BD Biosciences) for flow cytometry. Unpaired t-test. \*,  $P$ -value  $< 0.05$ ; \*\*,  $P$ -value  $< 0.01$ ; \*\*\*,  $P$ -value  $< 0.001$ .

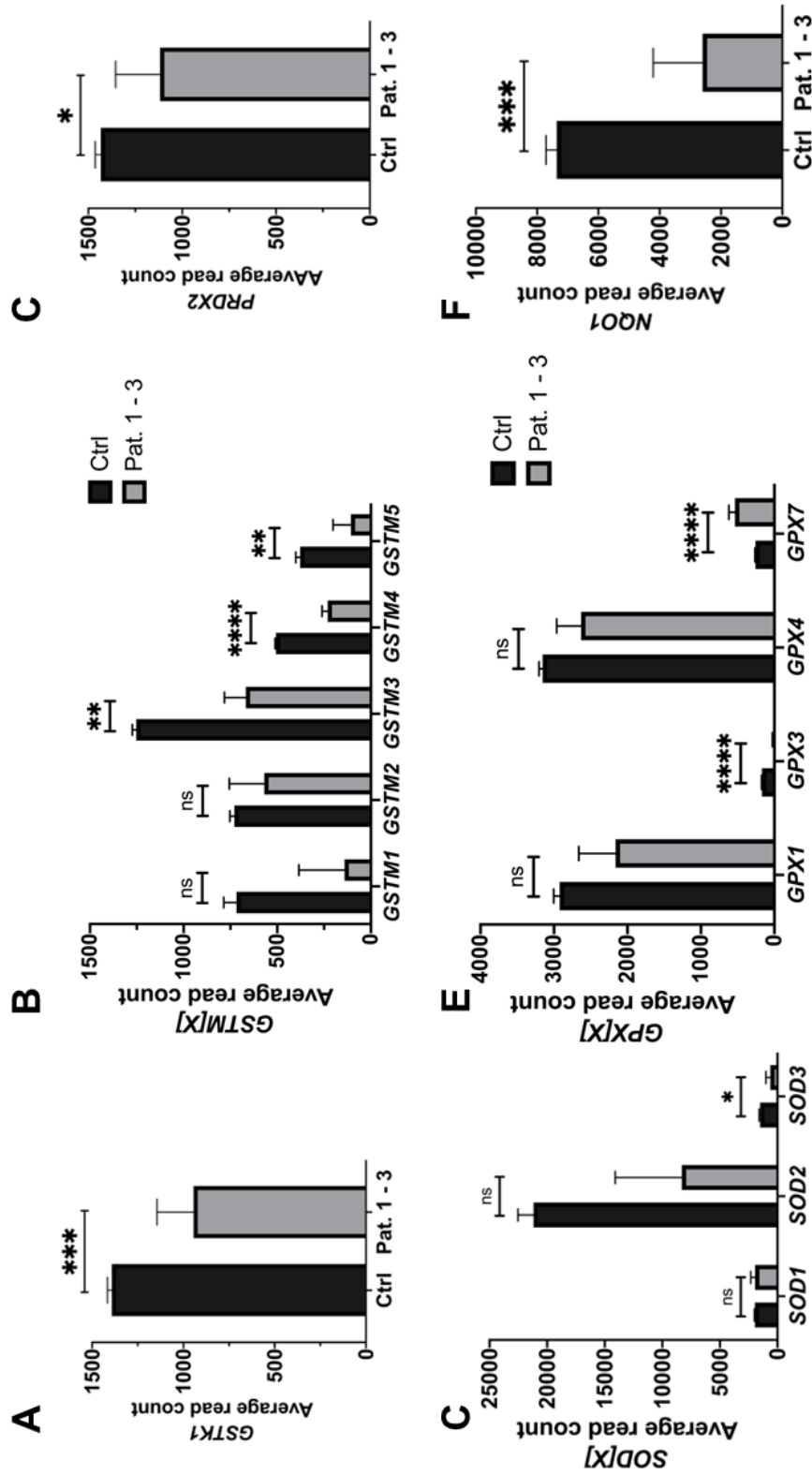
Besides GPX4, a broad variety of antioxidant response associated genes are controlled by *Nrf2/NFE2L2* – among these, glutathione associated genes are included, e.g. Glutathione S-transferase Mu (GSTM), Glutathione S-transferase kappa 1 (GSTK1) and other GPX genes. Transcriptome analysis revealed a couple of significantly downregulated genes: GSTM3 (1027.43 vs. 547.14 ARC;  $P$ -value: 0.0020, Q-value: 0.0175), GSTM4 (400.79 vs. 181.84 ARC;  $P$ -value: 0.0000014, Q-value: 0.0000517), GSTM5 (78.72 vs. 269.42 ARC;  $P$ -value: 0.0030, Q-value: 0.0239) (Fig. 23B), GSTK1 (1213.75 vs. 822.21 ARC;  $P$ -value: 0.0008, Q-value: 0.0088) (Fig. 23A), and GPX3 (104.75 vs. 11.65 ARC;  $P$ -value: 0.0000000003, Q-value: 0.0000000374) (Fig. 23E). In addition, GSTM1 (479.75 vs. 105.26 ARC;

## Results

*P*-value: 0.31249911; *Q*-value: 0.58042023), GSTM2 (658.58 vs. 516.19 ARC; *P*-value: 0.12492175; *Q*-value: 0.3279616) (Fig. 23B), GPX1 (2605.58 vs. 1928.03 ARC; *P*-value: 0.05105745; *Q*-value: 0.18247006), and GPX4 (2903.95 vs. 2415.81 ARC; *P*-value: 0.1700801; *Q*-value: 0.39979805) were downregulated, although not significantly (Fig. 23E). In contrast to this, GPX7 was significantly upregulated (300.11 vs. 626.14 ARC; *P*-value: 0.0000218, *Q*-value: 0.000501), which represented an exception (Fig. 23E).

PRDX2 is a heme-containing peroxidase that speeds up the breakdown of hydrogen peroxide and organic hydroperoxides into water and alcohols, respectively. It can neutralise peroxides and by this contributes to protection from oxidative stress. In addition, it acts as a sensor for hydrogen peroxide-related signalling events [127-129]. In patient's fibroblasts, its gene expression is significantly reduced from 1296.41 vs. 1009.74 ARC (*P*-value: 0.0377, *Q*-value: 0.1484) (Fig. 23C). Superoxide dismutases (SOD) contribute to the protection from ROS, too. SODs catalyse reactions that dismutate reactive superoxide ( $O_2^-$ ) anion radical into  $O_2$  and hydrogen peroxide ( $H_2O_2$ ). In human, three forms are identified: SOD1, 2 and 3 which are located in cytoplasm, mitochondria and extracellular space, respectively. Gene expression of SOD2 and SOD3 were downregulated in patient's fibroblasts with 16143.8 vs. 6498.34 ARC (*P*-value: 0.15267983; *Q*-value: 0.37315183) and 1168.98 vs. 491.12 ARC (*P*-value: 0.0213, *Q*-value: 0.0987), respectively (Fig. 23C). NAD(P)H dehydrogenase [quinone] 1 (NQO1) is an important enzyme for redox control for cell defence and its gene expression is controlled by AhR and *Nrf2*/NFE2L2 during cellular stress [130]. Transcriptomic analysis revealed that its gene expression is significantly decreased by more than 50 % from 5479.43 to 1969.74 ARC (*P*-value: 0.0007, *Q*-value: 0.0082) compared to control (Fig. 23F).

Taken together, SRD5A3-CDG patient-derived fibroblasts exhibited oxidative stress which is due to low antioxidative capacity. This is indicated by lower total glutathione level and downregulation of *Nrf2*/NFE2L2-related antioxidant response genes, such as NQO1, PRDX2, SODs and a variety of glutathione-associated genes.

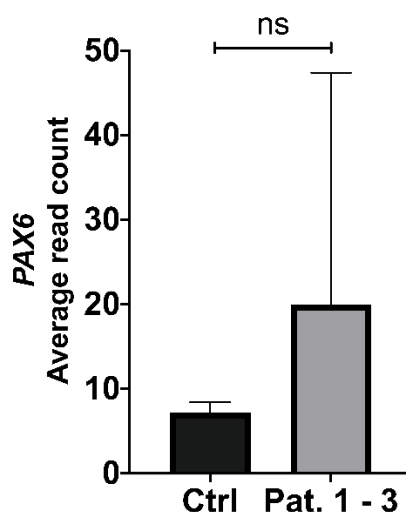


**Figure 23: Decreased gene expression of genes involved in the antioxidant response in SRD5A3-CDG patient-derived fibroblasts.**

Gene expression quantified by transcriptome analysis of *GSTK1*, *GSTM1* - 5, *PRDX2*, *SOD* 1 - 3, *GPX1/3/4/7* and *NQO1*, measured by average read counts in SRD5A3-CDG patient-derived fibroblasts and controls ( $n = 5$ ). The differential expression genes based on an absolute  $\log_2$ -Ratio of  $\geq 1$  and  $FDR \leq 0.001$ . Data produced jointly with BGI. ns, not significant; \*,  $P$ -value  $< 0.05$ ; \*\*,  $P$ -value  $< 0.01$ ; \*\*\*,  $P$ -value  $< 0.001$ ; \*\*\*\*,  $P$ -value  $< 0.0001$ .

## 6.9 Elevated expression of coloboma-associated gene *PAX6*

In a zebrafish model it could be shown that the fish *Cyp1b1* ortholog is regulating the expression of *Pax6* – a gene which is associated with the development of coloboma [67]. Transcriptome analysis revealed increased gene expression of *PAX6* in SRD5A3-CDG patient-derived fibroblasts as well, presenting with 8.08 vs. 27.06 ARC (*P*-value: 0.26154051; *Q*-value: 0.52195923) (Fig. 24).

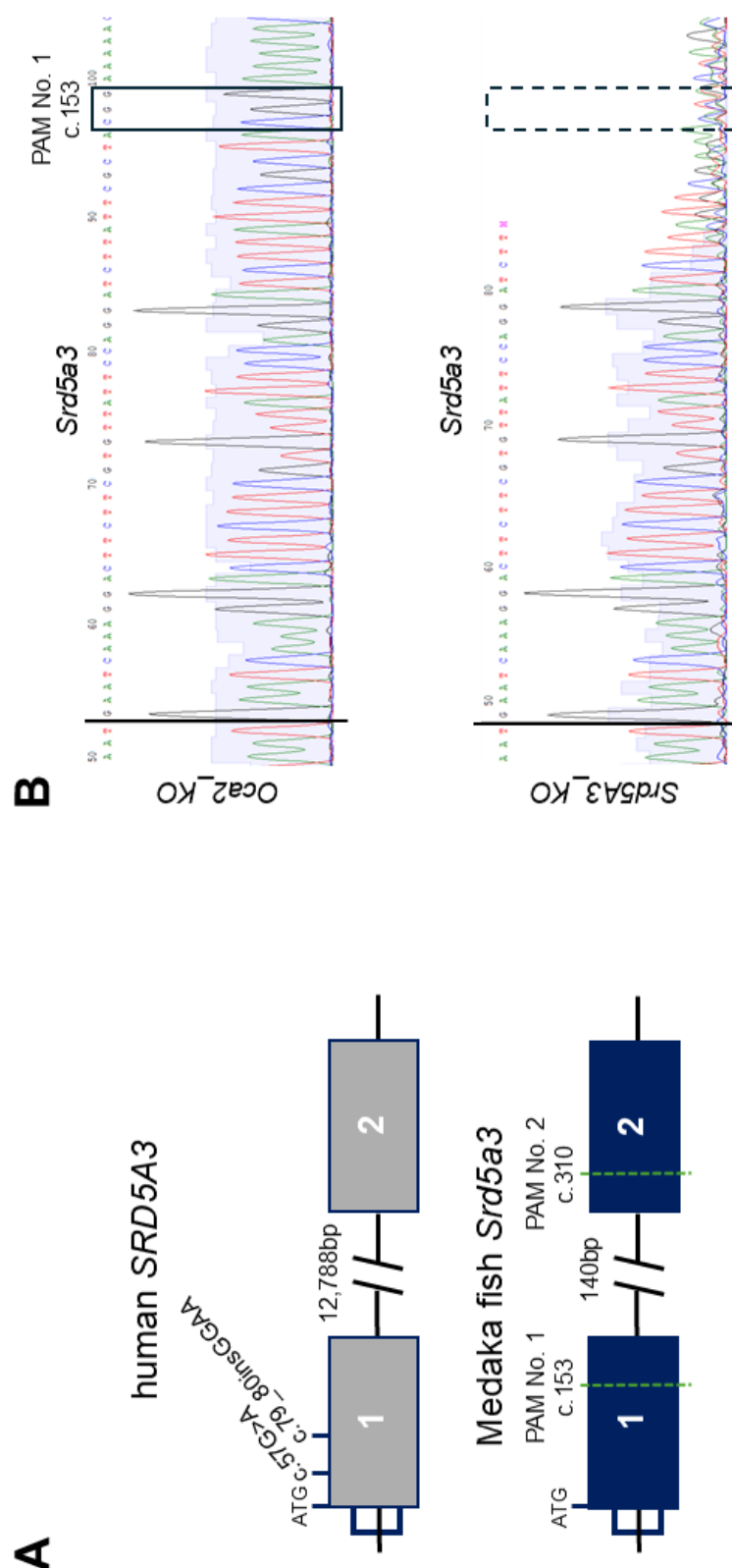


**Figure 24: Elevated transcript expression of coloboma-associated *PAX6* gene.**

Gene expression in SRD5A3-CDG patient-derived fibroblasts and controls (*n* = 5) quantified by whole transcriptome analysis of *PAX6* measured by average read counts. The differential expression genes based on an absolute log<sub>2</sub>-Ratio of log<sub>2</sub>-Ratio ≥ 1 and FDR ≤ 0.001. Data produced jointly with BGI. ns, not significant.

## 6.10 Validation and characterisation of *Srd5a3*-knock out in medaka fish embryos

I achieved a knock-out of *Srd5a3* (*Srd5a3*<sup>+/-</sup> and/or *Srd5a3*<sup>-/-</sup>; *Srd5a3*-KO) in Medaka fish embryos (*Oryzias latipes*) by using two single guide RNAs (sgRNA) targeting exon 1 and exon 2, resulting in the deletion of a ~297 base pair DNA fragment (Fig. 25A). Sanger sequencing showed a double strand break, starting close by the PAM region in exon 1. In contrast, the *Oca2* sgRNA, as microinjection control, resulted in no alteration of *Srd5a3*. Hence, the *Srd5a3*-KO was successfully achieved on genomic level (Fig. 25B). Since this technique does not allow to distinguish between *Srd5a3*<sup>+/-</sup> and/or *Srd5a3*<sup>-/-</sup> genotype the medaka fish embryos will be referred to as *Srd5a3*-KO for simplification reasons.



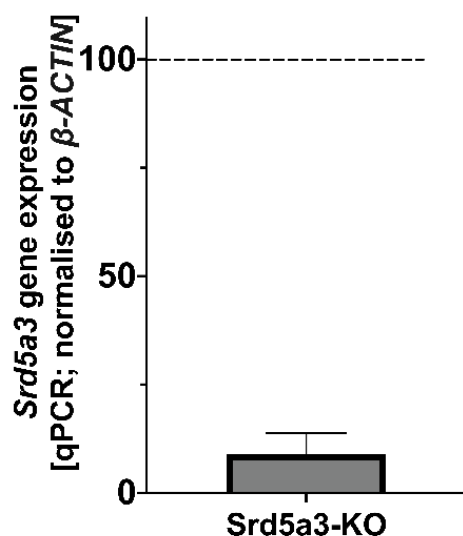
**Figure 25: Knock-out of *Srd5a3* in medaka fish embryos validated by Sanger sequencing.**

(A) Schematic illustration of the sgRNA design for the CRISPR/Cas9-mediated KO of *Srd5a3* in medaka fish embryos. Shown are the human *SRD5A3* exons 1 and 2 including the genetic variations of Pat. 1 – 3 in grey and medaka fish *Srd5a3* exons 1 and 2 including the PAM regions of the sgRNAs in blue. (B) Sanger sequencing of *Srd5a3* exon 1 in mutated medaka fish embryos ( $n = 10$ ). Shown are the electropherograms and the PAM region of sgRNA No. 1 in the *Oca2*-KO ( $n = 8$ ) as control. Black line, 5' end of the sgRNA exon 1; black box, PAM region of sgRNA exon 1.

I could show a successful genetic manipulation of *Srd5a3* on genetic level by sanger sequencing and qRT-PCR of *Srd5a3*. Sanger sequencing reveals a double strand break at the target site of the sgRNA against exon 1 in the *Srd5a3*-KO medaka fish embryos (Fig. 25). In addition, qRT-PCR reveals a strong decreased gene expression of mature *Srd5a3* mRNA with



remaining 8.97 % (SD:  $\pm 4.9$ ) compared to controls and normalised to  $\beta$ -Actin (Fig. 26). Usually, a KO is further validated on protein level by Western Blot. Unfortunately, commercially available antibodies from various species showed insufficient antigen specificity toward the medaka protein, denying validation of the Srd5a3-KO at the protein level. This therefore represents a limitation for validating the Srd5a3-KO in the medaka fish embryo model.



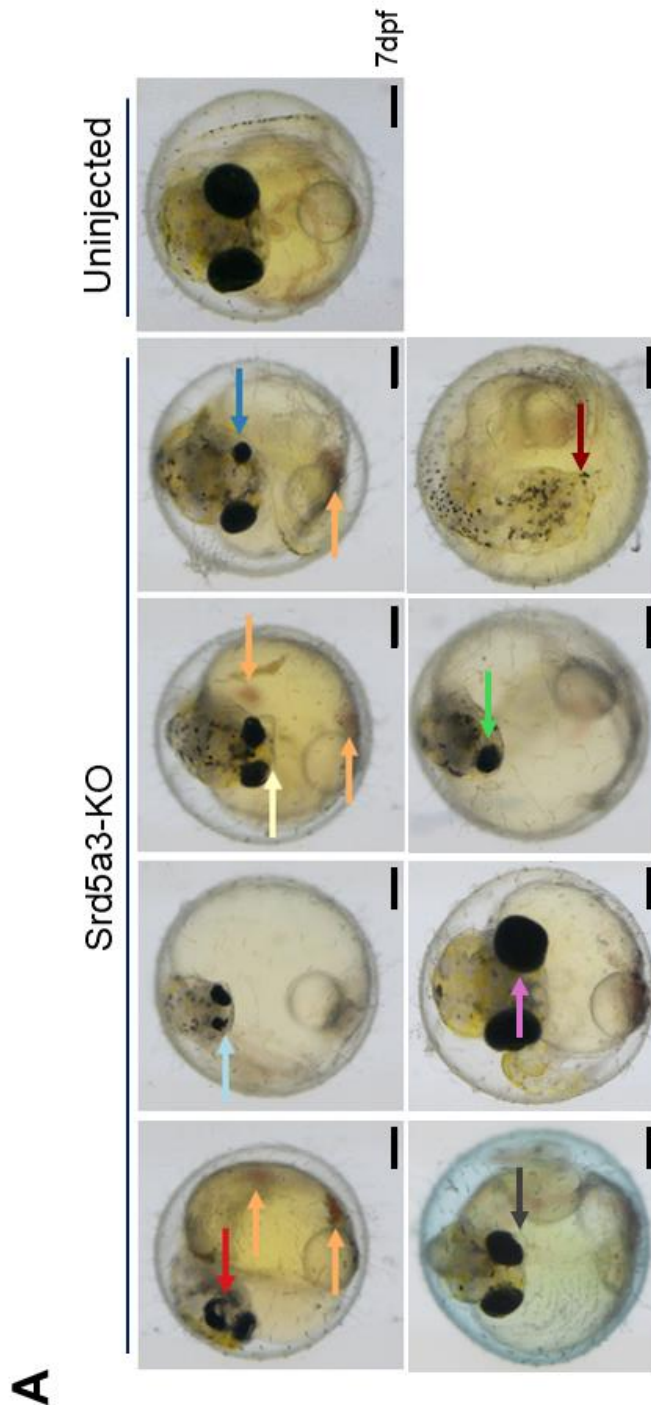
**Figure 26: Decreased gene expression of Srd5a3 after performing a knock-out by microinjection in medaka fish embryos.**

*Srd5a3* expression in Srd5a3-KO medaka fish embryos quantified by qRT-PCR. Expression of  $\beta$ -ACTIN was used to normalise the Ct values of *Srd5a3*.

Srd5a3-KO resulted in a spectrum of phenotypes. In general, phenotypes ranged from mild/normal phenotype over intermediate to severe phenotype. The ration of the three groups came close to 1:1:1 in all attempts and approaches. The mildly affected or without phenotype embryos showed no or very mild alternation phonotypically to uninjected control embryos. In contrast, intermediate affected embryos were defined by developmental delay, slight heart malformations as well as possible coagulopathies and ophthalmological abnormalities. Most of the intermediate affected embryos were able to hatch one or two days later than the control. The severe phenotype was defined by strong developmental delay, high lethality, ophthalmological abnormalities, possible strong heart malformations and coagulopathies. These embryos were mostly not able to hatch (Fig. 27A and Tab. 18). In total, several of these symptoms represented the clinical features which can be observed in SRD5A3-CDG patients. Especially, the recurring ophthalmological abnormalities in the intermediate and severely affected embryos were mimicking the clinical presentation of SRD5A3-CDG patients in a reproduceable and reliable manner.

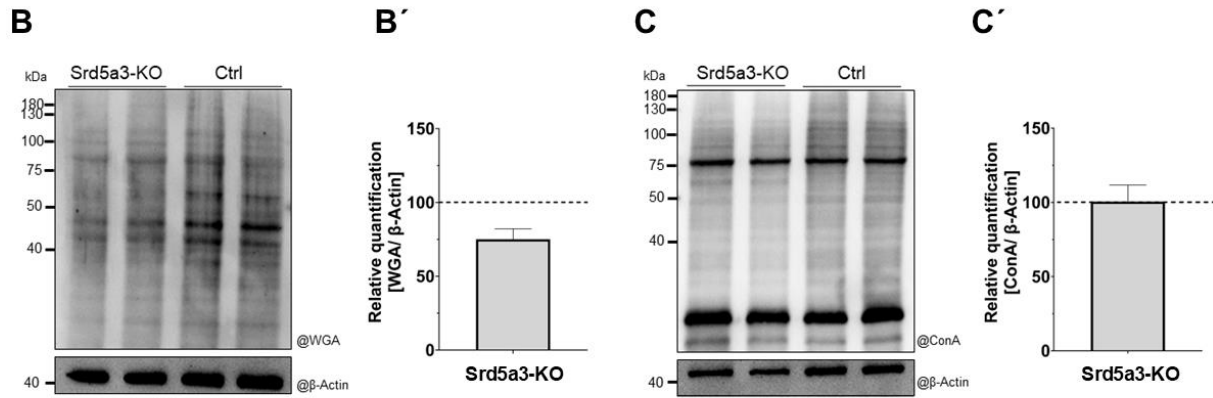
I examined the glycosylation status of the Srd5a3-KO medaka fish embryos compared to control embryos by lectin blots to investigate whether the genetic manipulation led to a hypoglycosylation phenotype. Here, WGA (binding N-acetyl-D-glucosamine and sialic acid) and ConA (nonreduced terminal  $\alpha$ -D-mannosyl and  $\alpha$ -D-glucosyl residues) were used for analysis of total protein. The WGA lectin blots revealed a signal decrease compared to control

of only 75 % (SD:  $\pm 7.15$ ) remaining relative signal. The band pattern changed between the Srd5a3-KO and control medaka fish embryos – presented in a vanished band around 50 kDa molecular weight in the KO embryos. This indicates indeed an impairment in *N*-glycosylation and protein expression in Srd5a3-KO medaka fish embryos (Fig. 27B). In contrast to WGA, the ConA lectin blots indicated no alteration in Srd5a3-KO medaka fish embryos with 100.5% relative signal (SD:  $\pm 11.12$ ) and no change in the band pattern with a sharply prominent band around 75 kDa and a broad band below 40 kDa (Fig. 27C).



**Figure 27: Srd5a3-KO medaka fish embryos mimic several clinical symptoms of SRD5A3-CDG patients.**

(A) Images of Srd5a3-KO and uninjected medaka fish embryos as control at 7 days post-fertilisation (dpf). Srd5a3-KO embryos appeared in a spectrum of mild to severe affected phenotypes. Shown are severely affected embryos and a uninjected control. Red arrow, coloboma; orange arrow, blood clot (coagulopathy); yellow arrow, facial deformation; bright blue, underdeveloped eyes; dark blue, unequal eye size; grey arrow, oedema; purple arrow, dislocated eye; green arrow, one eyed; deep red arrow, eyeless. Line = 200  $\mu$ m. (B,B') Lectin blot of Srd5a3-KO and uninjected embryos and its corresponding semi-quantification. N-acetyl-D-glucosamine and sialic acid glycan structures were stained by WGA. WGA luminescence signals were normalised to  $\beta$ -ACTIN. (C,C') Lectin blot of Srd5a3-KO (pooled, n = 10) and uninjected embryos (pooled, n = 10) 7 dpf and its corresponding semi-quantification. Nonreduced terminal  $\alpha$ -D-mannosyl and  $\alpha$ -D-glucosyl residues glycan structures were stained by ConA. ConA luminescence signals were normalised to  $\beta$ -ACTIN.



**Table 18: Distribution of severity of the Srd5a3- and Oca2-KO (injection-control) medaka fish embryos.**

Description of phenotype focused on ophthalmological abnormalities and development status. Dpf, days post fertilisation.

	<b>Srd5a3-KO</b>	<b>Oca2_KO (injection-control)</b>
<b>Injected</b>	183	87
<b>Viable (3 dpf)</b>	141	79
<b>Mild phenotype</b>	53 <ul style="list-style-type: none"> <li>Underdeveloped: None</li> <li>Eye edema: 2</li> <li>Unequal eye size: 1</li> </ul>	73 <ul style="list-style-type: none"> <li>Underdeveloped: None</li> <li>Loss of ocular pigmentation: All</li> </ul>
<b>Intermediate phenotype</b>	43 <ul style="list-style-type: none"> <li>Underdeveloped: All</li> <li>Eye Phenotype: 20 <ul style="list-style-type: none"> <li>Coloboma: 6</li> <li>Coloboma + edema: 1</li> <li>Coloboma + unequal eye size: 2</li> <li>Unequal eye size: 2</li> <li>Unequal eye size + edema: 1</li> <li>Eye oedema: 4</li> <li>Dislocated eye: 4</li> </ul> </li> </ul>	3 <ul style="list-style-type: none"> <li>Underdeveloped: 3</li> </ul>
<b>Severe phenotype</b>	45 <ul style="list-style-type: none"> <li>Underdeveloped: All</li> <li>Eye phenotype: All <ul style="list-style-type: none"> <li>Coloboma: 11</li> <li>Coloboma + oedema: 5</li> <li>Coloboma + unequal eye size: 6</li> <li>Coloboma + one eyed: 2</li> <li>Unequal eye size: 6</li> <li>Oedema: 1</li> <li>One eyed: 5</li> <li>Eyeless: 9</li> </ul> </li> </ul>	3 <ul style="list-style-type: none"> <li>Underdeveloped: 2</li> <li>Underdeveloped + eyeless: 1</li> </ul>

Based protein quantification, 25 µg of digested protein per sample were used for *N*-glycan release, APTS labelling, and subsequent xCGE-LIF analysis. Table 19 provides an overview

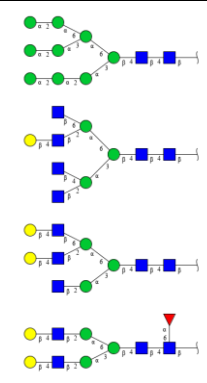
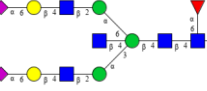
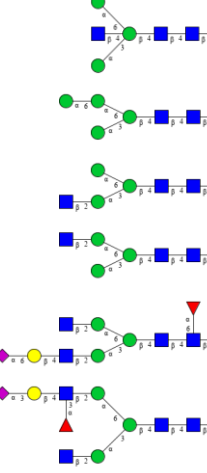
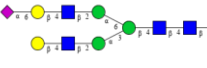
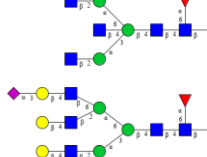
of the most altered *N*-glycan structures, which were identified based on migration time matching only. It is important to note that the applied database does not include fish-specific *N*-glycan structures, such as those containing NGNA or KDN sialic acids. Evaluation of the effects of SRD5A3 knockout was conducted by comparing the relative abundances of *N*-glycans across the different samples.

Comparing wild-type hatchlings with Srd5a3-KO hatchlings several altered glycan structure accumulations could be found. Srd5a3-KO hatchlings exhibited a striking reduction in complex-type *N*-glycans, Man4 but had higher accumulations of paucimannose- (Man3), oligomannose- (Man6–Man9) and the glucosylated oligomannose-type *N*-glycans (Tab. 19).

**Table 19: Altered accumulations of *N*-glycan structures in Srd5a3-KO medaka fish hatchlings compared to wild type.**

*N*-Glycan structures assigned by migration time matching with glyXbaseCE) to the peaks of the xCGE-LIF *N*-glycan fingerprints, derived from the medaka fish hatchlings proteomes of the Srd5a3 Wild Type 1 (WT1; *n* = 10), Srd5a3 Wild Type 2 (WT2; *n* = 10), Srd5a3 Knockout 1 (KO1; *n* = 10), and Srd5a3 Knockout 2 (KO2; *n* = 10) Samples. Data produced jointly with Ivan Andújar Martínez and Robert Burock from the Max Planck Institute for Dynamics of Complex Technical Systems. TPH, total peak height; purple, decreased % TPH; green, increased % TPH. *N*-glycan names are adapted from Oxford Nomenclature by GlyXera.

<i>N</i> -glycan structures	<i>N</i> -Glycan Names	Relative Peak Heights (%TPH)			
		WT1	WT2	KO1	KO2
	Man3 Man3[c]	2.526	2.036	4.635	10.132
	Man6	5.989	6.031	9.227	9.541
	Man7[D1]	1.206	1.285	2.009	2.117
	Man7[D3]	2.720	2.741	3.174	4.302
	FA2BG1[3] Man8[D1,D3] Man8 FA2G1F1(1,2)[6]	4.431	4.352	6.297	8.434

	Man9 A4G1 A3G2[2,6] FA2G2	4.261	4.063	9.405	15.782
	FA2BG2S2(2,6)	6.636	6.554	3.754	2.156
	Man3-B Man4↓ A1G0[3] A1G0[6] FA2G1S1(2,6) A2F1(1,3)[6]G1[6]S1 (2,3)[6]	10.038	11.393	6.016	5.033
	A2G2S1(2,6)	2.175	2.385	1.620	0.806
	FA2BG0 FA3G3S1(2,3)[2,6]	4.964	5.862	3.268	1.690

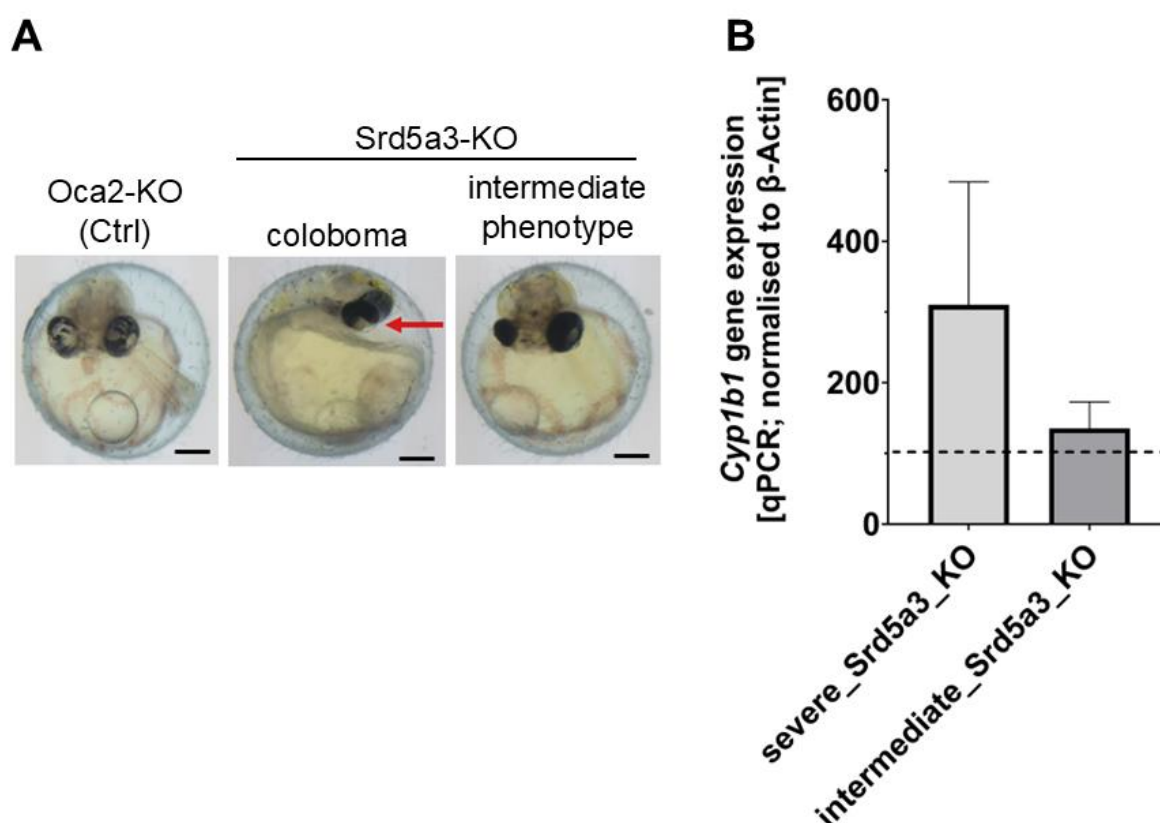
## 6.11 Increased expression of *Cyp1b1* Srd5a3-knock out medaka fish embryos correlating to phenotypical severity

Human CYP1B1 and medaka fish Cyp1b1 showed a 55 % identity on protein level. It could also been shown that human CYP1B1 could rescue a Cyp1b1 deficiency in zebra fish highlighting that its function is evolutionally conserved across species [67]. Hence, Srd5a3-KO medaka fish embryos serve as a reliable model for assessing *Cyp1b1* gene expression in a whole organism and can provide insights applicable to humans.

In zebrafish elevated *Cyp1b1* gene expression has been linked to the development of coloboma. Therefore, I assumed that Srd5a3-KO medaka fish embryos with ophthalmological

abnormalities, primarily coloboma, exhibit an elevated *Cyp1b1* gene expression. I quantified *Cyp1b1* gene expression in *Srd5a3*- and *Oca2*-KO medaka fish embryos seven days post-fertilisation by using qRT-PCR. Embryos which developed a coloboma displayed a strongly elevated *Cyp1b1* expression of +210.14 % (SD:  $\pm 173.88$ ) compared to *Oca2*-KO medaka fish embryos as injection control. In contrast, *Srd5a3*-KO medaka fish embryos with an intermediate phenotype exhibited a similar gene expression with only a slight elevation of +35.4 % (SD:  $\pm 37.22$ ) (Fig. 28A,B).

In conclusion, elevation of the *Cyp1b1* gene expression correlated with the development of coloboma in the *Srd5a3*-KO medaka fish. In addition, the *Cyp1b1* responsive and coloboma-associated gene *Pax6* could be shown to exhibit an elevated expression in SRD5A3-CDG patient-derived fibroblasts. This supported my hypothesis that SRD5A3-CDG related ophthalmological abnormalities could result from elevated CYP1B1 expression.



**Figure 28: Elevated expression of *Cyp1b1* in *Srd5a3*-KO medaka fish embryos with a severe phenotype.**

(A) Images of *Srd5a3*- and *Oca2*-KO medaka fish embryos 7dpf as representatives for the following qRT-PCR analysis to quantify the expression of *Cyp1b1*. Red arrow, coloboma in severely affected embryos. (B) Relative quantification of *Cyp1b1* expression in *Srd5a3*-KO medaka fish embryos (pooled,  $n = 4$ ) compared to *Oca2*-KO (pooled,  $n = 4$ ) as injection control. Expression of  $\beta$ -Actin was used to normalise the Ct values of *Cyp1b1*.

## 6.12 Rescue approach: Double KO of *Srd5a3* and *Cyp1b1* results in lethal phenotype

An increased expression of *Cyp1b1* appears to play a significant role in the pathological development of the eye, contributing to the development of coloboma in *Srd5a3*-KO medaka fish embryos – a common ophthalmological defect associated with SRD5A3-CDG. I hypothesized that an additional knockout (KO) of *Cyp1b1* might rescue the coloboma phenotype, potentially providing a basis for therapeutic strategies. Knockout of *Cyp1b1* did not cause any pathological changes, and the embryos developed similarly to the uninjected controls. However, instead of rescuing the coloboma phenotype, the double KO of *Cyp1b1* and *Srd5a3* led to a significant increase in lethality, with 81.7% mortality observed three days post-fertilization – nearly double the lethality seen in *Srd5a3*-KO embryos alone. In addition, the few embryos surviving more than three days post fertilisation, exhibited severe phenotypes such as a strong development delay, failure to thrive, and ophthalmological abnormalities such as different eye sizes (Tab. 20).

**Table 20: Lethality of *Srd5a3*-, *Srd5a3*- + *Cyp1b1*-KO, and uninjected medaka fish embryos.**

Ratios of vital and lethal embryos caused by a *Srd5a3*-KO, *Srd5a3*+*Cyp1b1*-KO and uninjected medaka fish embryos. Dpf, days post fertilisation.

	<b><i>Srd5a3</i>- + <i>Cyp1b1</i>-KO</b>	<b><i>Srd5a3</i>-KO</b>	<b>Uninjected</b>
<b>Injected</b>	131	119	81
<b>Viable (3 dpf)</b>	24	62	76
<b>Dead (3 dpf)</b>	107	57	5
<b>Lethality (3 dpf)</b>	81.7 %	47.9 %	6.2 %

## 7. Discussion

Glycosylation is an essential modification of protein and lipids that occurs in all living organisms and plays a key role in physiological development and maintaining homeostasis in all organs [14, 15]. Therefore, Congenital Disorders of Glycosylation (CDG), disruptions in the glycosylation pathway, often result in a multisystemic phenotype exhibiting significant clinical manifestations: Including growth failure, developmental delay, and neurological abnormalities as the most common symptoms [16, 41]. Ocular impairments, such as coloboma or retinitis pigmentosa, are also common in a broad variety of CDG types. SRD5A3-CDG is a CDG subtype which displays an excessive occurrence of ophthalmological abnormalities – making them the key clinical diagnostic feature [47, 48]. This made this ultra-rare CDG type to be a suitable model to investigate such impairments as a representative across CDGs. In my study, I used molecular and biochemical approaches in three independent SRD5A3-CDG patient-derived fibroblast cell lines and a generated and established Srd5a3-KO medaka fish embryo model to understand the development of ophthalmological abnormalities and find potential pharmacological targets for therapy options.

### 7.1 Validation confirms SRD5A3-CDG related hypoglycosylation phenotype in SRD5A3-CDG patient derived fibroblasts

The validation of a hypoglycosylation phenotype in the provided cell material was crucial to ensure legit and reproducible results – this lays the cornerstone of investigating ophthalmological abnormalities in CDG which marks the aim of this study. All three SRD5A3-CDG patients suffered from typical CDG-related symptoms, such as overall developmental retardation and problems with vision. IEF of serum transferrin revealed a CDG type-I typical pattern of strong tetra-, di- and asialotransferrin bands [50] indicating a CDG-I deficiency, as expected for SRD5A3-CDG. Mass spectrometric analysis of serum proteins is a growing and efficient tool to obtain a whole serum protein *N*-glycosylation profile of patients – so called *N*-glycoproteomic. This approach was used to detect the hypoglycosylation phenotype of SRD5A3-CDG patient 3. Elevated M3 and M4 peaks were detected and are considered to be accumulation of mannose-3 and mannose-4 *N*-linked oligosaccharides. In addition, the F(6)A2G(4)2S(3)1 peak could be detected in SRD5A3-CDG patient 3 as well as in the internal SRD5A3-CDG control in comparison to the healthy control pool. Future research on SRD5A3-CDG will provide more evidence if fucosylated glycan structures are a appropriate biomarker for this CDG-type.

Validation of LLOs after incorporation of [2-<sup>3</sup>H]mannose into dolichol-bound sugar structures revealed a unique accumulation of intermediate oligosaccharide structures Man5GlcNAc2-PP-



and Man9GlcNAc2-PP-dolichol. This accumulation is attributed to a deficiency in Dol-P-Man and Dol-P-Glc synthesis caused by *SRD5A3* deficiency.[131]

Sanger sequencing of the coding region of the patients' *SRD5A3* genes revealed biallelic variants in all cases. The female Pat. 1 inherited a c.57G>A variant (Variation ID: 96125; Accession: VCV000096125.43) which led to the amino acid change from tryptophane to a premature stop codon (p.Trp19Ter) in exon 1. The two male patients Pat. 2 and 3 inherited both a c.79\_80insGGAA variation which displayed an insertion of a four-base fragment leading to a frameshift and premature stop codon. According to ClinVar, the genetic variation of Pat. 1 was already published and was described as pathogenic. In contrast, the genetic variation in Pat. 2 and 3 is not described, yet. Since the genetic variations occur at an early position in terms of protein sequence, it can be suspected that the maturity of a functional protein is thereby strongly decreased, leading to a reduced or lack of physiological function. Taken together, the hypoglycosylation phenotype of the patients which was verified by IEF and LC-MS analysis and by the investigation of LLO. Together with the clinical presentation of patients, all genetic variants in the *SRD5A3* gene can be considered disease causing.

## 7.2 Lipidomics

Part of the biochemical characterisation of *SRD5A3*-CDG patient-derived fibroblasts was the mass spectrometric quantification of various lipid classes. Although, *SRD5A3*-CDG represents a multisystemic clinical phenotype, this lipidomic analysis revealed only slight differences compared to healthy controls. The amount of cholesterol was similar to controls. This was surprising because of two reasons: Firstly, the dolichol biosynthesis and the biosynthesis of cholesterol depend both on the mevalonate pathway and a deficiency of *SRD5A3* was hypothesised to interfere with the pathway, triggered by metabolite accumulation or feedback loops [17, 101, 102]. Secondly, transcriptome analysis by nCounter revealed significant downregulations of *C14Orf1* or *ERG28*, *DHCR24*, *DHCR7*, *FDFT1*, and *FGFR1* – genes directly and indirectly involved in the biosynthesis of cholesterol. This indicates a discrepancy between the transcriptome and lipidomic analysis data set. Despite that key cholesterol biosynthesis genes, such as *DHCR24*, *DHCR7*, *FDT1*, and *ERG28*, are downregulated other enzymes or pathways might compensate the deficiency [101, 103, 104]. In addition, the protein activity does not directly correlate with the transcription rate. That means, although these genes are downregulated, their activity might still be sufficient to synthesise cholesterol in physiological amounts or they even display increased enzyme activity. Also, a possible accumulation of substrates due to the block in the dolichol biosynthesis pathway might favour the substrate-enzyme kinetics towards the cholesterol biosynthesis. That could be verified in future projects to better understand the regulation of the mevalonate pathway and the biosynthesis of cholesterol in a *SRD5A3*-CDG setting.

However, some lipid classes displayed altered abundances: Lysophosphatidylcholine (LPC) and triacylglycerol (TAG) did reveal increased amounts, whereas phosphatidylglycerol (a/ePG) and alkylphosphatidic acid (a/ePA) were strongly decreased. LPC is known to recruit phagocytes, induced by apoptotic cells and is known to cause demyelination of neurones after injections to mimic and generate multiple sclerosis models for research purposes [132]. Alterations in these aspects could contribute to neurological symptoms, such as lethal microcephaly [133]. Given that SRD5A3-CDG patients suffer from neurodevelopmental dysfunctions, changes in the LPC might contribute to the clinical presentation [134, 135]. Furthermore, accumulations of LPC are known to disturb the integrity of mitochondria and induce apoptosis which consequently could lead to oxidative stress [134]. Oxidative stress could be identified in various CDG types [107]. Hence, it would be interesting to investigate whether accumulations of LPC are a common marker among CDG types which leads to oxidative stress and mitochondrial impairments. PG and PA both belong to the ester phospholipids. PA is known to be an intermediate molecule for the biosynthesis of glycerophospholipids TAG and diacylglycerols (DAG) [136]. Controversially, although PA has been found less abundant, TAG was more abundant whereas DAG remained similar. PG on the other hand is an intermediate product for the biosynthesis of cardiolipin [137, 138]. Cardiolipin is involved in the synthesis of ATP and plays a vital role in the composition of the cellular membrane in mitochondria [138]. Alterations on cardiolipin are associated with Barth syndrome. Barth syndrome is caused by an X-linked variation of the *TAFAZZIN* (*TAZ*) gene which leads to mitochondrial lipid alterations and the development of cardiomyopathy [139]. Yet, there are no reports assuming a connection between glycosylation and Barth syndrome. Still, cardiomyopathy has already been reported multiple times to be present in CDG as well [140-142]. Cardiolipin itself was not quantified in this analysis. Future studies should therefore investigate whether the decreased amount of PG also interferes with the amount of cardiolipin and consequently contribute to the development of cardiomyopathy in CDG.

### **7.3 Elevated expression of CYP1B1 is a molecular key characteristic among different subtypes of CDG**

The human cytochrome P450 superfamily included 57 functional members [143]. In mammals, including human, the CYP1As and CYP1Bs superfamilies are present [144-146]. Their role in the phase I metabolism of endogenous and exogenous substrates, such as the metabolism of steroid hormones, and lipids is common. Additionally, they are involved in the metabolism of carcinogens such as aryl hydrocarbons [146]. Human CYP1B1 displays a special position among those enzymes.

In contrast to most cytochrome P450 monooxygenases, it is expressed extrahepatically, present in almost all organs [77, 80, 81]. Functionally, it is developmentally important for ocular

structures [82]. Under physiological conditions, CYP1B1 mediates the eye development through the metabolism of retinoic acid (RA), a derivative of vitamin A – leading to correct differentiation and development of ocular structures [67, 79, 84]. Clinically speaking, deregulated CYP1B1 expressions are associated with different diseases: Depletion or CYP1B1 deficiency is known to be associated with development of primary congenital glaucoma. Primary congenital glaucoma comprises neurodegenerative ocular disorders, characterized by visual field defects, retinal ganglion cell death, and progressive degeneration of the optic nerve. Pathogenic variants of CYP1B1 associated with primary congenital glaucoma often occur in highly conserved regions of the gene, affecting the enzyme's stability and function [80, 81, 84-86]. Elevated expression of CYP1B1 on the other hand is also known with severe diseases: It is one of the key enzymes involved in the hydroxylation of oestrogens which is known to activate some carcinogens. In addition, it could be shown that carcinogens such as 7,12-dimethylbenz[a]anthracene is bioactivated by CYP1B1. All over, elevated levels of CYP1B1 can be found in a broad variety of cancer tissue, including brain, breast, colon, ovarian, and prostate cancers [81, 87, 88, 147, 148]. It is suspected that elevated levels of CYP1B1 leads to increased cell proliferation and metastasis which together promote tumor growth [149, 150]. Besides its association in the development of multiple malign tumors, elevated expression of CYP1B1 is also found to lead to coloboma development: In a zebrafish model it could be shown that overexpression of CYP1B1 inhibited the cell survival in the ventral ocular fissure, prevented fissure closure and therefore leads to coloboma through a retinoic acid-independent pathway [67]. This was of particular interest, since coloboma are a very common ocular symptom in SRD5A3-CDG patients [47, 62]. To investigate this further, I therefore quantified *CYP1B1* gene expression in SRD5A3-CDG patient-derived fibroblasts using three approaches: nCounter analysis, whole transcriptome analysis and qRT-PCR. All transcript-based analysis revealed consistent results, showing significantly elevated gene. nCounter analysis showed a significant ~2.5-fold increased expression which can be considered biological relevant. This upregulation was further confirmed by qRT-PCR, which also detected a strong increase in expression. Although the wh not reach statistical significance ( $P$ -value = 0.064048756), it s Discussion upregulation, supporting the results from the nCounter and qRT-PCR analyses.

SRD5A3 is involved in the *de-novo* biosynthesis of dolichol, just as dehydrodolichyl diphosphate synthase (DHDDS) and mevalonate kinase (MVK). DHDDS is catalysing cis-prenyl chain elongation to synthesise the dolichol polyprenyl backbone and MVK is phosphorylating mevalonate to form mevalonate-5-phosphate [17, 151]. Furthermore, retinitis pigmentosa, retinal degeneration and other ocular findings are characteristic features of these CDG deficiencies [151-154]. Due to the overlapping ophthalmological abnormalities and involvement in the same biosynthesis pathway, I also quantified *CYP1B1* gene expression in

DHDDS- and MVK-CDG fibroblasts and found them to be elevated in both cases as well, which supports my assumption that the increased expression of *CYP1B1* correlates with the clinical ophthalmological presentation. Most notably, mass spectrometry analysis based on a “shotgun-“proteomic approach revealed that the protein amount of CYP1B1 was increased in a broad variety of CDG types, including early (PMM2-, DHDDS-, ALG1-, ALG3-, and MPDU1-CDG) and late defects (SLC35A1-, SLC35A2-, SLC35C1-, and B4GALT1-CDG) as well as fucosylation defects (GFUS-CDG). This let assume a yet unknown general effect of hypoglycosylation on the expression of CYP1B1 on transcript and protein level.

According to bioinformatical predictions (NetNGlyc; DTU Health Tech) there are two potential *N*-glycosylation sites at position N267 and N519 with a probability of 67 % and 69 %, respectively. Still, there is no signal peptide which makes it highly unlikely to be glycosylated and there is no literature evidence that states CYP1B1 to be a glycoprotein or being dependent on glycosylation-related pathways and interaction partners. CYP1B1 is localised in the ER and mitochondria. It could therefore be assumed that ER-associated defects may have an impact on CYP1B1 due to proximity in the same cellular compartment. Instead, also CDG types with impaired proteins localised in the cytoplasm (PMM2-CDG) and Golgi apparatus (SLC35A1-, SLC35A2-, SLC35C1-, and B4GALT1-CDG) exhibit elevated CYP1B1 expression – PMM2-CDG fibroblasts have even the highest protein amount and represent by far the most common type of CDG.

Hence, I assumed that CYP1B1 is no glycoprotein nor being dependent on glycosylation known in literature, and its elevated expression is rather be caused by deregulations or compensatory mechanisms caused by general defects regarding glycosylation. My findings reveal CYP1B1’s elevated expression as a molecular alteration being present and provides a potent basis for drug development or drug repurposing to reduce ophthalmological abnormalities across many types of CDG.

#### **7.4 SRD5A3-KO medaka fish model: A suitable model to confirm organism wide elevated expression of CYP1B1’s ortholog, correlating to the development of coloboma**

Examining CYP1B1 expression in SRD5A3-CDG patient-derived fibroblasts provided a strong hint that glycosylation defects lead to increased expression. Still, cultured fibroblasts are only an artificial and inadequate model to investigate CYP1B1 depending ophthalmological abnormalities. Therefore, I generated a *Srd5a3*-KO medaka fish embryo model by microinjection in a CRISPR/Cas9 approach. Since CYP1B1 is expressed extrahepatically and is presents in most tissues, this model enables the quantification of its expression throughout

the entire organism, including very prominent ocular structures in fish. Human CYP1B1 and its medaka fish ortholog exhibit ~ 50 % identical nucleotide sequence, according to NCBI blast. However, it could be shown that CYP1B1's function is conserved between human and teleost fish (e.g. medaka and zebra fish). Depletion of Cyp1b1 in zebrafish could be rescue by induction of human CYP1B1 [67]. This highlights the medaka fish embryo model as very much suitable for investigating the CYP1B1 expression in an entire organism and its contribution to ophthalmological abnormalities.

Depletion of *Srd5a3* in medaka fish embryos mimicked several clinical characteristics of SRD5A3-CDG patients, including failure to thrive, developmental delays, coagulopathy, facial dysmorphology, heart anomalies, and eye abnormalities [47]. Phenotypes of the *Srd5a3*-KO embryos presented with a 1:1:1 ratio of mild, intermediate and severe phenotype. Fish embryos rely on nutrients provided by the mother animal through the yolk. Yolk consists of fat, carbohydrates, vitamins, minerals, and proteins, including glycoproteins. Hence, *Srd5a3*-KO medaka fish embryos can experience a maternal contribution which can partly rescue the hypoglycosylation phenotype, depending on the yolk quantity and quality. In addition, KO performed by microinjection usually leads to mosaic mutations, meaning some cells are and others are not genetically modified. The degree of modified and unmodified cells (mosaic composition) also interferes with the severity of phenotype, depending on impairment on organ functioning and ratio.[155] Abnormalities induced by off-target effects of CRISPR/Cas9 and lesions caused by microinjections could be excluded widely by the parallel injection of *Oca2*-KO as internal control. Sanger sequencing confirmed a double strand break induced at the target site of the gRNAs in the *Srd5a3* knockouts which led to a significant reduced *Srd5a3* transcript level, subsequently. To further elucidate whether the *Srd5a3* KO embryos were affected on the functional level as well, lectin blot analysis and *N*-glycan studies by XCE-GE-LIF of whole embryo material were carried out. Although only WGA lectin blots indicated a strong decrease of complex and mannose rich type *N*-glycans, the *N*-Glycomic analysis revealed a variety of altered accumulations of *N*-glycan structures. The *Srd5a3*-KO medaka fish hatchlings revealed increased amounts of paucimannose- (Man3), oligomannose- (Man6–Man9) type *N*-glycans as well as glucosylated oligomannose-type *N*-glycans. Furthermore, they exhibited lower amounts of Man4 and complex-type *N*-glycans compared to the wild types. Since the *Srd5a3*-KO presented with a *N*-hypoglycosylation phenotype, I claimed that the KO of *Srd5a3* is functional and has finally resulted in the observed clinical characteristics.

CYP1B1 plays a crucial role in regulating ocular fissure closure, which is essential for preventing coloboma. It is expressed in retinal and retinal pigment epithelial cells surrounding the ocular fissure [67]. Notably, corresponding to the severity of the phenotype and presence

of coloboma, the medaka *Cyp1b1* expression was strongly elevated. While embryos exhibiting coloboma showed elevated levels of gene expression, those with an intermediate phenotype (e.g., characterized by developmental delay) displayed gene expression levels comparable to the *Oca2*-KO injection control. Previous studies have demonstrated that induced overexpression of *Cyp1b1* in zebrafish leads to the development of coloboma. This phenotype arises through a retinoic acid (RA)-independent mechanism, in which *Cyp1b1* modulates the expression of key developmental genes such as *vsx2* and *pax6* [67]. Consistently, fibroblasts derived from SRD5A3-CDG patients also showed increased expression of PAX6, as revealed by whole-transcriptome analysis. This provides a potential link between elevated CYP1B1 levels and altered PAX6 expression, which may contribute to the pathogenesis of coloboma. In zebrafish models, *Pax6* expression is known to be regulated by *Cyp1b1*. Clinically, PAX6 deficiency is associated with ophthalmological abnormalities [67]. Whether increased PAX6 expression similarly contributes to ocular defects in SRD5A3-CDG remains unclear but warrants further investigation. My findings underscore the regulatory role of CYP1B1 in ocular development—particularly in coloboma formation—and suggest that its effects are mediated through mechanisms independent of RA signalling.

Therefore, it is highly likely that elevated CYP1B1 levels, resulting from severe *N*-glycosylation defects, contribute to coloboma development in SRD5A3-CDG through alterations in key ocular developmental genes, such as *PAX6*. Furthermore, the elevation of *Cyp1b1* is correlating to the severity caused by a *Srd5a3* deficiency.

## **7.5 Deregulated AhR and Nrf2/NFE2L2 signalling pathway are leading to increased oxidative stress in SRD5A3-CDG**

Oxidative stress is commonly observed in fibroblasts derived from CDG-patients, such as in PMM2-, ATP6AP1-, ALG8-, RFT1-, and SLC10A7-CDG [107]. This stress is likely driven by chronic endoplasmic reticulum (ER) stress and increased reactive oxygen species (ROS) levels [107]. FACS analysis using CellROX™ quantification revealed that also SRD5A3-CDG patient-derived fibroblasts exhibit increased oxidative stress – further supporting that oxidative stress is most likely to be associated with general glycosylation defects across an even more broader range of different CDG types.

*Nrf2/NFE2L2* is known to be the key transcription factor to induce the antioxidative response and maintain homeostasis [97, 98]. Validating its expression was crucial to understand if SRD5A3-CDG cells can sensor oxidative stress and respond to it by activating the antioxidative response through *Nrf2/NFE2L2*. Although *Nrf2/NFE2L2*'s gene expression and protein amount were similar to control, expression of a variety of downstream genes was drastically decreased,

including *SOD3*, *GSTM3-5*, *GSTK1*, *GPX3/7*, *PRDX2*, and *NQO1*. *GSTM3-5*, *GSTK1*, and *GPX3/7* which are involved in the metabolism of glutathione – the main ROS scavenger in human cells which marks the final product of the Nrf2/NFE2L2 antioxidative pathway. By quantifying the total glutathione level in the cell, it could also be shown that its amount in Pat. 1 was strongly reduced, which is consistent with the downregulation of glutathione-related genes. This provides strong hints that Nrf2/NFE2L2 mediated gene induction is impaired in SRD5A3-CDG, leading to reduced antioxidative capacity and thus tending to undergo increased oxidative stress. In addition, it is arguable that the sensor ability for oxidative stress is decreased since the Nrf2/NFE2L2's expression remains low and is not upregulated as it would be expected under physiological conditions. Western blot analysis of Nrf2/NFE2L2 revealed no expression changes, consistent with gene expression, but points out that its posttranslational modification might be affected in SRD5A3-CDG. Notably, Nrf2/NFE2L2 is not reported to be glycosylated and bioinformatic predictions that there is no signal peptide, indicating no *N*-glycosylation sites in Nrf2/NFE2L2. In addition, a PNGase F-mediated digestion did not reveal altered band pattern. A well understood posttranslational modification are ubiquitin attachments, transferred by KEAP1 [156]. KEAP1 works as the regulator of Nrf2/NFE2L2 which leads to its proteasomal degradation by ubiquitination. Lack of ubiquitinated Nrf2/NFE2L2 can therefore associated with increased activity, which is contradictory to decreased downstream gene expression, indicating that the Nrf2/NFE2L2 associated gene induction is impaired in SRD5A3-CDG. KEAP1 is mainly localised in the cytoplasm and partially in the nucleus. Immunofluorescence microscopy and Western blot analysis after nucleus isolation revealed decrease accumulations of KEAP1 in the nucleus. Lack of nuclear KEAP1 is not typically associated with a single, specific clinical feature. However, disruptions in the KEAP1-Nrf2 pathway are associated with neurological disorders such as Parkinson and Alzheimer disease [157, 158]. KEAP1's role in controlling oxidative stress and inflammation response is critical in protecting neuronal health. Impairments in this system may contribute to the development or progression of these diseases. Therefore, it can be hypothesized that the Nrf2/NFE2L2 pathway is impaired due to insufficient stress sensing or reduced activation of target genes. This leads to reduced antioxidant capacity and increased oxidative stress. A lack of ubiquitination, mediated by KEAP1, may serve as a compensatory mechanism to restore pathway activity, potentially allowing cells to sustain basal function, which is critical for survival. Although the issue of posttranslational modifications of Nrf2/NFE2L2 in SRD5A3-CDG patient-derived fibroblasts remains unsolved, the observed decrease in KEAP1 nuclear accumulation suggests lack of ubiquitination of Nrf2/NFE2L2.

Nrf2/NFE2L2 is not only known to induce the antioxidative response but stands also in a reciprocal relationship to the transcription factor Aryl hydrocarbon receptor (AhR) [96]. AhR is

a ligand-dependent transcription factor which response to both environmental and endogenous signals, such as 3-Methylcholanthrene (3MC), 2,3,7,8-tetrachlorodibenzo-p-dioxin (TCDD), and kynurenine metabolites, to maintain cellular homeostasis and act as a sensor for environmental changes [88-92]. It is known to play a crucial role in a variety of biological processes, including development (particularly in ocular tissues), immunity, hematopoiesis, and drug detoxification [89-92]. Dysregulation of this pathway has been linked to several eye-related diseases, such as age-related macular degeneration, autoimmune uveitis, retinitis pigmentosa, as well as certain cancers [90, 92-94]. Under physiological conditions, AhR undergoes a conformational change after binding to a ligand, translocates to the nucleus and heterodimerizes with the Aryl hydrocarbon receptor nuclear translocator (ARNT), leading to its gene inducing activity at the xenobiotic response elements (XRE) in DNA. AhR is controlled through its endogenous regressor, Aryl hydrocarbon receptor repressor (AhRR) which competes to heterodimerize with ARNT. Among AhR-responsive genes are cytochrome P450 enzymes like *CYP1A1*, *CYP1A2*, and *CYP1B1* [95, 96, 159]. It could be shown that *Nrf2*/NFE2L2 can induce AhR by binding to the CsMBE at position –230 of the AhR promoter, enhancing its expression: In *Nrf2*-knockout mouse embryonic fibroblasts, the expression of *Ahr*, *Cyp1a1*, and *Cyp1b1* was abolished. On the other hand, it is proposed that AhR-mediated upregulation of cytochrome P450 enzymes leads to increased production of free radicals and ROS, which in turn activate *Nrf2*/NFE2L2. Thereby, *Nrf2*/NFE2L2 and AhR influence their gene expression in a reciprocal relationship [96]. In SRD5A3-CDG patient-derived fibroblasts, the expression of the *Ahr* gene is significantly reduced, alongside many other target genes of *Nrf2*/NFE2L2, as described above. Given that AhR acts as a cellular stress sensor and SRD5A3-deficient cells experience increased cellular stress, I hypothesize that this condition would typically lead to increased AhR expression – as previously described in the context of cancer development [160, 161]. However, the reduced *Nrf2*/NFE2L2 activity observed may contribute to the lower expression of AhR. Interestingly, the expression of AhR's repressor, AhRR, is also significantly reduced – potentially working as a compensatory mechanism, which could result in increased AhR activity despite its reduced overall expression. Furthermore, ARNT expression remains physiologically, suggesting that the translocation of AhR and ARNT is not impaired. Nonetheless, factors responsible for the pronounced upregulation of CYP1B1 in the SRD5A3-CDG context remain unclear. Decreased expression of AhR could be also a trigger for very low cell proliferation as observed in maintaining and growing of SRD5A3-CDG patient-derived fibroblasts. It is well studied that AhR is one of the key players to promote cell proliferation, regulation of the cell cycle and cell proliferation.



## 7.6 Non-canonical or alternative pathways induce the elevated expression of CYP1B1 in a hypoglycosylation context

In the context of SRD5A3-CDG, patients' fibroblasts as well as KO medaka fish embryos exhibit a significantly elevated expression of CYP1B1. In addition, also other CDG patient-derived fibroblasts (DHDDS-, MVK-, PMM2-, DHDDS-, GFUS-, ALG3, ALG1-, MPDU1-, SLC35A2-, SLC35A1-, SLC35C1-, and B4GALT1-CDG) showed an elevated expression, assuming that deregulated expression is associated with general glycosylation defects. The fish embryo model could further show that the elevated expression corresponds to the severity of defect: The stronger the hypoglycosylation phenotype and development of coloboma, the higher the CYP1B1 expression.

To date, many studies confirmed AhR as the main transcription inducer of CYP1B1 by binding to the xenobiotic-response element (XRE) [88, 162]. Although AhR typically regulates CYP1B1 expression, its reduced levels suggest the involvement of an alternative regulatory mechanism for the observed elevation of CYP1B1. This could involve stress-response pathways that operate independently of the AhR-*Nrf2* interaction. This non-canonical regulatory mechanism might potentially serve as a cellular adaptation to hypoglycosylation-related stress. This proposed the existence of a yet unidentified endogenous substrate for *Cyp1b1* in the eye. In addition, beside CYP1B1 also the gene expression of CYP1A1 is mainly controlled by AhR. In contrast to CYP1B1, the expression of CYP1A1 was not deregulated, suggesting that the AhR-mediated induction of CYP1A1, and thus also CYP1B1, is not impaired and works physiologically. This further supports the idea that elevated expression of CYP1B1 is not caused through the canonical AhR pathway but rather non-canonical or alternative pathways which are responsive to glycosylation-mediated defects.

Potential alternative pathways which might induce the elevated expression of CYP1B1 in the context of glycosylation defects might be 3',5'-cyclic adenosine monophosphate (cAMP)-mediated pathways, hormonal regulated by estrogen receptors or inflammatory cytokines, such as tumor necrosis factor- $\alpha$  (TNF- $\alpha$ ) and interleukin-6 (IL-6) [125, 126]. The 5' upstream regulatory sequences of the mouse *Cyp1b1* gene contain motifs linked to steroidogenic transcription factor-1, which are involved in cAMP-dependent transcriptional activation of genes. CYP1B1 is consistently expressed in steroidogenic tissues, where its regulation is primarily influenced by hormones that control cAMP levels. CYP1B1 plays a key role in metabolizing 17 $\beta$ -estradiol, generating several metabolites, with 2- and 4-hydroxyestradiol accounting for 75 - 80% of the products. Furthermore, research has demonstrated that 17 $\beta$ -estradiol induces CYP1B1 expression in estrogen receptor (ER)-

positive MCF-7 breast cancer cells. This induction occurs through the direct interaction of ER- $\alpha$  with the estrogen response element (ERE) in the *CYP1B1* promoter region [163]. Interestingly, the estrogen receptor is indeed a glycoprotein with an O-linked GlcNAc glycosylation site at position 10. The expression of the corresponding gene, estrogen receptor 1 (*ESR1*) is significantly decreased in SRD5A3-CDG patient-derived fibroblasts. Since *ESR1* is low expressed, it is most unlikely that the elevated expression of *CYP1B1* is estrogen-mediated. Nevertheless, further research should be investigating the role of estrogen in SRD5A3-CDG and its potential clinical relevance since *CYP1B1* and the *ESR1* are significantly deregulated.

TNF- $\alpha$  is also known to induce the expression of *CYP1B1* [126]. But just as for estrogen, it is most unlikely that TNF- $\alpha$  is causing elevation of *CYP1B1*'s expression. IL-6 is highly upregulated in SRD5A3-CDG fibroblasts and also known to induce the expression of *CYP1B1* [126]. IL-6 is a glycoprotein carrying described- and O-glycans [164]. Its proper function can therefore be strongly questioned in the context of glycosylation defects such as SRD5A3-CDG. In addition, it is common among different types of CDG that patients suffer from dysfunctions of the immune system and are potentially immunodeficient [165]. Hence, immune system-mediated expression of *CYP1B1* through IL-6 and TNF- $\alpha$  is in total also unlikely. Yet, it cannot surely be ruled out since dysfunctions could potentially lead to unintentional consequences and IL-6 is indeed significantly upregulated in SRD5A3-CDG patient-derived fibroblasts.

Taken together, neither the commonly known key inducer AhR nor the rather unconventional inducers as estrogen- and immune system-mediated pathways through IL-6 and TNF- $\alpha$  seem to be a convincing cause to elevate expression of *CYP1B1*. Instead, I propose that a yet unidentified pathway which is associated with general glycosylation defects is activated or prone to induce an elevated expression of *CYP1B1* – independent of the type of CDG.

## **7.7 Potential therapeutic approach regarding ophthalmological abnormalities in CDG**

Patients suffering from CDG and their relatives are in a challenging situation – yet medical treatment is very limited to be supportive for most CDG-types and has only little good prospects due to the complexity of the diseases. Elevated expression of *CYP1B1* is usually observed in the development of cancer tissue [81, 87, 147]. Drug-screening studies suggested to reduce the activity and expression of *CYP1B1* which might be used in anti-cancer treatments and reduce cancer proliferation, therefore leading to extended survival. This led to the development of a variety of *CYP1B1*-specific inhibitory drugs, such as flavonoids, trans-stilbenes, estradiol derivatives, and carbazoles [147]. Most of these drugs are not suitable to

be applied for CDG patients because of their low safety profile – which is sufficient for cancer but not CDG-patients. For CDG patients a drug is needed which has a good safety profile and an efficiency to reduce CYP1B1 expression or activity back to physiological levels. Wang *et al.* proposed 2020 the re-assessment of a well-established drug named ‘carvedilol’ to be used as a novel CYP1B1 inhibitor. Carvedilol is a beta-blocker which is originally being used to treat high blood pressure and heart failure. Wang *et al.* could show that carvedilol exhibits an inhibitory activity against CYP1B1 with an  $IC_{50}$  of 1.11  $\mu$ M, according to ethoxyresorufin-O-deethylase (EROD) assay – EROD is an assay to evaluate the dioxin-like activity of a single substance [166]. Application of carvedilol could reduce the potentially pathological expression of CYP1B1 and hence improve the eye development, if applied at an early stage on CDG patients. Still, there are issues regarding this novel idea: The benefit/risk ratio of carvedilol is yet only validated in adults, leading to a drug authorization only for adults and the effectivity on eye development of a reduced CYP1B1 expression in the context of CDG is not yet proven and should be analysed in CDG animal models first.

I tested three approaches to reduce the Cyp1b1 in the Srd5a3-KO medaka fish model. The most comprehensive one was a double knock-out of Srd5a3 and Cyp1b1. Whereas the single knock-out of Cyp1b1 led to no pathological phenotype, the double knock-out was lethal for most embryos – which was not predicted. On the one hand the double knock-out did apparently not rescue the ophthalmological phenotype. On the other hand, it became obvious that Cyp1b1 was crucial for surviving in the context of a Srd5a3 deficiency and therefore has another important and still unknown role in metabolism. This finding provided evidence that the elevation of Cyp1b1's expression is a reasonable compensatory mechanism or crucial adaption to the Srd5a3-KO. Noteworthy, a CRISPR/Cas9-mediated KO leads to a mosaic but highly effective Cyp1b1 deficiency in affected cells which might have led to the lethal phenotype.

In contrast, CYP1B1-specific inhibitors can ensure a more sophisticated approach by only diminishing but not erasing its activity and expression, respectively. Regrettably, carvedilol led to strong precipitation in ERM fish media. Since these could not be dissolved even by using detergents, carvedilol could not be tested in Srd5a3-KO medaka fish embryos. Instead, 2,3',4,5'-Tetramethoxystilbene (TMS), a highly selective CYP1B1 inhibitor with an  $IC_{50}$  of 6 nM for human cell growth, was used. Applying 0.8 nM TMS to the cell media and refreshing the media every two days did not lead to any phenotypical change. Neither did an application of ~ 0.76 nM microinjected TMS into the fertilised oocyte changed the phenotype which led to the assumption that the Cyp1b1 fish ortholog is not homologous enough for the inhibitor. The Srd5a3-KO medaka fish embryo model might therefore not be suitable for drug screening to reduce Cyp1b1 to physiological level to improve the ocular development in the context of

Srd5a3 deficiency. Hence, I propose to validate the effects of CYP1B1 selective inhibitors in other, more suitable model organisms. The efficiency and effectiveness of TMS and carvedilol were already validated in rats and mice.[167-169] Multiple mouse models with Pmm2 deficiency, mimicking PMM2-CDG, are already established. Since PMM2-CDG patient-derived fibroblasts also exhibit elevated protein levels of CYP1B1, the ophthalmological effects of a drug-delivered CYP1B1 reduction could easily be validated in those mice [170-172].

## 8. Outlook

My findings indicate that increased CYP1B1 expression may play a significant role in the eye-related issues seen in SRD5A3- and other types of CDG, which suggests a broader hypoglycosylation cause for this elevation. The interactions between the AhR and *Nrf2*/NFE2L2 pathways suggest a complex regulatory network that may be disrupted in CDG and CYP1B1 might be elevated by a non-canonical pathway, associated with a hypoglycosylation environment. Future research should focus on understanding how CYP1B1 is deregulated in CDG, particularly in relation to oxidative and ER stress pathways, to identify potential treatment options for managing eye problems in affected patients.

My study already gives strong evidence of a relationship between the development of ophthalmological abnormalities and elevated expression of CYP1B1. However, I only quantified and validated the expression of transcript and protein. Yet, there is lack of knowledge about CYP1B1's activity in the context of hypoglycosylation phenotypes. Since CYP1B1 is a very well investigated enzyme, there are a couple of activity assays commercially available – e.g. the luminescence-based P450-Glo™ CYP1B1 Assay System by Promega. Quantifying the activity of CYP1B1 would complement the expression assays and allow more in detail understanding. In addition, the potential role of IL-6 as a glycoprotein in regulation of CYP1B1 might also reveal interesting and new insights.

Alongside the development of coloboma also retinitis pigmentosa is a very common symptom among a broad variety of different CDG types. The *Srd5a3*-KO medaka fish embryo model could further be used to investigate apoptosis rates of photoreceptors in the retina. According to Gücüm, et al. a terminal deoxynucleotidyl transferase dUTP nick end labelling (TUNEL) could be performed [105]. TUNEL staining marks apoptotic cells, which is a characteristic of photoreceptors in retinitis pigmentosa. In a *Alg2*-KO in medaka fish it could already been shown that the hypoglycosylation phenotype leads to increased rod photoreceptor loss. Hence, also the *Srd5a3*-KO might suffer from rod photoreceptor loss – whether this also correlates with the elevated expression of *Cyp1b1* unresolved, yet.

Regarding therapeutic approaches, inhibition of *Cyp1b1* did not reveal in a reduction of ophthalmological abnormalities in the medaka fish model which might be due to structural differences among human and medaka fish. New therapeutic approaches (e.g. by using carvedilol) should be conducted in a mammalian model. Since PMM2-CDG fibroblasts also exhibit elevated expression of *Cyp1b1*, an already established PMM2-KO mouse model could be used to investigate ophthalmological abnormalities after reducing *Cyp1b1*'s activity by carvedilol or TMS. If successful, carvedilol might be applied as off-label drug for children to improve the ocular development.

## 9. References

1. Ng, B.G. and H.H. Freeze, *Perspectives on Glycosylation and Its Congenital Disorders*. Trends Genet, 2018. **34**(6): p. 466-476.
2. Pradeep, P., H. Kang, and B. Lee, *Glycosylation and behavioral symptoms in neurological disorders*. Transl Psychiatry, 2023. **13**(1): p. 154.
3. Ohtsubo, K. and J.D. Marth, *Glycosylation in cellular mechanisms of health and disease*. Cell, 2006. **126**(5): p. 855-67.
4. Nothaft, H. and C.M. Szymanski, *Protein glycosylation in bacteria: sweeter than ever*. Nat Rev Microbiol, 2010. **8**(11): p. 765-78.
5. Breitling, J. and M. Aebi, *N-linked protein glycosylation in the endoplasmic reticulum*. Cold Spring Harb Perspect Biol, 2013. **5**(8): p. a013359.
6. Wilson, M.P., et al., *A pseudoautosomal glycosylation disorder prompts the revision of dolichol biosynthesis*. Cell, 2024. **187**(14): p. 3585-3601 e22.
7. Minakata, S., et al., *Protein C-Mannosylation and C-Mannosyl Tryptophan in Chemical Biology and Medicine*. Molecules, 2021. **26**(17).
8. Hirata, T., et al., *ER entry pathway and glycosylation of GPI-anchored proteins are determined by N-terminal signal sequence and C-terminal GPI-attachment sequence*. J Biol Chem, 2022. **298**(10): p. 102444.
9. Lu, H., Y. Zhang, and P. Yang, *Advancements in mass spectrometry-based glycoproteomics and glycomics*. National Science Review, 2016. **3**(3): p. 345-364.
10. Lauc, G., et al., *Mechanisms of disease: The human N-glycome*. Biochim Biophys Acta, 2016. **1860**(8): p. 1574-82.
11. Sairam, M.R., *Role of carbohydrates in glycoprotein hormone signal transduction*. FASEB J, 1989. **3**(8): p. 1915-26.
12. Marth, J.D. and P.K. Grewal, *Mammalian glycosylation in immunity*. Nat Rev Immunol, 2008. **8**(11): p. 874-87.
13. Alavi, A. and J.S. Axford, *Sweet and sour: the impact of sugars on disease*. Rheumatology (Oxford), 2008. **47**(6): p. 760-70.
14. Moremen, K.W., M. Tiemeyer, and A.V. Nairn, *Vertebrate protein glycosylation: diversity, synthesis and function*. Nat Rev Mol Cell Biol, 2012. **13**(7): p. 448-62.
15. Spiro, R.G., *Protein glycosylation: nature, distribution, enzymatic formation, and disease implications of glycopeptide bonds*. Glycobiology, 2002. **12**(4): p. 43R-56R.
16. Lefeber, D.J., et al., *Congenital Disorders of Glycosylation*, in *Essentials of Glycobiology*, A. Varki, et al., Editors. 2022: Cold Spring Harbor (NY). p. 599-614.
17. Buhaescu, I. and H. Izzedine, *Mevalonate pathway: a review of clinical and therapeutical implications*. Clin Biochem, 2007. **40**(9-10): p. 575-84.
18. Hudson H. Freeze, M.B., Natasha E. Zachara, Gerald W. Hart, and Ronald L. Schnaar, *Chapter 5 Glycosylation Precursors*, C.R. Varki A, Esko JD, et al., Editor. 2022, Cold Spring Harbor Laboratory Press.
19. Wang, N., et al., *Alg mannosyltransferases: From functional and structural analyses to the lipid-linked oligosaccharide pathway reconstitution*. Biochim Biophys Acta Gen Subj, 2022. **1866**(5): p. 130112.
20. Varelas, X., M.P. Bouchie, and M.A. Kukuruzinska, *Protein N-glycosylation in oral cancer: dysregulated cellular networks among DPAGT1, E-cadherin adhesion and canonical Wnt signaling*. Glycobiology, 2014. **24**(7): p. 579-91.
21. Quelhas, D., et al., *RFT1-CDG: Absence of Epilepsy and Deafness in Two Patients with Novel Pathogenic Variants*. JIMD Rep, 2019. **43**: p. 111-116.

22. Shrima, S., N.A. Cherepanova, and R. Gilmore, *Cotranslational and posttranslational N-glycosylation of proteins in the endoplasmic reticulum*. Semin Cell Dev Biol, 2015. **41**: p. 71-8.
23. Mukherjee, M.M., et al., *Selective bioorthogonal probe for N-glycan hybrid structures*. Res Sq, 2023.
24. Ramirez, A.S., et al., *Molecular basis for glycan recognition and reaction priming of eukaryotic oligosaccharyltransferase*. Nat Commun, 2022. **13**(1): p. 7296.
25. Shimada, S., et al., *Clinical, biochemical and genetic characteristics of MOGS-CDG: a rare congenital disorder of glycosylation*. J Med Genet, 2022.
26. De Masi, R. and S. Orlando, *GANAB and N-Glycans Substrates Are Relevant in Human Physiology, Polycystic Pathology and Multiple Sclerosis: A Review*. Int J Mol Sci, 2022. **23**(13).
27. Sakhi, S., et al., *MAN1B1-CDG: Three new individuals and associated biochemical profiles*. Mol Genet Metab Rep, 2021. **28**: p. 100775.
28. Iwamoto, S., et al., *Reconstructed glycan profile for evaluation of operating status of the endoplasmic reticulum glycoprotein quality control*. Glycobiology, 2013. **23**(1): p. 121-31.
29. Tu, H.C., et al., *Up-regulation of golgi alpha-mannosidase IA and down-regulation of golgi alpha-mannosidase IC activates unfolded protein response during hepatocarcinogenesis*. Hepatol Commun, 2017. **1**(3): p. 230-247.
30. Pamela Stanley, K.W.M., Nathan E. Lewis, Naoyuki Taniguchi, and Markus Aebi, *Chapter 9 N-Glycans*, C.R. Varki A, Esko JD, et al., Editor. 2022, Cold Spring Harbor Laboratory Press.
31. Stanley, P., *Golgi glycosylation*. Cold Spring Harb Perspect Biol, 2011. **3**(4).
32. Chen, Y., et al., *Galactosyltransferase B4GALT1 confers chemoresistance in pancreatic ductal adenocarcinomas by upregulating N-linked glycosylation of CDK11(p110)*. Cancer Lett, 2021. **500**: p. 228-243.
33. Harduin-Lepers, A., et al., *The animal sialyltransferases and sialyltransferase-related genes: a phylogenetic approach*. Glycobiology, 2005. **15**(8): p. 805-17.
34. Henslee, A.B. and T.A. Steele, *Combination statin and chemotherapy inhibits proliferation and cytotoxicity of an aggressive natural killer cell leukemia*. Biomark Res, 2018. **6**: p. 26.
35. Maier, C.R., et al., *USP28 controls SREBP2 and the mevalonate pathway to drive tumour growth in squamous cancer*. Cell Death Differ, 2023. **30**(7): p. 1710-1725.
36. Moutinho, M., M.J. Nunes, and E. Rodrigues, *The mevalonate pathway in neurons: It's not just about cholesterol*. Exp Cell Res, 2017. **360**(1): p. 55-60.
37. Haeuptle, M.A., et al., *Improvement of dolichol-linked oligosaccharide biosynthesis by the squalene synthase inhibitor zaragozic acid*. J Biol Chem, 2011. **286**(8): p. 6085-91.
38. Jaeken, J. and G. Matthijs, *Congenital disorders of glycosylation*. Annu Rev Genomics Hum Genet, 2001. **2**: p. 129-51.
39. Peanne, R., et al., *Congenital disorders of glycosylation (CDG): Quo vadis?* Eur J Med Genet, 2018. **61**(11): p. 643-663.
40. Thiel, C., et al., *Screening for congenital disorders of glycosylation in the first weeks of life*. J Inherit Metab Dis, 2013. **36**(5): p. 887-92.
41. Chang, I.J., M. He, and C.T. Lam, *Congenital disorders of glycosylation*. Ann Transl Med, 2018. **6**(24): p. 477.
42. Francisco, R., et al., *Congenital disorders of glycosylation (CDG): state of the art in 2022*. Orphanet J Rare Dis, 2023. **18**(1): p. 329.

43. Hall, P.L., et al., *Sensitivity of transferrin isoform analysis for PMM2-CDG*. Mol Genet Metab, 2024. **143**(1-2): p. 108564.
44. Jaeken, J., et al., *Familial psychomotor retardation with markedly fluctuating serum prolactin, FSH and GH levels, partial TBG-deficiency, increased serum arylsulphatase A and increased CSF protein: a new syndrome?*: 90. Pediatric Research, 1980. **14**(2): p. 179-179.
45. Himmelreich, N., Lübbehuisen, J., Körner, C., Lefeber, D.J., Thiel, C., *Congenital Disorders of Glycosylation*. 2024.
46. Lefeber, *Chapter 45 Congenital Disorders of Glycosylation*, in *Essentials of Glycobiology [Internet]*. 4th edition. 2022.
47. Kamarus Jaman, N., et al., *SRD5A3-CDG: Emerging Phenotypic Features of an Ultrarare CDG Subtype*. Front Genet, 2021. **12**: p. 737094.
48. Rieger, M., et al., *SRD5A3-CDG: Twins with an intragenic tandem duplication*. Eur J Med Genet, 2022. **65**(5): p. 104492.
49. Grunewald, S., G. Matthijs, and J. Jaeken, *Congenital disorders of glycosylation: a review*. Pediatr Res, 2002. **52**(5): p. 618-24.
50. Lipinski, P. and A. Tylki-Szymanska, *Congenital Disorders of Glycosylation: What Clinicians Need to Know?* Front Pediatr, 2021. **9**: p. 715151.
51. Westermeier, R., et al., *High-resolution two-dimensional electrophoresis with isoelectric focusing in immobilized pH gradients*. J Biochem Biophys Methods, 1983. **8**(4): p. 321-30.
52. Raynor, A., et al., *Biochemical diagnosis of congenital disorders of glycosylation*. Adv Clin Chem, 2024. **120**: p. 1-43.
53. Wopereis, S., et al., *Apolipoprotein C-III isofocusing in the diagnosis of genetic defects in O-glycan biosynthesis*. Clin Chem, 2003. **49**(11): p. 1839-45.
54. Wada, Y., M. Kadoya, and N. Okamoto, *Mass Spectrometry of Transferrin and Apolipoprotein CIII from Dried Blood Spots for Congenital Disorders of Glycosylation*. Mass Spectrom (Tokyo), 2022. **11**(1): p. A0113.
55. Casetta, B., et al., *A new strategy implementing mass spectrometry in the diagnosis of congenital disorders of N-glycosylation (CDG)*. Clin Chem Lab Med, 2020. **59**(1): p. 165-171.
56. Park, J.H. and T. Marquardt, *Treatment Options in Congenital Disorders of Glycosylation*. Front Genet, 2021. **12**: p. 735348.
57. Francisco, R., et al., *The challenge of CDG diagnosis*. Mol Genet Metab, 2019. **126**(1): p. 1-5.
58. Quelhas, D. and J. Jaeken, *Treatment of congenital disorders of glycosylation: An overview*. Mol Genet Metab, 2024. **143**(1-2): p. 108567.
59. Martinez-Monseny, A.F., et al., *AZATAx: Acetazolamide safety and efficacy in cerebellar syndrome in PMM2 congenital disorder of glycosylation (PMM2-CDG)*. Ann Neurol, 2019. **85**(5): p. 740-751.
60. Feichtinger, R.G., et al., *A spoonful of L-fucose-an efficient therapy for GFUS-CDG, a new glycosylation disorder*. EMBO Mol Med, 2021. **13**(9): p. e14332.
61. Hullen, A., et al., *Congenital disorders of glycosylation with defective fucosylation*. J Inherit Metab Dis, 2021. **44**(6): p. 1441-1452.
62. Cantagrel, V., et al., *SRD5A3 is required for converting polyprenol to dolichol and is mutated in a congenital glycosylation disorder*. Cell, 2010. **142**(2): p. 203-17.
63. Garapati, K., et al., *N-glycoproteomic and proteomic alterations in SRD5A3-deficient fibroblasts*. Glycobiology, 2024. **34**(11).
64. Buczkowska, A., E. Swiezewska, and D.J. Lefeber, *Genetic defects in dolichol metabolism*. J Inherit Metab Dis, 2015. **38**(1): p. 157-69.



65. Lemoine, H., et al., *Monoallelic pathogenic ALG5 variants cause atypical polycystic kidney disease and interstitial fibrosis*. Am J Hum Genet, 2022. **109**(8): p. 1484-1499.
66. Lingam, G., et al., *Ocular coloboma-a comprehensive review for the clinician*. Eye (Lond), 2021. **35**(8): p. 2086-2109.
67. Williams, A.L., et al., *Cyp1b1 Regulates Ocular Fissure Closure Through a Retinoic Acid-Independent Pathway*. Invest Ophthalmol Vis Sci, 2017. **58**(2): p. 1084-1097.
68. Hartong, D.T., E.L. Berson, and T.P. Dryja, *Retinitis pigmentosa*. Lancet, 2006. **368**(9549): p. 1795-809.
69. Kaur, S., et al., *Optic nerve hypoplasia*. Oman J Ophthalmol, 2013. **6**(2): p. 77-82.
70. Pflugfelder, S.C. and M.E. Stern, *Biological functions of tear film*. Exp Eye Res, 2020. **197**: p. 108115.
71. Spadea, L., et al., *Effect of corneal light scatter on vision: a review of the literature*. Int J Ophthalmol, 2016. **9**(3): p. 459-64.
72. Hoon, M., et al., *Functional architecture of the retina: development and disease*. Prog Retin Eye Res, 2014. **42**: p. 44-84.
73. Li, S., et al., *cGMP Signaling in Photoreceptor Degeneration*. Int J Mol Sci, 2023. **24**(13).
74. Acott, T.S., et al., *Normal and glaucomatous outflow regulation*. Prog Retin Eye Res, 2021. **82**: p. 100897.
75. Van Cruchten, S., et al., *Pre- and Postnatal Development of the Eye: A Species Comparison*. Birth Defects Res, 2017. **109**(19): p. 1540-1567.
76. Tamm, E.R. and A. Ohlmann, *[Development of the human eye]*. Ophthalmologe, 2012. **109**(9): p. 911-28.
77. Zhao, Y., C.M. Sorenson, and N. Sheibani, *Cytochrome P450 1B1 and Primary Congenital Glaucoma*. J Ophthalmic Vis Res, 2015. **10**(1): p. 60-7.
78. Zhao, Y., et al., *Cyp1b1 mediates periostin regulation of trabecular meshwork development by suppression of oxidative stress*. Mol Cell Biol, 2013. **33**(21): p. 4225-40.
79. Williams, A.L. and B.L. Bohnsack, *Neural crest derivatives in ocular development: discerning the eye of the storm*. Birth Defects Res C Embryo Today, 2015. **105**(2): p. 87-95.
80. Faiq, M.A., et al., *CYP1B1-mediated Pathobiology of Primary Congenital Glaucoma*. J Curr Glaucoma Pract, 2015. **9**(3): p. 77-80.
81. Alsubait, A., et al., *CYP1B1 gene: Implications in glaucoma and cancer*. J Cancer, 2020. **11**(16): p. 4652-4661.
82. Song, Y.S., et al., *Cytochrome P450 1B1: A Key Regulator of Ocular Iron Homeostasis and Oxidative Stress*. Cells, 2022. **11**(19).
83. Elfaki, I., et al., *Cytochrome P450: Polymorphisms and Roles in Cancer, Diabetes and Atherosclerosis*. Asian Pac J Cancer Prev, 2018. **19**(8): p. 2057-2070.
84. Shah, M., R. Bouhenni, and I. Benmerzouga, *Geographical Variability in CYP1B1 Mutations in Primary Congenital Glaucoma*. J Clin Med, 2022. **11**(7).
85. Chouiter, L. and S. Nadifi, *Analysis of CYP1B1 Gene Mutations in Patients with Primary Congenital Glaucoma*. J Pediatr Genet, 2017. **6**(4): p. 205-214.
86. Reis, L.M., et al., *Analysis of CYP1B1 in pediatric and adult glaucoma and other ocular phenotypes*. Mol Vis, 2016. **22**: p. 1229-1238.
87. Carrera, A.N., M.K.O. Grant, and B.N. Zordoky, *CYP1B1 as a therapeutic target in cardio-oncology*. Clin Sci (Lond), 2020. **134**(21): p. 2897-2927.

88. Yang, X., et al., *Constitutive regulation of CYP1B1 by the aryl hydrocarbon receptor (AhR) in pre-malignant and malignant mammary tissue*. J Cell Biochem, 2008. **104**(2): p. 402-17.
89. Larsen, M.C., et al., *AhR and CYP1B1 Control Oxygen Effects on Bone Marrow Progenitor Cells: The Enrichment of Multiple Olfactory Receptors as Potential Microbiome Sensors*. Int J Mol Sci, 2023. **24**(23).
90. Chong, Z.X., et al., *Deciphering the roles of aryl hydrocarbon receptor (AHR) in regulating carcinogenesis*. Toxicology, 2023. **495**: p. 153596.
91. Neavin, D.R., et al., *The Role of the Aryl Hydrocarbon Receptor (AHR) in Immune and Inflammatory Diseases*. Int J Mol Sci, 2018. **19**(12).
92. Choudhary, M. and G. Malek, *The Aryl Hydrocarbon Receptor: A Mediator and Potential Therapeutic Target for Ocular and Non-Ocular Neurodegenerative Diseases*. Int J Mol Sci, 2020. **21**(18).
93. Hammond, C.L., et al., *More than Meets the Eye: The Aryl Hydrocarbon Receptor is an Environmental Sensor, Physiological Regulator and a Therapeutic Target in Ocular Disease*. Front Toxicol, 2022. **4**: p. 791082.
94. Salminen, A., *Mutual antagonism between aryl hydrocarbon receptor and hypoxia-inducible factor-1alpha (AhR/HIF-1alpha) signaling: Impact on the aging process*. Cell Signal, 2022. **99**: p. 110445.
95. Sondermann, N.C., et al., *Functions of the aryl hydrocarbon receptor (AHR) beyond the canonical AHR/ARNT signaling pathway*. Biochem Pharmacol, 2023. **208**: p. 115371.
96. Edamitsu, T., et al., *AHR and NRF2 in Skin Homeostasis and Atopic Dermatitis*. Antioxidants (Basel), 2022. **11**(2).
97. Nguyen, T., P. Nioi, and C.B. Pickett, *The Nrf2-antioxidant response element signaling pathway and its activation by oxidative stress*. J Biol Chem, 2009. **284**(20): p. 13291-5.
98. Ngo, V. and M.L. Duennwald, *Nrf2 and Oxidative Stress: A General Overview of Mechanisms and Implications in Human Disease*. Antioxidants (Basel), 2022. **11**(12).
99. Thiruvengadam, M., et al., *Bioactive Compounds in Oxidative Stress-Mediated Diseases: Targeting the NRF2/ARE Signaling Pathway and Epigenetic Regulation*. Antioxidants (Basel), 2021. **10**(12).
100. Mbiandjeu, S.C.T., et al., *Nrf2 Plays a Key Role in Erythropoiesis during Aging*. Antioxidants (Basel), 2024. **13**(4).
101. Cerqueira, N.M., et al., *Cholesterol Biosynthesis: A Mechanistic Overview*. Biochemistry, 2016. **55**(39): p. 5483-5506.
102. Luo, J., H. Yang, and B.L. Song, *Mechanisms and regulation of cholesterol homeostasis*. Nat Rev Mol Cell Biol, 2020. **21**(4): p. 225-245.
103. Gorin, A., L. Gabitova, and I. Astsaturov, *Regulation of cholesterol biosynthesis and cancer signaling*. Curr Opin Pharmacol, 2012. **12**(6): p. 710-6.
104. Lin, C.Y., C.Y. Chiang, and H.J. Tsai, *Zebrafish and Medaka: new model organisms for modern biomedical research*. J Biomed Sci, 2016. **23**: p. 19.
105. Gucum, S., et al., *A patient-based medaka alg2 mutant as a model for hypo-N-glycosylation*. Development, 2021. **148**(11).
106. Mikula Mrstakova, S. and Z. Kozmik, *Genetic analysis of medaka fish illuminates conserved and divergent roles of Pax6 in vertebrate eye development*. Frontiers in Cell and Developmental Biology, 2024. **12**.
107. Ondruskova, N., et al., *Severe phenotype of ATP6AP1-CDG in two siblings with a novel mutation leading to a differential tissue-specific ATP6AP1 protein*

- pattern, cellular oxidative stress and hepatic copper accumulation*. J Inherit Metab Dis, 2020. **43**(4): p. 694-700.
108. Stemmer, M., et al., *CCTop: An Intuitive, Flexible and Reliable CRISPR/Cas9 Target Prediction Tool*. PLoS One, 2015. **10**(4): p. e0124633.
  109. Thumberger, T., et al., *Boosting targeted genome editing using the hei-tag*. Elife, 2022. **11**.
  110. Cornean, A., et al., *Precise in vivo functional analysis of DNA variants with base editing using ACEofBASEs target prediction*. Elife, 2022. **11**.
  111. Lischik, C.Q., L. Adelman, and J. Wittbrodt, *Enhanced in vivo-imaging in medaka by optimized anaesthesia, fluorescent protein selection and removal of pigmentation*. PLoS One, 2019. **14**(3): p. e0212956.
  112. Niehues, R., et al., *Carbohydrate-deficient glycoprotein syndrome type Ib. Phosphomannose isomerase deficiency and mannose therapy*. J Clin Invest, 1998. **101**(7): p. 1414-20.
  113. Interdonato, L., et al., *Assessing carnosinase 1 activity for diagnosing congenital disorders of glycosylation*. Mol Genet Metab, 2024. **143**(1-2): p. 108571.
  114. Korner, C., L. Lehle, and K. von Figura, *Abnormal synthesis of mannose 1-phosphate derived carbohydrates in carbohydrate-deficient glycoprotein syndrome type I fibroblasts with phosphomannomutase deficiency*. Glycobiology, 1998. **8**(2): p. 165-71.
  115. Lowry, O., et al., *Protein Measurement with the Folin Phenol Reagent*. Journal of Biological Chemistry, 1951. **193**(1): p. 265-275.
  116. Kwon, D.H., et al., *Protective Effect of Glutathione against Oxidative Stress-induced Cytotoxicity in RAW 264.7 Macrophages through Activating the Nuclear Factor Erythroid 2-Related Factor-2/Heme Oxygenase-1 Pathway*. Antioxidants (Basel), 2019. **8**(4).
  117. Liebisch, G., et al., *High throughput quantification of cholesterol and cholesteryl ester by electrospray ionization tandem mass spectrometry (ESI-MS/MS)*. Biochim Biophys Acta, 2006. **1761**(1): p. 121-8.
  118. Ozbalci, C., T. Sachsenheimer, and B. Brugger, *Quantitative analysis of cellular lipids by nano-electrospray ionization mass spectrometry*. Methods Mol Biol, 2013. **1033**: p. 3-20.
  119. Wessel, D. and U.I. Flugge, *A method for the quantitative recovery of protein in dilute solution in the presence of detergents and lipids*. Anal Biochem, 1984. **138**(1): p. 141-3.
  120. Hennig, R., et al., *Towards personalized diagnostics via longitudinal study of the human plasma N-glycome*. Biochim Biophys Acta, 2016. **1860**(8): p. 1728-38.
  121. Hennig, R., et al., *N-Glycosylation Fingerprinting of Viral Glycoproteins by xCGE-LIF*. Methods Mol Biol, 2015. **1331**: p. 123-43.
  122. Ceroni, A., et al., *GlycoWorkbench: a tool for the computer-assisted annotation of mass spectra of glycans*. J Proteome Res, 2008. **7**(4): p. 1650-9.
  123. Varki, A., et al., *Symbol nomenclature for glycan representation*. Proteomics, 2009. **9**(24): p. 5398-9.
  124. Mousa, J., et al., *Acetazolamide treatment in late onset CDG type 1 due to biallelic pathogenic DHDDS variants*. Mol Genet Metab Rep, 2022. **32**: p. 100901.
  125. Tsuchiya, Y., et al., *Human CYP1B1 is regulated by estradiol via estrogen receptor*. Cancer Res, 2004. **64**(9): p. 3119-25.

126. ElKhatib, M.A.W., et al., *Cytochrome P450 1B1 is critical in the development of TNF-alpha, IL-6, and LPS-induced cellular hypertrophy*. Can J Physiol Pharmacol, 2024. **102**(7): p. 408-421.
127. Li, H., et al., *Peroxiredoxin2 (Prdx2) Reduces Oxidative Stress and Apoptosis of Myocardial Cells Induced by Acute Myocardial Infarction by Inhibiting the TLR4/Nuclear Factor kappa B (NF-kappaB) Signaling Pathway*. Med Sci Monit, 2020. **26**: p. e926281.
128. Xu, G.L., et al., *Correlation between PRDX2 and spermatogenesis under oxidative stress*. Biochem Biophys Res Commun, 2023. **656**: p. 139-145.
129. Zhou, S., et al., *PRDX2 protects hepatocellular carcinoma SMMC-7721 cells from oxidative stress*. Oncol Lett, 2016. **12**(3): p. 2217-2221.
130. Ross, D. and D. Siegel, *The diverse functionality of NQO1 and its roles in redox control*. Redox Biol, 2021. **41**: p. 101950.
131. Kale, D., et al., *Quantification of Dolichyl Phosphates Using Phosphate Methylation and Reverse-Phase Liquid Chromatography-High Resolution Mass Spectrometry*. Anal Chem, 2023. **95**(6): p. 3210-3217.
132. Yamazaki, R. and N. Ohno, *Neutral Red Labeling: A Novel Vital Staining Method for Investigating Central and Peripheral Nervous System Lesions*. Acta Histochem Cytochem, 2024. **57**(4): p. 131-135.
133. Guemez-Gamboa, A., et al., *Inactivating mutations in MFSD2A, required for omega-3 fatty acid transport in brain, cause a lethal microcephaly syndrome*. Nat Genet, 2015. **47**(7): p. 809-13.
134. Law, S.H., et al., *An Updated Review of Lysophosphatidylcholine Metabolism in Human Diseases*. Int J Mol Sci, 2019. **20**(5).
135. Ren, J., et al., *Lysophosphatidylcholine: Potential Target for the Treatment of Chronic Pain*. Int J Mol Sci, 2022. **23**(15).
136. Athenstaedt, K. and G. Daum, *Phosphatidic acid, a key intermediate in lipid metabolism*. Eur J Biochem, 1999. **266**(1): p. 1-16.
137. Chen, W.W., et al., *Phosphatidylglycerol Incorporates into Cardiolipin to Improve Mitochondrial Activity and Inhibits Inflammation*. Sci Rep, 2018. **8**(1): p. 4919.
138. Hryc, C.F., et al., *Structural insights into cardiolipin replacement by phosphatidylglycerol in a cardiolipin-lacking yeast respiratory supercomplex*. Nat Commun, 2023. **14**(1): p. 2783.
139. Pang, J., et al., *Barth Syndrome Cardiomyopathy: An Update*. Genes (Basel), 2022. **13**(4).
140. Altassan, R., et al., *International consensus guidelines for phosphoglucomutase 1 deficiency (PGM1-CDG): Diagnosis, follow-up, and management*. J Inherit Metab Dis, 2021. **44**(1): p. 148-163.
141. Footitt, E.J., et al., *Cardiomyopathy in the congenital disorders of glycosylation (CDG): a case of late presentation and literature review*. J Inherit Metab Dis, 2009. **32 Suppl 1**: p. S313-9.
142. Zemet, R., et al., *Cardiomyopathy, an uncommon phenotype of congenital disorders of glycosylation: Recommendations for baseline screening and follow-up evaluation*. Mol Genet Metab, 2024. **142**(4): p. 108513.
143. Zhao, M., et al., *Cytochrome P450 Enzymes and Drug Metabolism in Humans*. Int J Mol Sci, 2021. **22**(23).
144. Iwamoto, D.V., et al., *Induction of cytochrome P450 family 1 mRNAs and activities in a cell line from the frog Xenopus laevis*. Aquat Toxicol, 2012. **114-115**: p. 165-72.

145. Sorhus, E., et al., *Untangling mechanisms of crude oil toxicity: Linking gene expression, morphology and PAHs at two developmental stages in a cold-water fish*. Sci Total Environ, 2021. **757**: p. 143896.
146. Monostory, K. and Z. Dvorak, *Steroid regulation of drug-metabolizing cytochromes P450*. Curr Drug Metab, 2011. **12**(2): p. 154-72.
147. Fabris, M., et al., *CYP1B1: A Promising Target in Cancer Drug Discovery*. Anticancer Agents Med Chem, 2023. **23**(9): p. 981-988.
148. Gajjar, K., P.L. Martin-Hirsch, and F.L. Martin, *CYP1B1 and hormone-induced cancer*. Cancer Lett, 2012. **324**(1): p. 13-30.
149. Mitsui, Y., et al., *CYP1B1 promotes tumorigenesis via altered expression of CDC20 and DAPK1 genes in renal cell carcinoma*. BMC Cancer, 2015. **15**: p. 942.
150. Kwon, Y.J., et al., *CYP1B1 Enhances Cell Proliferation and Metastasis through Induction of EMT and Activation of Wnt/beta-Catenin Signaling via Sp1 Upregulation*. PLoS One, 2016. **11**(3): p. e0151598.
151. Galosi, S., et al., *De novo DHDDS variants cause a neurodevelopmental and neurodegenerative disorder with myoclonus*. Brain, 2022. **145**(1): p. 208-223.
152. Zelinger, L., et al., *A missense mutation in DHDDS, encoding dehydrodolichyl diphosphate synthase, is associated with autosomal-recessive retinitis pigmentosa in Ashkenazi Jews*. Am J Hum Genet, 2011. **88**(2): p. 207-15.
153. Favier, L.A. and G.S. Schulert, *Mevalonate kinase deficiency: current perspectives*. Appl Clin Genet, 2016. **9**: p. 101-10.
154. Jeyaratnam, J. and J. Frenkel, *Management of Mevalonate Kinase Deficiency: A Pediatric Perspective*. Front Immunol, 2020. **11**: p. 1150.
155. Doering, L., et al., *CRISPR-based knockout and base editing confirm the role of MYRF in heart development and congenital heart disease*. Dis Model Mech, 2023. **16**(8).
156. Baird, L. and M. Yamamoto, *The Molecular Mechanisms Regulating the KEAP1-NRF2 Pathway*. Mol Cell Biol, 2020. **40**(13).
157. Kerr, F., et al., *Direct Keap1-Nrf2 disruption as a potential therapeutic target for Alzheimer's disease*. PLoS Genet, 2017. **13**(3): p. e1006593.
158. Kaur, T., et al., *Unraveling neuroprotection in Parkinson's disease: Nrf2-Keap1 pathway's vital role amidst pathogenic pathways*. Inflammopharmacology, 2024. **32**(5): p. 2801-2820.
159. Nebert, D.W., et al., *Role of aryl hydrocarbon receptor-mediated induction of the CYP1 enzymes in environmental toxicity and cancer*. J Biol Chem, 2004. **279**(23): p. 23847-50.
160. Perrot-Applanat, M., et al., *High Expression of AhR and Environmental Pollution as AhR-Linked Ligands Impact on Oncogenic Signaling Pathways in Western Patients with Gastric Cancer-A Pilot Study*. Biomedicines, 2024. **12**(8).
161. Vacher, S., et al., *High AHR expression in breast tumors correlates with expression of genes from several signaling pathways namely inflammation and endogenous tryptophan metabolism*. PLoS One, 2018. **13**(1): p. e0190619.
162. Jacob, A., et al., *Aryl hydrocarbon receptor-dependent upregulation of Cyp1b1 by TCDD and diesel exhaust particles in rat brain microvessels*. Fluids Barriers CNS, 2011. **8**: p. 23.
163. Falero-Perez J, S.Y., Sorenson CM, Sheibani N, *CYP1B1: A key regulator of redox homeostasis*. Trends in Cell & Molecular Biology, 2018. **13**:27-45.
164. May, L.T., et al., *Marked cell-type-specific differences in glycosylation of human interleukin-6*. Cytokine, 1991. **3**(3): p. 204-11.

165. Francisco, R., et al., *New Insights into Immunological Involvement in Congenital Disorders of Glycosylation (CDG) from a People-Centric Approach*. J Clin Med, 2020. **9**(7).
166. Wang, Y., et al., *Carvedilol serves as a novel CYP1B1 inhibitor, a systematic drug repurposing approach through structure-based virtual screening and experimental verification*. Eur J Med Chem, 2020. **193**: p. 112235.
167. Amirshahrokhi, K. and A. Niapour, *Carvedilol attenuates brain damage in mice with hepatic encephalopathy*. Int Immunopharmacol, 2022. **111**: p. 109119.
168. Lastuvkova, H., et al., *Carvedilol impairs bile acid homeostasis in mice: implication for nonalcoholic steatohepatitis*. Toxicol Sci, 2023. **196**(2): p. 200-217.
169. Zaabalawi, A., et al., *Internal Mammary Arteries as a Model to Demonstrate Restoration of the Impaired Vasodilation in Hypertension, Using Liposomal Delivery of the CYP1B1 Inhibitor, 2,3',4,5'-Tetramethoxystilbene*. Pharmaceuticals, 2022. **14**(10).
170. Chan, B., et al., *A mouse model of a human congenital disorder of glycosylation caused by loss of PMM2*. Hum Mol Genet, 2016. **25**(11): p. 2182-2193.
171. Yuste-Checa, P., et al., *The Effects of PMM2-CDG-Causing Mutations on the Folding, Activity, and Stability of the PMM2 Protein*. Hum Mutat, 2015. **36**(9): p. 851-60.
172. Schneider, A., et al., *Successful prenatal mannose treatment for congenital disorder of glycosylation-la in mice*. Nat Med, 2011. **18**(1): p. 71-3.

## 10. Supplementary information

**Table S1: Targeted genes in nCounter analysis and corresponding differential expression.**

The expression of 190 genes was quantified using nCounter analysis based on transcript quantity in SRD5A3-CDG patient-derived fibroblasts (n = 3) and controls (n = 5). Data produced jointly with the nCounter Core Facility of the Heidelberg University Hospital.

Gene	Significance ( <i>P</i> -value < 0.05)	<i>P</i> -value	<i>Q</i> -value	Log2 ratio (Patients/ Ctrl)
3B-HSD	No	0.114161	0.241703	0.70118102
ACOX3	No	0.837063	0.740457	0.10833187
ALG1	Yes	0.003322	0.0143	1.27906339
ALG11	No	0.141608	0.265054	0.65311674
ALG12	No	0.071154	0.18379	-0.74661576
ALG13	No	0.606469	0.626603	-0.23521484
ALG14	No	0.113487	0.241703	0.75382165
ALG2	No	0.252273	0.354142	0.51196188
ALG3	No	0.606469	0.626603	0.24013026
ALG5	No	0.606469	0.626603	0.24013026
ALG8	No	0.757692	0.709101	0.15202113
ALG9	Yes	0.011538	0.042577	1.11117676
ATF5	Yes	0.000175	0.001737	1.5849625
ATF6	No	0.054895	0.154124	-0.78972083
B3GalNAcT2	No	0.299126	0.402418	0.46571332
B3GLCT or B3GALT1	No	0.031119	0.098024	0.95234896
B4GALT1	Yes	0.000175	0.001737	1.5849625
B4GALT2	Yes	0.000175	0.001737	1.5849625
B4GALT7	No	0.173776	0.284091	0.60581515
C14orf1 or ERG28	Yes	0.003322	0.0143	-1.14536641
CASD1	No	0.528671	0.591677	-0.29552146
COQ2	Yes	0.005245	0.021168	-1.09911131
COQ3	No	>0.999999	0.827885	0.021575
COQ5	No	0.114161	0.241703	0.70118102
COQ6	No	0.407867	0.478873	0.37427105
COQ7	Yes	0.001224	0.006872	-1.23696542
CYP1B1	Yes	0.001224	0.006872	1.39775166
CYP51A1	No	0.606469	0.626603	0.24013026
DAD1	Yes	0.000175	0.001737	1.5849625
DDOST	No	0.090734	0.221101	-0.70391447
DHCR24	Yes	0.000175	0.001737	-1.37851162
DHCR7	Yes	0.003322	0.0143	-1.14536641
DHDDS	No	0.031119	0.098024	0.95234896
DOLK	No	0.918182	0.775053	-0.06449913
DOLPP1	Yes	0.002098	0.010838	1.33855967
DPAGT1	No	0.017582	0.063077	1.13082782
DPM1	No	0.620047	0.635548	-0.24798288

DPM2	No	0.837063	0.740457	-0.10732875
DPM3	No	0.407867	0.478873	0.37427105
DPY19L1	Yes	0.003322	0.0143	1.27906339
DPY19L3	No	0.031119	0.098024	0.95234896
DPY19L4	No	0.173776	0.284091	0.60581515
EBP	No	0.173776	0.284091	-0.57531233
EIF2AK3	No	0.606469	0.626603	0.24013026
ERN1	Yes	0.0004	0.002716	1.6520767
FDFT1	Yes	0.005245	0.021168	-1.09911131
FDPS	No	0.918182	0.775053	-0.06449913
FGFR1	Yes	0.000175	0.001737	-1.37851162
FUT8	No	0.090734	0.221101	0.74982497
GALE	Yes	0.0004	0.002716	-1.32192809
GANAB	No	0.536014	0.591677	0.2845958
GFPT1	Yes	0.00035	0.002716	1.52100099
GMPPA	No	0.21049	0.327527	-0.53311862
GMPPB	No	0.141608	0.265054	0.65311674
GNE	No	0.141608	0.265054	0.65311674
GPAA1	Yes	0.000175	0.001737	1.5849625
HiF1alpha	No	0.173776	0.284091	0.60581515
HMGCR	No	0.837063	0.740457	-0.10732875
HSD17B1	No	0.757692	0.709101	-0.15004521
HSD17B7	No	0.21049	0.327527	-0.53311862
HSPA5	No	0.035964	0.108018	-0.87446912
HSPD1	No	0.252273	0.354142	-0.48958733
IDI1	No	0.757692	0.709101	0.15202113
LDLR	No	0.071154	0.18379	-0.74661576
LFNG	No	0.469755	0.546567	0.32917287
LSS	No	0.680594	0.670983	-0.19266762
MAGT1	No	0.837063	0.740457	-0.10732875
MAN1A1	No	0.757692	0.709101	0.15202113
MAN1B1	Yes	0.0004	0.002716	1.6520767
MAN2A1	Yes	0.000175	0.001737	1.5849625
MGAT1	Yes	0.000175	0.001737	-1.37851162
MGAT2	No	0.252273	0.354142	0.51196188
MGAT5	Yes	0.000175	0.001737	-1.37851162
MOGS	No	0.407867	0.478873	0.37427105
MPDU1	No	0.351049	0.448891	0.41987673
MPI	No	0.757692	0.709101	0.15202113
mTOR	No	0.21049	0.327527	0.5586521
MVD	No	0.797203	0.740457	0.15204431
MVK	No	0.141608	0.265054	-0.61760889
NEU1	No	0.606469	0.626603	0.24013026
NEU3	Yes	0.011538	0.042577	-1.01000943
NGLY1	No	0.173776	0.284091	-0.57531233
NSDHL	No	0.536014	0.591677	0.2845958
NUS1 or NgBR	No	0.022902	0.077837	-0.92090848



# Supplementary information

OGA	No	0.918182	0.775053	0.06485688
OGT	No	0.407867	0.478873	0.37427105
OST4	Yes	0.000175	0.001737	1.5849625
OSTC	No	0.071154	0.18379	0.79908731
PDSS1	No	0.918182	0.775053	0.06485688
PDSS2	No	0.173776	0.284091	-0.57531233
PGAP1	No	0.252273	0.354142	0.51196188
PGAP2	No	0.837063	0.740457	0.10833187
PGAP3	No	0.837063	0.740457	-0.10732875
PGAP4	Yes	0.00035	0.002716	-1.33121315
PGM1	No	0.536014	0.591677	-0.27770554
PGM2	No	0.141608	0.265054	-0.61760889
PIGA	No	0.114161	0.241703	-0.66002694
PIGB	No	0.21049	0.327527	-0.53311862
PIGC	No	0.407867	0.478873	0.37427105
PIGF	No	0.23976	0.354142	0.61150966
PIGG	Yes	0.001224	0.006872	1.39775166
PIGL	No	0.606469	0.626603	-0.23521484
PIGM	No	0.173776	0.284091	-0.57531233
PIGN	No	0.114161	0.241703	-0.66002694
PIGO	No	0.918182	0.775053	0.06485688
PIGP	No	0.113487	0.241703	-0.68081186
PIGQ	No	0.141608	0.265054	0.65311674
PIGS	No	0.918182	0.775053	-0.06449913
PIGT	No	0.299126	0.402418	0.46571332
PIGU	No	0.407867	0.478873	-0.36244278
PIGV	No	0.351049	0.448891	-0.40507057
PIGW	No	0.680594	0.670983	0.19594644
PIGX	No	0.299126	0.402418	-0.44752456
PIGY	No	0.252273	0.354142	0.51196188
PMM1	No	0.141608	0.265054	0.65311674
PMM2	No	0.407867	0.478873	0.37427105
PMVK	No	0.536014	0.591677	0.2845958
POFUT1	Yes	0.000999	0.006451	1.73696559
POFUT2	No	0.173776	0.284091	0.60581515
POLR2A	Yes	0.00035	0.002716	1.52100099
POMGnT1	No	0.757692	0.709101	0.15202113
POMGnT2	No	0.680594	0.670983	-0.19266762
POMT1	No	0.173776	0.284091	0.60581515
POMT2	No	>0.999999	0.827885	-0.02153696
RFNG	No	0.351049	0.448891	0.41987673
RFT1	No	0.299126	0.402418	-0.44752456
RPL13A	No	>0.999999	0.827885	-0.02153696
RPN1	No	0.141608	0.265054	0.65311674
RPN2	No	0.173776	0.284091	0.60581515
SC4MOL or MSO1	No	0.054895	0.154124	0.85037604

SC5DL or SC5D	No	0.022902	0.077837	1.00424557
SGK1	No	0.918182	0.775053	0.06485688
SLC35A1	No	0.351049	0.448891	-0.40507057
SLC35A2	No	0.252273	0.354142	-0.48958733
SLC35A3	No	0.837063	0.740457	-0.10732875
SLC35A4	No	0.351049	0.448891	-0.40507057
SLC35A5	Yes	0.007592	0.029714	-1.07068606
SLC35B4	No	0.035964	0.108018	-0.87446912
SLC35C1	No	0.407867	0.478873	-0.36244278
SLC35C2	No	0.757692	0.709101	0.15202113
SLC35D1	No	0.680594	0.670983	0.19594644
SLC35D2	Yes	0.000175	0.001737	-1.37851162
SOD2	No	0.363636	0.460428	0.47387348
SPRING1	No	0.113487	0.241703	0.75382165
SQLE	No	0.252273	0.354142	-0.48958733
SRD5A3	No	0.606469	0.626603	-0.23521484
SREBF1	No	0.536014	0.591677	-0.27770554
ST3GAL1	No	0.090734	0.221101	0.74982497
ST3GAL2	No	0.680594	0.670983	-0.19266762
ST3GAL3	No	0.252273	0.354142	-0.48958733
STT3A	No	0.114161	0.241703	0.70118102
STT3B	Yes	0.003322	0.0143	1.27906339
TBP	No	0.041783	0.122643	-0.8340845
TMEM258	Yes	0.001554	0.008362	1.66296501
TUSC3	Yes	0.000175	0.001737	1.5849625
UAP1	No	0.071154	0.18379	0.79908731

**Table S2: Significantly deregulated transcripts in SRD5A3 patient-derived fibroblasts.**

Gene expression quantified by transcriptomic analysis of a variety of identified genes, measured by average read counts in three independent SRD5A3-CDG patient-derived fibroblasts and controls (n = 5). The differential expression genes based on an absolute log<sub>2</sub>-Ratio of log<sub>2</sub>-Ratio ≥ 1 and FDR ≤ 0.001. Data produced jointly with BGI. Green, significantly upregulated; purple, significantly downregulated.

ABCA2	KIAA1217	SYT8	EEF1A2	PI3
ABCB10	KIAA1549L	SYVN1	EEF1D	PIANP
ABHD14A-ACY1	KIAA1958	TAF13	EEPD1	PIAS1
ABHD14B	KIDINS220	TAF15	EFCAB14	PIF1
ABHD17A	KIF16B	TAF15ZIN	EFCAB2	PIH1D1
ABHD4	KIF1A	TANGO2	EFNA1	PIK3C2A
ABI3BP	KIFAP3	TANGO6	EFNA4	PIK3C2B
ABITRAM	KLF10	TAOK1	EFNB3	PIK3CB
ABTB2	KLF16	TARBP1	EGFL6	PIK3CD
ACAA2	KLF2	TASOR2	EGFL8	PIK3R1
ACADL	KLF6	TATDN3	EGFLAM	PIM1
ACAP2	KLF7	TAX1BP3	EGFR	PIM2
ACBD3	KLHDC7B	TBC1D10A	EHD1	PIM3
ACBD5	KLHL12	TBC1D12	EHD3	PINK1
ACKR2	KLHL18	TBC1D16	EHMT1	PITX1

# Supplementary information

ACLY	KLHL2	TBC1D20	EHMT2	PIWIL2
ACOT13	KLHL20	TBC1D24	EID2	PKD1L2
ACOT4	KLHL21	TBC1D30	EIF2A	PKIG
ACOX1	KLHL35	TBC1D32	EIF2AK1	PKN3
ACOX3	KLHL7	TBC1D9B	EIF2AK4	PLA2R1
ACSBG1	KLHL9	TBCD	EIF2B5	PLAAT4
ACTR10	KMT2C	TBCK	EIF3E	PLAC8
ACTR2	KPNA1	TBL2	EIF4A3	PLAGL2
ACY1	KPNA4	TBX1	EIF4B	PLAT
ACYP2	KRTAP2-3	TBX15	ELANE	PLB1
ADAM12	KRTCAP2	TCAF1	ELAPOR1	PLCB1
ADAM17	KSR1	TCEA1	ELF1	PLCG2
ADAM23	LACTB	TCEA2	ELF3	PLCXD1
ADAM32	LAGE3	TCF7L2	ELFN2	PLD1
ADAMTS10	LAMP3	TCHH	ELMO1	PLD5
ADAMTS12	LAMTOR3	TCP11L1	ELOVL7	PLEKHA5
ADAMTS4	LARP1	TCTA	EMB	PLEKHA6
ADAMTSL1	LARP4	TDG	EML2	PLEKHG4B
ADAMTSL3	LARP4B	TDP2	EML5	PLEKHG6
ADD2	LARP6	TEFM	EMP2	PLP1
ADGRF5	LARS1	TEK	EMSY	PLPP2
ADGRL1	LBX2	TENM3	ENG	PLPPR4
ADGRL4	LDHD	TENT5A	ENOX1	PLS1
ADO	LDLRAD2	TERF2IP	ENOX2	PLXNC1
ADPRS	LDLRAD4	TEX49	ENPEP	PM20D2
ADRA2C	LEFTY2	TEX9	ENTPD1	PMAIP1
ADTRP	LGI2	TFG	ENTPD3	PMF1
AFF4	LGR4	TFPT	ENY2	PMPCB
AGAP1	LGR5	TGDS	EPAS1	PNKD
AGO3	LHFPL2	TGFB1	EPB41	PNMA3
AGPS	LHX8	TGFB1	EPC2	PNMA6A
AHCYL2	LHX9	TGFBR2	EPCAM	PNMA8B
AHNAK2	LIF	TGM5	EPDR1	PNPLA2
AICDA	LIG3	THADA	EPHA4	POC1A
AIMP2	LIMA1	THAP8	EPHB4	POLE
AK4	LIMCH1	THBD	EPHB6	POLE4
AK6	LIMK2	THBS3	EPHX1	POLR1D
AKAP11	LIMS1	THSD1	EPHX2	POLR1E
AKAP13	LIN52	THUMPD2	EPHX4	POLR2B
AKTIP	LINGO1	TIAM1	EPOR	POLR2E
ALAS1	LMBRD2	TICAM1	EPS8L1	POLR2J
ALDH1L2	LMCD1	TIGAR	ERAP1	POLR3GL
ALG1	LMLN	TIGD7	ERBB3	PON2
ALG11	LMO4	TIMM17A	ERBIN	PPARA
ALG14	LMO7	TIMM22	ERC2	PPARGC1A
ALG2	LMTK2	TIMM29	EREG	PPM1B
ALPK3	LNPEP	TIMP1	ERFE	PPM1H
AMACR	LNPK	TIMP2	ERICH1	PPP1CA
AMDHD2	LOC101927345	TK2	ERMP1	PPP1CC
AMFR	LOC102724200	TLCD1	ERRFI1	PPP1R12B
AMIGO2	LOC107984512	TLE2	ESPNL	PPP1R12C
AMMECR1L	LOC107986762	TLE3	ESR1	PPP1R13B
ANAPC11	LOC107987457	TLL2	ETAA1	PPP1R26
ANGPT4	LOC112268052	TM2D2	ETFA	PPP1R3D
ANGPTL1	LOC112268437	TM9SF2	ETHE1	PPP1R7
ANGPTL4	LOC114841035	TMBIM1	ETNK2	PPP2R3A
ANGPTL6	LONP1	TMC7	ETV4	PPP2R5A
ANK2	LRATD2	TMDD1	ETV6	PPP4R4
ANK3	LRBA	TMED10	EVA1C	PPP6R3
ANKFY1	LRFN3	TMED7	EVI5L	PPT2
ANKHD1	LRFN4	TMEFF1	EXOC3	PPTC7
ANKIB1	LRFN5	TMEFF2	EXOC6	PQBP1
ANKLE2	LRP1	TMEM100	EXOSC10	PRDM1
ANKRD1	LRP11	TMEM104	EXPH5	PRDM11
ANKRD11	LRP2BP	TMEM11	EXTL3	PRDX2

ANKRD13B	LRP3	TMEM119	EYA1	PRELP
ANKRD24	LRP4	TMEM143	EZR	PRICKLE1
ANKRD30A	LRRC14	TMEM150A	F10	PRKAA2
ANKRD37	LRRC15	TMEM160	F2R	PRKACB
ANKRD40	LRRC32	TMEM167A	F2RL1	PRKAR1B
ANKRD44	LRRC4	TMEM169	F2RL2	PRKAR2B
ANKRD6	LRRC58	TMEM17	F7	PRKCA
ANXA4	LRRIQ1	TMEM181	FAAH	PRKCZ
ANXA5	LRRN2	TMEM184B	FAF1	PRMT1
ANXA7	LSM11	TMEM200A	FAHD2B	PROB1
AOPEP	LTBP2	TMEM204	FAM107B	PROK1
AP1AR	LTC4S	TMEM208	FAM111A	PROSER1
AP1G1	LTO1	TMEM217	FAM114A1	PRPF38B
AP2A2	LTV1	TMEM219	FAM117A	PRPS2
AP3S1	LURAP1L	TMEM223	FAM124A	PRR14
AP4E1	LUZP1	TMEM230	FAM131B	PRR19
AP5Z1	LUZP2	TMEM231	FAM136A	PRR29
APBA3	LUZP6	TMEM236	FAM13A	PRRG1
APBB3	LYPD6	TMEM241	FAM161A	PRRG3
APLP1	LYPD6B	TMEM250	FAM162B	PRRT1
ARAP1	LYRM7	TMEM254	FAM167A	PRRT2
ARAP2	LZIC	TMEM258	FAM167B	PRSS12
ARCNI	LZTR1	TMEM263	FAM169A	PRSS3
ARF4	M1AP	TMEM267	FAM189A1	PRSS35
ARF6	MACF1	TMEM268	FAM20A	PRTFDC1
ARFGAP1	MACO1	TMEM30B	FAM20C	PRTG
ARFGEF2	MAFG	TMEM33	FAM217B	PRXL2A
ARFIP1	MAFK	TMEM39A	FAM228A	PRXL2B
ARHGAP1	MAGIX	TMEM45A	FAM43A	PSD
ARHGAP24	MAMLD1	TMEM50A	FAM72C	PSD4
ARHGAP31	MAN1B1	TMEM63B	FAM72D	PSEN2
ARHGAP32	MAN2A1	TMEM68	FAM76B	PSG11
ARHGAP35	MAN2C1	TMEM70	FAM83H	PSG3
ARHGAP9	MAP1B	TMEM8B	FAM86B2	PSG4
ARHGDIG	MAP1LC3B	TNFAIP8L3	FAM89A	PSG5
ARHGEF10L	MAP1LC3B2	TNFRSF10D	FANCA	PSG6
ARHGEF40	MAP1S	TNFRSF12A	FANCB	PSG9
ARL1	MAP3K2	TNFSF4	FANCE	PSIP1
ARL10	MAP3K3	TNFSF9	FANCM	PSMB10
ARL8A	MAP3K4	TNKS2	FAR2	PSMB8
ARL8B	MAP3K7	TNPO2	FAXC	PSME1
ARMC2	MAP3K7CL	TNRC18	FAXDC2	PSRC1
ARMCX2	MAPK1	TNS1	FBL	PTDSS1
ARMCX3	MAPK6	TNXB	FBLIM1	PTGDS
ARMCX6	MAPK7	TOLLIP	FBLN1	PTGES3L
ARNTL	MARCHF1	TOM1	FBLN7	PTGFR
ARPC4	MARVELD1	TOMM7	FBP1	PTGIS
ARPC4-TTLL3	MARVELD2	TOR1A	FBXL2	PTGR1
ARVCF	MAST2	TOR1B	FBXL22	PTGS1
ASB1	MAT2A	TP53	FBXO2	PTGS2
ASB6	MATN3	TP53INP1	FBXO21	PTMA
ASPN	MAX	TP53RK	FBXO41	PTN
ASPSCR1	MBD1	TPGS1	FBXO5	PTOV1
ATAD1	MBD4	TPM1	FCGBP	PTP4A2
ATF5	MBOAT2	TPPP3	FCHO1	PTPN11
ATF7	MBTPS2	TPRG1L	FCHSD2	PTPN2
ATG101	MCL1	TPST2	FCMR	PTPN3
ATG16L2	MCRIP1	TRAF4	FEM1B	PTPRG
ATL3	MCUB	TRAK1	FER1L5	PTPRH
ATP10A	MDM2	TRAPPC10	FGD4	PTPRK
ATP10D	MED12L	TRAPPC2B	FGF10	PTPRN2
ATP11B	MED19	TRAPPC3	FGFR1	PTPRQ
ATP13A1	MED24	TRAPPC6B	FGFR3	PTPRS
ATP13A2	MEDAG	TRIAP1	FGR	PTPRU
ATP6AP1	MEF2C	TRIB2	FHDC1	PTRHD1

# Supplementary information

ATP6V0A1	MEF2D	TRIB3	FHIP1A	PURG
ATP6V0B	METRNL	TRIL	FHL1	PWWP3B
ATP6V1A	METTL1	TRIM23	FIBCD1	PYCARD
ATP6V1E1	MEX3C	TRIM26	FKBP1B	PYGL
ATP6V1G1	MEX3D	TRIM35	FKBP5	PYGO1
ATP6V1G3	MFAP2	TRMT2A	FKBPL	PYM1
ATP6V1H	MFAP3L	TRMT61A	FLII	PYROXD2
ATP8B2	MFAP4	TRNT1	FLOT1	QARS1
ATP9A	MFAP5	TRPC1	FLOT2	R3HDM1
ATXN3	MFRP	TRPC4AP	FLRT3	R3HDM2
AUP1	MFSD1	TRPM7	FLT1	RAB11FIP1
AUTS2	MFSD14A	TRPS1	FLVCR2	RAB13
B3GALT2	MFSD14C	TSC22D1	FMC1-LUC7L2	RAB20
B3GALT6	MFSD3	TSC22D2	FMO1	RAB26
B3GNT8	MGAT2	TSC22D3	FMO3	RAB27B
B4GALNT1	MGRN1	TSG101	FMO4	RAB34
B4GALNT3	MIA2	TSHZ2	FMR1	RAB36
B4GALT1	MICAL2	TSHZ3	FNDC11	RAB38
B4GALT2	MICOS13	TSKU	FOXD2	RAB3B
B4GALT3	MIGA1	TSN	FOXE1	RAB5B
B4GALT7	MILR1	TSNAX	FOXF1	RAB7B
BACE2	MISP	TSPAN12	FOXF2	RAC3
BACH2	MLF1	TSPAN31	FOXQ1	RAD1
BAG5	MLLT11	TSPAN8	FRAT1	RAD18
BAIAP2L2	MLXIP	TSPO	FRAT2	RAD51D
BAK1	MMAA	TSPYL1	FRG1	RAG1
BANK1	MMP10	TSPYL2	FSD1	RAI14
BBC3	MMP14	TSPYL4	FUCA1	RANBP10
BBLN	MMP28	TSSC4	FUOM	RAP1GAP2
BBS5	MN1	TSTD1	FXN	RAPGEF1
BCAS2	MON1A	TTC19	FXYD1	RAPGEF2
BCHE	MON2	TTC3	FYB1	RAPGEF4
BCL10	MORC2	TTL	FYCO1	RARB
BCL11B	MORN1	TTLL1	G0S2	RARRES1
BCL2	MORN4	TTLL3	G6PD	RARRES2
BEND7	MPPED2	TUFT1	GABARAPL1	RARS2
BEST1	MRAS	TULP4	GALNT14	RASA2
BET1	MRPL15	TUSC1	GALNT18	RASD1
BET1L	MRPL37	TUSC3	GALNT3	RASGRF1
BFAR	MRPS16	TVP23B	GARNL3	RASGRP1
BGN	MSC	TVP23C	GART	RASGRP2
BHLHA15	MSMO1	TXNDC11	GAS1	RASL10B
BHLHE40	MSR1	UAP1	GAS2L3	RASL11A
BHLHE41	MSTN	UBA1	GAS8	RASL12
BICD1	MSTO1	UBAC2	GATB	RASSF4
BLCAP	MSX1	UBC	GBA2	RAVER2
BLOC1S2	MTCH1	UBE2B	GBP3	RBFOX2
BLOC1S3	MTDH	UBE2G2	GCA	RBIS
BLZF1	MTFR1	UBE2K	GCHFR	RBM17
BMI1	MTMR7	UBE2Q2	GCK	RBM19
BMP6	MTMR9	UBE2W	GCNT2	RBM38
BMPR1B	MTPN	UBL3	GCNT3	RBM4
BMPR2	MTR	UBL5	GDA	RBM41
BMT2	MTURN	UBN1	GDAP1	RBMX
BNC1	MTX2	UFM1	GDE1	RBP7
BNIP2	MTX3	UGGT1	GDF7	RBPMS
BPNT2	MUL1	ULBP1	GEMIN6	RBPMS2
BRAF	MUSK	ULBP2	GFAP	RCAN2
BRAP	MXD1	ULK3	GFER	RCBTB2
BRF2	MXD4	ULK4	GFOD2	RCC1
BRWD1	MXRA5	UNC13A	GGT1	REEP2
BSDC1	MXRA7	UNC5B	GGT5	REPIN1
BSN	MXRA8	UNG	GGT7	RESF1
BST1	MYBBP1A	UPP1	GIMAP2	RET
BTAF1	MYCBP2	UQCRRF51	GIPC3	RFX3

BTBD10	MYCT1	URI1	GJA1	RGL1
BTBD19	MYH1	USP22	GJD3	RGL3
BTBD7	MYH2	USP35	GK	RGP1
C11orf24	MYH4	USP36	GKAP1	RGS10
C11orf96	MYH8	USP45	GLCC1	RGS17
C12orf4	MYL12A	UTP15	GLDN	RGS2
C15orf65	MYO1B	UTP25	GLE1	RGS5
C16orf72	MYO1D	UVSSA	GLIS3	RHBDF1
C16orf87	MYO1E	UXS1	GLRX5	RHCG
C17orf49	MYO6	VAMP2	GLT8D2	RHOBTB2
C18orf32	MYO9A	VARS1	GLUD2	RHOBTB3
C19orf12	MYOM1	VASN	GLUL	RHOF
C1GALT1	MYOM3	VCAM1	GMDS	RHOJ
C1orf109	N6AMT1	VCAN	GMNN	RIBC2
C1orf122	NAA50	VCPIP1	GMPR	RIC1
C1orf216	NAB2	VCPKMT	GNA14	RIC8B
C1orf52	NADK2	VDR	GNAI1	RILP
C1QTNF3	NAGK	VEGFA	GNAO1	RILPL2
C1QTNF5	NAGLU	VEGFB	GNAZ	RIN3
C2CD2L	NALCN	VGLL4	GNB5	RIPK2
C3orf38	NALF1	VKORC1	GNG10	RIPOR2
C3orf80	NAP1L3	VMP1	GOT2	RIPOR3
C4orf3	NAP1L5	VNN2	GPBP1	RMI2
C4orf47	NARS1	VPS13C	GPC3	RND2
C5AR1	NAV1	VPS26B	GPM6B	RNF114
C5AR2	NBAS	VPS28	GPR157	RNF144A
C5orf46	NBEAL1	VPS36	GPR160	RNF150
C6orf62	NBPF6	VPS53	GPR162	RNF157
C6orf89	NCALD	VPS8	GPR176	RNF175
C7orf50	NCAM1	VSNL1	GPR19	RNF207
C8orf33	NCDN	VSTM2L	GPR39	RNF26
C8orf58	NCKAP1	VXN	GPR4	RNF41
C9orf64	NCKAP5L	WARS1	GPR63	RNF8
C9orf78	NCR3LG1	WASF3	GPRC5A	RPAP3
CA13	NCSTN	WASL	GPRC5B	RPGR
CA5B	NDEL1	WBP1	GPRC5C	RPL14
CABLES1	NDFIP1	WDFY2	GPSM1	RPL18
CACNB1	NDNF	WDFY3	GPSM2	RPL18A
CACNB4	NDP	WDR47	GPSM3	RPL21
CADPS	NDST1	WDR83OS	GPX3	RPL22
CALB2	NDST2	WHRN	GRAMD1C	RPL23
CALCRL	NDUFAF6	WIPF3	GRB7	RPL23A
CALHM5	NDUFAF8	WIZ	GRHL1	RPL26
CALM1	NDUFB2	WNK1	GRIA1	RPL27A
CAMK2B	NEB	WNK3	GRIK1	RPL28
CAMKK1	NECAP1	WNT4	GRIK2	RPL29
CAMKK2	NECAP2	WNT9A	GRIK5	RPL32
CAMSAP2	NECTIN4	WSB2	GRIP1	RPL36A
CAPG	NEDD9	WTIP	GRIP2	RPL41
CAPRIN2	NEFH	WWC2	GRK3	RPL6
CARD6	NEK1	WWP1	GRK5	RPL7A
CASTOR1	NEK11	WWP2	GRK6	RPLP0
CAVIN2	NEK7	WWTR1	GRTP1	RPS10
CAVIN4	NEK8	XBP1	GSDMD	RPS11
CBFA2T2	NEO1	XIAP	GSPT2	RPS15A
CBFB	NFATC1	XPNPEP1	GSR	RPS20
CBLB	NFATC3	XPNPEP2	GSTK1	RPS25
CBWD1	NFE2L1	XPNPEP3	GSTM3	RPS26
CC2D1B	NFIB	XPO5	GSTM4	RPS27
CCDC142	NGEF	XPOT	GSTM5	RPS5
CCDC144A	NGRN	XRCC4	GSTT2B	RPS6
CCDC159	NHSL2	XXYLT1	GTF2IRD1	RPS6KA1
CCDC22	NIBAN1	XYLB	GTPBP8	RPS6KA5
CCDC24	NIFK	XYLT1	GUCY1A1	RPS6KA6
CCDC3	NINJ2	YIF1A	GUCY1B1	RPS6KL1

# Supplementary information

CCDC6	NIP7	YIPF2	GXYLT1	RPS7
CCDC80	NKAIN2	YIPF5	GYG2	RPS8
CCDC89	NKX3-1	YIPF6	GYPC	RPS9
CCDC9	NLRP1	YKT6	H1-10	RPSA
CCDC90B	NMNAT1	YME1L1	H2AW	RPUSD1
CCDC93	NMT1	YRDC	H2AX	RPUSD2
CCIN	NNMT	YTHDF1	H2AZ1	RSBN1
CCL26	NOCT	YTHDF3	H3-3A	RSBN1L
CCL28	NOD1	YWHAG	HAAO	RSP01
CCN1	NOL3	YY2	HACD4	RSP04
CCN2	NOMO1	ZACN	HAP1	RSRC1
CCND1	NOMO2	ZBTB1	HASPIN	RTL3
CCND2	NOS3	ZBTB11	HAUS1	RTN2
CCNO	NOSTRIN	ZBTB21	HAUS4	RTN4R
CCNY	NOTCH2	ZBTB22	HCLS1	RTN4RL2
CCPG1	NOTCH3	ZBTB25	HDAC1	RUNX1T1
CCSAP	NPAS1	ZBTB37	HDAC8	RUNX3
CCSER2	NPAS2	ZBTB41	HDGF	RWDD2B
CCZ1B	NPB	ZBTB47	HDGFL2	RYK
CD109	NPDC1	ZC3HAV1	HEBP1	S1PR3
CD163	NPHP4	ZCCHC14	HELB	S1PR5
CD24	NPIPA2	ZCWPW1	HEXD	SAFB
CD320	NPIPA7	ZCWPW2	HEYL	SAFB2
CD59	NPNT	ZDHHC1	HHEX	SALL1
CD70	NPR3	ZDHHC17	HHIP	SALL2
CDC42EP3	NPY1R	ZDHHC21	HIBADH	SAMD12
CDC42SE1	NR2C2	ZDHHC5	HIP1R	SAMD14
CDC73	NR3C1	ZFP36L1	HJURP	SAMD5
CDH1	NR3C2	ZFPL1	HK2	SAP30L
CDH10	NR4A1	ZFR	HLA-B	SAPCD2
CDH11	NR4A2	ZFTA	HLA-C	SARDH
CDH18	NR6A1	ZFYVE27	HLA-DMB	SARNP
CDH20	NRBF2	ZFYVE9	HLA-E	SAV1
CDH8	NRK	ZMAT3	HLA-F	SBNO2
CDHR1	NRP2	ZMAT4	HLTF	SBSPON
CDIN1	NTNG2	ZMIZ1	HMCES	SCARA5
CDIP1	NTRK3	ZMIZ2	HMG20B	SCARB1
CDK12	NUAK1	ZMPSTE24	HMGA1	SCN1A
CDK14	NUDCD3	ZNF117	HMGA2	SCN1B
CDK5R1	NUDT13	ZNF25	HMGB3	SCN3A
CDKL1	NUDT17	ZNF273	HMG3	SCN5A
CDKN1A	NUDT19	ZNF276	HMG4	SCN8A
CDKN2A	NUMB	ZNF281	HMG5	SCYL3
CDKN2B	OAT	ZNF304	HMSD	SDHA
CDR2	ODC1	ZNF320	HNMT	SDHAF3
CDR2L	ODR4	ZNF35	HNRNPA1	SDK1
CDYL2	OGA	ZNF385B	HNRNPA1L2	SDK2
CEBPG	OGFOD2	ZNF408	HNRNPF	SECISBP2
CELF6	OPCML	ZNF41	HNRNPL	SECTM1
CELSR1	OPHN1	ZNF428	HOMER3	SELENBP1
CEMP1	OR51E2	ZNF503	HOXA10	SELENOP
CEP170	ORAI2	ZNF529	HOXA11	SEMA3B
CEP170B	OSBPL11	ZNF568	HOXA13	SEMA3D
CERCAM	OSBPL2	ZNF587	HOXC12	SEMA3F
CERK	OSBPL6	ZNF592	HOXC13	SEMA4B
CERKL	OSBPL8	ZNF596	HOXD10	SEMA4C
CERS5	OSGEP	ZNF621	HOXD11	SEMA4D
CERS6	OSGIN1	ZNF622	HOXD13	SEMA4G
CFAP20	OSTC	ZNF696	HPS3	SEMA5A
CFAP251	OSTM1	ZNF699	HPSE	SEMA6B
CFAP300	OTOGL	ZNF704	HPSE2	SEMA6D
CFAP418	OTUD4	ZNF787	HR	SEPHS1
CFHR1	OXR1	ZNF789	HS2ST1	SEPTIN10
CGB7	P3H4	ZNF841	HSBP1L1	SEPTIN3
CGB8	P4HA2	ZNF85	HSD17B2	SERINC2



CH25H	P4HA3	ZXDA	HSPA12B	SERP2
CHID1	PADI2	A2M	HSPA1B	SERPINB10
CHM	PAFAH1B1	AAMDC	HSPB11	SERPINB2
CHMP5	PAK1IP1	AAMP	HSPB3	SERPINB4
CHN2	PALM	AASS	HTATIP2	SERPINB7
CHPF	PALM2AKAP2	ABCA10	HTR1B	SERPING1
CHPF2	PAM16	ABCA5	HTR2B	SETD1A
CHPT1	PANK3	ABCB7	HVCN1	SEZ6L2
CHRN2	PAPPA2	ABCB9	ICAM2	SF3A2
CHRNE	PARVB	ABCC2	ICAM4	SFMBT1
CHST6	PAX8	ABCC4	ICAM5	SFMBT2
CHSY1	PAX9	ABCC6	IDH2	SFRP1
CHSY3	PBRM1	ABCC9	IDH3A	SGCA
CIART	PC	ABCG1	IFI16	SGMS1
CIC	PCBP1	ABCG2	IFI27	SH2B2
CISD3	PCDH1	ABHD17C	IFITM2	SH2D5
CLCF1	PCDH10	ABHD5	IFT57	SH3BP1
CLCN3	PCDH15	ABI2	IFT74	SH3BP2
CLCNKA	PCDH18	ABL1	IFT81	SH3GL2
CLGN	PCDH7	ABLIM3	IGBP1	SH3GLB2
CLIC4	PCDHA10	ACAT1	IGF2	SH3RF3
CLINT1	PCDHA11	ACBD4	IGFBP2	SH3TC2
CLN8	PCDHA12	ACER3	IGFBP4	SHC3
CLOCK	PCDHA6	ACIN1	IGFBP5	SHF
CLSTN1	PCDHAC1	ACO1	IGFBPL1	SHMT1
CLTA	PCDHAC2	ACOT11	IGFLR1	SHOX
CLTC	PCDHB2	ACOT12	IGSF8	SHOX2
CLTCL1	PCDHB3	ACP3	IK	SHROOM1
CMKLR1	PCDHGA10	ACP5	IKBKB	SIAE
CNN3	PCDHGA11	ACP6	IKBKE	SIM1
CNPPD1	PCDHGA12	ACP7	IL13RA1	SIM2
CNPY2	PCDHGA4	ACSL1	IL15	SIMC1
CNPY4	PCDHGA5	ACSL5	IL17RA	SIN3A
CNST	PCDHGA7	ACSS2	IL17RB	SIN3B
CNTD1	PCDHGA8	ACSS3	IL17RD	SINHCAF
CNTN3	PCDHGB3	ACTG2	IL18	SIPA1
CNTN4	PCDHGC5	ACTR1B	IL1A	SIPA1L2
CNTN5	PCGF5	ACTR3B	IL1RN	SIRPB1
CNTNAP2	PCK2	ACTR3C	IL33	SIX2
COA7	PCNX3	ACVR2B	IL3RA	SIX4
COG3	PCOLCE2	ACYP1	IL6R	SKA2
COG8	PCSK1	ADAM19	IL6ST	SKIDA1
COL11A1	PCSK9	ADAM28	ILK	SKP2
COL12A1	PCYT1A	ADAM33	ILRUN	SLC10A6
COL14A1	PDCD4	ADAM9	IMPA2	SLC12A7
COL1A1	PDCD6IP	ADAMTS15	INA	SLC12A8
COL1A2	PDE11A	ADAMTS3	INCENP	SLC13A3
COL3A1	PDE1A	ADAMTSL4	ING1	SLC16A14
COL5A1	PDE4C	ADCY1	ING2	SLC16A2
COL5A2	PDE7A	ADCY3	ING5	SLC16A4
COL6A6	PDE8A	ADGRA3	INKA2	SLC16A7
COL8A1	PDF	ADGRB1	INPP4B	SLC19A1
COL8A2	PDGFC	ADGRB2	INPP5A	SLC19A3
COLGALT2	PDIK1L	ADGRE2	INPP5J	SLC1A7
COMMD5	PDPK1	ADGRG1	INTS8	SLC22A4
COMP	PEA15	ADH1B	INVS	SLC24A3
COP1	PEAK1	ADHFE1	IP6K3	SLC25A12
COPB1	PEBP1	ADI1	IPCEF1	SLC25A29
COPG1	PEDS1	ADK	IPO8	SLC25A44
COPS7A	PEDS1-UBE2V1	ADNP	IQCD	SLC25A53
COPS7B	PER1	ADORA1	IQSEC2	SLC26A6
COPS8	PET100	ADORA2B	IRAG1	SLC27A2
COPS9	PEX10	ADRB2	IRAK1BP1	SLC28A3
COPZ2	PEX26	AFF1	IRF2	SLC29A2
COQ10B	PEX3	AGBL2	IRF2BPL	SLC2A12



# Supplementary information

COQ4	PEX5L	AGBL3	IRS1	SLC2A5
CORO2B	PEX6	AGFG1	IRX6	SLC2A8
CPE	PEX7	AHR	ISCA2	SLC2A9
CPLANE2	PFKFB2	AHRR	ISL1	SLC35D2
CPSF4	PFN2	AK7	ISL2	SLC35E2B
CPT1A	PGAM2	AKAP1	ISOC1	SLC36A4
CPVL	PGAM4	AKAP12	ISYNA1	SLC37A1
CREB3L2	PGAP3	AKAP6	ITGA2B	SLC37A2
CRIM1	PGAP6	AKAP8L	ITGA8	SLC38A11
CRIP1	PGLS	AKIRIN2	ITGAE	SLC39A1
CRIP2	PGM1	AKNAD1	ITGB4	SLC41A3
CRISPLD1	PGM2L1	AKR1B1	ITGB8	SLC43A1
CRMP1	PGM3	AKR1B10	ITIH5	SLC45A1
CRY2	PGRMC2	AKT1	ITM2C	SLC46A1
CRYAB	PHETA2	ALDH1A1	ITPKA	SLC47A1
CRYM	PHF13	ALDH1A2	ITPKB	SLC6A16
CRYZL2P-SEC16B	PHF20L1	ALDH3A2	ITPRID2	SLC6A6
CSF2RB	PHLDA3	ALDH3B1	ITPRIPL1	SLC7A3
CSRNP1	PHLDB1	ALDH4A1	ITSN2	SLC7A7
CSRNP2	PI16	ALDOC	JADE2	SLC9A3R2
CST6	PICALM	ALKBH1	JAK3	SLCO3A1
CSTB	PIDD1	ALPK2	JAKMIP3	SLCO4A1
CTAGE15	PIGG	ALX1	JMJD7	SLF2
CTAGE8	PIGK	ALX4	JPH1	SLFN12
CTH	PIGY	AMD1	JPT2	SLFN12L
CTHRC1	PIK3IP1	AMDHD1	JRK	SLFN13
CTIF	PIK3R2	AMER1	JUP	SMARCA2
CTLA4	PIP4P1	ANGEL2	KALRN	SMARCC2
CUBN	PIP4P2	ANK1	KANK2	SMARCD3
CXXC5	PITHD1	ANKDD1A	KAT6A	SMC2
CYB561D2	PITPNA	ANKEF1	KAT6B	SMC3
CYB5R1	PITPNM2	ANKRD13A	KCNA3	SMCHD1
CYB5R3	PIWIL4	ANKRD18B	KCNAB3	SMIM1
CYBRD1	PJA2	ANKRD26	KCNB2	SMIM10L2A
CYP11A1	PKD1	ANKRD28	KCND1	SMIM10L2B
CYP20A1	PKNOX2	ANKRD29	KCNE1	SMOC2
CYS1	PKP2	ANKRD35	KCNG2	SMPD2
CYSTM1	PLA2G15	ANKRD49	KCNH5	SMPD3
CYTH1	PLAA	ANKRD53	KCNIP3	SMPDL3A
CYTH3	PLAC9	ANKS1A	KCNJ2	SNAP25
CYTL1	PLAGL1	ANKZF1	KCNJ8	SNAP29
DAB2	PLBD2	ANO3	KCNMB2	SNCG
DACT1	PLD4	ANO4	KCNN2	SNN
DAD1	PLEC	ANOS1	KCNQ4	SNRK
DCLK3	PLEKHA7	ANXA11	KCNS1	SNRNP40
DCTN4	PLEKHF1	ANXA3	KCNS2	SNRNP70
DCTN5	PLEKHG4	ANXA9	KCTD14	SNRPE
DCUN1D1	PLEKHH2	AP1G2	KCTD3	SNTB1
DCUN1D5	PLEKHH3	AP1S3	KHDRBS3	SNTB2
DDAH1	PLK3	AP3M1	KHK	SOCS1
DDAH2	PLOD2	APBA1	KIAA0040	SOCS2
DDIT3	PLPP5	APBA2	KIAA0753	SOCS3
DDX21	PLS3	APBB1	KIAA1143	SOCS5
DDX41	PLSCR3	APCDD1	KIAA1522	SOD3
DDX43	PLXDC1	APEH	KIAA1755	SORD
DDX49	PLXDC2	APELA	KIF15	SORL1
DENND2C	PLXNA1	APOB	KIF17	SOWAHC
DEPTOR	PLXNA2	APOBEC3F	KIF18B	SOWAHD
DERL1	PLXNA3	APOBEC3G	KIF1C	SOX12
DERL2	PMEPA1	APOC1	KIF22	SOX13
DEUP1	PMVK	APOE	KIF24	SOX15
DGCR6	PNMA1	APOL1	KIF26A	SP3
DGCR8	PNO1	APOL3	KIFC3	SP4
DGKB	PNP	APOLD1	KIRREL3	SPAG17
DGKI	PNPO	APP	KISS1	SPAG7

DGKQ	PNPT1	AQP11	KIZ	SPATA13
DHDDS	PODNL1	AQP9	KLF14	SPATA6
DHRS7B	PODXL	AR	KLF9	SPATA7
DIP2C	POFUT1	ARAP3	KLHL13	SPATS2
DIRAS1	POLD4	AREG	KLHL23	SPATS2L
DIRAS2	POLH	ARHGAP11A	KLHL25	SPC24
DISP2	POLR1A	ARHGAP18	KLHL33	SPEG
DLC1	POLR1G	ARHGAP6	KLHL5	SPHKAP
DLGAP4	POLR2K	ARHGEF1	KMT2E	SPIN2A
DLX1	POLR3C	ARHGEF25	KNDC1	SPINDOC
DLX2	POLRMT	ARHGEF39	KNL1	SPINT1
DMAC1	POM121	ARHGEF7	KPTN	SPIRE2
DMD	POM121C	ARHGEF9	KRT14	SPOCD1
DMRTA1	POMP	ARID1A	KRT15	SPON1
DMWD	POMT1	ARID5A	KRT17	SPON2
DNAAF4	POP4	ARID5B	KRT18	SPSB1
DNAAF8	PORCN	ARMC9	KRT19	SPTLC3
DNAAF9	POSTN	ARNT2	KRT32	SPTSSA
DNAH1	POTEC	ARPIN	KRT33B	SQOR
DNAH14	POU3F1	ARRB2	KRT38	SRD5A2
DNAI3	POU3F2	ARRDC1	KRT7	SRGAP2B
DNAJB1	PPIC	ARRDC3	KRT8	SRGN
DNAJB9	PPM1A	ARSD	KRT81	SRPK1
DNAJC10	PPM1E	ARSI	KRTAP3-1	SRRT
DNAJC12	PPP1R13L	ARSJ	KTN1	SRSF4
DNAJC19	PPP1R3B	ARSK	L1CAM	SSBP2
DNAJC24	PPP1R3F	ARSL	L1TD1	SSBP3
DNER	PPP4R2	ART5	L3MBTL4	SSH3
DNM3	PRCD	ARTN	LACC1	SSNA1
DNPH1	PRDM16	ASB13	LACTB2	SSRP1
DOHH	PRELID3A	ASB2	LAMA2	SST
DOK1	PREPL	ASB5	LAMA3	SSX2IP
DOK5	PRKAB2	ASB7	LAMA4	ST6GALNAC6
DOK6	PRKAR1A	ASIC1	LAMA5	STAG2
DPH2	PRKD1	ASPH	LAMB1	STAG3
DPM1	PRPSAP1	ASPHD1	LAMB3	STAMPB
DR1	PRR15	ASPM	LAMC1	STAMBPL1
DRD4	PRR16	ASRGL1	LAPTM5	STAP2
DSE	PRRC1	ASS1	LARP7	STARD3NL
DSG2	PRRC2B	ASTN1	LAYN	STARD7
DSP	PRSS23	ASXL1	LBR	STARD8
DUS1L	PRSS53	ATAD2	LCNL1	STARD9
DUSP11	PSAT1	ATG4D	LCORL	STAT5B
DUSP14	PSENEN	ATM	LCP1	STC1
DUSP18	PSKH1	ATN1	LDHA	STC2
DVL1	PSMC2	ATP13A3	LDB2	STEAP1B
DVL3	PSMD7	ATP1A2	LDHB	STEAP4
DYNC1I1	PSMG1	ATP23	LDOC1	STK17B
DYNC1LI2	PSMG3	ATP2A2	LEKR1	STK26
DYNC2LI1	PTBP3	ATP2A3	LEPR	STK3
DYRK2	PTCD1	ATP2B4	LGALS3BP	STK33
DYSF	PTGER3	ATP5F1A	LGALS9	STK4
E2F3	PTGR2	ATP5F1C	LGI4	STK40
EAF1	PTHLH	ATP5MC2	LIFR	STMN3
EAF2	PTP4A1	ATP5MG	LIMD1	STN1
EBF1	PTPDC1	ATP5PO	LIMS3	STOM
ECD	PTPN12	ATP6V0A4	LIMS4	STOX1
EDC3	PTPN14	ATP8B3	LIN54	STRA6
EDEM1	PTPN20	ATRNL1	LINC02210-CRHR1	STRADB
EDEM3	PTPN22	ATXN10	LIPE	STUM
EDIL3	PTPN9	ATXN2	LITAF	STX10
EFCAB13	PTPRB	ATXN7L1	LLGL2	STX11
EFR3A	PTPRM	ATXN7L2	LMOD1	STX17
EFR3B	PTPRZ1	AUH	LMTK3	STX8
EGR1	PTRH2	AURKB	LNP1	STXBP2

## Supplementary information

EGR2	PTTG1IP	AXL	LOC100653049	STXBP6
EGR3	PTX3	B2M	LOC102724813	SUCLG2
EIF3CL	PURB	B4GALNT2	LOC105374103	SULT1A4
ELL2	PWWP3A	B4GALNT4	LOC107984156	SULT2B1
ELMO2	PXDC1	BAIAP3	LOC107984449	SULT4A1
ELN	PXMP4	BARD1	LOC107984832	SUPT16H
EMC1	PYCR1	BCAM	LOC107986217	SUSD1
EMC10	PYCR2	BCL2L10	LOC110384692	SUSD2
EMC2	PYGB	BCL3	LOC389831	SUSD3
EME2	PYROXD1	BCL9	LOC728392	SUSD5
ENAH	PYURF	BDKRB2	LOXL3	SV2A
ENC1	QPCT	BDNF	LPAR4	SVBP
ENDOD1	QRICH2	BEX1	LPAR6	SVEP1
ENKUR	RAB11FIP5	BEX3	LPCAT3	SVIL
ENO3	RAB14	BFSP1	LPCAT4	SYCE1L
ENOPH1	RAB1A	BHLHE22	LPIN3	SYCP2
ENTPD4	RAB21	BHMT	LRATD1	SYF2
ENTPD5	RAB22A	BICRA	LRCH1	SYN1
EPG5	RAB23	BID	LRCH2	SYNE2
EPHA2	RAB28	BIN3	LRCH3	SYNE3
EPHA3	RAB2A	BIVM-ERCC5	LRCH4	SYNGR1
EPHB3	RAB2B	BLM	LRFN1	SYNGR2
EPRS1	RAB35	BMF	LRP1B	SYNGR3
EPS8	RAB39B	BMP2	LRP8	SYNPO2
EPYC	RAB3GAP2	BMP4	LRPPRC	SYNPO2L
ERBB4	RAB3IP	BMP8A	LRRC1	SYPL2
ERF	RAB5A	BNC2	LRRC37A	SYT3
ERG	RAB6A	BOD1	LRRC37A2	SYTL2
ERICH2	RAB7A	BORA	LRRC37B	SYTL4
ERLEC1	RAB8B	BPI	LRRC38	SYTL5
ERMN	RABEP1	BRD8	LRRC45	TAB1
ERN1	RABGGTB	BRF1	LRRC49	TACC2
ESD	RABL2B	BRINP2	LRRC61	TAF1C
ESRP2	RABL3	BRIP1	LRRC7	TAF4
ESYT3	RAD21L1	BRIX1	LRRC75A	TAF6
ETV3	RADX	BRPF3	LRRC8B	TAF8
ETV5	RALA	BRWD3	LRRC8C	TANK
EVA1A	RANBP2	BST2	LRRC8D	TARBP2
EVC	RANBP3L	BTBD2	LRRC8E	TARS3
EXOC5	RANBP9	BTN3A2	LRRFIP2	TAS1R1
EXOC8	RAPH1	BTRC	LRRK1	TAS1R3
EXOSC4	RASA1	BUD13	LSR	TAS2R1
EXOSC6	RASAL2	C10orf105	LTA4H	TASOR
EZH1	RASD2	C11orf49	LTBP4	TBC1D1
FAAP100	RASL11B	C11orf98	LTK	TBC1D14
FAF2	RASSF9	C14orf132	LUM	TBC1D3D
FAHD1	RBKS	C17orf67	LURAP1	TBC1D3E
FAM102A	RBM46	C17orf80	LXN	TBC1D4
FAM114A2	RBMS3	C1GALT1C1	LY6G5C	TBKBP1
FAM126A	RCAN1	C1orf115	LY6K	TBL1X
FAM133A	RCAN3	C1orf226	LY75	TBPL1
FAM161B	RCC1L	C1QTNF1	LY75-CD302	TBX2
FAM168A	RCC2	C1QTNF2	LYL1	TBX20
FAM168B	RCL1	C1QTNF7	LYN	TBX3
FAM174A	RCN3	C1R	LYPD1	TBX4
FAM177A1	RCOR3	C1RL	LYPD3	TBX5
FAM180A	RCVRN	C2	LYST	TCAF2
FAM20B	RDH10	C21orf91	LYZ	TCEAL1
FAM210A	RELA	C22orf15	MAB21L1	TCEAL3
FAM214B	RELN	C2orf74	MAGEL2	TCEAL4
FAM219B	REPS2	C3	MALT1	TCEAL9
FAM220A	RETSAT	C3orf62	MAMSTR	TCEANC2
FAM229B	REX1BD	C3orf70	MANSC1	TCF20
FAM3C	REXO2	C4orf36	MAOA	TCF21
FAM50A	RFLNA	C4orf46	MAOB	TCIM

FAM71F2	RFNG	C5	MAP2	TCOF1
FAM76A	RFTN1	C6orf141	MAP2K6	TDP1
FAM83G	RFTN2	C7orf31	MAP3K1	TDRD9
FAM89B	RFX7	C9orf40	MAP3K21	TDRP
FAT1	RGN	C9orf47	MAP3K5	TEAD1
FAT3	RGPD4	CA11	MAP3K9	TEAD3
FBLL1	RGPD8	CAB39	MAP4K2	TEAD4
FBN1	RHBDD2	CABLES2	MAP4K3	TEC
FBXL12	RHBDD3	CACNA1H	MAP6	TECPR2
FBXL15	RHCE	CACNB3	MAP7	TENT5B
FBXL8	RHEB	CACNG4	MAPK15	TENT5C
FBXO32	RHOBTB1	CACNG7	MAPK8IP1	TES
FBXO33	RILPL1	CADM2	MAPKBP1	TESK2
FBXW7	RIMKLB	CADM4	MAPT	TESMIN
FCHO2	RIMS1	CADPS2	MARCHF10	TEX29
FDX2	RIMS4	CALHM2	MARCKSL1	TFAP2A
FEM1A	RIOK3	CALY	MARK1	TFAP2C
FERMT3	RIOX1	CAMK1G	MASP1	TFAP4
FGF12	RIPK4	CAMK2A	MATK	TFEB
FGF14	RIPOR1	CAMK2N1	MB21D2	TFPI
FGF2	RLF	CAMTA1	MBNL3	TFR2
FGF7	RLIM	CAPN14	MBOAT1	TGFB11
FGF9	RNF103	CAPN6	MC1R	TGIF2
FGFRL1	RNF11	CARD11	MCM3	TGS1
FGL2	RNF111	CARD16	MCOLN2	THAP10
FHAD1	RNF112	CARD9	MCU	THAP11
FHIP1B	RNF121	CARHSP1	ME1	THEM4
FHIP2B	RNF122	CARMIL1	MECOM	THEM6
FHIT	RNF128	CASP1	MEIOC	THG1L
FHL3	RNF14	CASP10	MEIS1	THOC2
FICD	RNF144B	CASP2	MEMO1	THOC5
FIGN	RNF145	CAT	MEOX2	THPO
FIGNL2	RNF149	CAV1	MEST	THSD4
FJX1	RNF170	CBR3	METAP2	THY1
FLAD1	RNF185	CBX5	METRNL	TIA1
FLG	RNF187	CBX6	METTL26	TICRR
FLI1	RNF19B	CC2D2A	METTL3	TIFA
FLRT2	RNF215	CCDC102A	METTL7A	TIGD2
FMN1	RNF24	CCDC102B	MEX3A	TIMP4
FMNL2	RNFT1	CCDC122	MFF	TINAGL1
FMNL3	RNH1	CCDC134	MFSD2B	TIRAP
FN1	RO60	CCDC14	MFSD6	TJAP1
FNDC1	ROR1	CCDC146	MFSD9	TKT
FNDC10	RORA	CCDC173	MGARP	TLCD4
FNDC5	RP2	CCDC180	MGAT1	TLE4
FNIP2	RPE	CCDC188	MGAT3	TLR2
FOS	RPGRIP1L	CCDC189	MGAT5B	TLR4
FOSB	RPIA	CCDC190	MICAL1	TM4SF20
FOXD1	RPP14	CCDC25	MICB	TMC6
FOXJ3	RPRML	CCDC50	MICU3	TMCC3
FOXN2	RPS10-NUDT3	CCDC68	MID1	TMCO3
FOXS1	RPS6KA2	CCDC69	MIDEAS	TMCO4
FRMD5	RPS6KC1	CCDC96	MIS18BP1	TMEM121
FRMD6	RRAGC	CCL2	MITF	TMEM123
FRMD8	RRAGD	CCN3	MKKS	TMEM132A
FSCN1	RRM2B	CCN5	MKRN1	TMEM139
FSTL3	RRN3	CCNC	MLLT10	TMEM140
FTCDNL1	RRP1	CCNF	MLLT3	TMEM150C
FTO	RRP12	CCNI	MLPH	TMEM158
FTSJ1	RTCA	CCNJL	MMD	TMEM164
FUT11	RTL5	CCP110	MME	TMEM165
FUT4	RTL8C	CCR10	MMP25	TMEM176A
FYN	RTN1	CCR7	MMP3	TMEM176B
FYTTD1	RTN3	CD177	MOB3B	TMEM18
FZD6	RTN4	CD274	MOCS1	TMEM200B

# Supplementary information

FZD8	RTN4RL1	CD302	MOCS2	TMEM25
G3BP2	RUFY2	CD34	MON1B	TMEM255A
G6PC3	RUSC2	CD36	MOSPD1	TMEM26
GAA	RXFP3	CD40	MOV10	TMEM51
GABARAPL2	S100A13	CD7	MOV10L1	TMEM52B
GABPB2	S100A16	CD74	MPG	TMEM59L
GABRG1	SAMD3	CD79B	MPHOSPH6	TMEM64
GADD45B	SAMD4B	CD82	MPHOSPH8	TMEM69
GADD45G	SAMD8	CD9	MPST	TMEM9
GALNT1	SAP30	CDA	MRE11	TMEM97
GALNT10	SARS1	CDC25B	MRFAP1L1	TMOD1
GALNT11	SASH1	CDC42BPG	MRGBP	TMSB15A
GALNT12	SAT1	CDC42EP2	MRGPRF	TMSB15B
GALNT13	SATB2	CDC42EP4	MRPL11	TMTC2
GALNT16	SBF1	CDC42SE2	MRPL44	TNFAIP1
GALNT5	SCAF1	CDCP1	MRPL58	TNFAIP8L1
GAP43	SCAMP1	CDH24	MRPS22	TNFRSF11B
GAREM2	SCARB2	CDHR3	MRPS24	TNFRSF13C
GARS1	SCARF2	CDK11B	MRPS27	TNFRSF19
GAS2	SCG2	CDK15	MRPS6	TNFRSF1A
GAS6	SCO1	CDK18	MRTFB	TNFRSF6B
GAS7	SCO2	CDK19	MSLN	TNFSF13B
GATAD2A	SCOC	CDK2	MSRA	TNIP1
GATAD2B	SCRG1	CDK20	MSRB1	TNIP2
GATD1	SCRN1	CDK5RAP1	MST1R	TNK1
GBA	SCX	CDK5RAP3	MSX2	TNNC1
GCC1	SDAD1	CDK8	MT2A	TNNT1
GCLC	SDC2	CDKL2	MTA1	TNRC6A
GDF10	SDCCAG8	CDKN1B	MTA3	TNS4
GDF6	SDE2	CDKN2AIP	MTARC2	TOM1L1
GDI1	SDHC	CDKN2C	MTCL1	TONSL
GFPT1	SEC16A	CDX1	MTMR1	TOP1
GFPT2	SEC16B	CELSR2	MTMR10	TOP1MT
GGCX	SEC22C	CEMIP2	MTMR14	TOP2A
GHDC	SEC23B	CENATAC	MTMR4	TOP3B
GHITM	SEC24A	CEND1	MTMR8	TOR4A
GIMD1	SEC24B	CENPE	MTRF1	TOX2
GIPC1	SEC24C	CENPV	MTUS1	TP53BP2
GJB2	SEC24D	CEP112	MYBL2	TP53I11
GJD2	SEC31A	CEP131	MYH11	TP53INP2
GLG1	SEC61A1	CEP152	MYL6B	TPBG
GLIPR1L2	SEC61A2	CEP162	MYLK	TPCN1
GLIPR2	SEC61B	CEP19	MYO10	TPP2
GLIS2	SEC61G	CEP57	MYO18A	TPR
GLOD4	SEC63	CEP68	MYO7B	TPST1
GLRB	SEL1L	CEP83	MYOCD	TPT1
GLS	SELENOF	CFAP46	MYPN	TRABD
GLT8D1	SELENOS	CFAP53	MYRF	TRABD2A
GMPPB	SELENOW	CFI	MYZAP	TRAF2
GNA11	SEMA3C	CGAS	NAA16	TRAF3IP1
GNA13	SEMA7A	CHAF1A	NABP1	TRAK2
GNAS	SEN5	CHAMP1	NACA	TRAM1
GNB4	SEPTIN11	CHCHD3	NACAD	TRAPPC9
GNE	SERAC1	CHD2	NAIP	TRERF1
GNL3L	SERINC5	CHD3	NAMPT	TRHDE
GOLGA2	SERP1	CHD6	NANOS1	TRIB1
GOLGA3	SERPINE1	CHD8	NANS	TRIM16
GOLGA6L10	SERPINE2	CHDH	NARS2	TRIM16L
GOLGA8N	SERPINI1	CHEK1	NASP	TRIM17
GOLM1	SERTAD1	CHEK2	NAT1	TRIM28
GOLT1B	SERTAD2	CHMP4C	NBEAL2	TRIM45
GORASP2	SESN1	CHP1	NBPF14	TRIM46
GOSR1	SESN2	CHRD	NBPF19	TRIM55
GOT1	SESTD1	CHRD1	NBPF3	TRIM58
GPA1	SETD7	CHRM2	NBPF9	TRIM62

GPAM	SETX	CHRM3	NBR1	TRIM67
GPC1	SFXN4	CHRNA5	NCAPD2	TRIM7
GPC4	SGCG	CHST15	NCOA5	TRIM9
GPC6	SGCZ	CHST2	NDC80	TRIOBP
GPCPD1	SGMS2	CHURC1	NDUFA11	TRIR
GPLD1	SGPP1	CIAO2A	NDUFB4	TRMT10B
GPR107	SH3BP4	CIB2	NDUFB8	TRMT5
GPR141	SH3BP5	CIBAR1	NDUFB9	TRMT9B
GPR153	SH3BP5L	CIDEB	NDUFC2-KCTD14	TRO
GPR156	SH3PXD2A	CILP	NDUFS5	TRPM3
GPR18	SH3PXD2B	CIR1	NDUFV1	TRPM6
GPR27	SH3RF1	CITED4	NDUFV2	TRPV4
GPR68	SHANK3	CKS2	NECTIN1	TSGA10
GPR87	SHE	CLDN23	NECTIN2	TSHZ1
GPR89A	SHISA3	CLDND1	NECTIN3	TSPAN5
GPR89B	SHOC2	CLEC2A	NEDD4L	TSPAN9
GPT2	SHROOM4	CLIC6	NEIL1	TSPOAP1
GPX7	SIDT2	CLIP3	NEK4	TTC12
GRAMD2B	SIK1B	CLK1	NELFCD	TTC21B
GRAMD4	SIL1	CLK3	NEMP2	TTC38
GRB2	SIRT1	CLK4	NES	TTC39C
GREM2	SIRT2	CLSTN2	NETO2	TTL5
GRIN3A	SIRT5	CLUL1	NEURL1	TUBA4A
GRK4	SKAP2	CLYBL	NEURL1B	TUBGCP3
GSE1	SKI	CMC1	NEXN	TUBGCP4
GSK3B	SKIL	CMTM8	NFAM1	TUT4
GTF2H3	SLC10A3	CNFN	NFATC2	TUT7
GTF2H5	SLC14A1	CNKSR3	NFATC2IP	TXK
GTPBP2	SLC14A2	CNNM1	NFE2	TXLNB
GTPBP4	SLC16A1	CNOT11	NFE2L3	TXNRD2
GUK1	SLC19A2	CNOT7	NFIC	UBAP1
GXYLT2	SLC1A4	CNRIP1	NFIL3	UBASH3B
H2AC15	SLC1A5	CNTLN	NFKBIA	UBE2J2
H2BC15	SLC22A15	CNTN1	NFRKB	UBE2V1
H4C8	SLC22A23	CNTNAP1	NFYB	UBIAD1
HACD3	SLC23A2	COA6	NHEJ1	UBL4B
HAND2	SLC23A3	COBLL1	NHLRC4	UBXN2A
HAPLN1	SLC24A2	COCH	NID1	UBXN2B
HAPLN3	SLC25A16	COIL	NID2	UCN2
HAS2	SLC25A20	COL18A1	NIM1K	UCP2
HAUS7	SLC25A32	COL21A1	NINL	UFC1
HBEGF	SLC25A33	COL27A1	NIPA1	UIMC1
HCK	SLC25A37	COL4A1	NIPAL1	UNC45A
HCN1	SLC25A45	COL4A2	NIPAL2	UNC93B1
HCN3	SLC25A51	COL4A4	NIPAL4	UPF3B
HDAC9	SLC26A1	COL4A5	NIPSNAP1	UPK3BL2
HEMK1	SLC26A2	COL4A6	NKD2	UQCRB
HERC3	SLC27A4	COL7A1	NLGN3	UQCRC1
HERPUD1	SLC29A1	COL9A3	NLGN4X	URGCP
HES1	SLC2A13	COLEC10	NLRC5	USB1
HEXA	SLC30A1	COLEC12	NME5	USH2A
HGH1	SLC30A7	COLQ	NMNAT3	USP1
HIPK1	SLC31A1	COMMD6	NMRK1	USP3
HIVEP1	SLC31A2	COMMD7	NNT	USP33
HIVEP2	SLC33A1	COPS4	NONO	USP43
HK1	SLC35A3	COQ2	NOS1AP	USP44
HLX	SLC35B1	COQ8A	NOTCH1	USP54
HM13	SLC35C2	CORIN	NPAT	USP6NL
HMGCR	SLC35D1	CORO1B	NPC1	USP8
HMGXB3	SLC35E1	COTL1	NPEPPS	UTP14C
HNRNPA0	SLC35E4	COX10	NPIPA1	UTP20
HOMER1	SLC35F2	COX6B2	NPIP12	VASH1
HOMER2	SLC35F5	CPA3	NPIP3	VAV3
HOOK3	SLC36A1	CPA4	NPM1	VEZF1
HOXA4	SLC38A10	CPM	NPM2	VIT



# Supplementary information

HOXA5	SLC38A2	CPNE2	NPTX2	VPS16
HOXA6	SLC38A5	CPOX	NQO1	VPS72
HOXA7	SLC38A7	CPPED1	NR0B1	VSIG10
HOXB2	SLC39A11	CPS1	NR1H3	VSIR
HOXB4	SLC39A13	CPSF1	NR2F2	VSTM5
HOXB5	SLC39A3	CPSF6	NRDC	VTN
HOXB9	SLC39A6	CPT1C	NRGN	VWA1
HOXC4	SLC39A7	CPT2	NRIP1	VWA5A
HOXC5	SLC3A1	CPXM1	NRM	VWA7
HOXC6	SLC43A2	CPZ	NRTN	WARS2
HOXC8	SLC48A1	CRABP2	NSA2	WBP4
HOXC9	SLC4A4	CRACR2B	NSMCE4A	WDCP
HOXD1	SLC52A1	CREB3L1	NT5C	WDR33
HOXD3	SLC52A2	CREB3L4	NT5C3B	WDR48
HOXD4	SLC5A10	CRELD1	NT5DC1	WDR91
HOXD8	SLC5A12	CRISPLD2	NT5DC3	WEE1
HOXD9	SLC66A2	CSDC2	NTF3	WFDC1
HS3ST3A1	SLC7A1	CSF2	NTN1	WFS1
HS3ST3B1	SLC7A8	CSF2RA	NTN4	WLS
HSD17B14	SLC9A7	CSF3	NTSR1	WNT11
HSDL1	SLCO4C1	CSNK1D	NUAK2	WNT2
HSF4	SLFN11	CSPP1	NUDT10	WSCD1
HSPA13	SLIT3	CSRNP3	NUDT11	XAB2
HSPA4L	SLITRK1	CTBP2	NUDT16	XDH
HSPA9	SLITRK5	CTNNAL1	NUDT3	XKR5
HSPB1	SLITRK6	CTSC	NUDT4	XKR8
HSPB6	SMAD7	CTSH	NUDT5	XPC
HSPB7	SMARCA1	CTSW	NUMA1	XRN2
HSPG2	SMCO4	CUEDC2	NUP210	YAE1
HTR1D	SMG1	CUL1	NUP62	YPEL4
HTR1F	SMG9	CUL3	NUSAP1	YTHDC1
HTR2A	SMIM17	CUL4A	NXNL2	YY1AP1
HTRA2	SMIM4	CUL4B	NXPH3	ZADH2
HTT	SMIM7	CWC22	NXT2	ZBED5
IARS1	SMYD2	CX3CL1	NYAP1	ZBED6CL
IBTK	SMYD3	CXCL14	NYNRIN	ZBED9
ID2	SMYD4	CXXC1	OAF	ZBTB12
ID3	SMYD5	CYB5A	OBSCN	ZBTB17
ID4	SNAI1	CYB5R2	OCEL1	ZBTB20
IER3	SNAPC1	CYBA	OCIAD2	ZBTB39
IFI44L	SNAPC3	CYBC1	ODAD2	ZBTB46
IFI6	SNIP1	CYFIP2	OGFR	ZC3H14
IFITM10	SNPH	CYP2J2	OGFRL1	ZC3H3
IFNAR1	SNURF	CYP2S1	OLA1	ZC3H7B
IFRD1	SNX11	CYP7B1	OLFM4	ZCCHC10
IFT122	SNX21	CYRIB	OLFML1	ZCCHC3
IGFBP3	SNX22	DAAM2	OLFML2A	ZCCHC9
IKZF5	SNX25	DAGLB	ORAI1	ZCRB1
IL18R1	SNX30	DAPK1	OSMR	ZDHHC12
IL1RAP	SOAT1	DAXX	OSR2	ZDHHC13
IL1RAPL2	SOCs7	DBF4B	OTOF	ZDHHC15
IL1RL1	SOHLH2	DBNDD1	OTUB1	ZDHHC2
IL1RL2	SORBS2	DBP	OTULINL	ZDHHC3
IL27RA	SORCS2	DCAF6	OVGP1	ZFAND4
IL4R	SOS2	DCAF7	P3H2	ZFAT
IL6	SOX9	DCLRE1C	PAAF1	ZFHX2
ILDR2	SPAAR	DCN	PABPC1	ZFP1
ILVBL	SPACA9	DCP1B	PABPC1L	ZFP30
IMPACT	SPAG1	DDHD1	PAF1	ZFP92
IMPG2	SPAG9	DDIT4L	PAIP2	ZFYVE19
INAFM1	SPARC	DDX11	PAK1	ZHX2
INF2	SPATA18	DDX23	PALB2	ZHX3
INHBA	SPATA21	DDX52	PAN3	ZMYM3
INKA1	SPCS1	DECR1	PAPOLA	ZMYM4
INO80D	SPCS2	DEF6	PAPSS2	ZNF112

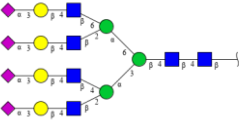

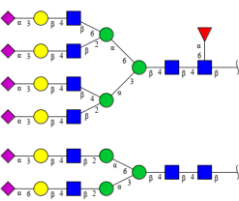
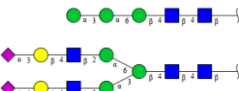
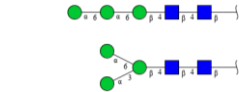
INPP4A	SPEN	DENND1A		ZNF131
INSIG2	SPHK1	DENND2A	PARD6B	ZNF133
INSR	SPHK2	DENND2B	PARP1	ZNF141
INSYN2A	SPIRE1	DENND3	PARP16	ZNF143
INSYN2B	SPNS1	DENND4C	PARP3	ZNF174
INTS1	SPOCK1	DES	PARP4	ZNF175
IPO13	SPP1	DFFB	PASK	ZNF182
IPO4	SPPL2B	DGKD	PATJ	ZNF185
IPP	SPRED2	DGKE	PBX2	ZNF205
IQGAP1	SPRYD3	DHPS	PBX3	ZNF211
IRAK1	SPRYD7	DHRS13	PCBD1	ZNF214
IRF2BP2	SPTBN1	DHRS3	PCBP2	ZNF225
IRS2	SPTBN5	DHRS4	PCBP3	ZNF226
IRX2	SPTLC1	DHRS4L2	PCCA	ZNF227
IRX3	SPTY2D1	DHTKD1	PCDHGA3	ZNF254
IRX5	SRA1	DHX8	PCDHGA6	ZNF280C
ISCU	SRD5A1	DIAPH2	PCDHGB1	ZNF296
ISLR2	SRP19	DIO3	PCDHGB5	ZNF300
IST1	SRPK3	DIPK2A	PCDHGB6	ZNF318
ITCH	SRPRA	DISC1	PCGF2	ZNF33A
ITGA11	SRPRB	DISP1	PCID2	ZNF33B
ITGA4	SS18L1	DLG3	PCLO	ZNF350
ITGA9	SS18L2	DLG4	PCOLCE	ZNF385A
ITGB2	SSC4D	DLK2	PCTP	ZNF395
ITGB5	SSC5D	DLL1	PDCD1LG2	ZNF423
ITGBL1	SSH1	DLL3	PDCD7	ZNF43
ITIH4	SSPN	DLL4	PDE3B	ZNF439
ITPRIPL2	SSR1	DMAC2	PDE4DIP	ZNF451
IVNS1ABP	ST3GAL5	DMKN	PDE5A	ZNF467
JADE1	ST3GAL6	DMPK	PDE8B	ZNF480
JAG1	ST6GALNAC2	DNAH10	PDGFRA	ZNF496
JAM3	ST6GALNAC3	DNAH2	PDGFRL	ZNF510
JCAD	ST7L	DNAJA4	PDK2	ZNF511
JDP2	ST8SIA1	DNAJC22	PDK3	ZNF516
JKAMP	ST8SIA4	DNAJC6	PDLIM1	ZNF518B
JMJD4	STAM	DNALI1	PDP2	ZNF521
JMJD6	STAM2	DNASE1L1	PDS5B	ZNF550
JOSD1	STARD10	DNMBP	PDZRN3	ZNF552
JRKL	STAT1	DNMT1	PELI2	ZNF554
JUNB	STAT4	DNMT3B	PERP	ZNF572
KCNA7	STEAP3	DOCK1	PET117	ZNF581
KCNAB1	STIMATE	DOCK10	PEX11A	ZNF594
KCNC4	STK17A	DOCK11	PFDN5	ZNF606
KCND2	STK19	DOCK2	PFKM	ZNF608
KCNE4	STK38L	DOCK5	PGAP4	ZNF609
KCNG1	STMP1	DOCK8	PGF	ZNF618
KCNH1	STOML1	DPF2	PGM5	ZNF655
KCNK15	STRAP	DPY19L2	PGR	ZNF658
KCNK2	STRN3	DRGX	PGRMC1	ZNF670
KCNN4	STT3A	DROSHA	PGS1	ZNF691
KCNQ5	STT3B	DTNA	PHACTR1	ZNF695
KCTD11	STX12	DTNB	PHB2	ZNF703
KCTD13	STX16	DUSP16	PHC1	ZNF709
KCTD2	STX7	E2F2	PHF10	ZNF71
KCTD5	STXBP1	EAPP	PHF12	ZNF74
KCTD7	SULF1	EBF4	PHF21A	ZNF740
KDELR2	SUPV3L1	EBI3	PHF3	ZNF765-ZNF761
KDELR3	SURF6	EBPL	PHF6	ZNF792
KDM1B	SWAP70	ECE1	PHIP	ZNF853
KDM4B	SWI5	ECHDC3	PHKA1	ZNF888
KDM5A	SYBU	ECI1	PHKG2	ZRANB1
KDM7A	SYMPK	ECT2	PHLDA1	ZSCAN29
KDR	SYNC	EDC4	PHLDA2	ZSWIM5
KHDC4	SYNE1	EDNRA	PHLDB2	ZSWIM9
KIAA0100	SYT12	EDNRB	PHOSPHO2	ZYG11A

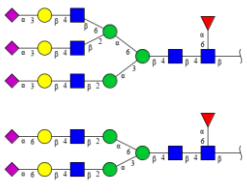
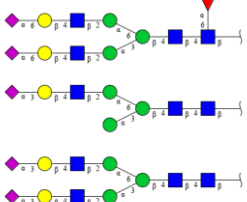
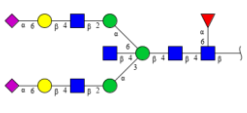
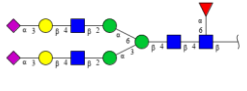
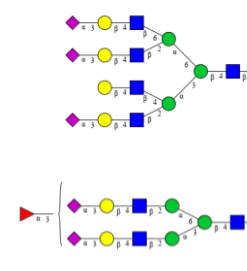
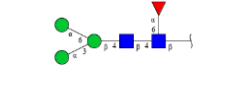
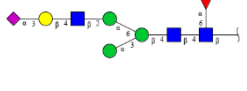


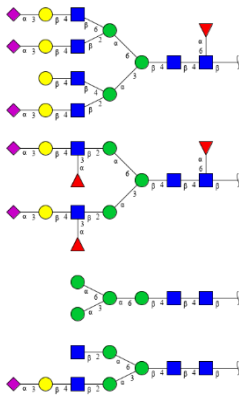
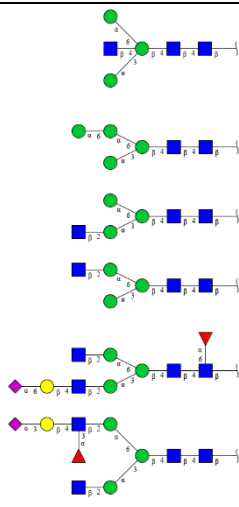
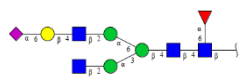
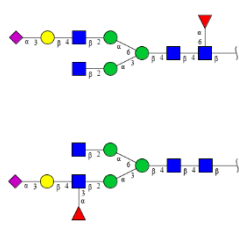
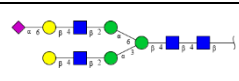
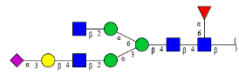
KIAA0754	SYT7	EDRF1	PHYHD1	ZYX
----------	------	-------	--------	-----

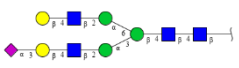
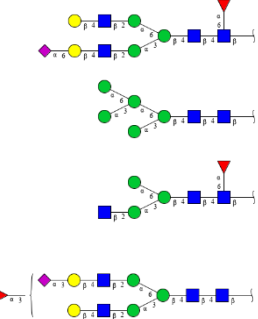
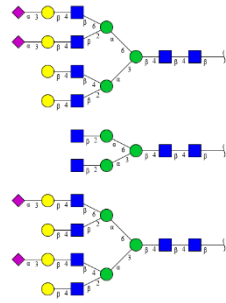
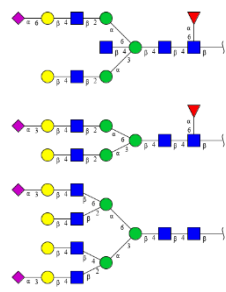

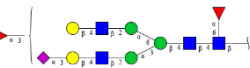
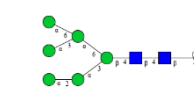
**Table S3: N-Glycomic analysis of Srd5a3-KO medaka fish hatchlings compared to wild type.**

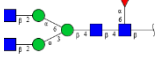
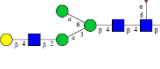
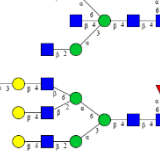
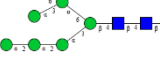

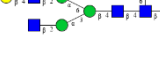
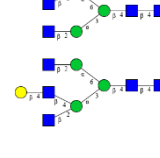
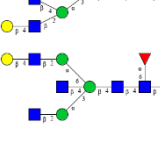
*N*-Glycan structures assigned by migration time matching with glyXbaseCE to the peaks of the xCGE-LIF *N*-glycan fingerprints, derived from the medaka fish hatchlings proteomes of the Srd5a3 Wild Type 1 (WT1; n = 10), Srd5a3 Wild Type 2 (WT2; n = 10), Srd5a3 Knockout 1 (KO1; n = 10), and Srd5a3 Knockout 2 (KO2; n = 10) Samples. Data produced jointly with Ivan Andújar Martínez and Robert Burock from the Max Planck Institute for Dynamics of Complex Technical Systems. TPH, total peak height; red, decreased % TPH; green, increased % TPH. *N*-glycan names are adapted from Oxford Nomenclature by GlyXera.

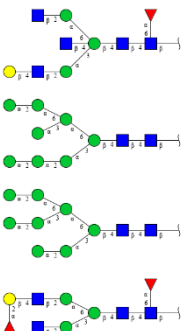
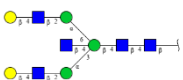
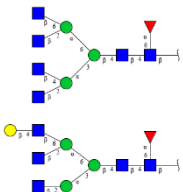
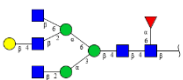
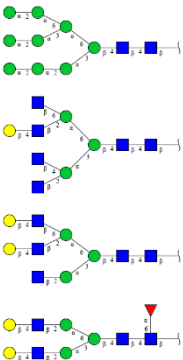
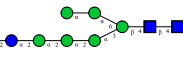
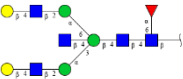
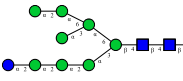
Peak	N-glycan structures	N-Glycan Names	Relative Peak Heights (%TPH)			
			WT1	WT2	KO1	KO2
1	—	—	0.777	0.565	0.335	—
2		A4G4S4(2,3)	—	—	0.824	—
3		A2G2S2(2,6)	1.161	1.221	1.677	0.433
4		FA2G2S1(2,6)S1(2,3)	0.544	0.590	—	0.229
5		Man3[b] A2G2S1(2,6)S1(2,3)	2.712	2.665	2.212	1.161
6	—	—	1.013	1.261	—	—
7		Man3 Man3[c]	2.526	2.036	4.635	10.132

8		FA3G3S3(2,3)[2,6] FA2G2S2(2,6)	2.381	2.471	2.821	—
9		FA2G2S2(2,6) A1G1S1(2,3)[6] A2G2S2(2,3)	4.968	4.882	5.147	5.954
10		FA2BG2S2(2,6)	6.636	6.554	3.754	2.156
11	—	—	2.262	2.229	1.004	0.441
12	—	—	—	—	0.923	0.457
13		FA2G2S2(2,3)	3.433	3.799	2.846	1.433
14	—	—	0.812	0.883	0.630	0.310
15		A4G4S3(2,3) FA2F1(1,3)G2S2(2,3)	0.792	0.849	1.308	0.872
16		FMan3	1.352	1.432	0.952	0.426
17		FA1G1S1(2,3)	0.874	0.840	—	—

18		FA4G4S3(2,3) FA2G2F2(1,3)S2(2,3) Man4↑ A2G1S1(2,3)[3]	0.836	0.746	0.930	1.060
19		Man3-B Man4↓ A1G0[3] A1G0[6] FA2G1S1(2,6) A2F1(1,3)[6]G1[6]S1(2,3)[6]	10.038	11.393	6.016	5.033
20		FA2G1S1(2,6)	2.057	2.157	1.311	0.650
21		FA2G1S1(2,3)[6] A2F1(1,3)[3]G1[3]S1(2,3)[3]	1.037	1.069	—	—
22	—	—	—	—	0.704	0.437
23	—	—	0.528	—	—	—
24		A2G2S1(2,6)	2.175	2.385	1.620	0.806
25		FA2G1S1(2,3)	0.997	—	0.740	0.420

26		A2G2S1(2,3)[3]	0.829	—	0.573	0.419
27	—	—	0.840	0.825	—	—
28		FA2G2S1(2,6) Man5 FA1G0[3] A2F1(1,3)G2S1(2,3) [6]	12.666	12.287	12.358	12.319
29		A4G4S2(2,3) A2G0 A4G4S2(2,3)	—	0.872	1.070	0.790
30		FA2BG2S1(2,6) FA2G2S1(2,3)[6] A4G4S2(2,3)	0.918	0.971	0.806	0.361
31		FA2G2S1(2,3)[3]	1.024	1.154	1.014	0.473
32	—	—	0.364	—	0.340	—
33		FA2F1(1,3)G2S1(2,3) [3]	0.876	0.977	0.560	0.239
34		Man6	5.989	6.031	9.227	9.541

35		FA2G0	1.314	1.468	1.157	0.764
36		FA1G1[3]	0.426	—	—	—
37		FA2BG0 FA3G3S1(2,3)[2,6]	4.964	5.862	3.268	1.690
38	—	—	0.482	0.590	—	—
39		Man7[D1]	1.206	1.285	2.009	2.117
40		Man7[D3]	2.720	2.741	3.174	4.302
41		FA2G1[6]	—	—	0.338	—
42		A3G1[2,6] A3G1[2,4]	0.635	0.686	0.430	—
43		A3G1[2,4] FA2BG1[6]	1.624	1.885	1.244	0.602
44	—	—	—	—	—	0.471

45		FA2BG1[3] Man8[D1,D3] Man8 FA2G1F1(1,2)[6]	4.431	4.352	6.297	8.434
46		A2BG2	—	—	0.331	0.435
47		FA4G0 FA3G1[2,6]	0.433	—	0.360	0.325
48		FA3G1[2,6]	1.705	1.907	1.205	0.486
49		Man9 A4G1 A3G2[2,6] FA2G2	4.261	4.063	9.405	15.782
50		Man6Glc2 (?)	—	—	—	0.564
51		FA2BG2	0.434	0.502	0.359	—
52		Man8Glc1	0.429	0.457	0.961	1.358
53	—	—	0.337	—	—	—

Supplementary information

<b>54</b>		Man9Glc1	0.631	0.476	2.278	4.563
<b>55</b>	—	—	0.551	0.585	0.405	—
<b>56</b>		Man8Glc2 (?)	—	—	0.442	0.803
<b>57</b>		Man9Glc2 (?)	—	—	—	0.753

## 11. Danksagung

Mein besonderer Dank gilt Prof. Dr. Britta Brügger für ihre Rolle als Erstgutachterin dieser Arbeit. Mit ihrer engagierten Betreuung und der stets angenehmen Atmosphäre bei den jährlichen TAC-Meetings hat sie maßgeblich zum Erfolg dieses Projekts beigetragen. Ihre klaren Rückmeldungen und klugen Anregungen haben mir immer wieder wichtige Impulse gegeben und mich motiviert dranzubleiben.

Ebenso danke ich PD Dr. Christian Thiel, der mir die Möglichkeit gegeben hat, meine Forschung in seiner Arbeitsgruppe durchzuführen und diese Dissertation dort zu verfassen. Für seine ständige Unterstützung und sein großes Vertrauen bin ich ihm besonders dankbar. Gerade in sehr komplizierten persönlichen Phasen hat er mir den nötigen Freiraum gelassen und mich nie hängen lassen – ohne diese Rückendeckung wäre dieses Projekt für mich niemals möglich gewesen.

Ein weiterer Dank geht an Dr. Mirko Völkers für seine hilfreichen Diskussionen und seinen konstruktiven Input während der TAC-Meetings. Auch Dr. Josephine Bageritz sowie Prof. Dr. Alexander Dalpke danke ich herzlich für ihre Teilnahme an meiner Abschlussprüfung.

Besonders bedanken möchte ich mich bei Virginia Geiger – für ihr offenes Ohr, ihre Geduld und dafür, dass sie mir mehr als einmal im Labor den ‚Allerwertesten‘ gerettet hat. Ihre Suchfähigkeiten, wenn mal wieder etwas für mich unauffindbar war, haben mich jedes Mal aufs Neue beeindruckt. Ich bin wirklich froh, dass wir uns das Labor teilen durften. Sorry an dieser Stelle für die Dauerbeschallung – ich hoffe, ich habe dich nicht komplett in den Wahnsinn getrieben.

Außerdem ein großes Dankeschön an die Kolleginnen der CDG-Routinediagnostik, Simone Hengst und Karolin Schaefer. Beide haben mir jederzeit mit ihrem fachlichen Wissen zum ‚Robert‘ zur Seite gestanden und mich mit Patientenmaterial versorgt.

Und was wäre eine Doktorarbeit ohne Mit-Doktoranden und Studis? Definitiv um einiges langweiliger. Der größte Dank geht hier an Dr. Kristina Falkenstein. Was mit meiner Einarbeitung begann – bei der du mir geduldig das 1x1 im Labor beigebracht hast – endete schließlich bei selbstgemachten Cocktails und dem ein oder anderen Fusel-Freitag. Besser konnte man ein Wochenende kaum starten. Auch die stressigen Phasen haben wir gemeinsam mit Virginia immer mit einer guten Portion



Humor weggesteckt – das hat den Alltag im Labor für mich enorm erleichtert. Ebenso danke ich meinen beiden Bachelor-Student:innen, Maté Vadja und Fabienne Rech, für viele lustige und schöne Momente. Und nicht zuletzt hat es mich sehr gefreut, im letzten Drittel noch neue Kolleg:innen aus den Nachbarlaboren kennengelernt zu haben – auch euch danke ich für euren Beitrag dazu, den täglichen Wahnsinn eines PhDs auszuhalten.

Ein dickes Dankeschön geht auch an die Fisch-Ladies, Kaisa Pakari und Encarnación Sánchez, sowie an Dr. Thomas Thumberger. Ihr habt mich fachlich immer top beraten und bei allem unterstützt. Ohne euch hätte ich auch wahrscheinlich nicht meine heißgeliebte Espressomaschine gekauft – allein dafür schulde ich euch schon einen riesiges Dankeschön. Außerdem möchte ich Prof. Dr. Jochen Wittbrodt danken dafür, dass ich in seiner Facility die Experimente durchführen durfte und mir die notwendigen Materialien bereitgestellt wurden.

Natürlich möchte ich mich auch bei meinen Freunden bedanken. Egal wie dunkel oder schwierig es manchmal wurde – ich wusste immer, dass ich mich auf euch verlassen kann. Ihr habt mich aufgebaut und mir in all dem Chaos immer wieder ein Stück Normalität gegeben.

Ein besonders großes Dankeschön geht auch an meine Freundin Dr. Sevinj Sultanli, die trotz eigener Herausforderungen immer für mich da war und mich in diesen Zeiten emotional aufzufangen und an mich geglaubt hat.

Zu guter Letzt: Danke an meine Familie. Ohne euch wäre ich gar nicht erst in diese Position gekommen. Mama und Pa – ihr habt wirklich alles gegeben, um mich zu unterstützen, nicht nur in den letzten Jahren. An dieser Arbeit habt ihr einen viel größeren Anteil, als ihr vielleicht denkt. Danke für alles!